GFZ

Helmholtz-Zentrum
POTSDAM

HELMHOLTZ-ZENTRUM POTSDAM
DEUTSCHES
GEOFORSCHUNGSZENTRUM

Ansgar Schepers

Effects of Fluid-Rock Interactions on Electrical Conductivity and Permeability of Feldspar-rich Sandstones

Scientific Technical Report STR12/07

www.gfz-potsdam.de

HELMHOLTZ
GEMEINSCHAFT

Imprint

Helmholtz Centre Potsdam
GFZ German Research Centre for Geosciences

Telegrafenberg
D-14473 Potsdam

Printed in Potsdam, Germany
May 2012

ISSN 1610-0956

DOI: 10.2312/GFZ.b103-12079
URN: urn:nbn:de:kobv:b103-12079

This work is published in the GFZ series
Scientific Technical Report (STR)
and electronically available at GFZ website
www.gfz-potsdam.de > News > GFZ Publications

Ansgar Schepers

Effects of Fluid-Rock Interactions on Electrical Conductivity and Permeability of Feldspar-rich Sandstones

Doctoral thesis submitted to the

Faculty of Geosciences
Ruhr-Universität Bochum

in partial fulfillment of the requirements for the degree of
doctor rerum naturalium (Dr. rer. nat.)

April 2012

Scientific Technical Report STR12/07

Scientific Technical Report STR 12/07
DOI: 10.2312/GFZ.b103-12079

Effects of Fluid-Rock Interactions on Electrical Conductivity and Permeability of Feldspar-rich Sandstones

Doctoral thesis submitted to the
Faculty of Geosciences
Ruhr-Universität Bochum
in partial fulfillment of the requirements for the degree of
doctor rerum naturalium (Dr. rer. nat.)

submitted by
Ansgar Schepers

Thesis committee

Professor Jörg Renner
Assistant Professor Thomas Müller
Professor Michael Alber

Defense of doctoral thesis April 20, 2012

Bochum, 2012

Scientific Technical Report STR 12/07
DOI: 10.2312/GFZ.b103-12079
Deutsches GeoForschungsZentrum GFZ

Scientific Technical Report STR 12/07
DOI: 10.2312/GFZ.b103-12079

Contents

Scientific Technical Report STR 12/07
DOI: 10.2312/GFZ.b103-12079

Scientific Technical Report STR 12/07
DOI: 10.2312/GFZ.b103-12079

Scientific Technical Report STR 12/07
DOI: 10.2312/GFZ.b103-12079

Scientific Technical Report STR 12/07
DOI: 10.2312/GFZ.b103-12079

Symbols and Abbreviations

Symbol	Description	Units
A	area or a geometrical parameter in the model by Sen et al. (1988)	m^2, $S\,m^2/eq$
A^*	pre-exponential proportionality factor in the Arrhenius equation	s^{-1}
a	empirical parameter in Archie's law	
α_x	temperature correction coefficient for electrical conductivity	$°C^{-1}$
α_f	temperature correction coefficient for electrical conductivity of fluids	$°C^{-1}$
α_r	temperature correction coefficient for electrical conductivity of rocks	$°C^{-1}$
α_s	temperature correction coefficient for electrical conductivity of mineral surfaces in contact with a fluid phase	$°C^{-1}$
α_i	degree of dissociation of ionic materials in solution	
B	geometric factor in the percolation model by Mavko and Nur (1997)	
$B = \mu_{\mathrm{dl}}$	ionic mobility in the double layer	$S\,m^2/eq$
C	a geometrical parameter in the model by Sen et al. (1988)	$S\,m^2/eq$
c_i	concentration of dissolved ionic species i	mol/L
χ	volume fraction of clay minerals in the bulk sample	m^3/m^3
D	fractal dimension	
d	particle diameter or distance	m
ΔG_r	change in Gibbs energy of reaction	J/mol
ΔG_f^0	standard Gibbs energy of formation from the elements	J/mol
ΔH_r	enthalpy of reaction	J/mol
ΔH_f^0	standard enthalpy of formation from the elements	J/mol
ΔS_f^0	standard entropy of formation from the elements	J/mol K
E	electrical field or a geometrical parameter in the model by Sen et al. (1988)	V/m, $S\,m^2/eq$
eq	equivalent, $\mathrm{eq}_i = n_i z_i$, where n and z are the amount of substance and the valence of ion i, respectively	mol

Scientific Technical Report STR 12/07
DOI: 10.2312/GFZ.b103-12079

η	dynamic viscosity	$\mathrm{Pa\,s}$
F	formation resistivity factor	
F^*	formation resistivity factor for shaly sandstones	
f_i	mass fraction of element i in the solid material	g/g
ϕ	porosity	$\mathrm{m^3/m^3}$
g	standard gravity	$\mathrm{m/s^2}$
γ	phase angle in impedance measurements	rad
I	electrical current	A
K	hydraulic conductivity	m/s
K_s	solubility constant	
k	permeability	$\mathrm{m^2}$
k^*	rate constant of a thermally activated process	$\mathrm{s^{-1}}$
L	length	m
l	microscopic real path length	m
m	mass or cementation exponent in Archie's law or dynamic radius	g, m
μ_{dl}	ionic mobility in the double layer	$\mathrm{S\,m^2/eq}$
μ_i	ionic mobility	$\mathrm{m^2/s\,V}$
n	amount of substance	mol
nl_i	apparent mass loss of element i from the solid material	$\mathrm{mol/m^2}$
$P_{\mathrm{p,w}}$	wetted pore perimeter	m
p	pressure or an exponent which represents the connectivity of the clay minerals in the model by Glover et al. (2000)	Pa
p_c	confining pressure	Pa
p_{eff}	effective pressure, $p_{\mathrm{eff}} = p_c - p_p$	Pa
p_p	pore pressure	Pa
Q_v	volume concentration of clay exchange cations	$\mathrm{eq/m^3}$
q	specific discharge (Darcy velocity)	m/s
R	electrical resistance	Ω
R^*	gas constant	$8.314\ \mathrm{J/mol\,K}$
Re	Reynolds number	
r	radius	m
r_i	hydrated radius of ionic species i	m
r_{dis}	apparent dissolution rate	$\mathrm{mol\,m^{-2}\,s^{-1}}$
ρ	density	$\mathrm{g/m^3}$
SA	specific surface area	$\mathrm{m^2/g}$
$\mathrm{SA_v}$	surface area of the pores per unit volume of solids	$\mathrm{m^2/m^3}$
σ_c	electrical conductivity of clay minerals	S/m

Scientific Technical Report STR 12/07
DOI: 10.2312/GFZ.b103-12079

σ_f	electrical conductivity of fluids	S/m
σ_g	electrical conductivity of the grain matrix	S/m
σ_s	electrical conductivity of the mineral surface in contact with a fluid phase	S/m
σ_r	electrical conductivity of rocks and porous solids	S/m
T	temperature	°C
T_0	standard temperature	25 °C
T_{abs}	thermodynamic temperature	K
t	time	s, h, d
τ_e	electrical tortuosity	m/m
τ_h	hydraulic tortuosity	m/m
U	voltage, electrical potential	V
U_{str}	streaming potential	V
$\dot{V}$	flow rate	m^3/s
v	average velocity	m/s
v_i	stoichiometric content of element i in a mineral	
Z	impedance	Ω

Abbreviation	**Description**
a.u.	arbitrary units
BET	Brunauer-Emmett-Teller method
BSE	back-scattered electrons
b.r.	batch reactor
CT	computed tomography
d.s.	dry sieved
EDL	electrical diffuse layer
EDX	energy dispersive X-ray spectroscopy
EELS	electron energy loss spectroscopy
EMPA	electron microprobe analysis
FEP	fluorinated ethylene propylene
FIB	focused ion beam
HAADF	high-angle angular dark field imaging
HPT	high pressure and temperature (permeameter)
HRTEM	high resolution transmission electron microscopy
IAP	ion activity product
IC	ion chromatography
ICP-OES	inductively coupled plasma - optical emission spectroscopy
MIP	mercury intrusion porosimetry
m.s.	mineral surface

Scientific Technical Report STR 12/07
DOI: 10.2312/GFZ.b103-12079

n.a.	not applicable, not analyzed
n.k.	not known
p.a.	pro analysis
p.b.r.	pressurized batch reactor
PEEK	polyether ether ketone
PTFE	polytetrafluorethylene
PRV	pressure relief valve
QL	quartz–labradorite-andesine
QLM	quartz–labradorite-andesine–microcline
QLMI	quartz–labradorite-andesine–microcline–illite
QLMIC	quartz–labradorite-andesine–microcline–illite–calcite
SE	secondary electrons
SEM	scanning electron microscopy
SI	saturation index
SMA	simple moving average
S.p.	Stern plane
SST	sandstone
STEM	scanning transmission electron microscopy
TEM	transmission electron microscopy
u.c.	ultrasonically cleaned
w.s.	wet sieved
XRD	X-ray powder diffraction
XRF	X-ray fluorescence spectroscopy

Scientific Technical Report STR 12/07
DOI: 10.2312/GFZ.b103-12079

Abstract

In the course of this study, laboratory experiments and hydrogeochemical simulations in the system quartz–feldspar–clay-minerals–water were conducted within the context of low enthalpy geothermal energy production from deep sedimentary reservoirs. To constrain the effects of fluid-rock interactions on permeability under hydrothermal in situ conditions, an interdisciplinary approach covering rock physical, petrological and hydrogeochemical methods was applied. In this study long term hydrothermal batch and flow-through experiments were conducted with feldspar-rich porous materials at temperatures up to approximately 170 °C, under hydrostatic pressure conditions, and durations up to approximately 4 months to investigate the influence of dissolution-precipitation reactions on the rock physical transport properties, electrical conductivity of rocks, σ_r, and permeability k. This study contributes to a risk assessment of the long term evolution of k of deep sedimentary geothermal reservoirs in the North German Basin by means of the investigation of model systems.

Long term flow-through experiments were conducted in a flow-through apparatus (HPT-permeameter). Feldspar-rich sandstones (Lower Permian, Upper Rotliegend Flechtinger sandstone), pure quartz arenites (Fontainebleau sandstone), as well as sandwich samples containing a quartz-feldspar granular aggregate of defined grain size and composition were investigated. Complementary, batch experiments were performed with quartz-feldspar granular aggregates and Rotliegend rock samples to constrain the mechanisms and kinetics of potentially occurring hydrothermal reactions. The starting fluids of the experiments ranged from deionized H_2O to 2 mol/L $NaCl_{aq}$ solution. σ_r was continuously monitored in flow-through experiments while the electrical conductivity of fluids, σ_f, and k were discontinuously measured in the flow-through and batch experiments. Chemical fluid analyses were performed with ICP-OES and IC to constrain the concentrations c_i of the system's major cations ($i = Na^+, Al^{3+}, Si^{4+}, K^+, Ca^{2+}$) and anions ($i = Cl^-, SO_4^{2-}$), respectively. pH was measured on fluid aliquots. Based on the chemical inventory of the fluid-solid system, the hydrothermal reactions were modeled with PHREEQC. Aliquots of the solid materials were characterized before and after the experiments with BET, EMPA, MIP, SEM, TEM, and XRD. One Rotliegend sample was analyzed with X-ray CT before and after a flow-through experiment to image the pore space in situ.

Heating and cooling cycles during the flow-through experiments triggered thermo-mechanical k-changing effects, i.e., k decreased with temperature and only partly recovered upon cooling. Fluid exchange procedures, in which $NaCl_{aq}$ solutions were replaced by fluids with lower salinities and H_2O (and vice versa), resulted in k reduction due to the swelling behavior of clay-minerals in the illite-bearing Rotliegend rock samples. Electrical conductivities σ_r and σ_f as well as c_i and k showed time dependent changes at constant temperature and pressure in the course of the experiments. Increases of σ_r and σ_f with decreasing rates with time resulted from kinetically controlled changes of c_i due to dissolution-precipitation reactions in the fluid-solid systems. Apparent activation energies of the σ_r evolution at constant temperature and pressure were within the range of activation energies of the dissolution of silicates in aqueous solutions ($\approx 60 \times 10^3$ J/mol). Changes in pore throat radius distribution and in the formation factor indicated that dissolution-precipitation processes led to a mass redistribution

Scientific Technical Report STR 12/07
DOI: 10.2312/GFZ.b103-12079

in the pore space, the clogging of narrow pores and pore throats, and consequently to an increasing hydraulic tortuosity, which resulted in a k impairment of the flown-through samples at constant temperature and pressure. Reaction products were identified as sub-micrometer sized amorphous particles on mineral grains resulting from batch and flow-through experiments with granular aggregates.

The following implications for geothermal energy production from deep sedimentary reservoirs arising from this laboratory based model study can be identified: Disequilibrium conditions between the fluid and the porous feldspar-rich rocks at in situ reservoir temperatures hold the potential of inducing the precipitation of secondary minerals in the pore space. The precipitates increase the hydraulic tortuosity of the porous rocks leading to formation damage.

Scientific Technical Report STR 12/07
DOI: 10.2312/GFZ.b103-12079

1 Introduction and Scope

1.1 Introduction

Fluids in rocks are agents of energy and matter transport and contribute to changes in the mechanical and chemical properties of rocks in the earth's crust during alteration in diagenesis and metamorphism. The effects of fluids in the earth's crust on mechanical and chemical properties of rocks have been widely studied and are a subject of ongoing research. It has been shown that water is prevalent in the crust and is involved in many metamorphic reactions leading to mineralogical and structural changes of rocks (e.g., Etheridge et al., 1983, 1984; Watson and Brenan, 1987; Brenan and Watson, 1988). Dissolution-precipitation reactions change the composition of mineral assemblages during reequilibration of rocks in metamorphism (e.g., Putnis, 2009; Putnis and Austrheim, 2010; Putnis and John, 2010). Fluids influence the deformation of rocks by mechanical means and by complex chemical reactions (e.g., Carter et al., 1990; Hickman et al., 1995; Yardley, 2009). Transport of fluids through the crust occurs on the grain scale up to the scale of tectonic plates due to mechanical and chemical feedbacks between fluids and rocks (e.g., Jamtveit and Yardley, 1997; Jamtveit and Austrheim, 2010). The processes leading to changes of the mechanical and chemical properties of rocks due to the presence of a fluid phase are commonly referred to as fluid-rock or water-rock interactions (e.g., Stober and Bucher, 2002).

Fluid-rock interactions not only play an important role in diagenesis and metamorphism but also in geotechnical applications, such as nuclear waste storage (e.g., Long and Ewing, 2004), acid mine drainage (e.g., Lefebvre et al., 2001), CO_2 storage (e.g., Matter and Kelemen, 2009), and geothermal energy production (e.g., Kühn et al., 2002). An important issue in geotechnical applications is to assess the effects of fluid-rock interactions on rock physical transport properties, especially on the permeability. Current research in this field addresses questions of dissolution, transport, precipitation as well as of feedbacks between these processes leading to alterations of thermal, hydraulic, mechanical, and chemical properties of fluid-rock systems (e.g., Shao et al., 2009). Specific processes involve, e.g., the dissolution of clayey or concrete barriers, cap rocks, or primary minerals comprising an aquifer rock (e.g., Giggenbach, 1981; Gaucher and Blanc, 2006; Gherardi et al., 2007). Transport has been investigated with respect to, e.g., transport of radioactive nuclides, CO_2, or dissolved ions (e.g., Bachu et al., 1994; Rutqvist and Tsang, 2003; Xu et al., 2006). Precipitation of sparingly soluble phases containing radioactive nuclides, of carbonates (mineral trapping), or of secondary minerals in geothermal applications (scaling) has been widely studied (e.g., Duff et al., 2002; André et al., 2006; Matter and Kelemen, 2009).

Previous investigations of fluid-rock interactions employed field observations, modeling approaches, or laboratory studies. It has been shown by several authors that dissolution and/or precipitation in the pore space and in fractures may lead to changes in pore and fracture geometries, as well as to changes in the chemical state of the fluid-rock system (e.g., Moore et al., 1983; Kühn et al., 1998; Tenthorey et al., 1998; Colón et al., 2004; Yasuhara et al., 2006). Modeling studies of different geothermal energy production scenarios have shown that the

Scientific Technical Report STR 12/07
DOI: 10.2312/GFZ.b103-12079
Deutsches GeoForschungsZentrum GFZ

permeability of geothermal reservoir rocks may increase or decrease depending on the specific situation with respect to rock type, mineralogy, temperature, pressure, and fluid composition (e.g., White and Mroczek, 1998; O'Sullivan et al., 2001; Kühn et al., 2002; André et al., 2006; Xu et al., 2006; Taron and Elsworth, 2009, 2010). For an investigation of the evolution of the permeability of a specific geological or geotechnical setting it is therefore important to address the specific geological, physical, and chemical parameters pertaining to this setting.

The present study investigates the effects of fluid-rock interactions on permeability and the related transport property electrical conductivity of rocks in the context of geothermal energy production from deep sedimentary reservoirs that exist, e.g., in the North German Basin. Geothermal energy production interferes with thermodynamic fluid-mineral equilibria due to the extraction of heat from the fluid-rock system. In the case of geothermal energy production from deep sedimentary reservoirs in the North German Basin, it is assumed that the fluid initially present in the reservoir is approximately at equilibrium with the rock, because of the long residence time of the fluid over geological time scales (Lüders et al., 2010). Thus, it can be expected that after the extraction of heat from the system above ground and the re-injection of the cooled fluid into the reservoir, different dissolution and/or precipitation reactions will be induced when the fluid-rock system approaches a new equilibrium.

The rock physical transport properties permeability and electrical conductivity of rocks are interrelated via porosity, tortuosity, electrical conductivity at mineral-fluid interfaces, electrical conductivity of pore fluids, and the concentrations of dissolved ionic species. These interrelations are described by concepts like Archie's law, the Kozeny-Carman equation, or Kohlrausch's law. It is obvious that redistribution of mass in the course of dissolution-precipitation reactions can lead to changes in porosity or hydraulic tortuosity of a porous rock and thus to permeability changes. Moreover, dissolution-precipitation reactions affect the concentration of dissolved ionic species in the pore fluid, and thus its electrical conductivity. In this study a combined experimental and modeling approach is used to investigate the effects of induced dissolution-precipitation reactions on the evolution of the permeability and the electrical conductivity of porous feldspar-rich materials.

The motivation of the present study is to gain an understanding of the electrical conductivity- and permeability-changing processes that may occur in porous feldspar-rich sandstones of a deep sedimentary geothermal reservoir subjected to heat extraction. Since the reservoir rocks are not directly accessible during heat extraction from the reservoir, experimental work is required approximating the reservoir conditions with respect to pressure, temperature, and chemical inventory in the laboratory. The combination of such laboratory experiments with hydrogeochemical simulations provides insights into fluid-rock interactions occurring at the pore scale. Furthermore, this approach provides insights into fluid-rock interactions between silicates and aqueous fluids that are kinetically inhibited and thus exceed typical laboratory time scales. Limitations of this approach arise from the necessity to simplify the real fluid-rock system to a model system by using analogue materials, relatively small sample sizes, and relatively simple chemical inventories. A further limitation of the present study arises from restricted capabilities of the experimental equipment with respect to pressure and corrosion resistance against hot chloride-bearing corrosive fluids typically encountered in deep sedimentary reservoirs.

Scientific Technical Report STR 12/07
DOI: 10.2312/GFZ.b103-12079
Deutsches GeoForschungsZentrum GFZ

1.2 Previous Work

Electrical conductivity of rocks has been frequently investigated as to its relation to electrical conductivity of the pore fluid, electrical conductivity of mineral-fluid interfaces, and temperature (e.g., Waxman and Smits, 1968; Roberts and Schwartz, 1985; Sen et al., 1988; Sen and Goode, 1992; Glover et al., 1994; Nettelblad et al., 1995; Ruffet et al., 1995; Revil and Glover, 1997; Revil et al., 1998; Revil and Glover, 1998; Roberts et al., 2001). Little data exist on the evolution of the electrical conductivity of rocks in the course of fluid-rock interactions (Piwinskii and Weed, 1976; Weed et al., 1977; Kristinsdóttir et al., 2010).

The evolution of permeability during fluid-rock interactions has been studied by means of laboratory experiments for different hydrothermal fluid-solid systems. Such experiments have been performed with mainly H_2O and secondarily aqueous salt solutions as the fluid phases and granite (e.g., Moore et al., 1983; Morrow et al., 2001), novaculite (e.g., Polak et al., 2003; Yasuhara et al., 2006), sandstone (e.g., Kühn et al., 1998; Tenthorey et al., 2003), synthetic fault gouge (e.g., Tenthorey and Fitz Gerald, 2006; Giger et al., 2007), and granular mineral aggregates (e.g., Aharonov et al., 1998; Tenthorey et al., 1998; Tenthorey and Scholz, 2002) as the solid materials, respectively. Permeability changes due to dissolution-precipitation reactions were not only investigated on porous materials but also on fractured samples (e.g., Lowell et al., 1993; Durham et al., 2001; Polak et al., 2003; Hilgers and Tenthorey, 2004; Yasuhara et al., 2004; Barker et al., 2006; Elsworth and Yasuhara, 2006; Liu et al., 2006; Chaudhuri et al., 2009; Min et al., 2009; Ledésert et al., 2010; Yasuhara et al., 2011).

Investigations of the hydrothermal quartz-feldspar-water system by means of flow-through experiments with H_2O and granular aggregates of quartz and labradorite have shown that the permeability of the aggregates decreased in the course of the experiments even though compaction of the aggregates was negligible and the porosity of the aggregates remained unchanged. It has been conclude that the permeability reductions resulted from dissolution of mainly labradorite and precipitation of zeolites and smectite in narrow pores and pore throats (Scholz et al., 1995; Aharonov et al., 1998; Tenthorey et al., 1998; Tenthorey and Scholz, 2002). Batch experiments with various rock types, including graywacke samples consisting of quartz, feldspar, calcite, dolomite and > 5 % clay minerals, and tap-water at room temperature yielded a time-dependent behavior of the electrical conductivity of the rock samples. Specificly, the electrical conductivity of the rock samples first increased with time with decreasing rate, passed a maximum, and then slightly decreased and approached a constant value. Concurrently, the electrical conductivity of the fluid in contact with the rock samples increased monotonically with time with decreasing rate. The time-dependent behavior of the electrical conductivity of the rock samples and the fluid resulted from dissolution of the minerals in the rock samples (Piwinskii and Weed, 1976; Weed et al., 1977). Flow-through experiments with altered volcanic rock samples (hyaloclastites and basalts containing different clay minerals) saturated with synthetic geothermal fluids yielded a time-dependent increase of the electrical conductivity of the rock samples with decreasing rates at 150 °C constant temperature and constant confining and pore pressure of up to 28×10^6 Pa and 10×10^6 Pa, respectively. It has been concluded that the time-dependent behavior of the electrical conductivity of the rock samples at constant p-T conditions resulted from an ion exchange between the clay minerals and the pore fluid (Kristinsdóttir et al., 2010).

Scientific Technical Report STR 12/07
DOI: 10.2312/GFZ.b103-12079
Deutsches GeoForschungsZentrum GFZ

1.3 Scope of the Study

The present study investigates the evolution of the electrical conductivity and the permeability of rocks, accompanying chemical reactions in the fluid-solid system, by means of laboratory experiments. Electrical conductivity measurements of solid and fluid samples have been used as indicators for time-dependent changes of the chemical state of the fluid-solid system. Hydrogeochemical simulations demonstrate saturation indices of fluid samples with respect to various mineral phases.

Specific questions that are addressed in the present study are:

- Can the electrical conductivity of porous samples be used as a proxy for the porosity and the permeability, as Archie's law and the Kozeny-Carman equation suggest, when the fluid-rock system is subjected to time-dependent chemical changes?
- Can the electrical conductivity of porous samples be qualified as a proxy for time-dependent changes of the electrical conductivity of the pore fluid and the concentration of dissolved ions in the pore fluid of a fluid-rock system under disequilibrium conditions?
- Do disequilibrium conditions lead to dissolution-precipitation reactions and thus to a redistribution of mass in a fluid-rock system?
- How do dissolution-precipitation reactions affect the porosity, the pore space microstructure, and the permeability?
- What is the reaction mechanism of dissolution-precipitation reactions on the pore scale?

In order to answer these questions, experiments and simulations were carried out investigating model systems with respect to solid starting materials, starting fluids, and applied temperature and pressure conditions. The study aimed at imitating situations in a real fluid-rock system located in the subsurface. Temperature conditions and solid starting materials were similar to those in deep sedimentary reservoirs. Yet, pressures were much lower due to limitations of the experimental equipment. Furthermore, the chemical compositions of the starting fluids used in the present study (mainly H_2O and $NaCl_{aq}$ solutions) were simple in comparison to highly saline brines typically encountered in deep sedimentary reservoirs.

The system quartz-feldspar-clay minerals-water approximates feldspar-rich sandstones as geothermal reservoir rocks, such as in the North German Basin where geothermal brine is produced from Lower Permian sandstone reservoirs. An example of such a system is the Groß Schönebeck geothermal doublet system in which the reservoir rocks are located at a depth of approximately 4100 to 4200 m (Milsch et al., 2009; Moeck et al., 2009). Core samples of the reservoir sandstones were heterogeneous with respect to bedding and grain size sorting and yielded variable porosities and permeabilities ranging between 9.8 to 18.3 % and approximately 3 to 100×10^{-15} m^2, respectively. The rocks are mainly composed of quartz ($\approx$ 80 %) and 10 to 20 % feldspar and rock fragments. Small amounts of illite, carbonates, and anhydrite have been found in the solid samples (Trautwein and Huenges, 2005). The reservoir formation pore pressure at this site is approximately 43×10^6 Pa and the vertical stress (the overburden pressure) has been estimated as approximately 10^8 Pa (Moeck et al., 2009). The reservoir temperature is approximately 150 °C. The geothermal fluid is a Ca-Na-Cl type fluid including additional amounts of K, Ca, Mg, Sr, Ba, Fe, Mn, Zn, Pb, Cu, Si, and SO_4 in variable concentrations. The salinity (the total dissolved solids) amounts to $\leq$ 265 g/L (Regenspurg et al., 2010). The

Scientific Technical Report STR 12/07
DOI: 10.2312/GFZ.b103-12079

production-injection scenario in the geothermal doublet system involves the production of the geothermal fluid at approximately 150 °C, conversion of heat into power aboveground, as well as the re-injection into the reservoir at approximately 70 °C. Fluid pressure is maintained at a pressure of $\geq 0.15 \times 10^6$ Pa throughout the geothermal loop to prevent the fluid from boiling and dissolved gases from degassing (Francke and Thorade, 2010).

The present study is structured as follows: After a brief introduction of the theoretical background (Chapter 2), the methodology is explained (Chapter 3). The results of this study are reported in Chapter 4. In Chapters 5 and 6 the results are discussed and conclusions are drawn that are relevant for geotechnical and geothermal applications.

Scientific Technical Report STR 12/07
DOI: 10.2312/GFZ.b103-12079

Scientific Technical Report STR 12/07
DOI: 10.2312/GFZ.b103-12079

2 Theoretical Background

2.1 Transport Properties of Rocks

The electrical conductivity, σ_r, and the permeability k of rocks are important rock physical transport properties. Both transport properties are interrelated via porosity ϕ, tortuosity τ, electrical conductivity at the mineral-fluid interface, σ_s, electrical conductivity of the pore fluid, σ_f, and the concentrations of dissolved ionic species in the pore fluid, c_i. The formation factor F relates the ratio σ_f/σ_r to ϕ and τ (Archie's law). Kohlrausch's law relates σ_f to the square root of c_i. Kozeny-Carman type equations or fractal theory provide the basis for k-ϕ relationships. There is no theoretical reason for universal $k \propto \phi$ or $F \propto \phi$ correlations (Guéguen and Palciauskas, 1994). The diagenetic history of a rock affects the microstructure of the pore space and thus the tortuosity (Bernabé et al., 2003).

Tortuosity is generally defined as the ratio of the microscopic real path length l to the macroscopic apparent (sample) length L, $\tau = l/L$ (Guéguen and Palciauskas, 1994). Hydraulic tortuosity τ_h is principally not identical to the electrical tortuosity τ_e, because the pathways for electrical conduction and hydrodynamic flow can be different in a porous medium (Clennell, 1997). In simple networks with a bivariate channel radius distribution $\tau_e < \tau_h$, but the difference between τ_e and τ_h is small (Dullien, 1992). Numerical simulations on 2D networks representing the pore space in porous rocks have shown that $\tau_h \approx 1.5\,\tau_e$ (David, 1993). However, pore space models utilizing the notion of bundles of capillaries assume that the pathways for electrical conduction and hydrodynamic flow are approximately the same ($\tau_e \approx \tau_h$).

2.1.1 Electrical Conductivity of Rocks

Three processes contribute to the bulk electrical conductivity of rocks: electrical conduction through the pore fluid, through the mineral grains, and at the mineral-fluid interface (Bussian, 1983; Guéguen and Palciauskas, 1994; Revil and Glover, 1997). Silicate grains are regarded as insulators with very low electrical conductivity on the order of 10^{-14} to 10^{-10} S/m at 25 °C (Guéguen and Palciauskas, 1994). Thus, in a porous rock mainly composed of silicate mineral grains and cements, σ_r results primarily from electrolyte conductivity of the fluids in the pore space and from electrochemical interactions at the solid-fluid interfaces (Schön, 1996). The electrical conductivity at the surface of the minerals, σ_s, results from a net structural charge imbalance of minerals causing attraction of counterions from the pore fluid to the mineral-fluid interface (Ruffet et al., 1995). Clay minerals dominantly contribute to σ_s in sedimentary rocks by a permanent negative surface charge. The distribution of charge carriers at the fluid-mineral interface is described by the Gouy-Chapman-Stern model (Figure 2.1). This model consists of H_2O molecules and positive charge carriers (protons) adsorbed to the negatively charged silicate mineral surface - the so-called Stern layer - followed by an electrical diffuse layer, EDL, of hydrated cations and anions. The EDL has a relatively high concentration of hydrated cations in the vicinity of the Stern-layer (Revil and Glover, 1998). With increasing distance from the mineral surface, the relatively high concentration of hydrated cations levels off to

Scientific Technical Report STR 12/07
DOI: 10.2312/GFZ.b103-12079
Deutsches GeoForschungsZentrum GFZ

values of the bulk pore fluid. The Stern layer and the EDL comprise the so-called double layer (Revil and Glover, 1997).

Electrical Conductivity of Fluids

The electrical conductivity of fluids depends on the concentration of ions in solution, c_i, and inter-ionic forces as described by Kohlrausch's law and the Debye-Hueckel-Onsager theory, as well as on the drift speed of the ions in solution, v_i. The drift speed in an externally applied electrical field E is governed by the ions' acceleration due to their valence z_i and an opposing force, the viscous drag, which is dependent on the hydrated ionic radii r_i and the viscosity of the fluid, η (Stokes' law). The mobility of ions in solution, μ_i, is defined by the ratio of the drift speed to the magnitude of the electrical field $\mu_i = v_i/E$ or equivalently by $\mu_i = z_i/6\pi\eta r_i$ (Atkins and de Paula, 2006). Hydrated ionic radii increase with the valence of the ions and decrease with atomic number in each group of the periodic table (Volkov et al., 1997; Blume et al., 2010). Hydrated ionic radii follow the order: $r_{Al^{3+}} > r_{Be^{2+}} > r_{Mg^{2+}} > r_{Ca^{2+}} \approx r_{Sr^{2+}} > r_{Ba^{2+}} > r_{Li^{+}} > r_{Na^{+}} > r_{K^{+}} > r_{Rb^{+}} \approx r_{Cs^{+}}$. The mobilities of ions in fluids follow the order: $\mu_{Rb^{+}} \approx \mu_{Cs^{+}} > \mu_{K^{+}} > \mu_{Ca^{2+}} > \mu_{Mg^{2+}} > \mu_{Na^{+}} > \mu_{Li^{+}}$. The dimension of ionic mobility is $L^2\,t^{-1}\,U^{-1}$, where L is length, t is time, and U is voltage (Revil et al., 1998).

The complex interrelations of σ_f, c_i, μ_i, z_i, and the degree of dissociation, α_i, are subjects of ongoing investigations and beyond the scope of this study (e.g. Bagchi, 1998; Chandra and Bagchi, 1999; Corti et al., 2004; Atkins and de Paula, 2006). However, σ_f is formally proportional to the sum of z_i, μ_i, c_i, and α_i, for low concentrations of ions in solution (Schön, 1996):

$$\sigma_f \propto \sum_{i=1}^{n} \alpha_i\, c_i\, z_i\, \mu_i, \tag{2.1}$$

where n components contribute to σ_f.

Temperature influences the viscosity of a fluid and thus the ions' drift speeds in the fluid leading to a temperature dependence of σ_f. This dependence is linear and can be calculated for a given temperature using (Revil et al., 1998):

$$\sigma_x(T) = \sigma_x(T_0)\,[1 + \alpha_x\,(T - T_0)], \tag{2.2}$$

with $x = f, s$, where subscripts f and s represent fluid and surface, respectively. The reference temperature is $T_0 = 25\,^{\circ}\mathrm{C}$, the temperature correction coefficients are $\alpha_f \approx 0.023\,^{\circ}\mathrm{C}^{-1}$ and $\alpha_s \approx 0.040 \pm 0.002\,^{\circ}\mathrm{C}^{-1}$ for Na^{+}. Values of α_s for other ions are reported in the literature (Revil and Glover, 1998).

Formation Resistivity Factor

The formation resistivity factor, F, is the ratio of σ_f to σ_r and is defined for fully fluid-saturated porous media in which electrolytic conduction of the pore fluid is the dominant conduction mechanism ($\sigma_f >> \sigma_s$). The pore space geometrical properties, i.e., the microstructure and the porosity, govern F (Revil et al., 1998). The porosity is related to F by the empirically derived Archie's law (Archie, 1942):

$$F = \frac{\sigma_f}{\sigma_r} = \phi^{-m}, \tag{2.3}$$

Scientific Technical Report STR 12/07
DOI: 10.2312/GFZ.b103-12079

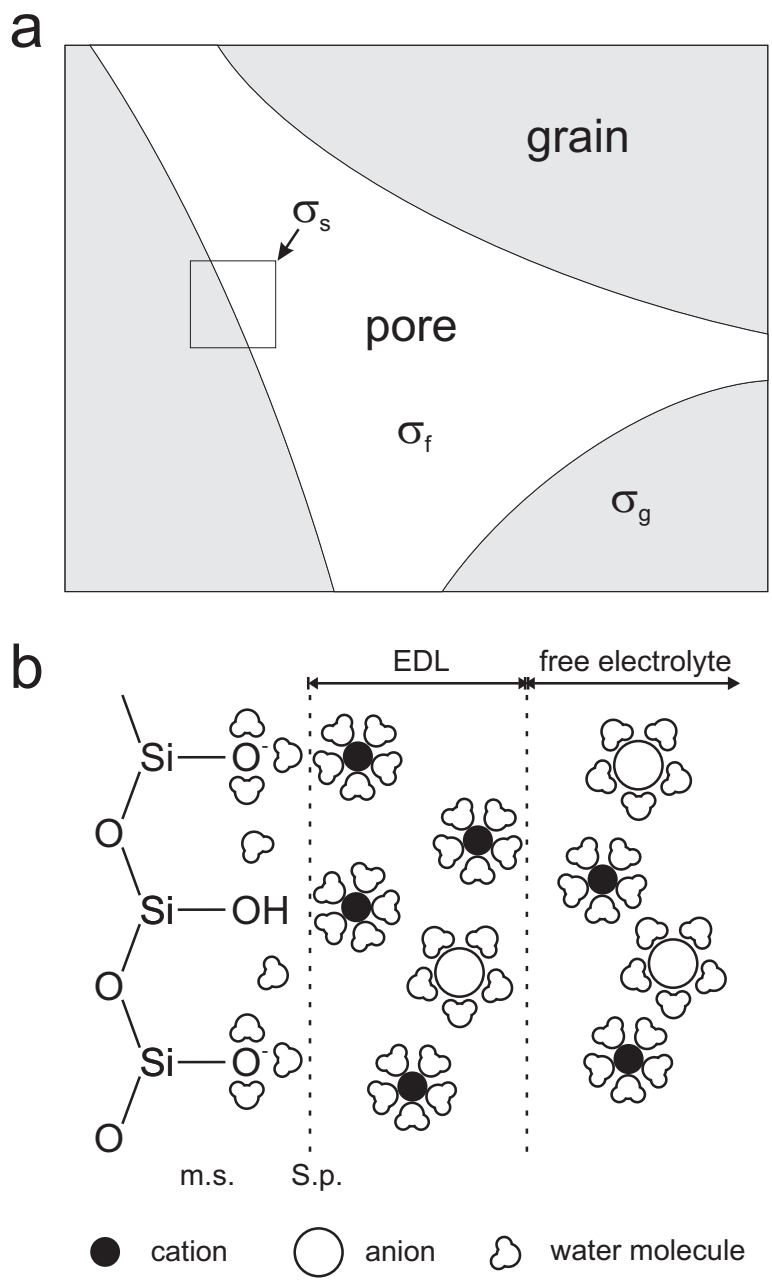

Figure 2.1: Schematic of the different conductivities within a porous sedimentary rock. The macroscopic situation is represented in a). The gray areas are the silicate grains and the white area is a pore. A magnification of the situation at the silicate mineral-fluid interface (the small rectangle) shows the distribution of charge carriers as described by the Gouy-Chapman-Stern model (b). EDL, m.s., and S.p. denote the electrical diffuse layer, the negatively charged silicate mineral surface, and the Stern plane, respectively. The (water) molecules directly adsorbed to the mineral surface comprise the Stern layer. The Stern layer and the EDL comprise the double layer (modified after: Revil and Glover, 1997).

Scientific Technical Report STR 12/07
DOI: 10.2312/GFZ.b103-12079

where m is the cementation exponent ranging between 1.5 and 2.5 for most sedimentary rocks. The majority of sandstones exhibits m values close to 2 (Guéguen and Palciauskas, 1994). Due to the practical importance of Archie's law, which relates the relatively easy measurable properties σ_f and σ_r to the important reservoir property ϕ, many authors have extended Equation 2.3 to better fit experimental data of different reservoir rocks (Schön, 1996). For example, the empirical parameter a has been introduced to give:

$$F = \frac{\sigma_f}{\sigma_r} = \frac{a}{\phi^m}, \tag{2.4}$$

with $a = 0.62$ and $m = 1.95$ for well-cemented Paleozoic sedimentary rocks with a porosity range from 5 to 25 % (Keller, 1989). The Rotliegend (Flechtinger) sandstone used in the present study falls into this porosity range (Table 3.1). The parameters a and m are related to the electrical tortuosity yielding (Schön, 1996):

$$F = \frac{\sigma_f}{\sigma_r} = \frac{a}{\phi^m} = \frac{\tau_e}{\phi}. \tag{2.5}$$

Electrical Conductivity of Mineral-Fluid Interfaces

The electrical conductivity of mineral-fluid interfaces is in general dependent on ionic conduction in the double layer (Figure 2.1). Mobilities of counter cations in the double layer follow the order: $\mu_{\mathrm{dl,Na^+}} > \mu_{\mathrm{dl,Li^+}} > \mu_{\mathrm{dl,K^+}} > \mu_{\mathrm{dl,Rb^+}} > \mu_{\mathrm{dl,Cs^+}} > \mu_{\mathrm{dl,Ca^{2+}}} > \mu_{\mathrm{dl,Mg^{2+}}}$ (Revil et al., 1998). The mobility of counter cations in the double layer depends on hydrated ionic radii, the valence of the counter cations, as well as on temperature. In the case of interfaces between pore fluids and silica or aluminosilicates, the conduction through the electrical diffuse layer is comparatively small and can be neglected (Revil and Glover, 1997, 1998). Thus, at pH-values between 5 and 8, σ_s is governed by the mobility of hydrated counter cations and protons adsorbed to the mineral surface in the Stern layer. The sites for adsorption on the silica and aluminosilicate mineral surfaces are already occupied at very low concentrations of dissolved ions. As a consequence, the electrical conductivity of mineral-fluid interfaces in shaly sands, saturated with a NaCl-bearing pore fluid at $T = 25$ °C, is independent of concentration, if $c_i > 10^{-3}$ mol/L (Revil et al., 1998). An interpretation of this observation combined with Equation 2.2 suggests that the relative contribution of σ_s to σ_r increases with temperature, because $\alpha_s > \alpha_f$, and decreases with the salinity of the pore fluid.

Models for Electrical Conductivity of Clay-bearing Sedimentary Rocks

Most models for the electrical conductivity of clay-bearing sedimentary rocks with significant surface conductivity are based on the fundamental concept of a parallel conductor system (Schön, 1996). In general, the models can be subdivided into two groups. One group consists of empirically derived models on the basis of Archie's law. The other group consists of mixing models or effective medium models constructed on the basis of studies by Maxwell and Wagner (e.g., Wagner, 1914; Bruggeman, 1935; Hanai, 1960; Hashin and Shtrikman, 1963).

A simple model adds a constant surface conductivity term, σ_s, to Archie's law (David et al., 1993). So, Equation 2.3 becomes:

$$\sigma_r = \phi^m \sigma_f + \sigma_s. \tag{2.6}$$

Scientific Technical Report STR 12/07
DOI: 10.2312/GFZ.b103-12079
Deutsches GeoForschungsZentrum GFZ

This model yields a straight line with slope $1/F$ or ϕ^m and a y-axis intercept equal to σ_s at $\sigma_f = 0$ S/m in a linear plot σ_r versus σ_f.

Archie's law has been extended by an empirically derived term for the contribution of electrical conduction at mineral-fluid interfaces to σ_r (Waxman and Smits, 1968):

$$\sigma_r = \phi^m \left(BQ_v + \sigma_f\right), \tag{2.7}$$

with

$$B = [1 - 0.6 \exp(-\sigma_f/1.3)]\, 0.0046, \tag{2.8}$$

where B is in $\mathrm{Sm}^2/\mathrm{eq}$ and is originally described as the equivalent conductance of clay exchange cations (Na^+) as a function of σ_f at 25 °C. An important feature of the model is that the conduction pathways for σ_s are the same as the conduction pathways for σ_f. Thus, the tortuosities of both pathways are assumed to be identical. The term B is equal to the mobility of ions in the double layer, $B = \mu_{\mathrm{dl}}$ (Ruffet et al., 1995; Glover et al., 2000). The unit of Q_v is $\mathrm{eq/m}^3$ and it is originally described as the volume concentration of clay exchange cations. The product BQ_v is equal to the electrical conductivity of clay minerals, σ_c, and is not constant but depends on σ_f (Glover et al., 2000). The quantity eq_i of an ion i is an equivalent and is defined as $\mathrm{eq}_i = n_i\, z_i$, where n_i is the amount of substance and z_i is the valence of the respective ion. The model was fitted to data obtained from 27 samples of clay-bearing sandstones and a large number of other rock types. Waxman and Smits (1968) introduced the formation resistivity factor for shaly sandstones, F^*, being the inverse of the slope of a linear σ_r versus σ_f plot.

An empirical model for clay-bearing sandstones has been fitted to data from 140 core samples of clay-bearing sandstones by introducing geometrical fitting parameters (Sen et al., 1988). This model is based on a physical model for spherical particles coated with a layer of constant conductivity (Johnson and Sen, 1988). The empirical model is:

$$\sigma_r = \phi^m \frac{\sigma_f + AQ_v}{1 + (CQ_v/\sigma_f)} + EQ_v, \tag{2.9}$$

where A, C, and E are constants depending on the pore space geometry and the effective mobility of ions in the double layer. Moreover, $A = \mu_{\mathrm{dl}}\, m$ (in the original formulation of Johnson and Sen (1988) m has a different value than the cementation exponent, but Sen et al. (1988) have shown that this distinction is not necessary). The ionic mobility in the double layer was estimated to be $\mu_{\mathrm{dl}} = 1.93 \times 10^{-3}\ \mathrm{Sm}^2/\mathrm{eq}$. The term CQ_v is a fitting parameter with a value of 0.7 S/m. The term EQ_v represents the electrical conductivity of the mineral-fluid interface at $\sigma_f = 0$ S/m.

A solution of an effective medium model for granular aggregate of insulating silicate spheres coated by a conductive clay layer is valid for $\sigma_f >> \sigma_s$ (Bussian, 1983; de Lima and Sharma, 1990; Ruffet et al., 1995):

$$\sigma_r = \phi^m \sigma_f + m(1 - \phi^m)\sigma_s, \tag{2.10}$$

with

$$\sigma_s = \frac{2\,\chi\,\sigma_c}{3 - \chi}, \tag{2.11}$$

where σ_c is the electrical conductivity of the clay minerals, and χ is the volume fraction of the

Scientific Technical Report STR 12/07
DOI: 10.2312/GFZ.b103-12079
Deutsches GeoForschungsZentrum GFZ

clay minerals in the bulk sample.

An effective medium modification of Archie's law for two conducting phases is (Glover et al., 2000):

$$\sigma_r = \sigma_s(1-\phi)^p + \sigma_f\,\phi^m, \tag{2.12}$$

with

$$p = \frac{\log(1-\phi^m)}{\log(1-\phi)}, \tag{2.13}$$

where p represents the connectivity of the clay minerals and is related to the electrical tortuosity of σ_s. The different connectivities or tortuosities pertaining to the electrical conduction through the pore fluid and at the clay mineral-fluid interface are represented by variable exponents, m and p, similar to the cementation exponent in Archie's law.

The unknowns in the models presented above are Q_v, σ_c, and σ_s. Mean Q_v values of clay-bearing sandstones with approximately 10 % porosity range between 375 and 645 eq/m^3 (Waxman and Smits, 1968; Sen et al., 1988). Q_v is related to the cation exchange capacitiy of clay minerals by CEC $= Q_v\,\phi/[(1-\phi)\rho_c]$, where ρ_c is the density of a specific clay mineral. The suitable Q_v value for the illite-bearing Flechtinger sandstone (Table 3.1) can be approximated using literature data for the CEC of illite ranging between 10^{-4} and 6×10^{-4} eq/g (Schön, 1996; Blume et al., 2010). The resulting mean value of Q_v of illite is 7788 eq/m^3. Multiplication by the volume fraction of illite in the Flechtinger sandstone, 0.064, yields $Q_v \approx 498$ eq/m^3. This value is close to the mean value of $Q_v = 510$ eq/m^3 for clay-bearing sandstones (Waxman and Smits, 1968; Sen et al., 1988). The electrical conductivity of the clay minerals is calculated by $\sigma_c = \mu_{\mathrm{dl}}\,Q_v$ (Glover et al., 2000). σ_s is related to σ_c by (Johnson et al., 1986; Johnson and Sen, 1988; Ruffet et al., 1995):

$$\sigma_s = \phi^m m\,\mu_{\mathrm{dl}}\,Q_v. \tag{2.14}$$

2.1.2 Permeability

Darcy's law

Darcy's law was stated as an empirical description of flow-through experiments with water and vertically homogeneous sand filters which revealed that the flow rate $\dot{V}$ is proportional to the constant cross-sectional area A, proportional to the difference in hydraulic head across the filter, Δh, and inversely proportional to the length of the sand filter column, ΔL:

$$\dot{V} = K\,\frac{A\,\Delta h}{\Delta L}. \tag{2.15}$$

The coefficient of proportionality, K, is called hydraulic conductivity and is expressed in dimensions of L/t (Bear, 1988). Using the relationship:

$$K = \frac{k\,\rho\,g}{\eta}, \tag{2.16}$$

where η is the dynamic fluid viscosity, g is the standard gravity, k is the permeability, and ρ is the fluid density we obtain:

Scientific Technical Report STR 12/07
DOI: 10.2312/GFZ.b103-12079
Deutsches GeoForschungsZentrum GFZ

$$\dot{V} = \frac{k\,\rho\,g\,A\,\Delta h}{\eta\,\Delta L}. \tag{2.17}$$

Substituting $\rho\,g\,\Delta h$ for the pressure difference over the sample length, Δp, leads to:

$$\dot{V} = A\,\frac{k\,\Delta p}{\eta\,\Delta L}. \tag{2.18}$$

Equation 2.18 represents the form of Darcy's law that was used for the permeability measurements performed in the present study.

The specific discharge, or Darcy velocity, q, is defined as $q = \dot{V}/A$ (Bear, 1988). The Darcy velocity is related to the average velocity v of the fluid in a porous medium with the porosity ϕ by a law attributed to Dupuit and Forchheimer, $v = q/\phi$ (Guéguen and Palciauskas, 1994). Using this law, the Reynolds number Re can be calculated by:

$$\mathrm{Re} = \frac{\rho\,v\,l}{\eta}, \tag{2.19}$$

where l is a characteristic length fixed by the pore dimensions, and ρ is the fluid density. Laminar flow prevails as long as $\mathrm{Re} << 1$ (Guéguen and Palciauskas, 1994). Laminar flow is one of the prerequisites for the validity of Darcy's law in porous materials. Limitations for the validity of Darcy's law arise from, e.g., the compressibility of the pore fluid, interface forces at the internal surface of a porous medium, chemical fluid-rock interactions leading to changes of η, and time-dependent changes of Δp resulting from changes in the pore structure due to hydrodynamic flow (Dullien, 1992; Schön, 1996). Despite these limitations, the applicability of Darcy's law for the determination of permeabilities has been shown for many unconsolidated and consolidated sedimentary rocks (Schön, 1996).

Permeability Models

Permeability models can be subdivided into two groups: models involving networks of capillary tubes and models utilizing the notion of hydraulic radius r_h (Guéguen and Palciauskas, 1994). Under the assumption that the pore space of a porous medium can be approximated by a homogeneous and isotropic distribution of capillaries with average radius r, length l, and distance between the tubes, d, the first group yields:

$$k = \frac{\pi}{8}\,\frac{r^4\,l}{d^3} = \frac{r^2}{8}\,\phi. \tag{2.20}$$

The second group of models yields:

$$k = a\,m^2\phi = \frac{a}{\mathrm{SA}_\mathrm{v}^2}\,\frac{\phi^3}{(l-\phi)^2}, \tag{2.21}$$

where a is a dimensionless constant close to 1, m is the dynamic radius defined by $m = V_p/A_p = r/2$ (r is the radius of cylindrical capillaries), SA_v is the surface area of the pores per unit volume of solids defined by $\mathrm{SA}_\mathrm{v} = A_p/V(1-\phi)$, and ϕ is the porosity. Subscripts p and v refer to pore and volume, respectively. Equation 2.21 is a representation of the classical Kozeny-Carman equation for a bundle of cylindrical capillaries.

A form of the Kozeny-Carman equation including the hydraulic radius, r_h, and a cross section shape factor, χ, is useful for capillary cross section types other than circles (Schön, 1996):

Scientific Technical Report STR 12/07
DOI: 10.2312/GFZ.b103-12079
Deutsches GeoForschungsZentrum GFZ

$$k = \frac{\phi\, r_h^2}{4\,\tau_h^2\,\chi}, \tag{2.22}$$

where τ_h is the hydraulic tortuosity, and the dimensionless values for χ range between 2 and 3. The hydraulic radius is defined by:

$$r_h = 2\,\frac{A_p}{P_{\mathrm{p,w}}}, \tag{2.23}$$

where A_p is the pore cross sectional area normal to flow, and $P_{\mathrm{p,w}}$ is the wetted pore perimeter. In the case of a bundle of cylindrical capillaries, i.e., the classical Kozeny-Carman equation, $\chi = 2$ and $r_h = r$. As a consequence, Equation 2.22 can be written as (Schön, 1996; Pape et al., 1999):

$$k = \frac{\phi\, r^2}{8\,\tau_h^2} = \frac{r^2}{8\,F}, \tag{2.24}$$

where the formation resistivity factor $F \approx \tau_h/\phi$. Equations 2.20 to 2.24 assume a perfect interconnectivity between the capillaries that approximate the pore space of a porous medium.

The concept of percolation theory states that there must be a minimum (critical) threshold porosity, ϕ_c, before a connected cluster of through-going pores exists, which is required for transport through a porous rock (e.g., Kirkpatrick, 1973; Sahimi, 1994; Mavko and Nur, 1997). An expression for packings of spheres with diameter d based on the Kozeny-Carman equation is (Mavko and Nur, 1997):

$$k = B\,\frac{\phi^3}{(1-\phi)^2}\,d^2, \tag{2.25}$$

with $B = 3/2$. To account only for the porosity in excess of the minimum (critical) threshold porosity ϕ can be replaced by $(\phi - \phi_c)$. Assuming $\phi_c < \phi << 1$ holds particularly for low porosities, and we obtain:

$$k \approx B(\phi - \phi_c)^3\,d^2. \tag{2.26}$$

Fractal models for porous media are based on the notion that the inner surfaces of rock pores show self-similarity (e.g., Pape et al., 1999; Costa, 2006). The fundamental parameters in the fractal model by Pape et al. (1999) are the fractal dimension D, the grain radius r_g, the effective hydraulic capillary radius r_{eff}, the electrical tortuosity τ_e, and the formation resistivity factor F. The general equation related to this model is:

$$k = A\phi + B\phi^m + C(10\phi)^{\frac{m+2}{c_1(3-D)}}, \tag{2.27}$$

where A, B, and C are constants, m is the Archie's law cementation exponent, which is related to F and τ_e by Equation 2.5, the fractal dimension is $2 < D < 2.5$ for most rocks, and $0.39 < c_1 < 1$ resulting from an empirical relation of r_g and r_{eff} for sandstones. Investigations of Kozeny-Carman type k-ϕ relationships of various porous media based on the assumption of a fractal pore space geometry yielded (Costa, 2006):

$$k \propto a\,\frac{\phi^m}{1-\phi}, \tag{2.28}$$

Scientific Technical Report STR 12/07
DOI: 10.2312/GFZ.b103-12079

where a is an empirically derived constant and m is the Archie's law cementation exponent.

Permeability-Porosity-Relationships

Experiments with porous silica glass and literature reviews of k-ϕ relationships of synthetic and rock materials have shown that there is no universal k-ϕ relationship valid for all porous media and all permeability-changing processes (Mok et al., 2002; Bernabé et al., 2003). However, permeability and porosity are generally related to each other by a power law:

$$k \approx \phi^{\alpha}, \tag{2.29}$$

where α is a variable exponent for different permeability-changing processes and can have values between ≈ 1 and ≈ 25. The variable exponent α is related to the ratio of the effective to the non-effective porosity. Diagenetic processes incorporating, e.g., compaction and chemical alteration of rock constituents yield $\alpha \approx 2$ for sedimentary rocks with $\phi < 0.1$.

The permeability-porosity relationship of Fontainebleau sandstone in a porosity range of 3 to 28 % shows two distinct power-law correlations for low porosities of 3 to 9 % and for high porosities of 9 to 28 % with exponents of ≈ 7.3 and ≈ 3, respectively (Bourbie and Zinszner, 1985):

$$k = 2.75 \times 10^{-5}\, \phi^{7.33}, \tag{2.30}$$

and

$$k = 0.303\, \phi^{3.05}. \tag{2.31}$$

The large decrease of k with decreasing ϕ in the low ϕ region is attributed to a percolation threshold phenomenon. Further investigation of this percolation threshold phenomenon yielded a continuous k-ϕ relationship for Fontainebleau sandstone (Mavko and Nur, 1997):

$$k \approx 5(\phi - \phi_c)^3\, d^2, \tag{2.32}$$

where $\phi_c \approx 0.025$, and $d = 250 \times 10^{-6}$ m. In this semi-empirical approach, the resulting unit for k is milli-Darcy approximately equal to 10^{-15} m^2.

Dissolution experiments with Fontainebleau sandstone samples with initial porosities ranging between ≈ 5 and ≈ 17 % have shown that a simple k-ϕ relationship of the form $k \approx \phi^3$ only holds for samples with very low initial porosities. Samples with higher initial porosities showed permeabilities far lower than expected by simple k-ϕ relationships. This observation has been interpreted as resulting from dissolution mainly in large pores rather than in pore throats. The permeability of the sandstone cores was largely unaffected in the course of the dissolution experiments (Colón et al., 2004).

The response of k to diagenetic changes in a reservoir sandstone (Dunbar oil field, North Sea) has shown that simple k-ϕ relationships cannot reproduce the facies-dependent k variations encountered in this specific sandstone. It has been shown that the facies-dependent k variations resulted from variable illite content and morphology (Le Gallo et al., 1998).

A fractal pore space model (Equation 2.27) yielded k-ϕ relationships for several rock types including 640 Lower Permian Rotliegend sandstone samples from northeast Germany (Pape et al., 1999). Nonlinear regression of the k-ϕ data resulted in the empirical relationship:

Scientific Technical Report STR 12/07
DOI: 10.2312/GFZ.b103-12079
Deutsches GeoForschungsZentrum GFZ

$$k = 155\phi + 37315\phi^2 + 630(10\phi)^{10}, \tag{2.33}$$

where k has the unit 10^{-9} m^2.

A linear k-ϕ relationship prevails in any porous medium, if the porosity of a porous medium can be approximated by cylindrical capillaries with a constant radius r (Guéguen and Palciauskas, 1994):

$$k = a\, r^2 \phi, \tag{2.34}$$

where a is a dimensionless constant of magnitude close to 1.

2.2 Mineral Dissolution and Precipitation in the Quartz-Feldspar-Water System

Dissolution and precipitation in the quartz-feldspar-water system has been widely studied due to the abundance of the minerals in the earth's crust and due to the fundamental impact of dissolution-precipitation processes on weathering, nuclear waste disposal, geological CO_2 storage, water quality changes, and geothermal energy production. The aspects of dissolution-precipitation processes in the quartz-feldspar-water system can be subdivided into thermodynamic, kinetic, and molecular mechanistic aspects. Experimental studies and field observations reported in the literature focused on the effects of background electrolytes, alteration products, and distance from equilibrium on reaction progress.

2.2.1 Thermodynamics of Dissolution and Precipitation in the Quartz-Feldspar-Water System

The reactions to be considered in the quartz-feldspar-water system in the near-neutral to acidic pH range can be described as the equilibrium between quartz and dissolved silica (Equation 2.35), congruent dissolution of feldspar (K-feldspar is given as an example in Equation 2.36), and incongruent dissolution of feldspar involving the precipitation of secondary phases (Equation 2.37) (Appelo and Postma, 1999; Gunnársson and Arnórsson, 2000; Fu et al., 2009; Blume et al., 2010):

$$SiO_2 + H_2O \rightleftharpoons H_4SiO_4^0, \tag{2.35}$$

$$KAlSi_3O_8 + 4H^+ + 4H_2O \rightarrow K^+ + Al_3^+ + 3H_4SiO_4^0, \tag{2.36}$$

$$2KAlSi_3O_8 + 2H^+ + 9H_2O \rightarrow 2K^+ + Al_2Si_2O_5(OH)_4 + 4H_4SiO_4^0. \tag{2.37}$$

The arrows indicate the irreversibility of reactions 2.36 and 2.37 (Appelo and Postma, 1999). Other secondary phases than kaolinite ($Al_2Si_2O_5(OH)_4$) such as boehmite ($AlO(OH)$), gibbsite ($Al(OH)_3$), and even micas (e.g., muscovite $KAl_3Si_3O_{10}(OH)_2$) are reported in the literature.

At equilibrium and with activities of the solid phases and H_2O equal to 1, the solubility constants K_s of reactions 2.35, 2.36 and 2.37 can be stated according to the law of mass action in logarithmic form as:

Scientific Technical Report STR 12/07
DOI: 10.2312/GFZ.b103-12079

$$\log K_{s,\mathrm{SiO_2}} = \log[\mathrm{H_4SiO_4^0}], \tag{2.38}$$

$$\log K_{s,\mathrm{KAlSi_3O_8,congruent}} = \log[\mathrm{K^+}] + \log[\mathrm{Al_3^+}] + 3\log[\mathrm{H_4SiO_4^0}] - 4\log[\mathrm{H^+}], \tag{2.39}$$

$$\log K_{s,\mathrm{KAlSi_3O_8,incongruent}} = 2\log[\mathrm{K^+}] + 4\log[\mathrm{H_4SiO_4^0}] - 2\log[\mathrm{H^+}], \tag{2.40}$$

respectively, where brackets denote the activities of the species in solution. The change in Gibbs energy of a reaction, ΔG_r, in aqueous solution is defined as:

$$\Delta G_r = \Delta G_r^0 + R^* T_{\mathrm{abs}} \ln \mathrm{IAP}, \tag{2.41}$$

where ΔG_r^0 is the standard Gibbs energy of reaction (standard refers to 25 °C and 10^5 Pa), R^* is the gas constant, T_{abs} is the thermodynamic temperature, and IAP is the ion activity product, i.e., the quotient of the activities of the products over the activities of the reactants (sometimes referred to as the reaction quotient Q). The change in Gibbs energy of reaction indicates the direction in which a reaction proceeds. The reaction proceeds in the direction of the reactants, if $\Delta G_r > 0$. The reaction is at equilibrium, if $\Delta G_r = 0$. The reaction proceeds in the direction of the products, if $\Delta G_r < 0$. At equilibrium ($\Delta G_r = 0$) Equation 2.41 reduces to:

$$\Delta G_r^0 = -R^* T_{\mathrm{abs}} \ln \mathrm{IAP}. \tag{2.42}$$

Furthermore, at equilibrium IAP = K_s leading to:

$$\Delta G_r^0 = -R^* T_{\mathrm{abs}} \ln K_s. \tag{2.43}$$

Substitution of Equation 2.43 into Equation 2.41 yields:

$$\Delta G_r = -R^* T_{\mathrm{abs}} \ln K_s + R^* T_{\mathrm{abs}} \ln \mathrm{IAP}, \tag{2.44}$$

indicating the distance from equilibrium of a reaction in aqueous solution. The distance from equilibrium is often described as the saturation index, SI:

$$\mathrm{SI} = \log \frac{\mathrm{IAP}}{K_s}. \tag{2.45}$$

Consequently, SI < 0 indicates undersaturation, SI $= 0$ indicates saturation (equilibrium), and SI > 0 indicates supersaturation. Minerals dissolve in contact with a solvent (in the present case H_2O), if the solvent is undersaturated with respect to the constituents comprising a mineral. If the solvent is supersaturated with a specific mineral phase, this phase tends to precipitate from the fluid (Merkel and Planer-Friedrich, 2008).

The standard Gibbs energy of reaction, ΔG_r^0, can be calculated from tabulated values of the standard Gibbs energy of formation from the elements, ΔG_f^0:

$$\Delta G_r^0 = \sum \Delta G_{f,\mathrm{products}}^0 - \sum \Delta G_{f,\mathrm{reactants}}^0. \tag{2.46}$$

The standard Gibbs energy of formation from the elements can also be calculated using standard entropies of formation from the elements, ΔS_f^0, and standard enthalpies of formation from the elements, ΔH_f^0:

Scientific Technical Report STR 12/07
DOI: 10.2312/GFZ.b103-12079
Deutsches GeoForschungsZentrum GFZ

$$\Delta G_f^0 = \Delta H_f^0 - T\Delta S_f^0. \tag{2.47}$$

Thus, tabulated thermodynamic data for reactions from the elements can be used to calculate solubility constants for any reaction in aqueous environment at a standard state. Pressure effects are normally neglected in thermodynamic calculations in hydrochemistry, when negligible molar volume changes of products occur relative to reactants (Le Chatlier's principle). Temperature effects are calculated by either the Van't Hoff equation or by experimentally determined polynomial functions of the variations of K_s with T. Empirical K_s-T relationships for feldspars, quartz, and amorphous silica can be found in the literature (e.g., Arnórsson and Stefánsson, 1999; Gunnársson and Arnórsson, 2000).

Thermodynamic calculations use activities of species in solution (e.g., Equations 2.38, 2.39, and 2.40). Activities can be derived from the Debye-Hueckel theory for low ionic strength and the Pitzer approach for high ionic strength of the solution. The calculations of activities, stability constants of aqueous complexes, speciation, ionic strength, K_s, IAP, and the temperature variation of K_s can be performed with hydrogeochemical simulation codes using tabulated thermodynamic data of standard $\log K_s$ of a wide variety of chemical equilibria, ΔH_r^0, ΔH_f^0, and functions of the variations of K_s with T. Throughout the present study PHREEQC (Parkhurst and Appelo, 1999) was used for hydrogeochemical simulations. The PHREEQC database LLNL.dat was used for the simulations. The database is valid up to 300 °C for most minerals, including quartz and feldspars.

2.2.2 Kinetics of Dissolution and Precipitation in the Quartz-Feldspar-Water System

Previous studies have shown that dissolution and precipitation of quartz and feldspars are heterogeneous reactions, because the reactions occur at the interface of the solid and the fluid phase. Moreover, the reactions are overall reactions which may incorporate several elementary reactions at the molecular level (Lasaga, 1983). In general, for the simple hypothetical overall reaction:

$$\mathrm{A} \rightarrow \mathrm{B} \tag{2.48}$$

the rate of the reaction can be expressed as the concentration change $\mathrm{d}c_i$ per time increment $\mathrm{d}t$ of the reactants and/or the products (e.g., Appelo and Postma, 1999; Lasaga, 1983):

$$-\frac{\mathrm{d}c_A}{\mathrm{d}t} = \frac{\mathrm{d}c_B}{\mathrm{d}t} = k\, c_A^{n_a}\, c_B^{n_b}, \tag{2.49}$$

where k is the rate constant and the exponent n_i is the reaction order with respect to reactant i. Empirical relationships between rates, rate constants and reaction orders are termed rate laws and can be determined by various methods, including the differential method (Appelo and Postma, 1999). Investigations on the dissolution kinetics of albite in aqueous solutions have shown that the reaction can be traced by the consumption of H^+. The reaction order with respect to H^+, n_{H^+}, and the dissolution rate constant, k_{dis}, of albite can be derived by (Chen and Brantley, 1997):

$$\log r_{\mathrm{dis}} = \log k_{\mathrm{dis}} + n_{\mathrm{H^+}} \log[\mathrm{H^+}]. \tag{2.50}$$

Scientific Technical Report STR 12/07
DOI: 10.2312/GFZ.b103-12079

The terms n_{H^+} and $\log[H^+]$ can be replaced by terms for other species involved in the dissolution reaction. In the special case of congruent dissolution, the dissolution rate of a mineral, $r_{dis,i}$, is (Lasaga, 1984):

$$r_{dis,i} = \frac{dc_i}{dt} = \frac{A}{V} v_i k_{dis}, \tag{2.51}$$

where A is the surface area of the mineral in contact with the solution, V is the volume of the solution, v_i is the stoichiometric content of element i in the mineral, and k_{dis} is the rate constant of the dissolution reaction.

Recent publications have shown that dissolution rates of quartz and feldspars vary non-linearly with distance from equilibrium, pH, and concentration of dissolved ions in the solution, e.g., Al^{3+} (Hellmann and Tisserand, 2006; Schott et al., 2009; Arvidson and Lüttge, 2010). Conditions far from equilibrium yield constant dissolution rates. These conditions prevail when the minerals are in contact with flowing H_2O or when the solvent has a low pH. As the fluid-solid systems approach equilibrium, dissolution rates decrease (Appelo and Postma, 1999). Equilibrium can be attained in natural groundwaters or in batch reactors. A plot of distance from equilibrium, indicated by ΔG_r, versus dissolution rate typically shows a sigmoidal behavior for feldspars with a constant dissolution rate far from equilibrium, a large decrease of dissolution rates in a so-called transition equilibrium region, and an approach to zero dissolution rate in the near equilibrium region (Hellmann and Tisserand, 2006; Schott et al., 2009). The pH of the solution influences the dissolution rates of quartz and feldspars. Quartz dissolution rates are lowest in the region around pH $\approx$ 3 (Brady and Walther, 1990). Albite dissolution rates are lowest in the near-neutral pH region (Chou and Wollast, 1985). The rate constant is proportional to the activity of H^+ in the acidic to near-neutral pH region (Lasaga, 1984; Chen and Brantley, 1997):

$$k_{dis} \propto [H^+]^n, \tag{2.52}$$

where $0 \leq n \leq 1$ is an empirically derived constant.

The effect of concentrations of dissolved ions on dissolution rates of feldspars are complex (e.g., Schott et al., 2009). The logarithm of the dissolution rate of albite at 150 °C and pH = 9 is a decreasing linear function of the logarithm of the concentration of Al in solution (Oelkers et al., 1994), whereas the concentration of Al in solution does not influence the dissolution rate of anorthite at conditions far from equilibrium (Oelkers, 2001; Schott et al., 2009).

In general, the temperature dependence of k_{dis} follows the Arrhenius equation (e.g., Chen and Brantley, 1997):

$$k_{dis} = A^* \exp(-E_a / R^* T_{abs}), \tag{2.53}$$

where A^* is a pre-exponential factor, E_a is the Arrhenius activation energy in J/mol, R^* is the gas constant (8.314 J/mol K), and T_{abs} is the thermodynamic temperature in K. Relationships between k_{dis} and T have been determined for the quartz-water system and temperatures up to 625 °C (Dove, 1994; Tester et al., 1994). The relationship between k_{dis}, T, and pH has been constrained for the albite-water system and temperatures up to 300 °C in the acidic pH region (Chen and Brantley, 1997).

Dissolution rates obtained from laboratory experiments are in general not directly comparable to those obtained from field observations. Dissolution rates obtained by field investigations are generally much slower than rates obtained in the laboratory (Appelo and Postma, 1999).

Scientific Technical Report STR 12/07
DOI: 10.2312/GFZ.b103-12079
Deutsches GeoForschungsZentrum GFZ

The difficulties of comparing dissolution rates obtained by experiments and field investigations arise from different ΔG_r, pH, and solution composition conditions. It has been shown that feldspar dissolution rates in an aquifer are $\approx 10^5$ times lower than feldspar dissolution rates measured in the laboratory at comparable temperature and pH but under conditions far from equilibrium (Zhu et al., 2006). Slow precipitation kinetics of secondary mineral phases and metastable phases coupled with the dissolution kinetics of feldspars may have an inhibiting effect on the field-observed overall dissolution kinetics (Fu et al., 2009). However, mineral dissolution rates obtained under conditions far from equilibrium can be related to dissolution rates at near-equilibrium conditions using transition state theory, TST (Schott et al., 2009).

2.2.3 Molecular Scale Mechanisms of Dissolution and Precipitation in the Quartz-Feldspar-Water System

Generally speaking, dissolution and precipitation in the quartz-feldspar-water system is dependent on the breaking and formation of Si–O–Si bonds or Al–O–Si bonds at the mineral-fluid interface (Dove, 1999; Zhang and Lüttge, 2009b). Silicates dissolve in contact with H_2O via hydrolysis, i.e., H^+ and/or OH^- are involved in the elementary reactions comprising silicate dissolution (e.g., Blume et al., 2010). Transition state theory, surface chemistry, and surface complexation models provide the theoretical basis for the interpretation of molecular scale mechanisms involved in quartz and feldspar dissolution (e.g., Aagaard and Helgeson, 1982; Blum and Lasaga, 1991; Lasaga and Lüttge, 2003; Arvidson and Lüttge, 2010). In the framework of TST, a so-called activated complex forms which overcomes the energy barrier between reactants and products of an elementary reaction. The reaction rate of the forward reaction, r_+, in a dynamic equilibrium between reactants and the activated complex is described by (Schott et al., 2009):

$$r_+ = k\,[AB^*], \tag{2.54}$$

where $[AB^*]$ is the concentration of the activated complex and k is the respective rate constant. For the overall rate of an elementary reaction, Equation 2.54 can be written as (Aagaard and Helgeson, 1982; Lasaga, 1983; Schott et al., 2009):

$$r = r_+\,[1 - \exp(\Delta G_r / RT)], \tag{2.55}$$

combining the thermodynamic property ΔG_r and the concentration of species involved in the formation of the activated complex with TST. Although the activated complex is rather hypothetical, studies on the surface chemistry of quartz and feldspar in contact with aqueous solutions suggest that the activated complexes are stoichiometrically similar to surface complexes that form on the mineral-fluid interface (e.g., Schott et al., 2009).

The energetics of dissolution and/or precipitation at different sites of the mineral surface is another aspect of molecular scale mechanisms of quartz and feldspar dissolution and precipitation. The dissolution and precipitation of quartz or feldspar in aqueous solutions are surface controlled. The dissolution or growth of precipitates occur on energetically favorable sites like kinks, steps, clusters, and etch pits in surface controlled reactions (e.g., Appelo and Postma, 1999). Molecular scale dissolution mechanism of minerals, including plagioclase, have been investigated using statistical mechanics of different surface sites (Lasaga and Lüttge, 2004; Zhang and Lüttge, 2007, 2009a,b). Furthermore, nucleation theory may be a means of understanding mineral dissolution and precipitation in general on a mechanistic basis. The dissolution and precipitation of quartz

Scientific Technical Report STR 12/07
DOI: 10.2312/GFZ.b103-12079

occurs at different surface sites, steps, crystal defects, or etch pits, depending on the degree of undersaturation of the fluid (Dove et al., 2005).

2.2.4 Experimental Studies of Dissolution and Precipitation in the Quartz-Feldspar-Water System

Experiments investigating the interactions of aqueous solutions with quartz-feldspar mixtures or rock materials have yielded a variety of alteration products depending on the experimental conditions. Experiments with mixtures of K-feldspar, albite, quartz, and calcite in contact with KCl_{aq} solutions up to 2 mol/L or simulated geothermal brines at temperatures up to 300 °C in sealed silver tubes yielded alteration products that consisted mainly of illite and zeolites (Divis and McKenzie, 1975). Flow-through experiments with feldspar-rich sand and simulated seawater at 200 °C and 10^8 Pa showed that cation-exchange reactions between the fluid and the solid occurred, resulting in smectite as the dominant alteration product (Hajash and Bloom, 1991). Flow-through experiments with granular aggregates of plagioclase-quartz mixtures and simulated brines at 40 and 70×10^6 Pa pore- and confining pressure, respectively, at an axial load of 93×10^6 Pa and at 129 °C yielded clay minerals and zeolites as alteration products that covered quartz and feldspar surfaces. Moreover, the experiments indicated that dissolution-precipitation reactions may account for mass transfer-dependent porosity and permeability changes of sedimentary rocks (Karner and Schreiber, 1993). Long-term batch experiments (up to 500 d) with aqueous solutions and granodiorite, amphibolite, and K-feldspar at ambient conditions resulted in oscillations of Si and Al concentrations with time in the fluids. This observation has been interpreted as resulting from the formation of aluminosilicate polymers in supersaturated aqueous solutions (Faimon, 1996). Flow-through experiments with granular aggregates of labradorite-quartz mixtures and Sr- and Ba-bearing aqueous solutions have been performed at 10 and 60×10^6 Pa pore- and confining pressure, respectively, at an axial load of 75×10^6 Pa and at 200 °C and yielded mainly zeolite, strontianite, and calcite as alteration products that formed in regions of fine-grained material and narrow pore throats. The alteration products incorporated Sr and Ba from the aqueous solution and led to a decrease of permeability to approximately 20 % of initial permeability (Tenthorey and Scholz, 2002).

Investigations of the reactions of aqueous solutions with single phase feldspar aggregates have shown that mainly $Al(OH)_3$ and aluminosilicate phases precipitated on the original feldspars. Kaolinite precipitated homogeneously at room temperature from Al- and Si-bearing acidic solutions that were in contact with dissolving K-feldspar. Fluid/solid mass ratios were ≈ 66 and the duration of the experiments was up to 50 d (La Iglesia et al., 1976). Alteration products were not observed in batch experiments performed with albite at near-neutral pH, ambient p-T-conditions, and at fluid/solid mass ratios ≈ 14 (Holdren and Berner, 1979). Batch experiments with labradorite granular aggregates and HCl solutions at temperatures up to 245 °C resulted in the pH-dependent formation of amorphous silica, boehmite, amorphous Al-Si phases, and kaolinite (Tsuzuki and Suzuki, 1980). Batch experiments were performed with granular aggregates of Sr-doped synthetic labradorite and anorthite in contact with a dilute aqueous HCl solution as well as a solution initially at equilibrium with the solid phases. The experiments lasted up to 270 d at 180 °C and revealed that at conditions far from equilibrium plagioclase transformed to smectite, and that at near-equilibrium conditions a paragenesis of quartz, kaolinite, prehnite, and smectite formed (Zuddas and Michard, 1993). Series of long-term batch experiments (up to 355 d) with anorthite and moderately acidic aqueous solutions at temperatures up to 210 °C have shown that a time-dependent sequence of boehmite, so-called

Scientific Technical Report STR 12/07
DOI: 10.2312/GFZ.b103-12079

modified boehmite, and kaolinite precipitated on the anorthite surfaces (Murakami et al., 1998). Flow-through experiments with granular albite aggregates at variable pH conditions and temperatures up to 300 °C yielded boehmite as well as a not further specified aggregate of sub-micrometer sized precipitates on the feldspar surfaces (Hellmann et al., 1989; Hellmann, 1994, 1995; Hellmann and Tisserand, 2006). The replacement of albite by K-feldspar has been investigated by batch experiments with KCl_{aq} solutions doped with ^{18}O at 600 °C and 2×10^8 Pa. The experiments with a run duration up to 14 d revealed that the replacement reaction was pseudomorphic, and that ^{18}O was incorporated into the K-feldspar, indicating that the reaction proceeded via an interface-coupled dissolution-precipitation mechanism (Niedermeier et al., 2009). Batch experiments performed at 200 °C and 30×10^6 Pa for up to 78 d showed a coupling of dissolution kinetics of perthitic K-feldspar with precipitation kinetics of alteration products, such as boehmite and kaolinite (Fu et al., 2009; Zhu and Lu, 2009).

The effect of background electrolytes on the solubility and dissolution kinetics of SiO_2 but also feldspar is a subject of debate and has been addressed by many experimental studies. Experiments conducted with amorphous SiO_2 and $NaNO_{3aq}$ solutions at temperatures up to 300 °C indicated that silica solubility is a decreasing function of the $NaNO_{3aq}$ concentration up to approximately 6 mol/L (Marshall, 1980). The solubility of quartz is correlated to the $NaCl_{aq}$ concentration of the solution up to approximately 0.05 mol/L at 200 °C. The dissolution rate of quartz was enhanced by the presence of ions in solution and the rate-enhancing trend followed: $H_2O < Mg^{2+} < Ca^{2+} \approx Li^+ \approx Na^+ \approx K^+ < Ba^{2+}$. The proposed molecular scale mechanism for the dissolution enhancing behavior of dissolved cations involves adsorption of the cations onto negatively charged surface sites leading to weakening of Si–O bonds. Furthermore, no dissolution enhancing behavior of dissolved cations on feldspar dissolution has been observed, because the effect of additional adsorbed cations on the electrostatic regime of the silicate-fluid interface is negligible for cation-bearing silicates (Dove and Crerar, 1990; Dove and Elston, 1992; Dove, 1994, 1999). Experimental studies have shown that the quartz solubility increased in $NaCl_{aq}$ solutions relative to H_2O in the p-T region 20 to 100×10^6 Pa and 200 to 450 °C. An empirical equation has been derived for the enhancing effect of $NaCl_{aq}$ on quartz solubility valid for $NaCl_{aq}$ concentrations up to at least 0.5 mol/L (von Damm et al., 1991). Experiments with granular aggregates of plagioclase and NaCl-bearing acidic solutions at 25 °C indicated that dissolution rates of plagioclase decreased with increasing $NaCl_{aq}$ concentration up to ≈ 0.1 mol/L (Stillings and Brantley, 1995). A study on the precipitation kinetics of quartz has shown that the precipitation kinetic was not affected by $NaCl_{aq}$ solutions > 0.1 mol/L at 180 °C (Ganor et al., 2005). Investigations on the quartz solubility in $NaCl_{aq}$ solutions at very high p-T conditions (10^9 Pa and 900 °C) have shown that the dependence of quartz solubility on pressure and NaCl concentration is complex (Evans, 2007).

The debate on the effect of background electrolytes on quartz and feldspar dissolution behavior described above shows that the underlying molecular scale mechanisms, leading to changes of the dissolution behavior of quartz and feldspars relative to H_2O, are complex and not well understood. However, general findings reported in the literature show that dissolved ions affect the solubility of silicates in three ways: (i) by changing the activity and the electrical properties of H_2O, (ii) by altering the electrical properties of the fluid-mineral interface (e.g., bond weakening effects), and (iii) by changing the solubility constant of the equilibrium between solid phases and dissolved ions (the common-ion effect).

Scientific Technical Report STR 12/07
DOI: 10.2312/GFZ.b103-12079

2.3 Effects of Dissolution and Precipitation on Electrical Conductivity and Permeability

2.3.1 Effects of Dissolution and Precipitation on Electrical Conductivity

The effect of dissolution and precipitation on electrical conductivity of rocks is obvious: dissolution of solids leads to increasing concentration of dissolved ions in the pore fluid and thus to increasing σ_f, precipitation leads to a removal of ions from the pore fluid and thus to decreasing σ_f. The electrical conductivity of rocks is dependent on σ_f at very low concentration of dissolved ions in the pore fluid, $c_i > 10^{-3}$ mol/L, because electrical conduction at the fluid-mineral interface is then independent on c_i (Revil et al., 1998). Batch experiments with various rock types, including graywacke samples consisting of quartz, feldspar, calcite, dolomite and > 5 % clay minerals, and tap-water at room temperature yielded a time-dependent behavior of σ_r. Specificly, σ_r first increased with time with decreasing rate, passed a maximum, and then slightly decreased and approached a constant value. Concurrently, σ_f of the fluid in contact with the rock samples increased monotonically with time with decreasing rate. The time-dependent behavior of σ_r and σ_f resulted from the dissolution of minerals in the rock samples (Piwinskii and Weed, 1976; Weed et al., 1977).

2.3.2 Experimental Studies on the Effects of Dissolution and Precipitation on Permeability

The effect of dissolution and precipitation on permeability is dependent on the specific fluid-solid system under investigation. Hydrothermal experiments with different fluid-solid systems, including granite, novaculite, sandstone, and granular mineral aggregates as the solid materials, and mainly H_2O and secondarily aqueous salt solutions as the fluid phases have shown that k changes due to dissolution and precipitation. The sense of the k change, i.e., increase or reduction, is dependent on the experimental p-T parameters and the dominant pore or fracture space changing processes.

Hydrothermal experiments with granite and deionized H_2O at temperatures up to 300 °C, confining pressure p_c up to 150×10^6 Pa, and pore pressure p_p up to 100×10^6 Pa yielded significant k decreases in the first 5 d of the experiments. One type of experiments was performed with a decreasing temperature gradient in the direction of flow. Another type of experiments was performed under isothermal conditions. The experiments indicated that the k decrease is due to the dissolution of primary minerals comprising the granite and precipitation of secondary minerals, e.g., hydrothermal quartz, feldspars, and smectite, in pores and fractures (Moore et al., 1983; Morrow et al., 2001).

Hydrothermal experiments conducted with naturally fractured novaculite (almost pure SiO_2) and H_2O resulted in a k decrease by a factor of ≈ 100. The experiments were performed at temperatures up to 150 °C under isothermal conditions along the rock sample, the confining pressure was $p_c = 3.5 \times 10^6$ Pa, and the total duration of the experiments was 37.5 d (Polak et al., 2003). A similar experiment with isothermal temperature stages up to 120 °C, $p_c = 1.72 \times 10^6$ Pa, $p_p = 1.38 \times 10^6$ Pa, and a total duration of approximately 131 d has shown that k changes were time-dependent, i.e., k first decreased and then increased during the experiment (Yasuhara et al., 2006). These investigations illustrated that k decreases resulted from net dissolution of propping asperities (pressure solution) in the fracture and concurrent fracture aperture decrease (Polak et al., 2003; Yasuhara et al., 2004, 2006). A numerical model was built

Scientific Technical Report STR 12/07
DOI: 10.2312/GFZ.b103-12079

on the basis of the former experiments incorporating competing processes of pressure solution and free-face dissolution and precipitation of quartz. The model explains that in the early stage of the experiments, pressure solution of propping asperities leads to a decrease of fracture aperture, while in the later stage of the experiments free-face dissolution leads to an increase of fracture aperture (Yasuhara and Elsworth, 2006). Thus, the evolution of k of a fractured quartz dominated rock is dependent on the dominant dissolution or precipitation process.

Investigations of the effects of dissolution and precipitation processes on k of sandstones have shown that k generally decreased during hydrothermal flow-through experiments. Flow-through experiments with Triassic Contorta sandstone samples and an initially anoxic geothermal brine of Na-Ca-Mg-K-Cl-SO_4 type with a high salinity (total dissolved solids > 214 g/L) resulted in a k decrease due to the clogging of pores with colloidal Fe hydroxide particles. The experiments were conducted at 90 °C constant temperature, $p_c = 25 \times 10^6$ Pa, $p_p = 3 \times 10^6$ Pa, and with a total duration of approximately 5 d. Hydrodynamic mobilization of fine particles and a subsequent clogging of pores led to a further k decrease. Moreover, oxidizing the initially anoxic brine led to the precipitation of Fe hydroxides from the brine and to a total loss of permeability after approximately 2 d (Kühn et al., 1998). Flow-through experiments with initially intact Fontainebleau sandstone samples that were fractured in a triaxial apparatus and subsequently subjected to hydrothermal conditions have shown that bulk sample permeability decreased by a factor of ≈ 2 in 10 h. The experiments were performed at 927 °C constant temperature, $p_c = 250 \times 10^6$ Pa, and $p_p = 200 \times 10^6$ Pa with H_2O as the pore fluid. The k decrease resulted from dissolution-precipitation processes with pressure solution as the main driving force leading to the healing and sealing of fractures and concurrent porosity reduction (Tenthorey et al., 2003).

Hydrothermal flow-through experiments with granular aggregates of quartz and labradorite as well as H_2O as the pore fluid resulted in a k decrease but ϕ remained largely unaffected (Scholz et al., 1995; Aharonov et al., 1998; Tenthorey et al., 1998; Tenthorey and Scholz, 2002). The experiments were performed at up to 350 °C constant temperature, $p_c \leq 10^8$ Pa, $p_p \leq 5 \times 10^7$ Pa and had a total duration of up to 4 d. The samples were subjected to deviatoric stress conditions with up to 215×10^6 Pa. H_2O was the starting fluid in most experiments. One type of experiments was performed with aqueous solutions of Sr- and Ba-nitrate (Tenthorey and Scholz, 2002). The general observation was that k decreased after mechanical compaction of the aggregates had ceased. In the phase of negligible mechanical compaction, ϕ of the aggregates was largely unchanged. The general conclusion of theses studies was that the k reduction resulted from dissolution of mainly labradorite and precipitation of zeolites and smectite in narrow pores and pore throats. The permeability of the granular aggregates decreased in the hydrothermal phase at 200 °C by up to a factor of ≈ 10 in 1 d (Scholz et al., 1995).

2.3.3 Formation Damage

The sum of permeability-reducing effects in reservoir rocks is termed formation damage (a concept of the petroleum industry). Such k changes can in general be attributed to physico-chemical, chemical, biological, hydrodynamic, and thermal interactions of the porous material, particles, and fluids, as well as to mechanical deformation of the reservoir rock under stress (Civan, 2000). The experimental conditions of the present study rule out any biological interactions with the porous material as potential factors for k changes in hydrothermal flow-through experiments.

Fines migration and clay swelling are the primary reasons for formation damage of a reservoir

Scientific Technical Report STR 12/07
DOI: 10.2312/GFZ.b103-12079

rock (Civan, 2007). The fundamental particle generation mechanisms in the pore space are hydrodynamic mobilization, colloidal expulsion, liberation of fine particles due to dissolution of rock constituents (cements and grains), liberation of fine particles due to deformation of the porous rock, and formation of fine particles due to precipitation (Civan, 2000). The flow of dispersed particles in the pore space may lead to a pore diameter constriction and eventually to a pore throat plugging and thus to a k reduction. Fines migration can lead to a permanent reduction of k (Mohan et al., 1999; Blume et al., 2002).

Clay minerals generally swell due to the exchange of cations against H_2O or dissolved cations. The source of the exchange cations is the interlayer between the tetrahedral and octahedral coordinated sheets comprising the structure of a clay mineral (e.g., Anderson et al., 2010). Clay swelling occurs in two different regimes, i.e., intracrystalline and osmotic clay swelling. Intracrystalline swelling is the initial mode in which interlayer cations are exchanged. The initial mode is followed by a continuous osmotic swelling that is dependent on concentration gradients between the clay particle aggregate and the solution in contact with the aggregate. Osmotic swelling is a continuous process leading to wide spaces between individual sheets. Consequently, clay swelling is a decreasing function of the concentration of ions in the pore fluid. The relative swelling intensity of different clay minerals is given by the order kaolinite < illite < smectite (Heim, 1990). Not only the swelling behavior but also the morphology of the clay minerals is an important factor for the effect of clay mineral content on k of a sandstone, i.e., fibrous illite aggregates affect k of a sandstone to a larger extent than platy booklet-type kaolinite aggregates (Appelo and Postma, 1999). The clay mineral fraction of the Flechtinger sandstone samples used in the present study consists mainly of illite (Table 3.1). The major reservoir problem caused by illite is the plugging of pore throats with migrating fines. Moreover, the leaching of K^+ from the mineral changes illite to an expandable clay mineral leading to enhanced formation damage (Civan, 2000).

Laboratory studies on formation damage of different porous media including sandstones samples have shown that k changes are dependent on the fluid chemistry and the distribution of the clay mineral phase. Flow-through experiments with sandstones of variable clay mineral content revealed that the k reduction is dependent on the concentration of dissolved cations in solution. Moreover, the k reduction is larger with dissolved monovalent cations than with divalent cations, and the type of anions in solution does not influence the swelling behavior of clay minerals (Omar, 1990). Flow-through experiments with granular aggregates of clay minerals and with sandstone samples have shown that at acidic pH, smectite-bearing sandstones exhibit a k reduction with decreasing $NaCl_{aq}$ concentration of the pore fluid, while kaolinite-bearing sandstones do not behave that way. The k reduction is dependent on the different degree of fines migration in the two types of experiments (Mohan and Fogler, 1997). Experiments with sandstone cores containing expandable clay minerals like smectite showed irreversible k reductions in the course of fluid exchange experiments. The irreversible k reduction was due to fines liberation in the osmotic swelling regime and subsequent fines migration (Mohan et al., 1999). Flow-through experiments with granular aggregates of quartz and 10 % smectite with variable spatial distributions of the clay mineral phase have shown that k is dependent on the distribution of clay minerals in the porous samples. The smectite phase was dispersed homogeneously, arranged in layers parallel to the flow direction, as well as in clusters. The dispersed arrangement had a permeability two orders of magnitude lower than the other two configurations. The permeabilities of smectite arrangements in layers parallel to the flow direction and in clusters where only slightly lower than k of a pure quartz sand sample (Wildenschild et al., 2000).

Scientific Technical Report STR 12/07
DOI: 10.2312/GFZ.b103-12079
Deutsches GeoForschungsZentrum GFZ

Scientific Technical Report STR 12/07
DOI: 10.2312/GFZ.b103-12079

3 Methodology

Flow-through experiments were carried out to constrain the evolution of the permeability k and the electrical conductivity, σ_r, of porous samples at temperatures up to 170 °C, confining pressures up to 10×10^6 Pa, and pore pressures up to 5×10^6 Pa. Two types of porous samples were examined in the flow-through experiments: (i) core samples of Rotliegend sandstone, Fontainebleau sandstone, and porous PTFE, as well as (ii) sandwich samples consisting of porous discs that confine granular aggregates of quartz and feldspar. Batch experiments were performed with Rotliegend rock samples and granular aggregates of the main mineral phases the rock comprises, in order to investigate the effects of fluid-mineral reactions on the electrical conductivity of fluids, σ_f, on the concentration of dissolved species in the fluid phase, c_i, and on mineralogical and microstructural properties of the solid phases. The concentrations of dissolved cations and anions were determined by ICP-OES and ion chromatography, respectively. The fluid compositions were used as input parameters for hydrogeochemical simulations. The solid materials were characterized by X-ray powder diffraction, X-ray fluorescence spectroscopy, mercury intrusion porosimetry, BET gas adsorption, electron microscopic methods (SEM, TEM, and EMPA), and X-ray CT.

3.1 Sample Material and Sample Preparation

3.1.1 Solid Starting Materials

One type of solid starting materials in the flow-through experiments were intact rock samples, the other type were sandwiched granular aggregates of quartz, feldspars, and/or illite (Table 3.2). The rock samples were a Lower Permian (Upper Rotliegend) sandstone quarried from an outcrop in Flechtingen near Magdeburg, Germany (in the following referred to as Flechtinger sandstone), and a quartz sandstone of Oligocene age quarried from an outcrop in the Ile de France region near Paris, France (in the following referred to as Fontainebleau sandstone). Cylindrical cores with a length of 4×10^{-2} m and a diameter of 3×10^{-2} m were produced with orientations parallel and perpendicular to the bedding of macroscopically homogeneous blocks of these sandstones. The Flechtinger sandstone serves as an analogue material for the deeply buried sedimentary reservoir rocks of Upper Rotliegend age located in the North German Basin (Fischer et al., 2007). The sandwich samples consisted of porous discs that sandwiched a granular aggregate of quartz, plagioclase, K-feldspar, and in one particular case, illite (Figure 3.1b). In the following, the sandwich samples will be referred to as L-, QL-, QLM-, or QLMI-sandwiches, where I, L, M, and Q denote illite, labradorite-andesine, microcline, and quartz, respectively. The sandwiching porous discs were prepared from porous PTFE with a porosity of 20 % and from Fontainebleau sandstone samples with variable porosity. The mineral grains for the sandwiched granular aggregates were prepared from natural rock samples (Table 3.1). The mineral mass ratios approximated the composition of the Flechtinger sandstone in most sandwich experiments.

Batch experiments were performed with Rotliegend rock samples and granular aggregates

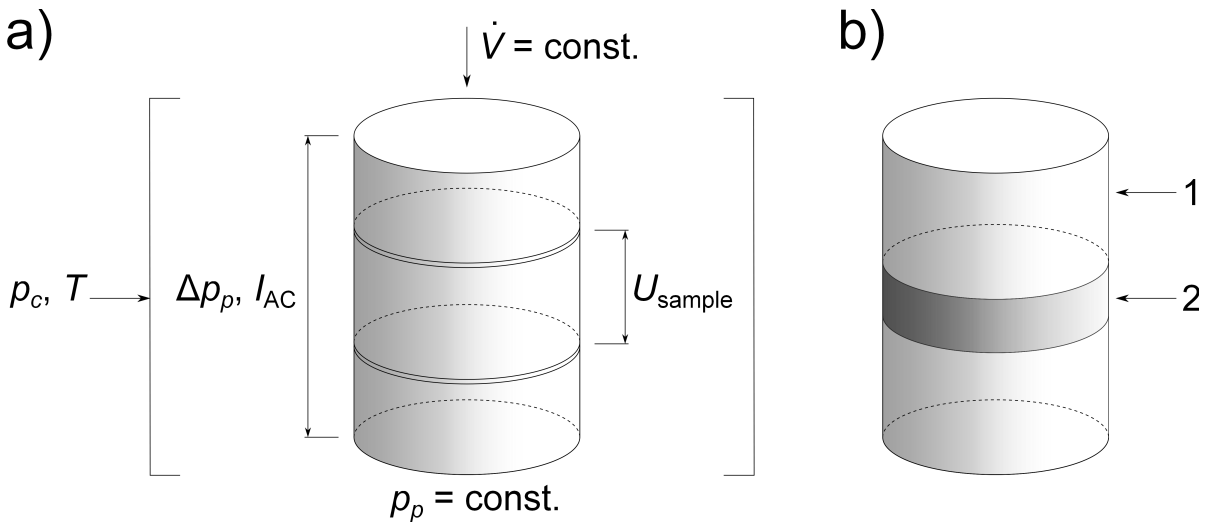

Figure 3.1: Schematic of the sample materials and the approach of the flow-through experiments. a) represents a cylindrical rock sample (Flechtinger SST or Fontainebleau SST) painted with silver paint rings that serve as potential electrodes between which the voltage U_{sample} was measured. AC current I_{AC} was imposed over the full length of the sample via stainless steel end caps (not shown) acting as the current electrodes in the four electrode arrangement. The flow rate $\dot{V}$ was constant during permeability measurements and the pore pressure p_p was held constant on the downstream side of the samples. The pore pressure difference over the sample length, Δp_p, was monitored by the pressure transducer of the upstream pump and the value of k was calculated at steady state Δp_p conditions. Hydrostatic confining pressure p_c and temperature T were imposed on the samples by means of an oil filled pressure vessel. b) represents a cylindrical sandwich sample. The experimental approach is identical to a) except that a two electrode arrangement (measurement of U_{sample} over the full length of the sample) was employed. 1) denotes the porous materials (porous PTFE or Fontainebleau SST) confining the granular aggregates. 2) denotes granular aggregates composed of quartz, feldspar, and illite grains.

Scientific Technical Report STR 12/07
DOI: 10.2312/GFZ.b103-12079

quartz, labradorite-andesine, microcline, illite, and calcite. The granular aggregates are referred to as QL-, QLM-, QLMI-, or QLMIC-samples, where C, I, L, M, and Q denote calcite, illite, labradorite-andesine, microcline, and quartz, respectively (Table 3.3). The stoichiometry of the QLM samples was determined by X-ray fluorescence spectroscopy. The mineral mass ratios of the granular aggregates approximated the composition of the Flechtinger sandstone in most batch experiments. Quartz grains were prepared from a quarried Fontainebleau sandstone. Labradorite-andesine and microcline grains originated from pegmatitic crystals supplied by Dr. F. Krantz Rheinisches Mineralienkontor, Bonn, Germany. Illite samples were quarried from a clay deposit of Oligocene age in Le Puy-en-Velay, France. The samples were obtained from Paul-Scherrer-Institute PSI, Lausanne, Switzerland. In one batch experiment calcite of pro analysis (p.a.) quality, manufactured by Merck, was used as a starting material.

The grains were produced by grinding the rocks and dry sieving the resulting powder to a grain size of $< 355 \times 10^{-6}$ m. Magnetic particles occurring in these samples were removed with a Frantz LB-1 magnetic barrier laboratory separator (current 0.4 A, voltage ≈ 23 V). The resulting powders were dry sieved to obtain a grain size fraction of 63 to 125×10^{-6} m. Larger particles were ground in an agate pulverizer and dry sieved again. In general, the 63 to 125×10^{-6} m grain size fraction was ultrasonically cleaned for 1200 s in H_2O to remove small particles sticking to the grains and was then wet sieved to obtain two grain size fractions $< 63 \times 10^{-6}$ m and 63 to 125×10^{-6} m. X-ray powder diffraction, XRD, analyses and scanning electron microscopic, SEM, micrographs of the powders showed that pure mineral phases of quartz, labradorite-andesine, and microcline were obtained by this preparation method (Figures 4.15 and 4.20). Illite and calcite were used as received. The illite sample had a grain size of $\approx 10^{-6}$ to 10^{-4} m. The composition and the chemical analysis of the illite sample were taken from Bradbury and Baeyens (2009), who described the material in detail.

The mineralogical compositions of the starting materials resulted from XRD analyses, and the petrological compositions resulted from XRF and EMPA investigations (Table 3.1). Petrological classification yielded that the Flechtinger sandstone is a sublith-arenite and the Fontainebleau sandstone a quartz arenite (Pettijohn et al., 1987). Mercury intrusion porosimetry data of unaltered Flechtinger sandstone samples showed that the material was relatively homogeneous with respect to specific surface area, average pore radius, porosity, and bulk density (Table 4.5). The Fontainebleau sandstone samples were homogeneous in composition (almost 100% SiO_2) but varied significantly in the degree of cementation and thus in porosity and geometry of the pore space (Bourbie and Zinszner, 1985; Fredrich et al., 1993; Song and Renner, 2008).

Scientific Technical Report STR 12/07
DOI: 10.2312/GFZ.b103-12079
Deutsches GeoForschungsZentrum GFZ

Starting material	**Petrological composition**	**Mineralogical composition**
quartz	rounded quartz grains from Fontainebleau SST	SiO_2
labradorite-andesine	pegmatitic crystals from Ihosy, Madagascar	$(Ca_{0.51}Na_{0.42}K_{0.03})Al_{1.49}Si_{2.47}O_8$
microcline with perthitic exsolution lamellae	pegmatitic crystals from Kragerø, Norway	$(K_{0.6}Na_{0.36})Al_{1.01}Si_{2.96}O_8$
illite	88 % illite, 12 % K-feldspar	$(K_{1.28}Na_{0.24}Ca_{0.08})(Al_{2.34}Fe_{0.98}Mg_{0.66})[(Al_{0.96}Si_{7.04})O_{20}(OH)_4]$*
calcium carbonate p.a. (Merck)	calcite	$CaCO_3$
Flechtinger sandstone	$\approx$ 65 % quartz	SiO_2
	$\approx$ 14 % K-feldspar	$KAlSi_3O_8$
	$\approx$ 10 % corroded plagioclase	$Na_{0.5}Ca_{0.5}Al_{1.5}Si_{2.5}O_8$**
	$\approx 7-8$ % illite (pore filling)	$(Ca_{0.05}Na_{0.03}K_{0.61})(Al_{1.53}Fe^{3+}_{0.22}Fe^{2+}_{0.03}Mg_{0.28})(Si_{3.4}Al_{0.6})O_{10}(OH)_2$***
	$\approx$ 3 % calcite cement	$CaCO_3$
	other cements	e.g. Fe_2O_3
	volcanic rock fragments	various
	accessory minerals	e.g. $BaSO_4$, TiO_2
Fontainebleau sandstone	quartz	SiO_2

* chemical composition taken from Bradbury and Baeyens (2009).
** chemical composition of labradorite-andesine.
*** average chemical composition taken from Moore and Reynolds (1989).

Table 3.1: Starting materials for the experiments. Petrological compositions are given as mass fractions in %. Mineralogical compositions are derived from XRD, XRF, and EMPA measurements as well as from the literature.

Scientific Technical Report STR 12/07
DOI: 10.2312/GFZ.b103-12079

3.1.2 Starting Fluids

In the majority of the flow-through and batch experiments deionized water, H_2O with $\sigma_f(T_0) \approx 2.5 \times 10^{-3}$ S/m, was used as the starting fluid. Some experiments were conducted with $NaCl_{aq}$ solutions of various concentrations ranging from 0.001 to 2 mol/L. As a measure of caution, these solutions were flushed with N_2 for approximately 0.5 d until the concentration of dissolved O_2 were lowered from ≈ 2 to $\approx 0.4 \times 10^{-3}$ g/L to prevent corrosion of the metal parts of the HPT-permeameters (Section 3.2.1). Some flow-through experiments were performed with fluids resulting from batch experiments with H_2O, quartz, labradorite-andesine, microcline, illite, and/or calcite at temperatures up to 150 °C (Section 3.2.2).

3.2 Experimental Procedure

3.2.1 Flow-through Experiments

Two types of flow-through experiments were performed: (i) stepwise heating and cooling of the samples and (ii) fluid exchange experiments. The stepwise heating and cooling experiments were conducted to investigate the effects of temperature on σ_r and k. The time-dependent evolution of σ_r at constant temperature stages was monitored as a proxy signal for the time-dependent evolution of the chemical saturation state of the fluid-rock systems following the rationale that σ_r is related to σ_f (e.g., Equation 2.3), and σ_f is related to the concentration and identity of dissolved species in solution (e.g., Equation 2.1). The heating and cooling of the samples was performed to deliberately induce undersaturated and oversaturated conditions in the fluid-rock systems. Fluid exchange experiments were carried out to investigate the effects of fluids with known concentration of dissolved species and known σ_f on σ_r and k. The formation resistivity factor F and the magnitude of σ_s were determined by this method. Furthermore, the effect of clay swelling on k was investigated in fluid exchange experiments.

The electrical conductivity of the porous samples was continuously monitored, whereas k was discontinuously measured during the flow-through experiments (Figure 3.2). Flow prevailed during permeability measurements; but stagnant conditions prevailed in the remainder of the experiments. The stagnant phases were typically much longer than the flow phases, i.e., the fluid-rock system was undisturbed during the longest period of the experiments. The temperature intervals during the heating or cooling mostly ranged between 20 and 30 °C. The heating or cooling procedure was performed with 20 °C/h and it took approximately 2 h until temperature was equilibrated at each constant temperature stage.

Experimental Set-up of the Flow-through Experiments

The flow-through experiments were conducted by means of two high pressure and temperature HPT-permeameters (Milsch et al., 2008). The HPT-permeameters used for the flow-through experiments consist of a confining pressure system and a separate pore pressure system (Figures 3.3, 3.4, and 3.5).

The main part of the confining pressure system is a pressure vessel manufactured by Voggenreiter, Mainleus, Germany, which is equipped with an internal resistance heating element (Thermocoax). The heating element is connected to a DC-power supply (Agilent 6675A) that is controlled by an external temperature controller (West 4100+, West 4200). The controller is connected to a type K thermocouple mounted inside the pressure vessel. The confining pressure and heat transfer medium used in the framework of the present study was Shell Thermia Oil B.

Scientific Technical Report STR 12/07
DOI: 10.2312/GFZ.b103-12079
Deutsches GeoForschungsZentrum GFZ

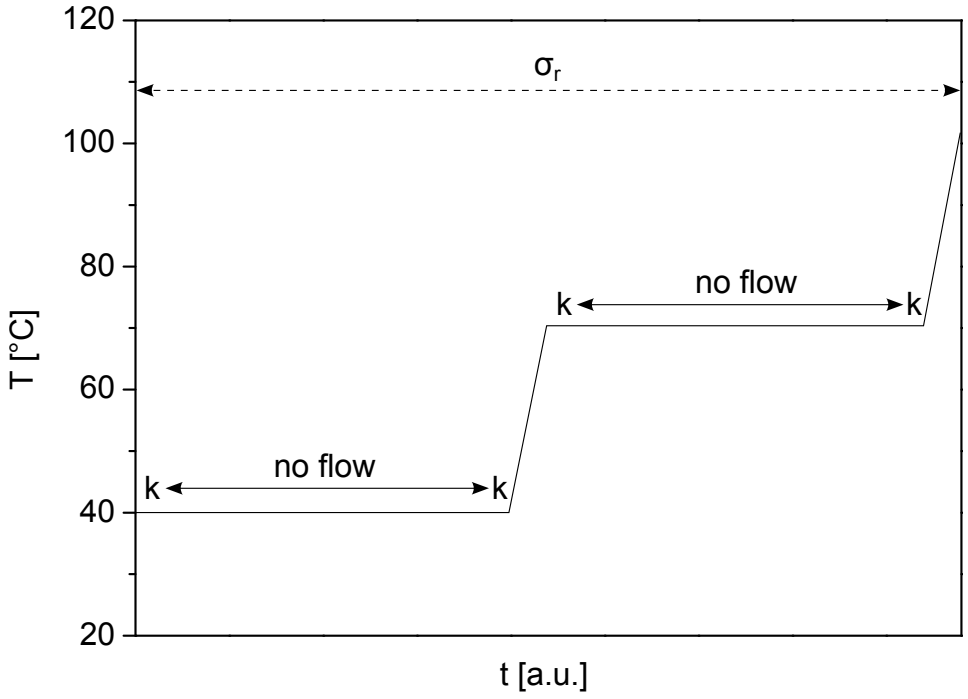

Figure 3.2: Schematic of the experimental procedure of the flow-through experiments. Temperature is plotted as a function of time in arbitrary units (illustrated by a solid line). Flow phases are denoted by k (permeability measurements). Shut-in phases are denoted by *no flow* labeled arrows. The electrical conductivity of the samples, σ_r, was continuously monitored during the experiments (dashed arrow).

Scientific Technical Report STR 12/07
DOI: 10.2312/GFZ.b103-12079

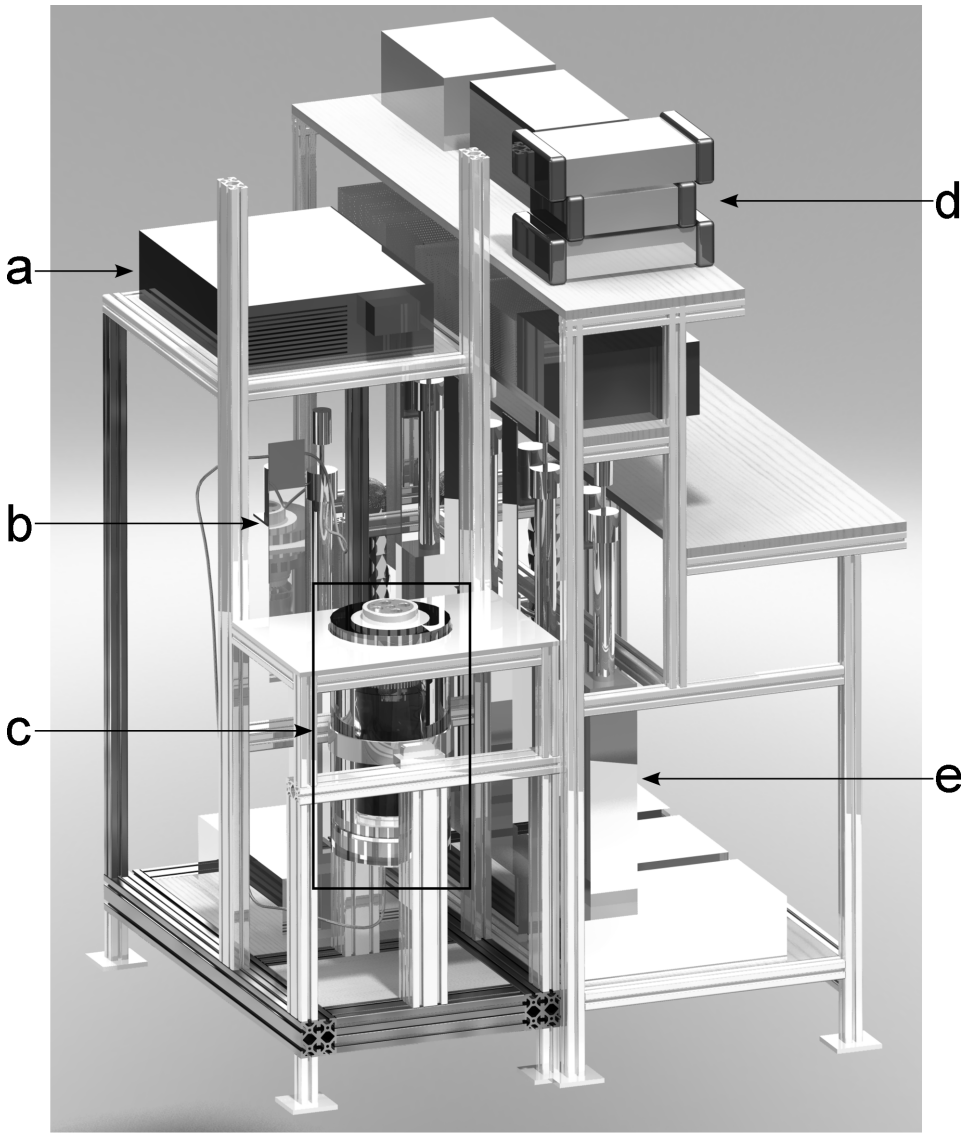

Figure 3.3: Representation of the flow-through apparatus. a), b), c), d), and e) denote the DC-power supply for the heating element, the confining pressure pump, the pressure vessel (marked by a rectangle), instrumentation for signal generation and data acquisition, and the pore fluid pumps, respectively. (Image: M. Hillebrand)

Scientific Technical Report STR 12/07
DOI: 10.2312/GFZ.b103-12079

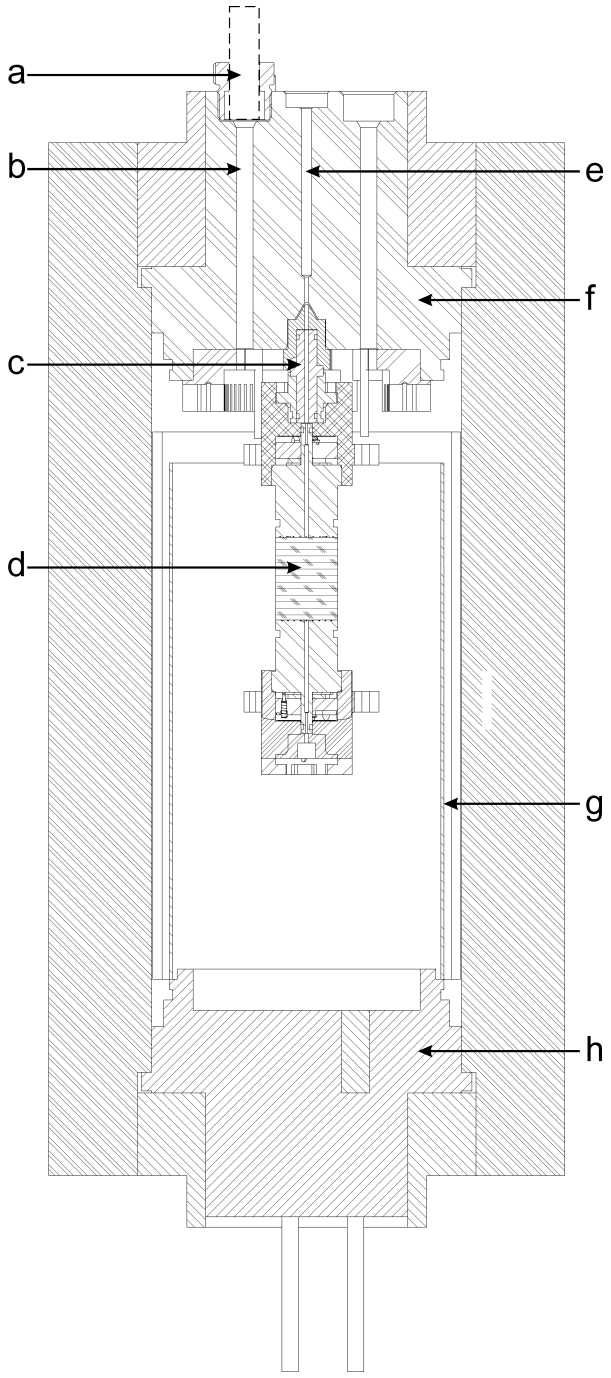

Figure 3.4: Technical drawing of the pressure vessel. a), b), c), d), e), f), g), and h) denote an electrical feedthrough, a channel for the insulated copper wires, the PEEK connector, a rock sample, the central bore for the downstream connection of the sample assembly to the capillary system, the top plug, the heating element, and the bottom plug, respectively. The upstream connection of the specimen assembly to the capillary system is not shown. (Image: R. Giese)

Scientific Technical Report STR 12/07
DOI: 10.2312/GFZ.b103-12079

The confining pressure was maintained by a high pressure syringe pump (Teledyne Isco 65D) that is controlled by an electronic servo controller unit. This unit also controls two air actuated constant volume valves (Vindum Engineering, Canada) enabling oil refill from, or oil release to, a reservoir at ambient pressure, while the pressure in the pressure vessel remains unchanged. The pressure inside the pressure vessel was stable to $\pm 0.05 \times 10^6$ Pa, and the temperature was stable to ± 0.5 °C at a given pressure and/or temperature interval. Except when otherwise specified, the confining pressure was held constant during the experiments at 10^7 Pa, and the temperature ranged between room temperature and a maximum temperature of approximately 175 °C.

The pore pressure system consists of the specimen assembly (Figure 3.5), a 1/8 inch (3.175×10^{-3} m) outer diameter stainless steel capillary system (Swagelok 316/316L seamless tubings with a wall thickness of 0.889×10^{-3} m), and two high pressure syringe pumps (Teledyne Isco 260D) at either side upstream and downstream of the specimen assembly. The measured dead volume on the upstream side of the sample is approximately 9×10^{-3} L. The upstream and downstream pump pairs are controlled by electrical servo controller units connected to a set of electrical valves. The pumps can be run in either constant pressure or constant flow rate mode. Pressure is measured at the top of the syringe pumps by pressure transducers with an accuracy of $\pm 10^3$ Pa. Except when otherwise specified, the pore pressure was held constant by the active downstream pump at 5×10^6 Pa, i.e., half the confining pressure. Throughout the experiments conducted in the present study, only one upstream and one downstream pump were used at a time. The other two pumps were held on standby or used for the subsequent injection of fluids other than H_2O.

For the purpose of sampling the pore fluid from a sample without dropping the pore pressure, a pressure relief valve, PRV, was installed in the capillary system on top of the downstream capillary fitting. Three ball valves are installed in the capillary system allowing to hold the pore pressure constant, to maintain flow through the sample, or to bypass the sample. The specimen assembly is sealed against the confining pressure medium by means of several Viton® 80Shore O-rings and a FEP jacket around the sample.

Electrical insulation of the upstream side against the downstream side of the sample was achieved by connecting the specimen assembly to the top plug of the pressure vessel with a PEEK connector (c in Figure 3.4). However, the PEEK connector was not completely electrically insulating because the fluid filled bore could act as a pathway for charge carriers. Estimations of the conductance of the H_2O filled bore with a radius of 10^{-3} m and a length of 45×10^{-3} m yielded a conductance of approximately 6.8×10^{-7} S at 150 °C. This conductance was lower by a factor of ≈ 1000 compared to typical values for Flechtinger sandstone samples with H_2O as the pore fluid at the same temperature. If the conductance of the porous sample was very low (as in the QLM-sandwich experiment ft-s-3), the conductance of the fluid filled PEEK connector was only lower by a factor of ≈ 50. When a highly conducting 2 mol/L $NaCl_{aq}$ solution was used as the pore fluid, the conductance of the fluid filled PEEK connector was only lower by a factor of ≈ 3 compared to a Flechtinger sandstone sample at 70 °C (ft-Fl-12).

Capillary and electrical connections were made via high pressure Swagelok tube fittings and electrical feedthroughs, respectively. These electrical feedthroughs were composed of high pressure steel tubing (Sitec) filled with epoxy (Araldite) that cements and seals insulated copper wires inside each tubing.

Two experiments were conducted with a special set-up differing from the set-up described above:

(i) One of these set-ups was designed to transfer fluids under isothermal and nearly isobaric

Scientific Technical Report STR 12/07
DOI: 10.2312/GFZ.b103-12079
Deutsches GeoForschungsZentrum GFZ

Figure 3.5: Detail of a mounted specimen assembly shown in 180° tilted position. A Fontainebleau sandstone sample is located in the center. The silvery-gray spiral is the upstream connection of the specimen assembly to the capillary system enabling maintenance of pore pressure and fluid flow. Two Pt100 sensors and electrical connections to the current and potential electrodes are shown. Current electrodes are the end caps below and above the rock sample. Silver paint rings act as the potential electrodes in the four electrode arrangement.

Scientific Technical Report STR 12/07
DOI: 10.2312/GFZ.b103-12079

conditions from a BR-300 autoclave (High Preactor supplied by Berghof, Germany) into the sample located in the pressure vessel of the HPT-permeameter (flow-through experiment ft-Fl-12). A BR-300 autoclave was connected to the upstream side of the capillary system using a number of ball and needle valves. The BR-300 autoclave was heated by a conventional heating plate equipped with a magnetic stirrer. Temperature inside the autoclave was monitored using a type K thermocouple in combination with an Agilent HP34970A Data Acquisition/Switch Unit. Pressure inside the autoclave was maintained by Ar gas pressure. A pressure regulator connected to an Ar gas bottle kept the pressure constant at 6×10^6 Pa. A dip tube was used for fluid transfer from the autoclave to the HPT-permeameter's capillary system. To prevent the cooling of the transferred fluid on its way from the autoclave to the capillary system, the connecting capillary was thermally insulated. Two filters (Swagelok) with a pore size of 2×10^{-6} m and 0.5×10^{-6} m were installed in line in the connecting capillary to prevent the injection of fine particles from the BR-300 autoclave into the HPT-permeameter's capillary system.

(ii) The other experiment with a special set-up was conducted with a small cylindrical Flechtinger sandstone with a length of 20×10^{-3} m and a radius of 3×10^{-3} m in the HPT-permeameter (experiment ft-Fl-13, Figure 3.6). Adapters for the reduction of the cross-sectional area of the end caps were used. The adapters were sealed against the confining pressure medium with Viton® 80Shore O-rings. The jacket consisted of a Viton® hose with a wall thickness of 1.5×10^{-3} m and an inner diameter of 6×10^{-3} m supplied by Lézaud, Marpingen, Germany. For mechanical stability a PEEK bushing, precisely fitting the outer diameter of the adapters, was used to support the fragile sample assembly. The electrical conductivity was measured over the full length of the sample employing a two-electrode arrangement in which the adapters acted as the current and potential electrodes.

Data acquisition and storage was performed with a Data Acquisition/Switch Unit (Agilent 34970A) connected to a laptop computer. With the aid of the labVIEW software package (National Instruments), temperature, pressure, pump volume, and voltage signals were measured and stored at intervals of 30 s in a tabulator separated ASCII text file. For the σ_r and k calculations (Section 3.2.1), values of temperature and voltage were required. Absolute errors of temperature measured with a Pt100 are specified by the instrument manufacturer as 0.06 °C. Relative errors of measured voltages are specified as approximately 0.005 % for voltages up to 1 V.

Electrical Conductivity and Permeability Measurements in the HPT-Permeameters

The HPT-permeameters were used for the measurements of σ_r and k of the investigated porous materials. The electrical conductivity of the samples was mostly measured in a four-electrode arrangement with a variable shunt-resistor making use of Ohm's law, $U = I\,R = I\,L/(\sigma_r\,A)$ (Ohm, 1826). The voltage measured over the shunt yields the imposed current and is combined with the voltage measured over the length L of the sample between the potential electrodes. From this follows:

$$\sigma_r = \frac{L}{A\,R} = \frac{U_{\text{shunt}}\,L}{U_{\text{sample}}\,R_{\text{shunt}}\,A}, \tag{3.1}$$

where A, R, and U are the cross sectional area of the sample, the resistance, and the voltage, respectively. For σ_r measurements, the cylindrical samples with a diameter of 3×10^{-2} m and a length of $\approx 4 \times 10^{-2}$ m were painted with two rings of silver conductive paint that acted

Scientific Technical Report STR 12/07
DOI: 10.2312/GFZ.b103-12079
Deutsches GeoForschungsZentrum GFZ

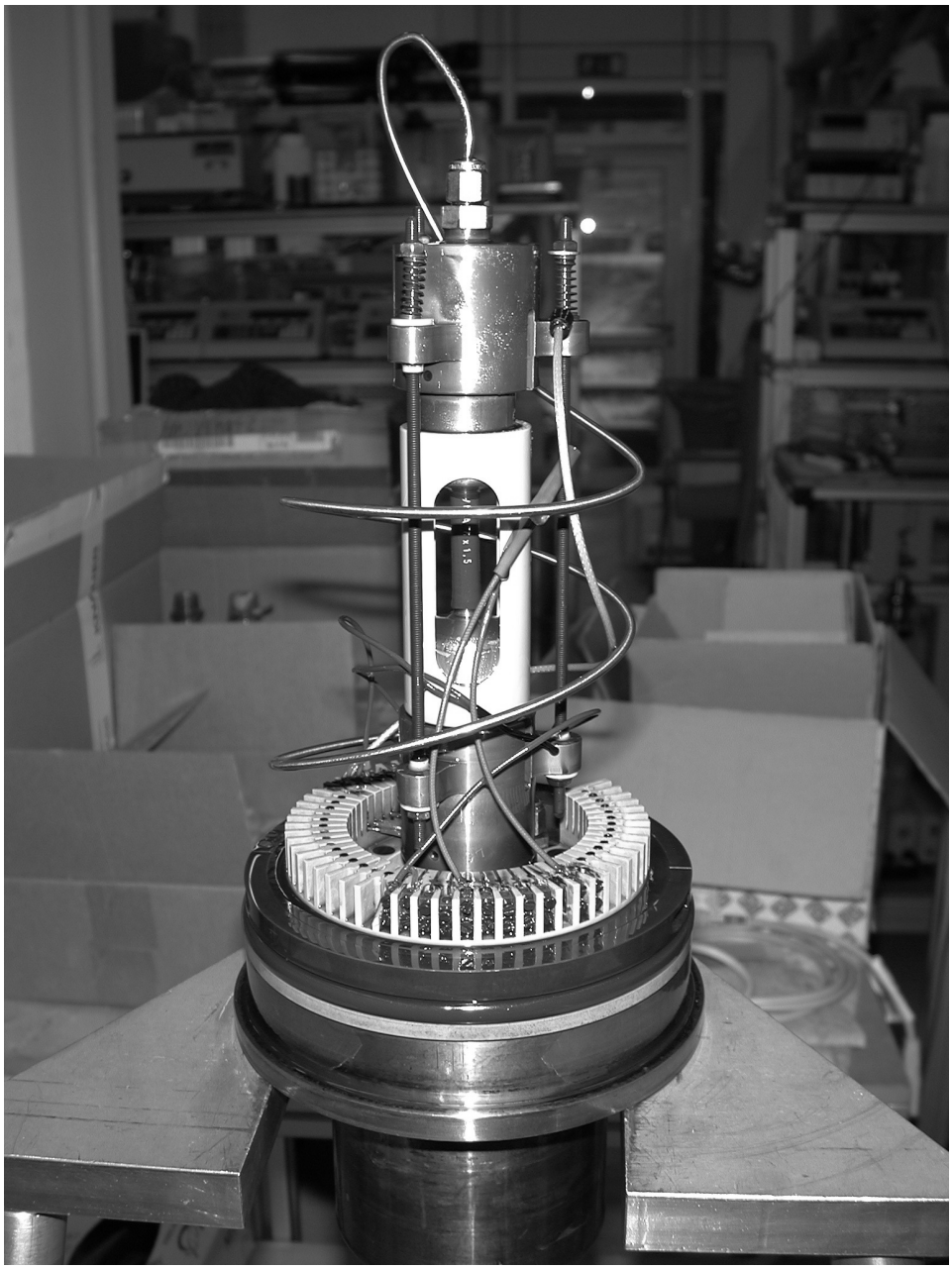

Figure 3.6: Detail of the small sample assembly (ft-Fl-13). A small Flechtinger sandstone sample is located in the center of the assembly. A bright gray PEEK bushing provides mechanical stability. The springs at the ends of the thread rods regulate the axial stress on the fragile rock sample.

Scientific Technical Report STR 12/07
DOI: 10.2312/GFZ.b103-12079

as the potential electrodes with $L = 25 \times 10^{-3}$ m in the four-electrode arrangement (Figure 3.1a). Current electrodes were the stainless steel end caps. The voltage was imposed with an Agilent 33220A function generator set to produce a 1 V AC sinus peak-to-peak signal with a frequency of 13 Hz. This set-up prevented the polarization at the current electrodes, the reaching of the decomposition voltage of water, and the interference with radio frequencies (E. Spangenberg, personal communication). Although the measurements were carried out with an impressed AC signal, applicability of Ohm's law is assumed. Ohm's law is valid for AC circuits containing resistive elements and no inductances or capacitances. Impedance spectroscopic measurements on a Flechtinger sandstone sample showed that at low frequencies $< 10^3$ Hz the measured phase angles were small indicating that inductances or capacitances were negligible and that the complex impedance was represented by the ohmic resistance of this material at the experimental conditions of the present study (Figure 3.8). Thus, the assumption of the applicability of Ohm's law is justified in the present case.

Relative errors of the σ_r measurements amount to approximately 4 to 8 %. Relative errors were calculated by an error propagation of relative errors of the voltage measurements and the length measurements involved in determining σ_r (Equation 3.1). The width of the potential electrode is within the region of 10^{-3} m and thus contributes significantly to the uncertainty of σ_r measurements resulting in relative errors as high as 8 % (Milsch et al., 2008). However, since errors in the length measurements are assumed to be fairly constant throughout a single experiment, relative measured changes of σ_r in the course of a single experiment were exact to a much higher extent. Electrical conductance through the PEEK connector (Figure 3.4c) led to larger errors of σ_r in the limits of a highly conducting fluid and/or when sample materials with a very low electrical conductivity were used.

The permeability was calculated from measured pressure differences, Δp, over the cylindrical samples with known geometries $\Delta L/A$ at steady-state flow and pressure conditions using a rearrangement of Equation 2.18:

$$k = \frac{\dot{V}\,\eta\,\Delta L}{A\,\Delta p}. \tag{3.2}$$

The permeability measurements were conducted under hydrostatic confining pressure p_c conditions. The pressure difference over the sample length is the pore pressure p_p difference. The difference between p_c and p_p is the effective pressure $p_{\text{eff}} = p_c - p_p$ defined by Terzaghi's principle (Terzaghi, 1923; de Boer and Ehlers, 1990). The dynamic viscosity and density of the initial pore fluids (H_2O and NaCl-solutions) were calculated for the respective pressures and temperatures of each experiment (Francke and Thorade, 2010). The dynamic viscosity and the density of H_2O were obtained from the REFPROP software (NIST - National Institute of Standards and Technology). Dynamic viscosity and density data of the NaCl-solutions were compiled from the literature (Rowe and Chou, 1970; Kestin et al., 1981; Mao and Duan, 2009).

Low Reynolds numbers indicated that laminar flow prevailed in the porous samples (Milsch et al., 2008). Reynolds numbers were calculated using Equation 2.19 for the specific conditions pertaining to the experiments conducted in the present study. For the temperature range 25 to 175 °C, a porosity of 10 %, a characteristic length of the pore dimensions of 10×10^{-6} m, and a typical flow rate $\dot{V}$ of $\approx 1.67 \times 10^{-9}$ m^3/s, the Reynolds numbers range between 2.6×10^{-5} and 1.4×10^{-3}. Since laminar flow is assumed for Re $<< 1$ (Section 2.1.2), the assumption of laminar flow in the porous samples is justified.

Scientific Technical Report STR 12/07
DOI: 10.2312/GFZ.b103-12079
Deutsches GeoForschungsZentrum GFZ

Experimental Conditions of the Flow-through Experiments

The flow-through experiments were performed within the temperature range of 25 to 175 °C and mostly at hydrostatic confining pressure $p_c = 10 \times 10^6$ Pa, and pore pressure $p_p = 5 \times 10^6$ Pa (Table 3.2). Prior to most flow-through experiments, several pore volumes of deionized water with a very low electrical conductivity ($\sigma_f(T_0) \approx 2.5 \times 10^{-3}$ S/m, where $T_0 = 25$ °C) were flown through the samples to obtain starting conditions far from chemical equilibrium. In one experiment (ft-Fl-10), however, the initial pore fluid was a 1 mol/L $NaCl_{aq}$ solution. Experimental details of the flow-through experiments are described in the appendix.

The nomenclature of the flow-through experiments follows the scheme *ft-material-number*, where *ft* denotes "flow-through", *material* is replaced by *s* for "sandwich", *Fo* for "Fontainebleau sandstone", *P* for "porous PTFE", and *Fl* for "Flechtinger sandstone", and *number* is the running number of the experiment.

Scientific Technical Report STR 12/07
DOI: 10.2312/GFZ.b103-12079

Number	**Type**	**Porous Material**	**Grain Size** $\times 10^{-6}$ m	**Fluid**	**Description**	T**-Range** °C	**Total Duration** d	**Analyses of/with****
ft-s-1	L-sandwich	Fontainebleau SST	125-355	H_2O	T-steps	40-172	43	1
ft-s-2	QL-sandwich	Fontainebleau SST	125-355	H_2O	T-steps	30-170	21	1
ft-s-3	QLM-sandwich	Fontainebleau SST	63-125	H_2O	T-steps	40-150	75	2, 3, 5, 7, 11
ft-s-4	QLM-sandwich	PTFE discs	63-125	H_2O	T-steps	40-150	48	1, 2, 4, 7, 8
ft-s-5	QLMI-sandwich	PTFE discs	63-125 (*)	H_2O	T-steps	40-150	48	1
ft-Fo-6	core	Fontainebleau SST	n.a.	H_2O	T-steps	40-162	40	1, 2, 3
ft-P-7	core	PTFE, Fontainebleau SST	n.a.	H_2O–0.1 mol/L $NaCl_{aq}$	T-steps, fluid exchange	60	35	1, 3
ft-Fl-8	core	Flechtinger SST	n.a.	H_2O	T-steps	30-164	136	1, 3
ft-Fl-9	core	Flechtinger SST	n.a.	H_2O	T-steps	40-150	90	1, 2, 3, 5, 6, 11, 12
ft-Fl-10	core	Flechtinger SST	n.a.	1 mol/L $NaCl_{aq}$	T-steps	40-150	65	1, 3, 5, 6
ft-Fl-11	core	Flechtinger SST	n.a.	H_2O–0.5 mol/L $NaCl_{aq}$	T-steps, fluid exchange	40-70	42	1, 3, 6
ft-Fl-12	core	Flechtinger SST	n.a.	H_2O–2 mol/L $NaCl_{aq}$	T-steps, fluid exchange	40-150	139	1, 3, 6
ft-Fl-13	small core	Flechtinger SST	n.a.	H_2O	T-steps	40-150	70	1, 3, 9

(*) illite was used as received, see Table 3.1.
** 1) k, 2) c_i, 3) σ_r, 4) σ_f, 5) BET, 6) MIP, 7) SEM, 8) TEM, 9) X-ray CT, 10) pH, 11) XRD, 12) EMPA.

Table 3.2: Overview of the conducted flow-through experiments. Further details are reported in the appendix.

Scientific Technical Report STR 12/07
DOI: 10.2312/GFZ.b103-12079

Deutsches GeoForschungsZentrum GFZ

3.2.2 Batch Experiments

Batch experiments were conducted to investigate the effects of fluid-mineral reactions on σ_f, on the concentration of dissolved species in the fluid phase, and on mineralogical and microstructural properties of the solid phases. The evolution of σ_f was monitored as a proxy signal for the evolution of the chemical state of the fluid-solid systems. Stepwise heating and cooling was performed in some experiments to investigate the effects of temperature on σ_f. The experiments were performed under controlled pressure and temperature conditions and with defined fluid volumes as well as defined chemical compositions of the fluid-solid systems. The batch experiments provided insights into processes occurring at the fluid-solid interfaces and were thus valuable for the interpretation of processes occurring in the pore space of the porous materials that were investigated in the flow-through experiments.

Experimental Set-up of the Batch Experiments

Batch experiments were performed in the same temperature range as the flow-through experiments but under different pressure conditions. Three types of batch experiments were performed:

(i) One type of batch experiments was conducted in 10×10^{-3} and 20×10^{-3} L PTFE autoclaves supplied by Bola, Germany. The resulting saturation vapor pressures in the temperature range of 70 to 150 °C were between approximately 0.1 and 0.45×10^6 Pa. The experiments were conducted at constant temperature conditions in a Memmert drying oven. At 70 °C, the accuracy of the oven was estimated to be ±2 °C by repeated measurements with a reference thermometer (ASL Pt25).

(ii) The second type of the batch experiments was performed with pressurized 0.1 and 0.3 L PTFE lined autoclaves (BR-100 and BR-300, High Preactor supplied by Berghof, Germany) with thermal insulation. Pressure was maintained at approximately 5×10^6 Pa by Ar gas feeding. Temperature was monitored with a type K thermocouple. In this set-up temperatures were stable at 70 ± 2 °C and 150 ± 2 °C. When a powder was used as the solid starting material, a magnetic stirrer was installed in the autoclave.

(iii) In the third type of the batch experiments the evolution of σ_r of an initially H_2O saturated Flechtinger sandstone was monitored at constant temperature, and the resulting pore fluid was sampled (b-Fl-17). A large cylindrical Flechtinger sandstone sample with a length of 0.1 m and a radius of 0.025 m was jacketed with a FEP heat shrink tubing and confined on both end planes by a steel plug. The FEP jacket was mechanically supported by a collar consisting of a rubber sleeve and several stainless steel hose band clips. The steel plugs had a bore and a machined grid on the side touching the sample for fluid distribution. By means of a Swagelok fitting plus end cap and a Viton® 80Shore O-ring, both steel plugs were sealed (Figure 3.7). The assembly was saturated with H_2O in an exsiccator and was subsequently stored in a water bath at a constant temperature of 70 ± 2 °C.

The frequency dependent impedance Z (in Ω) and the phase angle γ (in rad) of the assembly were measured at irregular intervals in a two electrode arrangement by means of a Zahner Zennium Electrochemical Workstation impedance spectrometer. Measurements were performed as a function of the frequency of a sinusoidal AC signal ranging from 1 to 10^3 Hz (Figure 3.8). The scanning of this frequency range was performed in a loop with 47 steps and a start and end value of 10^3 Hz. The impedance spectrometer is a high precision device with a high input resistance making it suitable especially for measurements on samples of low

Scientific Technical Report STR 12/07
DOI: 10.2312/GFZ.b103-12079

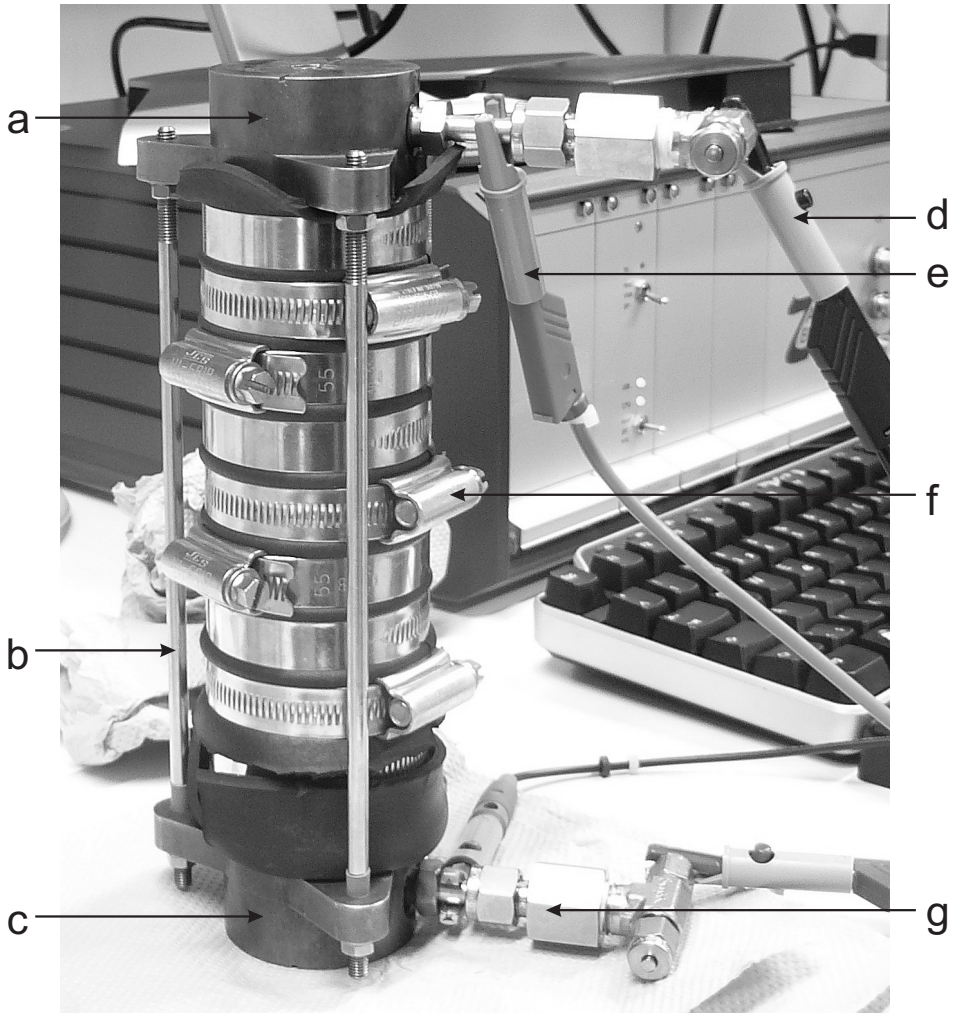

Figure 3.7: Detail of the impedance spectrometry experiment b-Fl-17. a), b), c), d), e), f), and g) denote a steel plug, an isolated thread rod, a second steel plug, a current electrode, a potential electrode, the collar with the hose band clips, and a Swagelok fitting with end caps, respectively.

Scientific Technical Report STR 12/07
DOI: 10.2312/GFZ.b103-12079

electrical conductivity. The assembly was taken out of the water bath for the measurements. Measurements were made after carefully drying the assembly on the outside to prevent leakage currents along the jacket or the isolated thread rods. With the assumption of negligible impedance of the steel plugs compared to the Flechtinger sandstone sample the electrical conductivity of the sample was:

$$\sigma_r = \frac{L}{\cos\gamma\, Z\, A}, \tag{3.3}$$

where A is the cross sectional area of the sample, γ is the phase angle, L is the sample length, and Z is the impedance. The impedance is expressed as a complex number with a real part and an imaginary part. From the real part of the impedance the ohmic resistance R is calculated by $R = \cos\gamma\, Z$. In the AC frequency range examined in this study the ratio of the ohmic resistance R to the impedance Z was close to 1 due to small phase angles (Figure 3.8). Thus, the imaginary part of the impedance could be neglected and the AC circuit could be treated as a DC circuit in which Ohm's law applies. Consequently, the electrical conductivity of the rock sample was determined using the ohmic resistance:

$$\sigma_r = \frac{L}{R\, A}. \tag{3.4}$$

For comparability to the measurements in the flow-through experiments, σ_r values were reported for the first branch of the loop and at 12 Hz, which was the nearest value of the scanned frequency spectrum to the AC frequency applied in the HPT-permeameter (13 Hz). All measurements were performed at approximately the same time (300 ± 60 s) after taking the assembly from the water bath to prevent inconsistencies. After each measurement the assembly was reinserted into the water bath. At the end of the experiment the pore fluid was sampled with the aid of Ar pressure and was analyzed with respect to σ_f, pH, concentrations of major cations, and concentrations of F^-, Cl^-, and SO_4^{2-}.

Experimental Conditions of the Batch Experiments

The majority of the batch experiments were performed with deionized H_2O as the starting fluid, while the starting fluids in the experiment series conducted with granular quartz-feldspar aggregates were H_2O and 0.1 mol/L $NaCl_{aq}$ (b-QLM-3). An overview of the batch experiments and the experimental parameters is given in Table 3.3. Further experimental details are listed in the appendix.

The nomenclature of the batch experiments follows the scheme *b-material-number*, where *b* denotes "batch", *material* is replaced by combinations of *Q* for "quartz grains", *L* for "labradorite-andesine grains", *M* for "microcline grains", *I* for "illite grains", and *C* for "calcite grains", or, when rock samples were used, *material* is replaced by *Fl* for "Flechtinger sandstone". The running number of the experiment is denoted by *number*.

Scientific Technical Report STR 12/07
DOI: 10.2312/GFZ.b103-12079

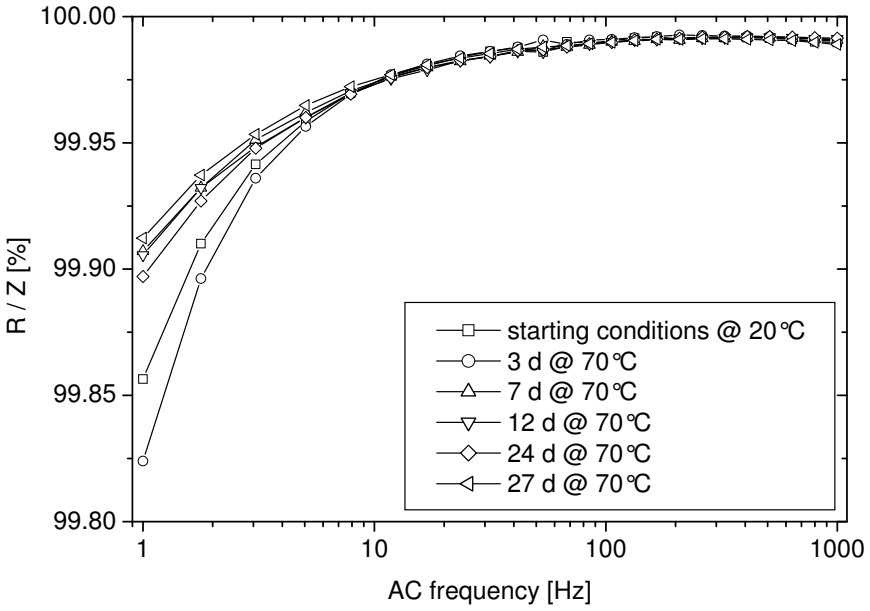

Figure 3.8: The ratio of ohmic resistance to complex impedance, R/Z, in % as a function of AC frequency in Hz for batch experiment b-Fl-17. R is almost equal to Z in the AC frequency range 1 to 1000 Hz. R/Z is independent of temperature and run duration of the experiment at AC frequencies > 10 Hz. The electrical conductivity of the samples in flow-through and batch experiments was calculated by Equation 3.4 using R values measured at 13 and 12 Hz, respectively.

Scientific Technical Report STR 12/07
DOI: 10.2312/GFZ.b103-12079

Number	**Type**	**Grain Size** $\times 10^{-6}$ m	**Solid Mass** g	**Fluid Volume** $\times 10^{-3}$ L	**Preparation**	T**-Range** °C	**Maximum Pressure** $\times 10^{6}$ Pa	**Total Duration** d	**Analyses of/with***
b-QL-1	QL-series	125-355	2 ± 0.024	5	d.s.	150	≈ 0.45	22	2, 7, 11
b-QL-2	QL-series	63-125	1 ± 0.009	5	d.s.	150	≈ 0.45	20	2, 10, 4, 7, 11
b-QLM-3	QLM-series	63-125	1 ± 0.013	5*	u.c., w.s.	150	≈ 0.45	7	2, 4, 7, 11
b-QLM-4	QLM	63-125	1.003	5	u.c., w.s.	70-150	≈ 0.45	52	2, 4, 5, 7
b-QLM-5	QLM	63-125	1.006	5	u.c., w.s.	150	≈ 0.45	70	2, 4, 5, 7, 11, 12
b-QLM-6	QLM	$<<63$	2.007	40	w.s.	25-150	≈ 0.45	141	4, 7
b-QLM-7	QLM	$<<63$	1.006	5	w.s.	70-150	≈ 0.45	41	4, 7
b-QLM-8	QLM	<63	1.005	15	w.s.	70-150	≈ 0.45	70	4, 5, 7, 11
b-QLM-9	QLM	<63	1.007	5	w.s.	70-150	≈ 0.45	63	4, 7
b-QLMI-10	QLMI	63-125**	1.001	5	u.c., w.s.	150	≈ 0.45	70	2, 4, 7
b-QLMI-11	QLMI	$<<63$**	1.002	5	w.s.	70-150	≈ 0.45	41	4, 7
b-QLMI-12	QLMI	<63**	1.005	15	w.s.	70-150	≈ 0.45	70	4, 7
b-QLMI-13	QLMI	<63**	1.003	5	w.s.	70-150	≈ 0.45	63	4, 7
b-QLMIC-14	QLMIC	<63**	10.1	6.1	u.c, w.s.	70	≈ 0.1	31	4, 10
b-Fl-15	Flechtinger SST fragment	n.a.	0.931	5	n.a.	70-150	≈ 0.45	90	2, 4, 7
b-Fl-16	Flechtinger SST core, p.b.r.	n.a.	66.85	240	n.a.	70-150	5	82	2, 4, 5, 6, 7, 10
b-Fl-17	Flechtinger SST core	n.a.	468.94	19.57	n.a.	70	≈ 0.1	38	2, 3, 4, 10

* H_2O and 0.1 mol/L $NaCl_{aq}$ were used as the starting fluids.
** Illite was used as received, see Table 3.1.
*** 1) k, 2) c_i, 3) σ_r, 4) σ_f, 5) BET, 6) MIP, 7) SEM, 8) TEM, 9) X-ray CT, 10) pH, 11) XRD, 12) EMPA.

Table 3.3: Overview of the conducted batch experiments. Further details are reported in the appendix.

Scientific Technical Report STR 12/07
DOI: 10.2312/GFZ.b103-12079

Deutsches GeoForschungsZentrum GFZ

3.3 Analytical Techniques

3.3.1 Fluid Analyses

Fluid sampling from different autoclave types required three different sampling techniques: (i) Fluid samples were carefully taken from the batch autoclaves with a pipette to prevent solids from entering the fluid sample. After sampling, the fluids were centrifuged at 3000 rounds per minute for 10 min. (ii) Fluid samples were taken through a dip tube from the pressurized batch reactors (BR-100 and BR-300) and were filtered with a 2×10^{-6} m filter to remove dispersed particles. Particles $< 2 \times 10^{-6}$ m were removed by centrifugation. (iii) Fluid samples were taken from the flow-through apparatus downstream of the solid sample mostly by means of a pressure relief valve, PRV. The valve was set to the pore pressure of the experiments to prevent a pressure drop in the pore pressure system during fluid sampling. In one case, fluid sampling was performed through a capillary at ambient outflow pressure.

Most fluid samples were analyzed with respect to σ_f and concentration of dissolved cations. Some fluid samples were additionally analyzed with respect to O_2 concentration and pH. The electrical conductivity of fluids was measured with a WTW TetraCon 325 conductivity probe connected to a WTW LF 325 conductivity meter making use of a linear temperature correction with a reference temperature $T_0 = 25$ °C, and a temperature correction coefficient $\alpha_f = 0.02$ °C^{-1} (Equation 2.2). During the batch experiments, measurements were performed at ≈ 50 °C. For this purpose, the experiments had to be quenched by cooling the autoclaves rapidly below boiling temperature. After the measurements the autoclaves were quickly heated to the same temperature as before the quenching. The O_2 concentration of NaCl starting solutions was measured with a WTW CellOx 325 probe connected to a WTW Oxi 340i device. At the end of some experiments, pH was measured with a WTW SenTix 81 pH glass electrode in combination with a WTW Multi 340i device.

Aliquots were taken from fluid samples for cation analysis and in one case for anion analysis. The aliquots (1 to 2×10^{-3} L) were diluted with 7.5×10^{-3} L H_2O and acidified with 0.5×10^{-3} L concentrated HNO_3 (65 %) to obtain a pH of the solutions of < 1. Permanently clear fluid samples were thus obtained. The samples were analyzed with inductively coupled plasma–optical emission spectroscopy, ICP-OES, using a Varian Vista MPX with a radial geometry of the spectrometer with respect to the Ar-plasma. Calibration of the ICP-OES was performed using ultra-pure solutions containing Na, Al, Si, K, Ca, and in one case Fe and Ni. The analyzed wavelenghts were 589.592, 279.553, 396.152, 251.611, 769.897, 396.847, 589.592, 238.204, and 231.604×10^{-9} m for Na, Mg, Al, Si, K, Ca, Mn, Fe, and Ni, respectively. On one Flechtinger sandstone pore fluid sample (b-Fl-17), anions were analyzed with a Dionex Dx-120 ion chromatograph. The as sampled fluid was used for the anion analysis. The Dx-120 was equipped with IonPac AG9-HC and AS9-HC anion exchange columns. An aqueous solution of Na_2CO_3 with a concentration of 9×10^{-3} mol/L was used as the eluent.

Apparent Normalized Element Losses

Results of the chemical fluid analyses are reported as concentrations of dissolved ionic species in the fluid, c_i, and apparent normalized element losses, nl_i, providing a means for direct comparison of fluid chemical data obtained from experiments conducted with different solids, fluids, and fluid/solid ratios. Normalized element losses were calculated by (Ji et al., 2005; Icenhower et al., 2006):

Scientific Technical Report STR 12/07
DOI: 10.2312/GFZ.b103-12079
Deutsches GeoForschungsZentrum GFZ

$$nl_i = \frac{c_i\, V}{A\, f_i}, \tag{3.5}$$

where V is the fluid volume in contact with the solid material, A is the surface area of the solid material, and f_i is the mass fraction of element i in the solid material. As a consequence, the unit of nl_i is mol/m^2. In the present study nl_i is defined as the apparent loss of element i from the solid material, because the concentration of an ionic species in the fluid phase is not only dependent on the dissolution per unit area of solid material but also on the decrease in concentration of that ionic species by precipitation.

The surface area of the granular starting materials was either determined by experimentally derived values of BET specific surface area, $\mathrm{SA_{BET}}$ (Table 4.6), or by geometric specific surface areas, $\mathrm{SA_{geo}}$. The fluid volume, the mass fraction of element i in the solid material, and the concentrations of dissolved ionic species in the fluid were known parameters. The geometric specific surface area was calculated from particle sizes obtained from sieve aperture diameters (Gautier et al., 2001):

$$\mathrm{SA_{geo}} = \frac{6}{\rho\, d_e}, \tag{3.6}$$

where ρ is the mean density value of a 1/1 mixture of quartz and labradorite-andesine amounting to 2.69×10^6 g/m^3 and d_e is the effective spherical diameter of the grains. Particles were assumed to be smooth spheres. The effective spherical diameter d_e was calculated assuming homogeneous particle distribution (Tester et al., 1994):

$$d_e = \frac{d_{\max} - d_{\min}}{\ln(\frac{d_{\max}}{d_{\min}})}, \tag{3.7}$$

where $d_{\min}$ and $d_{\max}$ represent the minimum and maximum particle diameters obtained from sieve apertures. Equations 3.6 and 3.7 were tested against the $\mathrm{SA_{BET}}$ value of the QLM starting material with the grain size fraction 63 to 125×10^{-6} m (Table 4.6). The BET determined value was 0.0431 ± 0.0001 m^2/g, and the corresponding value using Equations 3.6 and 3.7 was 0.025 m^2/g. Thus, $\mathrm{SA_{geo}}$ is a suitable approximation for the specific surface areas of the QLM grains. For experiments with the grain size fraction 125 to 355×10^{-6} m, $\mathrm{SA_{geo}}$ is approximately 0.01 m^2/g.

Error Estimation of Chemical Fluid Analyses

Errors of c_i were estimated using an error propagation of the relative errors of sample volumes V_s, added volumes of H_2O for dilution, V_d, and relative errors estimated from the standard deviations from the mean of repeated measurements performed for each analyzed element:

$$\frac{\Delta c_i}{c_i} = \pm\sqrt{(\frac{\Delta V_s}{V_s})^2 + (\frac{\Delta V_d}{V_d})^2 + (\frac{\Delta V_{\mathrm{HNO_3}}}{V_{\mathrm{HNO_3}}})^2 + (\frac{\Delta c_{i,m}}{c_{i,m}})^2}, \tag{3.8}$$

where $V_{\mathrm{HNO_3}}$ and $c_{i,m}$ are the volume of added HNO_3 and the concentration of each element in the fluid as measured with ICP-OES or ion chromatography, respectively.

Errors of nl_i were estimated using an error propagation of the relative errors of c_i, surface area A, and measured masses of solids, m:

Scientific Technical Report STR 12/07
DOI: 10.2312/GFZ.b103-12079
Deutsches GeoForschungsZentrum GFZ

$$\frac{\Delta nl_i}{nl_i} = \pm\sqrt{(\frac{\Delta c_i}{c_i})^2 + (\frac{\Delta A}{A})^2 + (\frac{\Delta m}{m})^2}. \tag{3.9}$$

Relative volume errors are 0.12 % as declared by the pipette manufacturer (Eppendorf Reference variable pipette with 2.5×10^{-3} L). Relative errors of the determination of masses are in the range of 0.3 % (laboratory balance Sartorius MC-1 ls220). Estimated relative errors of surface areas are approximately 2 % (BET-measurements). The mass fraction of elements in the solid material was calculated from the stoichiometry of the starting materials resulting from XRF measurements and was assumed to be accurate.

3.3.2 Analyses of Solid Materials

X-Ray Powder Diffraction and X-Ray Fluorescence

Analyses of the solid starting material and the solid materials resulting from experiments were performed with X-ray powder diffraction and X-ray fluorescence spectroscopy. For XRD analyses, a Siemens D5000 and a STOE STADIP diffractometer were used operating with Cu-K_α radiation. Analyses were performed on 1 to 3 g powdered material with a grain size of $< 30 \times 10^{-6}$ m. Crystalline phases were qualitatively and quantitatively analyzed using the GSAS software package for Rietveld refinements (Larson and Von Dreele, 2000) with the graphical user interface EXPGUI (Toby, 2001). XRF analyses were performed with a PANalytical Axios^{mAX} – Advanced operating with a Rh anode.

Mercury Intrusion Porosimetry

Mercury intrusion porosimetry, MIP, yielded the specific surface area, average pore radius, porosity, and bulk density of the porous samples as well as a pore throat radii distribution. MIP was conducted with a Fisons Instruments WS2000 mercury porosimeter equipped with a low-pressure unit ($\leq 25 \times 10^4$ Pa) for the determination of macro-pores and a high-pressure unit ($\leq 2 \times 10^8$ Pa) for the determination of micro-pores down to pore throat radii of $\approx 4 \times 10^{-9}$ m (Adolphs et al., 2002). The method is based on the assumption that a non-wetting fluid, Hg, is first forced into large and then into smaller connected pores by increasing pressure increments. Flechtinger sandstone samples with an approximate mass of 15 g were used for the measurements. The samples were dried at 40 °C for at least 24 h prior to each measurement. A common value for the contact angle of Hg on silicate surfaces is $\Phi_{Hg} = 141.3°$. The Hg density was taken as 13.534 g/cm^3 and the Hg surface tension was taken as $\gamma_{Hg} = 0.48$ N/m (Adolphs et al., 2002). Data were analyzed using the software Pascal 140/240/440 version 1.02 by CE Instruments ThermoQuest, Milano, Italy. When the cumulative volume of intruded and extruded Hg is plotted as a function of pressure, the intrusion curves typically show a S-shaped form in the present case. The extrusion curves depict a similar form but with a small hysteresis. This behavior suggests a conical form of the pore model used for specific surface area calculations in the software. Pore throat radii are calculated using the Washburn equation:

$$r = -\frac{2\gamma_{Hg}\cos\Phi_{Hg}}{p}, \tag{3.10}$$

where p is the Hg intrusion pressure. The average pore radius is reported as the pore radius corresponding to 50 % of the total intruded cumulative Hg volume.

Scientific Technical Report STR 12/07
DOI: 10.2312/GFZ.b103-12079
Deutsches GeoForschungsZentrum GFZ

BET Gas Adsorption

Specific surface areas were also determined with the BET gas adsorption method (Brunauer et al., 1938). QLM granular materials and Flechtinger sandstone intact rock samples were analyzed. The measurements were performed as multipoint-analyses according to DIN ISO 9277 with Kr and in two cases with N_2 as the adsorbates. QLM samples were dried under vacuum at 25 °C for 24 h, and Flechtinger sandstone samples were dried under vacuum at 50 °C for 5 h prior to the measurements. Approximately 1 and 3 g of dried QLM and Flechtinger sandstone material, respectively, were used for the measurements. Analyses were performed at −196.15 °C with a Quantachrome Autosorb-6 by Quantachrome, Odelzhausen, Germany.

3.3.3 Imaging Techniques

Electron Microprobe Analysis

Electron microprobe analysis, EMPA, was carried out with a JEOL JXA-8500F field-emission electron probe micro analyzer equipped with five wavelength dispersive X-ray spectrometers and an energy dispersive X-ray EDX spectrometer. Polished cross sections of the Flechtinger sandstone starting material and of altered samples were investigated. Additionaly, granular starting and altered materials resulting from batch experiments were investigated. All analyzed samples were coated with C (thickness $\approx 20 \times 10^{-9}$ m). Standard analyses were performed at a working distance of 11×10^{-3} m with an acceleration voltage of 15×10^{3} V and a probe current of 11×10^{-9} A. For the identification of surface features with a size less than approximately 10^{-6} m, a lower acceleration voltage of 5×10^{3} V and higher probe currents in the range of 13.5 to 20×10^{-9} A were applied. The size of the source region, governed by the penetration of the incident electrons and the spreading of their trajectories in the specimen (Reed, 2005), was estimated for K-feldspar and for each acceleration voltage using the free software CASINO version 2.42 (Drouin et al., 2007). The trajectories of 2000 electrons were simulated in a Monte Carlo simulation resulting in a source region with a diameter of approximately 1.8×10^{-6} m and 0.35×10^{-6} m for acceleration voltages of 15×10^{3} and 5×10^{3} V, respectively.

Scanning Electron Microscopy

Scanning electron microscopy, SEM, was performed on polished cross sections and on individual rock mounts with broken surfaces. Starting materials and altered materials of flow-through and batch experiments were investigated. All analyzed samples were coated with C (thickness $\approx 20 \times 10^{-9}$ m). SEM investigations were performed with a Carl Zeiss SMT Ultra 55 Plus field-emission SEM equipped with an EDX spectroscopy system (UltraDry SDD detector by Thermo Fisher Scientific) for standard-free quantitative element analysis. An acceleration voltage of 20×10^{3} V was mostly applied for imaging and EDX analyses. Secondary electron, SE, and back-scattered electron, BSE, micrographs of polished cross sections were analyzed with respect to the distribution and area fraction of two-dimensional porosity using the java based open source software ImageJ version 1.43u (Abramoff et al., 2004). Image segmentation was performed by threshold selection of grayscale images. The so produced binary (black and white) images were analyzed with respect to area fractions yielding the 2D porosity (Figure 3.9).

The histograms of both micrograph types show significant differences in their gray-scale value distribution. The SE micrographs contain two broad gray-scale value peaks. The dark gray-scale

Scientific Technical Report STR 12/07
DOI: 10.2312/GFZ.b103-12079
Deutsches GeoForschungsZentrum GFZ

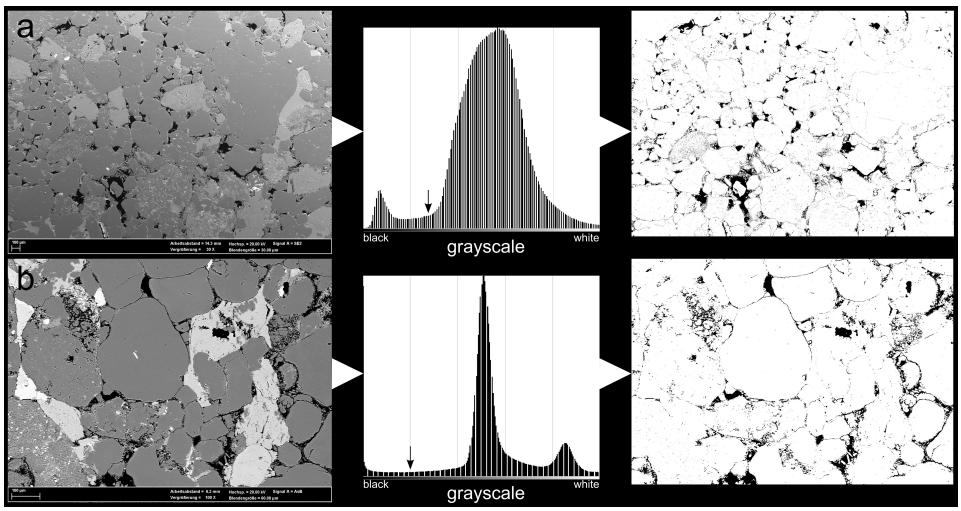

Figure 3.9: Schematic of the segmentation process of SE micrographs (a) and BSE micrographs (b). The histograms were used for the selection of gray-scale value thresholds (indicated by small arrows). Binary images yielded the 2D porosity of the samples.

value peak represents the pores. The large peak summarizes all solid materials (Figure 3.9a). In the BSE micrographs the individual features like pores and at least three classes of solid material appear black, dark gray, light gray, and almost white leading to narrower peaks in the histogram (Figure 3.9b). The different contrast of both micrograph types required different strategies for threshold selection. Best results in the segmentation of pores and solid materials were obtained by setting the threshold to the beginning of the large peak (SE micrographs) and by setting it into the valley between the black and the dark gray peak (BSE micrographs).

High Resolution Transmission Electron Microscopy

High resolution transmission electron microscopy, HRTEM, was performed with a FEI Tecnai G^2 F20 X-Twin equipped with a field-emission electron source operated at an acceleration voltage of 200×10^3 V. Element distributions were analyzed at a nanometer scale spatial resolution by means of an attached EDX system. High-angle annular dark-field, HAADF, images were produced in scanning transmission electron microscopy, STEM, mode. Element distribution mapping was performed with EDX and electron energy loss spectroscopy, EELS.

The focused ion beam, FIB, technique was used to produce site-specific electron transparent foils with a thickness of 0.15×10^{-6} m perpendicular to the surface of feldspar crystals (Figure 3.10a). The length of the foils was 15×10^{-6} m and the depth was 6×10^{-6} m. A FEI FIB200 was used for the preparation of the foils. Two foils were prepared from a labradorite-andesine grain and a microcline grain. The labradorite-andesine grain was coated with C the microcline grain was coated with Au. The region of interest on the crystal surface was coated with a Pt-strap to prevent surface structures from destruction by subsequent Ga^+ bombardment. Ga^+ ions were accelerated in an electrical field up to 30×10^3 eV and were used to cut two trenches in front and behind the volume of interest dedicated to be the electron transparent foil (Figure 3.10b and c). After cutting the trenches, the foil was polished to its final thickness and then cut at the bottom and the sides. By means of an ex situ micromanipulator, the foil was placed

Scientific Technical Report STR 12/07
DOI: 10.2312/GFZ.b103-12079

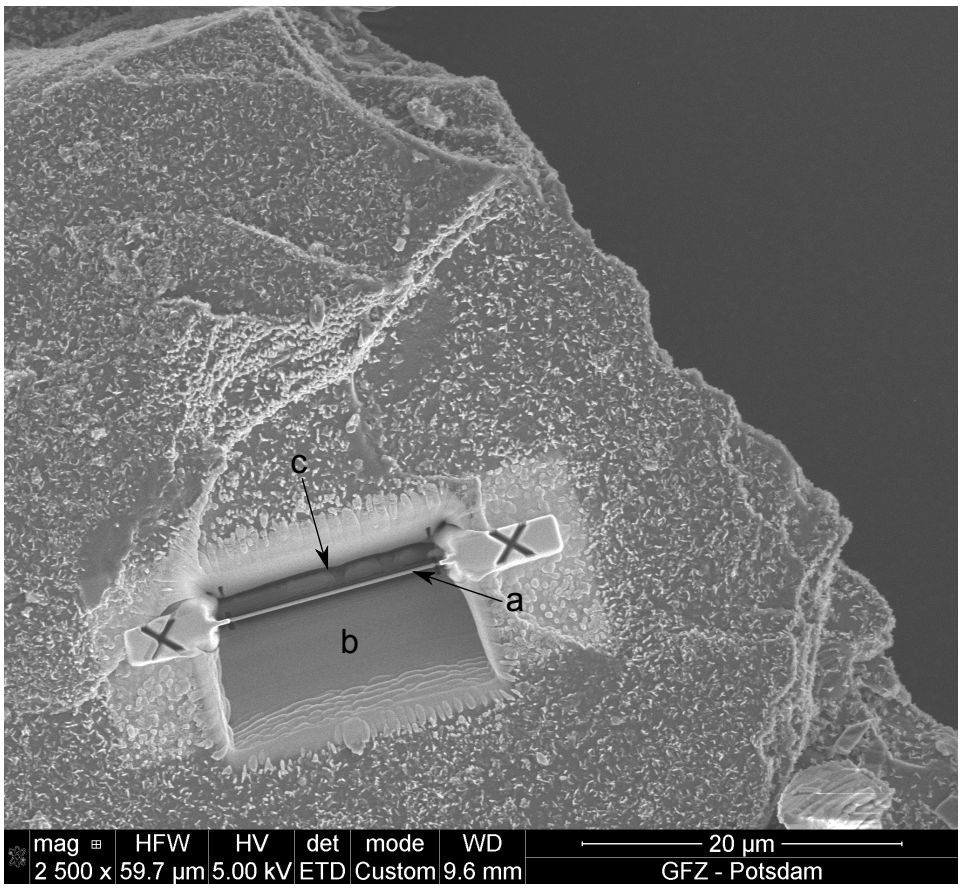

Figure 3.10: SE micrograph of a site-specific electron transparent foil prepared with the FIB technique. The foil was prepared from an altered labradorite-andesine surface resulting from experiment ft-s-4. a), b), and c) denote the electron transparent foil with a thickness of 0.15×10^{-6} m, a trench in front of the foil, and a trench behind the foil, respectively. Both trenches were cut by Ga^{+} bombardment. (Image: A. Schreiber)

on a holey carbon film. The carbon film was placed on a carbon coated conventional TEM copper grid. More specific details of the FIB technique and the combination of SEM with FIB are reported in Wirth (2004), Wirth (2009), and Lee (2010).

X-Ray Computed Tomography

In order to produce 3D representations of inner structures like porosity and material inhomogeneities, X-ray CT scans were performed on a small Flechtinger sandstone sample (ft-Fl-13) with a phoenix/x-ray nanotom® 180NF nanofocus computed tomography system. This device is a high resolution cone beam X-ray tomograph. An upright cylindrical sample was rotated in the optical path of the tomograph. The sample with a length of 20×10^{-3} m and a diameter of 6×10^{-3} m was scanned parallel to its long axis with 1440 pictures per 360° rotation. A voxel size of 2×10^{-6} m was achieved by using a voltage of 78×10^{3} V, a current of 110×10^{-6} A,

Scientific Technical Report STR 12/07
DOI: 10.2312/GFZ.b103-12079

and an exposure time of 2 s. A 0.1 $\times 10^{-3}$m thick Cu-foil was placed in front of the X-ray source to reduce beam hardening artifacts.

3.4 Hydrogeochemical Modeling

Hydrogeochemical modeling was performed to investigate the stabilities of solid phases in fluids resulting from experiments. Concentration data obtained from ICP-OES analyses were the input parameters for the simulations. Saturation indices (Equation 2.45) were calculated with PHREEQC version 2.17.4761 (Parkhurst and Appelo, 1999) using the built in LLNL.dat database. If SI is zero or in the range of -0.05 to 0.05, a solution is in equilibrium or quasi-equilibrium with the solid phase (Appelo and Postma, 1999; Merkel and Planer-Friedrich, 2008).

Scientific Technical Report STR 12/07
DOI: 10.2312/GFZ.b103-12079

Scientific Technical Report STR 12/07
DOI: 10.2312/GFZ.b103-12079

4 Results

4.1 Flow-through Experiments

The results of the flow-through experiments are subdivided into the electrical conductivity of porous samples, chemical analyses of pore fluids in combination with hydrogeochemical modeling, the permeability of the porous samples, investigations of the pore space, and investigations of mineralogical and microstructural changes. The electrical conductivity of flown-through porous samples were investigated with respect to its evolution at constant temperature and pressure, its relation to temperature, and its dependence on the electrical conductivity of the pore fluid during fluid exchange experiments. Chemical analyses of fluids resulting from flow-through experiments were combined with hydrogeochemical modeling and illustrate chemical changes of the pore fluids and potentials for secondary mineral precipitation. The temperature dependence of permeability, the evolution of permeability at constant temperature and pressure, and the effects of pore fluid salinity on permeability were investigated. The pore space of the samples and the mineralogical content were analyzed by various methods (MIP, BET, X-ray CT, XRD, EMPA). In addition, electron microscopic techniques were employed to examine the microstructure of the samples.

In total, 13 flow-through experiments were conducted (Table 3.2). Sandwich experiments acted as model experiments for the Flechtinger sandstone material (ft-s-1 to ft-s-5). Experiments with Fontainebleau sandstone and porous PTFE samples were performed to discriminate the effects of clay mineral and feldspar content on changes in electrical conductivity and permeability (ft-Fo-6 and ft-P-7). Experiments with Flechtinger sandstone samples were conducted to investigate the effects of fluid-rock interactions on electrical conductivity and permeability of feldspar-rich Rotliegend sandstones (ft-Fl-8 to ft-Fl-13).

4.1.1 Electrical Conductivity of Porous Samples

General Observations of the Electrical Conductivity of Porous Samples

The flow-through experiments yielded three general observations of the electrical conductivity of the solid samples:

(i) Temperature changes affected σ_r instantaneously. The temperature dependence of σ_r can be deduced from 70 to 150 °C and 40 to 70 °C temperature steps (Figure 4.1b and Figure 4.1c). The temperature correction coefficient, α_r, was calculated by:

$$\alpha_r = \frac{\frac{\sigma_r(T_h)}{\sigma_r(T_l)} - 1}{\Delta T}. \tag{4.1}$$

Equation 4.1 is a rearrangement of Equation 2.2 with the replacement of α_x by α_r, T_0 by T_l, and T by T_h, where $\sigma_r(T_h)$ is the bulk electrical conductivity of the porous samples at the higher temperature, $\sigma_r(T_l)$ is the bulk electrical conductivity of the porous samples at the lower temperature, and ΔT is the temperature difference $T_h - T_l$. For a Flechtinger sandstone sample

Scientific Technical Report STR 12/07
DOI: 10.2312/GFZ.b103-12079

(ft-Fl-9), the calculated value of α_r is 0.014 °C^{-1} with T_l = 70 °C and T_h = 150 °C (Figure 4.1b). Its cooling from 70 °C to 40 °C and reheating yielded α_r = 0.022 °C^{-1}.

(ii) The bulk electrical conductivity of porous samples increased with time with decreasing rates at constant temperature and pressure and approached a temperature-dependent steady state. At 70 °C constant temperature, σ_r of a Flechtinger sandstone rock sample approached a steady state of approximately 37×10^{-3} S/m (Figure 4.1b). During the first 70 °C phase, σ_r increased from 16.6 to 34.5×10^{-3} S/m. In the following 150 °C phase, a further increase from 73.1 to 76.3×10^{-3} S/m was measured. The subsequent cooling to 70 °C resulted in a σ_r decrease to 38.1×10^{-3} S/m. Thus, the difference between σ_r values of the first and the second 70 °C stage before and after the 150 °C phase is $\Delta\sigma_r = 3.6 \times 10^{-3}$ S/m. It is therefore is in the same range as the increase during the 150 °C phase ($\Delta\sigma_r = 3.2 \times 10^{-3}$ S/m). In the course of the second 70 °C period, σ_r slowly decreased to values of 37.2×10^{-3} S/m.

In an experiment with a QLM sandwich (ft-s-3), σ_r slowly increased during the first 70 °C phase from 0.08 to 0.19×10^{-3} S/m (Figure 4.1c). During the following 150 °C stage, a further increase from approximately 1 to a maximum value of 1.7×10^{-3} S/m was observed. However, the σ_r data at the 150 °C period showed substantial noise. Due to the cooling to 70 °C, σ_r decreased to 0.32×10^{-3} S/m. During this 70 °C phase, σ_r slowly decreased to 0.31×10^{-3} S/m followed by an abrupt decrease to 0.27×10^{-3} S/m.

(iii) Flushing the samples with H_2O with $\sigma_f(T_0) \approx 2.5 \times 10^{-3}$ S/m during permeability measurements and fluid sampling led to a reset of σ_r values to temperature-dependent base levels. In the course of permeability measurements, the samples were flushed by several pore volumes of H_2O. Temperature-dependent σ_r base levels of a Flechtinger sandstone sample (ft-Fl-8) were approximately 7.3, 12.3, 22.3, and 36.7×10^{-3} S/m at 30, 51, 90, and 164 °C, respectively (Figure 4.1a). At 70 °C, the σ_r base level of another Flechtinger sandstone sample (ft-Fl-9) was approximately 16.9×10^{-3} S/m (Figure 4.1b). In a QLM sandwich experiment (ft-s-3) the σ_r base level was 0.05×10^{-3} S/m (Figure 4.1c).

Evolution of the Electrical Conductivity of Porous Samples at Constant Temperature and Pressure

The electrical conductivity of the porous samples increased with time with decreasing rate at constant temperatures and stagnant conditions. The comparison of the data resulting from three Flechtinger sandstone experiments (ft-Fl-9, ft-Fl-11, and ft-Fl-12) and from one QLM sandwich experiment (ft-s-3) at a constant temperature of 70 °C shows that σ_r behaves qualitatively similar in the experiments with the two different materials (Figure 4.2). However, there is a significant difference in the absolute σ_r values of the QLM sandwich and the Flechtinger sandstone experiments. The QLM-sandwich experiment had a σ_r starting value of approximately 0.08×10^{-3} S/m and a maximum increase of 0.12×10^{-3} S/m after 44 d. In comparison, the σ_r starting values of the Flechtinger sandstone experiments were much higher, varying from 15 to 37×10^{-3} S/m. The maximum increase of σ_r was approximately 15, 7, and 5×10^{-3} S/m. After flushing a Flechtinger sandstone sample with H_2O σ_r increased only slightly by approximately 0.8×10^{-3} S/m in approximately 11 d (ft-Fl-9b).

Relation of the Electrical Conductivity of Porous Samples to Temperature

The electrical conductivity strongly depends on temperature (Equations 2.2 and 4.1). Changes in σ_r as a function of temperature are incorporated in the temperature correction coefficient, α_r

Scientific Technical Report STR 12/07
DOI: 10.2312/GFZ.b103-12079

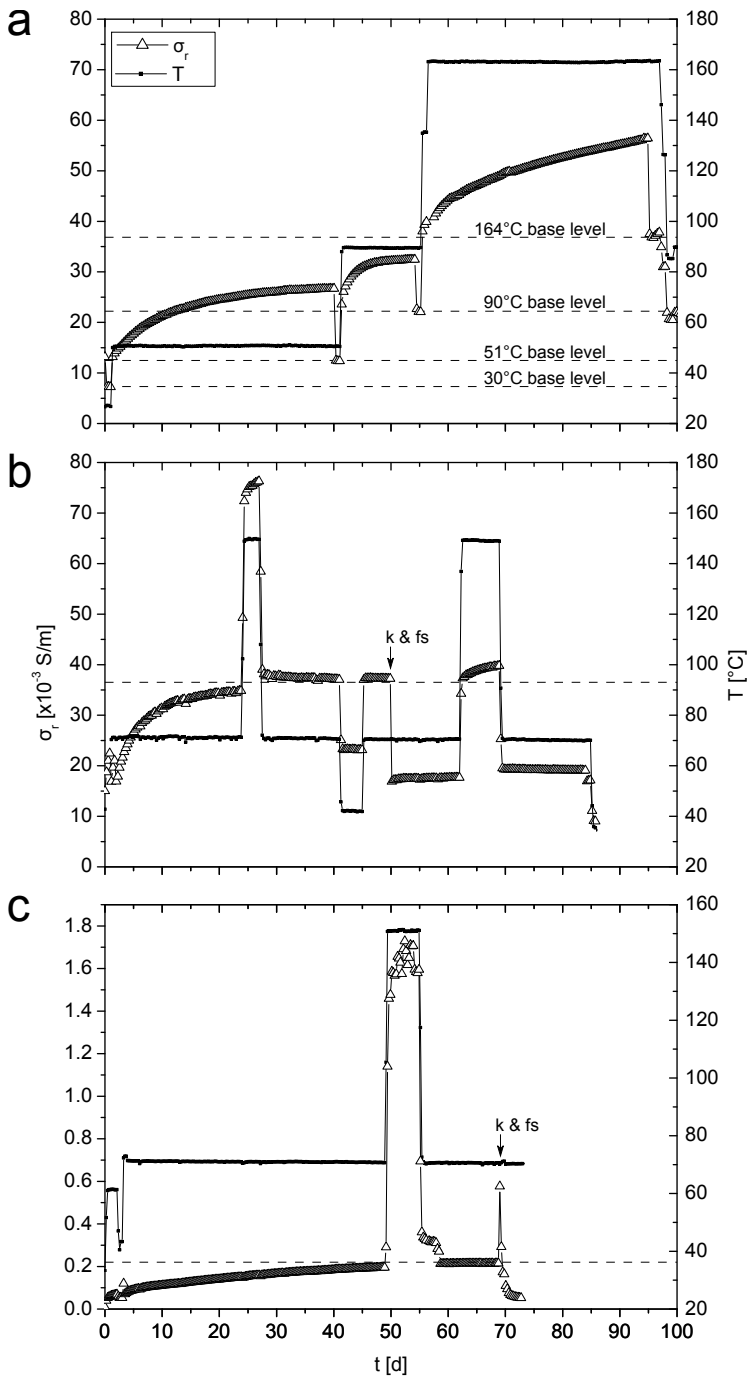

Figure 4.1: Electrical conductivity of bulk samples, σ_r, and temperature as a function of time for flow-through experiments ft-Fl-8 (a), ft-Fl-9 (b), and ft-s-3 (c). The dashed lines in a) indicate temperature-dependent σ_r base levels. The dashed lines in b) and c) approximate σ_r levels that were approached during 70 °C stages of the experiments. Stagnant conditions prevailed except at the beginning and the end of each constant temperature stage of ft-Fl-8 and at k & fs labeled phases in ft-Fl-9 and ft-s-3. Arrows labeled k & fs denote permeability measurements and fluid sampling.

Scientific Technical Report STR 12/07
DOI: 10.2312/GFZ.b103-12079

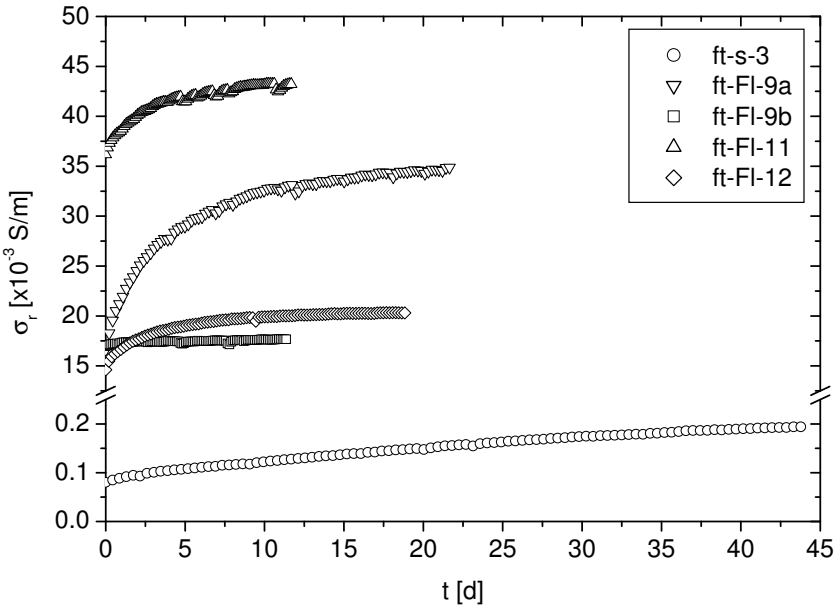

Figure 4.2: Electrical conductivity of bulk samples, σ_r, as a function of time at 70 °C for flow-through experiments ft-s-3, ft-Fl-9, ft-Fl-11, and ft-Fl-12. Experiment ft-s-3 is a QLM sandwich experiment, whereas the other experiments were performed with Flechtinger sandstone samples. The initial pore fluid of each experiment was H_2O. ft-Fl-9a represents the early stage of experiment ft-Fl-9. ft-Fl-9b shows the late stage of the experiment after a total duration of approximately 50 d (Figure 4.1b). All experiments show an increase of σ_r with time. The increase of σ_r with time of ft-Fl-9b is low compared to the other Flechtinger sandstone experiments.

Scientific Technical Report STR 12/07
DOI: 10.2312/GFZ.b103-12079

Table 4.1: Temperature correction coefficients for experiments ft-s-3, ft-Fo-6, ft-Fo-7, ft-P-7, ft-Fl-8, ft-Fl-9, ft-Fl-10, and ft-Fl-12.

Experiments	**Solid Material**	**Fluid**	**Mean** α_r $^{\circ}C^{-1}$
ft-Fo-6, ft-Fo-7	Fontainebleau SST	n.k.	0.012 ± 0.008
ft-P-7	porous PTFE	H_2O	0.017 ± 0.008
ft-Fl-8, ft-Fl-12	Flechtinger SST	H_2O	0.016 ± 0.007
ft-Fl-9	Flechtinger SST	H_2O, n.k.	0.018 ± 0.005
ft-Fl-10	Flechtinger SST	1 mol/L $NaCl_{aq}$	0.013 ± 0.004
ft-s-3	QLM-sandwich	n.k.	0.06 ± 0.02

n.k. indicates that the pore fluid composition at that time is not known, because the initial pore fluid has evolved over time (Section 4.1.2).

(Table 4.1). For the α_r calculation, $\sigma_r(T_l)$ and $\sigma_r(T_h)$ were determined directly before and after the heating or cooling of the porous samples. The duration of the heating or cooling procedure was short compared to the experiment durations ($<$ 1 d versus up to 139 d). Time-dependent changes of σ_r occurred in time scales of days rather than hours. Thus, σ_r was mainly affected by temperature changes and not by chemical changes of the pore fluid during the heating or cooling procedure.

Based on the assumption that the differences between the α_r values are indicative for the underlying conduction mechanisms, it can be deduced that samples with α_r values in the range of $\approx 0.023\ ^{\circ}C^{-1}$ were dominated by electrolytic conduction through the pore fluid, whereas samples with α_r values in the range of $\approx 0.04\ ^{\circ}C^{-1}$ were dominated by conduction at the grain-fluid interfaces. Mean values of α_r were in the range of 0.012 ± 0.008 to $0.018 \pm 0.005\ ^{\circ}C^{-1}$ for the rock samples and the porous PTFE sample. One of the QLM sandwich experiment (ft-s-3) yielded $\alpha_r \approx 0.06 \pm 0.02\ ^{\circ}C^{-1}$ (Table 4.1). Comparison to the literature shows that the temperature correction coefficient for fluids is $\alpha_f \approx 0.023\ ^{\circ}C^{-1}$. The temperature correction coefficient for electrical conductivity at the mineral-fluid interface is even higher, $\alpha_s \approx 0.040 \pm 0.002\ ^{\circ}C^{-1}$ (Revil and Glover, 1998; Sen and Goode, 1992). Thus, the measured α_r values obtained in the experiments may indicate that the electrical conduction in the rock samples and the PTFE sample was dominated by electrolytic conduction through the pore fluid irrespective of the starting pore fluid. The mean α_r value of the QLM sandwich experiment (ft-s-3) suggests that conduction at the grain-fluid interface was the dominant conduction mechanism in this sample.

The temperature correction coefficients of the Fontainebleau sandstone and PTFE samples tended to increase with increasing temperature (Figure 4.3a), whereas the Flechtinger sandstone samples showed the opposite trend (Figure 4.3b). The composition of the actual pore fluid during the heating or cooling procedure is not known because the initial pore fluid had evolved over time during the stagnant conditions prevailing during the experiments. The PTFE sample is assumed to be chemically inert under the present experimental conditions, thus leaving the initial pore fluid (H_2O) unaltered. The decreasing trend of α_r with temperature in the Flechtinger sandstone experiments was independent of the pore fluid composition (initial pore fluids ranged from H_2O to 1 mol/L $NaCl_{aq}$).

Scientific Technical Report STR 12/07
DOI: 10.2312/GFZ.b103-12079
Deutsches GeoForschungsZentrum GFZ

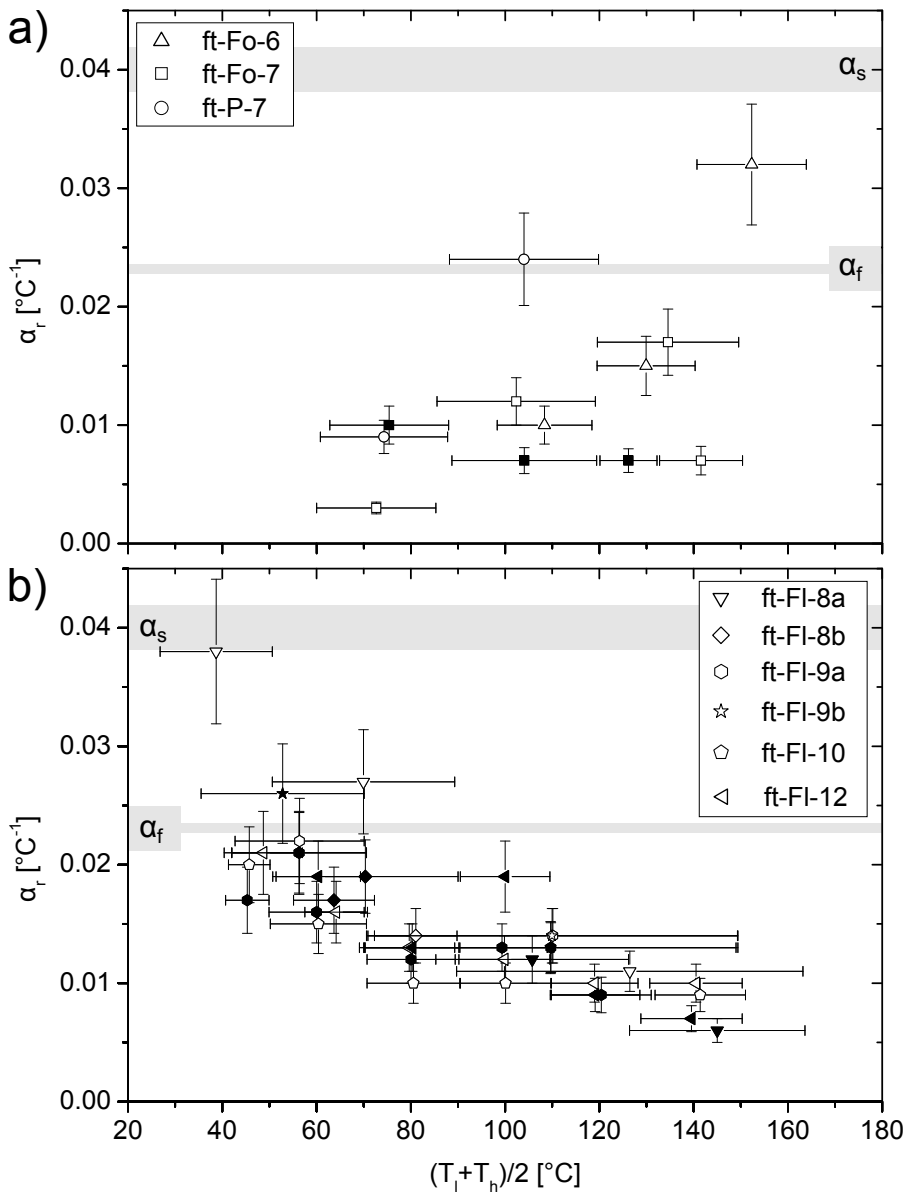

Figure 4.3: Temperature correction coefficient, α_r, as a function of the mean of temperature intervals $(T_l + T_h)/2$ for a) experiments with Fontainebleau sandstone samples (ft-Fo-6, ft-Fo-7) and a porous PTFE sample (ft-P-7) and b) experiments with Flechtinger sandstone samples (ft-Fl-8, ft-Fl-9, ft-Fl-10, and ft-Fl-12). Subscripts l and h denote lower and higher temperature, respectively. Horizontal bars illustrate the temperature intervals. Errors of α_r result from errors of temperature and σ_r measurements. Open and solid symbols denote up and down steps in the temperature intervals, respectively. Gray shaded areas represent $\alpha_f \approx 0.023$ for electrical conductivity of fluids and $\alpha_s = 0.040 \pm 0.002\ °C^{-1}$ for electrical conductivity of fluid-mineral interfaces (Revil et al., 1998). Initial pore fluids and mean values of α_r are reported in Table 4.1.

Scientific Technical Report STR 12/07
DOI: 10.2312/GFZ.b103-12079

Table 4.2: Electrical conductivity of pore fluids, $\sigma_f(T)$, and Flechtinger sandstone samples, $\sigma_r(T)$, resulting from fluid exchange experiments ft-Fl-11 and ft-Fl-12.

Experiment	**c $NaCl_{aq}$** mol/L	T °C	$\sigma_f(T)$* S/m	$\sigma_r(T)$** S/m
ft-Fl-11	0	42	0.0035 ± 0.0001	0.0209 ± 0.0009
ft-Fl-11	0.001	42	0.0219 ± 0.0008	0.024 ± 0.001
ft-Fl-11	0.01	42	0.171 ± 0.006	0.031 ± 0.001
ft-Fl-12	0.0432	70	0.97 ± 0.03	0.037 ± 0.002
ft-Fl-11	0.1	42	1.47 ± 0.05	0.055 ± 0.002
ft-Fl-11	0.25	42	3.5 ± 0.1	0.085 ± 0.003
ft-Fl-11	0.5	42	6.6 ± 0.2	0.115 ± 0.005
ft-Fl-11	1	43	14.6 ± 0.5	0.205 ± 0.008
ft-Fl-12	2	69.3	31 ± 1	0.41 ± 0.02

* calculated with Equation 2.2.
** measured in the HPT-permeameter.

Evolution of Electrical Conductivity of Sandstone Samples During Fluid Exchange Experiments

In fluid exchange experiments, during which the initial pore fluid was replaced by $NaCl_{aq}$ solutions, the electrical conductivity of Flechtinger sandstone samples increased as a function of σ_f (Table 4.2). The fluid exchange experiments yielded the formation resistivity factor for shaly sandstones, F^*, and the contribution of the electrical conductivity of fluid-mineral interfaces, σ_s, to σ_r (as will be investigated in more detail in the discussion chapter, Figure 5.2 and Table 5.2). Temperature corrections of the electrical conductivity of the fluids measured at room temperature, $\sigma_f(T_0)$, were performed by Equation 2.2 yielding $\sigma_f(T)$, where T is the temperature of the experiment. The errors of the $\sigma_f(T)$ and $\sigma_r(T)$ measurements were estimated from the uncertainties of the $\sigma_f(T_0)$ measurements, the temperature correction, and of temperature measurements and temperature stability during the experiments. However, errors of $\sigma_r(T)$ may have been underestimated in experiments with fluids with a high electrical conductivity, $\sigma_f(T) > 31$ S/m (ft-Fl-12), because of an unknown amount of back current through the PEEK connector in the HPT-permeameter (Section 3.2.1).

4.1.2 Fluid Chemistry

Chemical Fluid Analyses

The compositions of the fluid samples from the flow-through experiments were analyzed with respect to dissolved Na, Mg, Al, Si, K, Ca, Mn, Fe, and Ni (Table 5.4). The fluid samples were either taken at the end of the flow-through experiments (ft-s-3 and ft-Fo-6) or during the experiments (at run durations of approximately 30 and 50 d of experiments ft-s-4 and ft-Fl-9, respectively). The temperature in the HPT-permeameter was approximately 70 °C during fluid sampling. Electrical conductivity was measured on a set of fluid samples from a QLM-sandwich experiment (ft-s-4). Estimated analytical errors of the ICP-OES measurements are generally small (mostly on the order of the symbol sizes in Figures 4.4 to 4.7).

Plots of concentrations of dissolved cationic species, c_i, as functions of cumulative sampled

Scientific Technical Report STR 12/07
DOI: 10.2312/GFZ.b103-12079

volumes from the flow-through experiments typically showed bell shaped curves with maxima approximating the pore fluid composition (Figures 4.4, 4.5, 4.6, and 4.7). The electrical conductivity of fluids resulting from a QLM sandwich experiment (ft-s-4) showed a similar behavior (Figure 4.5). The maxima of the bell shaped curves are at 5 to 12×10^{-3} L cumulative sampled volume (Figures 4.4, 4.5, and 4.7). The mixing with up- and downstream fluid (H_2O) is constrained to cumulative sampled volumes of approximately 6 to 8×10^{-3} L. This volume is lower than the measured dead volume on the upstream side of each sample (Section 3.2.1). A Fontainebleau sandstone experiment (ft-Fo-6) showed c_i maxima at the lowest cumulative sampled volumes, which is due to the relatively large volume of the first fluid sample compared to the fluid volume downstream of the porous sample (Figure 4.6).

Fluids resulting from two QLM sandwich experiments (ft-s-3 and ft-s-4) were in contact with the same granular QLM material and yielded similar pore fluid composition with respect to Na, Al, K, and Ca but different pore fluid compositions with respect to Si (Table 3.2). Differences in both experiments were the porous disc materials, the effective pressure p_{eff}, the residence time of the fluid in the porous sample at stagnant conditions, and the temperature history of this period. One QLM sandwich experiment (ft-s-3) was performed with Fontainebleau sandstone discs, $p_{\text{eff}} = 5 \times 10^6$ Pa, the residence time of the fluid in the porous sample was 68.5 d, and the sample was held at 60, 70, 150, and 70 °C for a duration of approximately 2, 46, 6, and 18 d, respectively. The other QLM sandwich experiment (ft-s-4) was performed with porous PTFE discs, $p_{\text{eff}} = 2.5 \times 10^6$ Pa, the residence time of the fluid in the porous sample was 16 d, and the temperature history during this residence time was 14 and 2 d at approximately 150 and 71 °C, respectively.

The dissolution of a Fontainebleau sandstone core led to high concentrations of Si in the pore fluid (Figure 4.6 and Table 5.4). The residence time of the fluid at stagnant conditions was approximately 7 d with a temperature history of approximately 4 and 3 d at 162 and 79 °C, respectively. The concentrations of Si in the fluid samples resulted from the rock sample. The Si concentration was high in the first fluid sample. Na exhibited relatively high concentrations in the pore fluid with a slight decrease with increasing cumulative sampled volume. The Na concentration in the upstream fluid was approximately the same as the concentration in the pore fluid. Due to the fact that Na is an abundant element, this behavior of the Na concentration points towards a contamination of the pore fluid system with Na. The same behavior can be observed for Ni but with concentrations approximately two orders of magnitude lower than the Na concentrations. Ca and Fe showed similar trends as Si indicating that the measured concentrations resulted mainly from dissolution of the rock sample. Mg, Al, K, and Mn displayed similar behaviors to Si, Ca, and Fe but with smalled concentrations of $< 0.02 \times 10^{-3}$ mol/L (Table 5.4). In summary, these results show that Mg, Al, Si, K, Ca, Mn, and Fe were dissolved from the Fontainebleau sandstone sample, whereas Na and Ni can be regarded as contaminations of the pore fluid system. The overall low concentrations of Fe and Ni in the upstream fluid showed that slight corrosion of the fluid touching stainless steel parts of the HPT-permeameter had a negligible effect on the fluid composition. However, slight corrosion was observed on fittings and the end caps of the specimen assembly. Contact corrosion, potentially taking place at the contact area of the end caps to the rock sample, may have played a role in the alteration of the pore fluid during the experiment.

The dissolution of rock constituents of a Flechtinger sandstone core sample yielded relatively high concentrations of Na, Si, K, and Ca in the pore fluid (Figure 4.7 and Table 5.4). The residence time of the fluid in the pore space at stagnant conditions was approximately 48 d with a temperature history of approximately 22, 3, 14, 4, and 5 d at 70, 150, 70, 42, and 70 °C,

Scientific Technical Report STR 12/07
DOI: 10.2312/GFZ.b103-12079

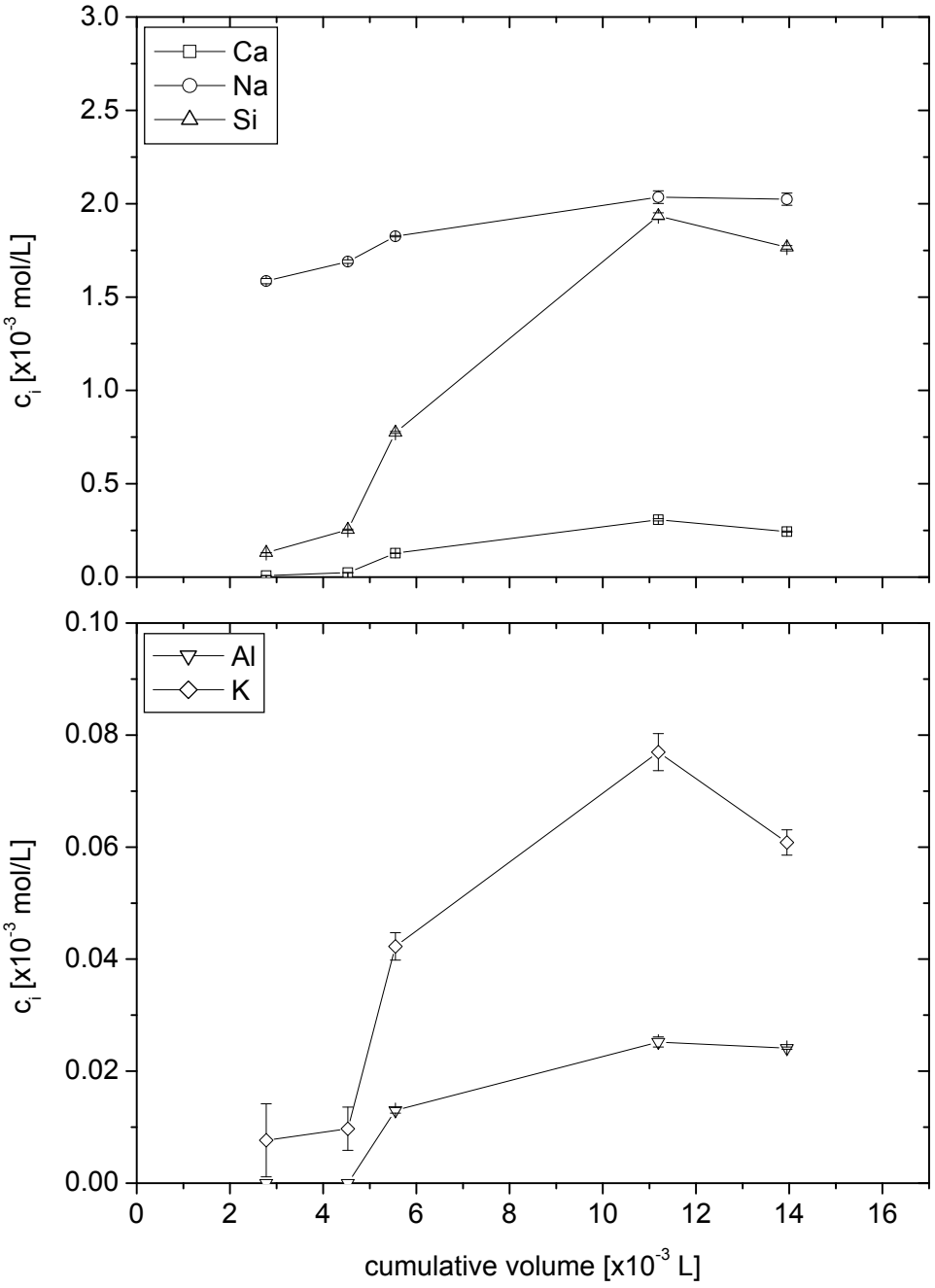

Figure 4.4: Concentrations of Na, Al, Si, K, and Ca as a function of cumulative sampled volume from experiment ft-s-3. Maximum concentrations of the analyzed elements are at approximately 11.2×10^{-3} L cumulative volume. These concentrations are regarded as an approximation to the pore fluid composition.

Scientific Technical Report STR 12/07
DOI: 10.2312/GFZ.b103-12079

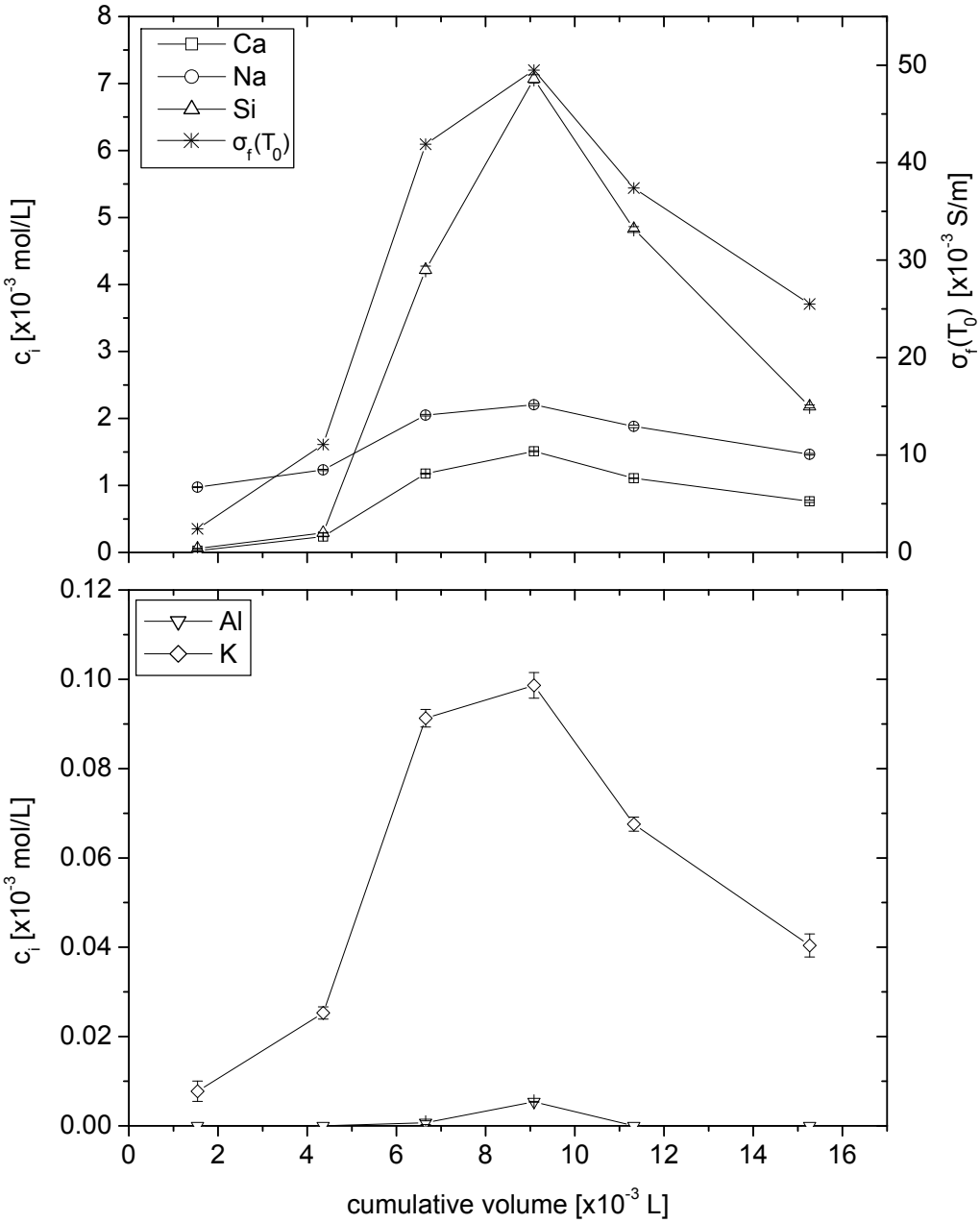

Figure 4.5: Concentrations of Na, Al, Si, K, and Ca as well as the electrical conductivity of the fluid, $\sigma_f(T_0)$, as a function of cumulative sampled volume from experiment ft-s-4. Maximum concentrations of the analyzed elements are at approximately 9.1×10^{-3} L cumulative volume. These concentrations are regarded as an approximation to the pore fluid composition.

Scientific Technical Report STR 12/07
DOI: 10.2312/GFZ.b103-12079

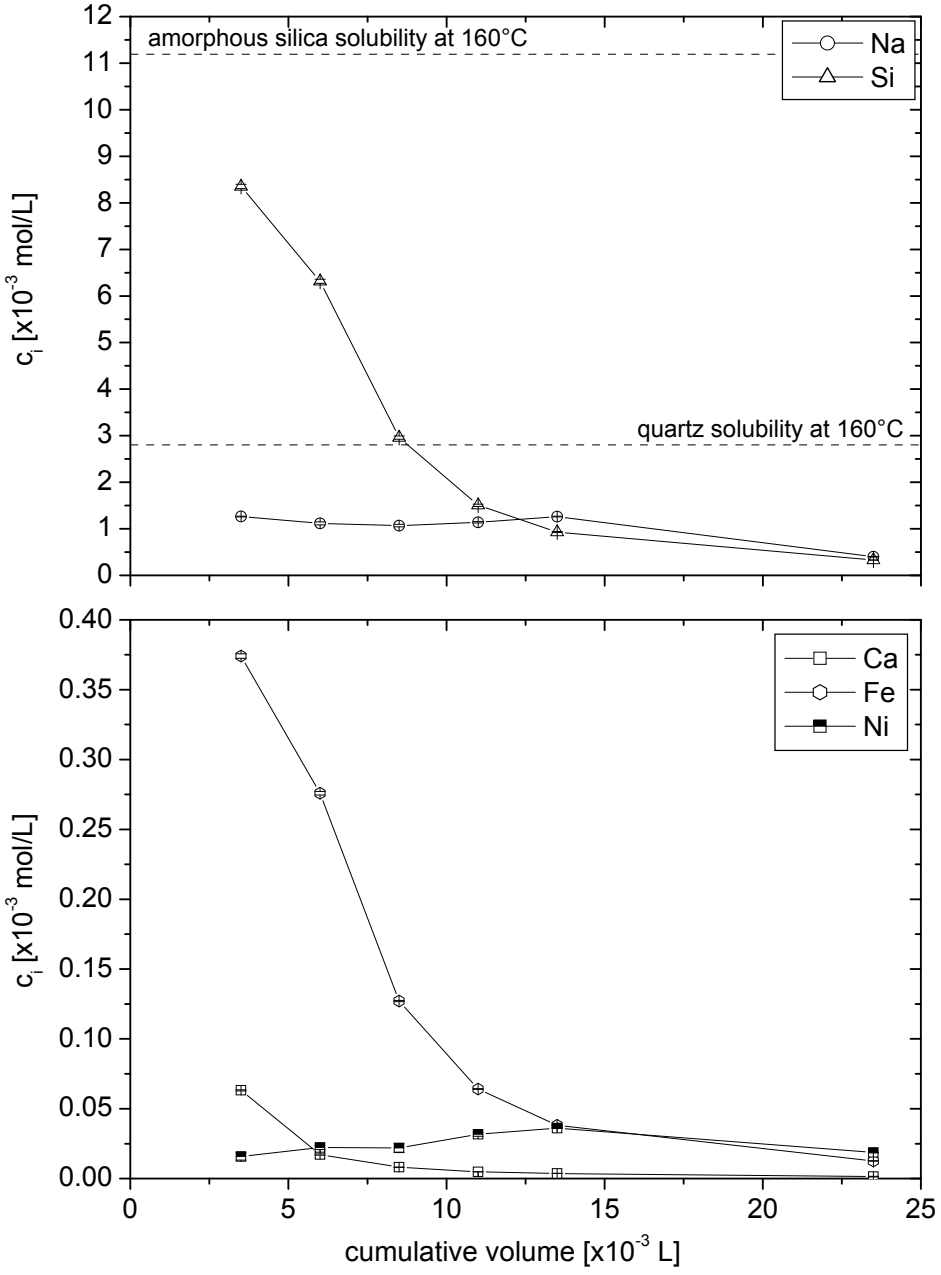

Figure 4.6: Concentrations of Na, Si, Ca, Fe, and Ni as a function of cumulative sampled volume from experiment ft-Fo-6. Maximum concentrations of the analyzed elements are at 3.5×10^{-3} L cumulative volume. These concentrations are regarded as an approximation to the pore fluid composition. The dashed lines represent solubilities of amorphous silica and quartz at 160 °C and saturation vapor pressure (Marshall, 1980; Gunnársson and Arnórsson, 2000).

Scientific Technical Report STR 12/07
DOI: 10.2312/GFZ.b103-12079

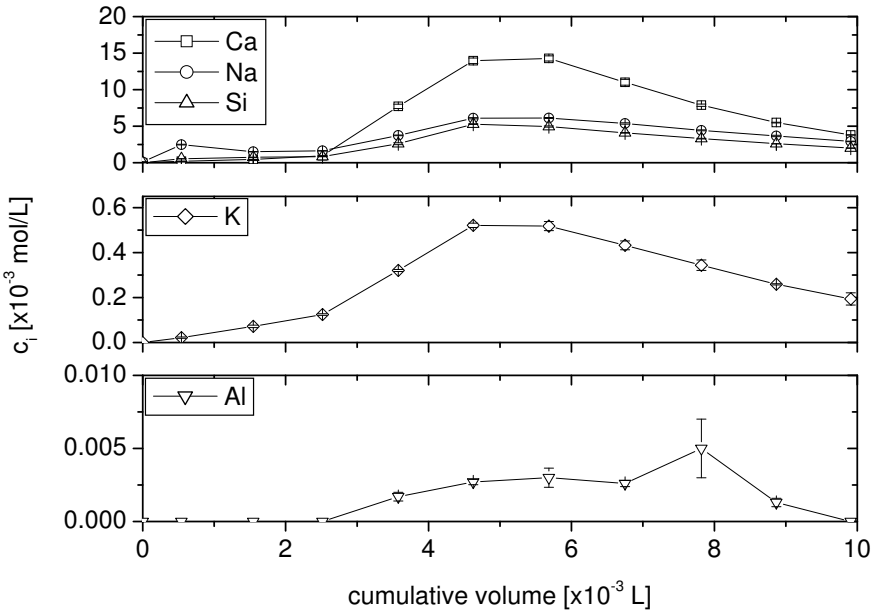

Figure 4.7: Concentrations of Na, Al, Si, K, and Ca as a function of cumulative sampled volume from experiment ft-Fl-9. Maximum concentrations of the analyzed elements are at approximately 5.7×10^{-3} L cumulative volume. These concentrations are regarded as an approximation to the pore fluid composition. The data point of the Al concentration at 7.8×10^{-3} L cumulative sampled volume is assumed to be an outlier value.

Scientific Technical Report STR 12/07
DOI: 10.2312/GFZ.b103-12079

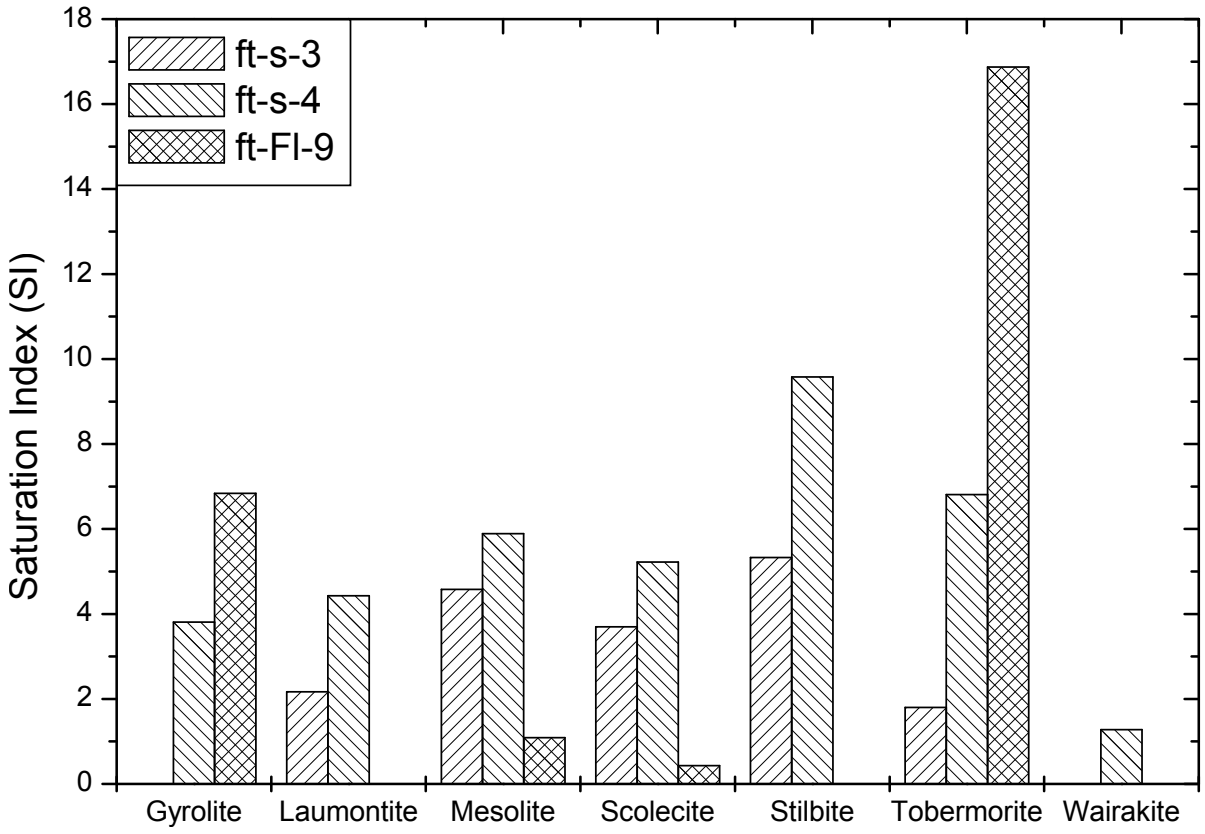

Figure 4.8: Saturation indices of selected stable minerals calculated with PHREEQC for the fluids resulting from flow-through experiments ft-s-3, ft-s-4, and ft-Fl-9. The temperature is 70 °C. The PHREEQC built-in LLNL.dat database was used for the simulation.

respectively.

Hydrogeochemical Modeling

Several low temperature hydrothermal mineral phases were supersaturated in the fluids resulting from flow-through experiments at 70 °C according to hydrogeochemical modeling with PHREEQC (Figure 4.8). The concentrations of cations in solution were used as input parameters for the simulations (Table 5.4). Charge balance was achieved by adjusting the pH-value of the solutions. Modeled pH-values were in the range of 9.6 to 11.2. Measured pH-values were not available. The simulations with PHREEQC using the LLNL.dat database yielded many more stable mineral phases with saturation indices as high as approximately 10 (e.g., grossular). Most of these phases were high temperature and high pressure phases indicative of metamorphic conditions. Mineral phases pertaining to low temperature hydrothermal and sedimentary conditions were selected: Gyrolite and tobermorite are Ca-rich Al-free phyllosilicates. Laumontite, mesolite, scolecite, stilbite, and wairakite belong to the zeolite group of the aluminosilicates.

Scientific Technical Report STR 12/07
DOI: 10.2312/GFZ.b103-12079

4.1.3 Permeability

Initial Permeability and Porosity

The relationship of initial permeability k_0 to porosity ϕ was dependent on the sample material (Figure 4.9). Initial permeabilities were measured in the beginning of flow-through experiments at $25 \leq T \leq 40$ °C. The porosity was measured on the Fontainebleau sandstone porous discs of the sandwich samples (ft-s-1, ft-s-2, and ft-s-3), whereas k_0 was measured on the sandwich samples themselves. However, the permeability of the confined grain aggregates in the sandwich samples did not significantly affect the permeability of the sandwich samples, i.e., k_0 of the Fontainebleau materials with $\phi \approx 7$ % is similar for the core and the sandwich samples. The initial permeability and porosity of the Flechtinger sandstone samples ranged between 0.16 and 0.6×10^{-15} m^2, and 9.9 and 11.5 %, respectively. The initial porosity of the porous PTFE was 20 % but is assumed to have been significantly lower at an effective pressure $p_{\text{eff}} = p_c - p_p = 2.5 \times 10^6$ Pa (with $p_c = 5 \times 10^6$ Pa and $p_p = 2.5 \times 10^6$ Pa) in the HPT-permeameter due to the deformability of the material. Initial permeabilities of the PTFE core sample (ft-P-7) showed a higher k_0 value (1.34×10^{-15} m^2) than sandwich experiments with the same material as the porous discs. The initial permeability of one of the QLM sandwich experiments (ft-s-4) was $k_0 = 0.16 \times 10^{-15}$ m^2, and the illite-bearing QLMI sandwich experiment (ft-s-5) exhibited an even lower k_0 value of 1.4×10^{-18} m^2.

Permeability as a Function of Temperature

Normalized permeability k/k_0 decreased with temperature irrespective of different sample types, experimental durations, and pore fluids of the experiments (Figure 4.10). Normalized permeabilities decreased to approximately 10 to 60 % of the initial permeability during heating (the mean value of k/k_0 at maximum temperatures is approximately 0.33 with a standard deviation of 0.26, Figure 4.10a). A QLM sandwich with porous PTFE discs and a Flechtinger sandstone sample with 1 mol/L $NaCl_{aq}$ solution as the pore fluid exhibited an increase of k in the temperature interval 40 to 70 °C followed by a decrease upon further heating to 150 °C (ft-s-4 and ft-Fl-10). One Flechtinger sandstone sample showed a significant k decrease in the temperature interval 30 to 51 °C (ft-Fl-8). This k decrease was followed by an insignificant change during further heating to 164 °C. The timespan from the k_0 measurement to the first permeability measurement at 164 °C was long (57 d) and permeability was measured at irregular intervals during this timespan. Thus, there is no information about the evolution of k during this period.

Generally, k/k_0 partly recovered during cooling of the samples (Figure 4.10b). An exception to this rule is a Flechtinger sandstone experiment in which k/k_0 only slightly increased with decreasing temperature (ft-Fl-10). The k value at the lowest temperature of each experiment is labeled k_{cooled} (Table 4.3).

Evolution of Permeability at Constant Temperature and Pressure

The permeability decrease with time at constant temperature and pressure conditions was independent of sample types and pore fluids. Permeability was normalized to the initial k value at the respective constant temperature interval of each experiment, k_{heated} (Figure 4.11). Absolute values of permeability changes at constant temperature and pressure can be deduced from the difference between k_{heated} and minimum values at the constant temperature stage,

Scientific Technical Report STR 12/07
DOI: 10.2312/GFZ.b103-12079

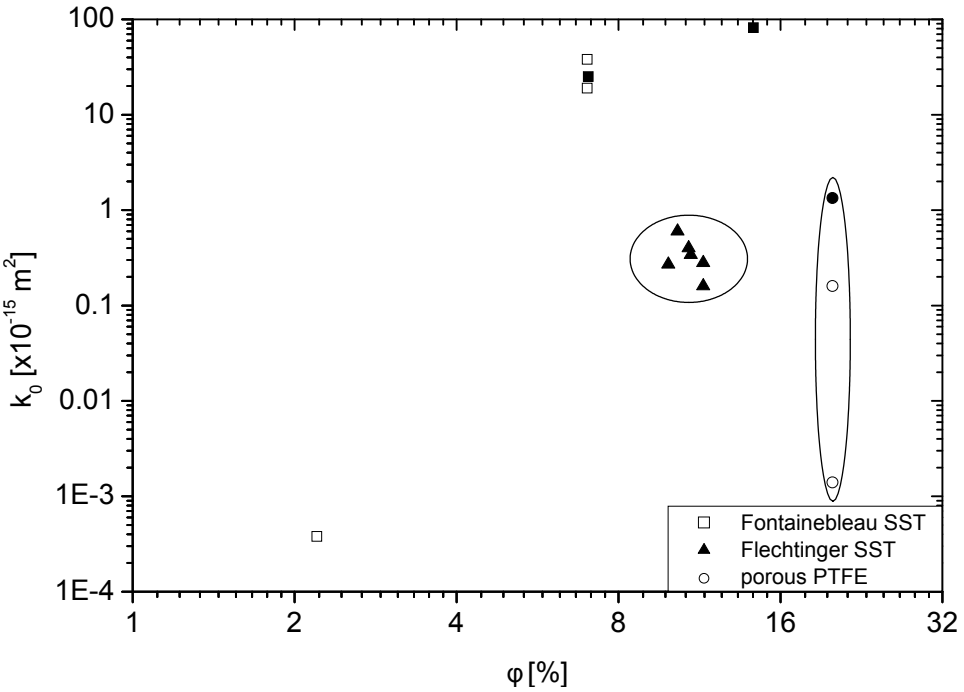

Figure 4.9: Logarithmic plot of initial permeability k_0 as a function of porosity ϕ of Fontainebleau sandstone, Flechtinger sandstone, and porous PTFE samples. Permeability data resulted from core samples (solid symbols) and sandwich samples (open symbols). The Flechtinger sandstone data clusters in the area marked by an ellipse. The initial permeability of the porous PTFE core sample and the sandwich samples with porous PTFE depends on the type of sandwiched granular aggregates. The core sample shows the highest k_0 value, the QLM sandwich experiment ft-s-4 exhibits a medium k_0 value, and the illite-bearing QLMI sandwich experiment ft-s-5 shows the lowest k_0 value.

Scientific Technical Report STR 12/07
DOI: 10.2312/GFZ.b103-12079

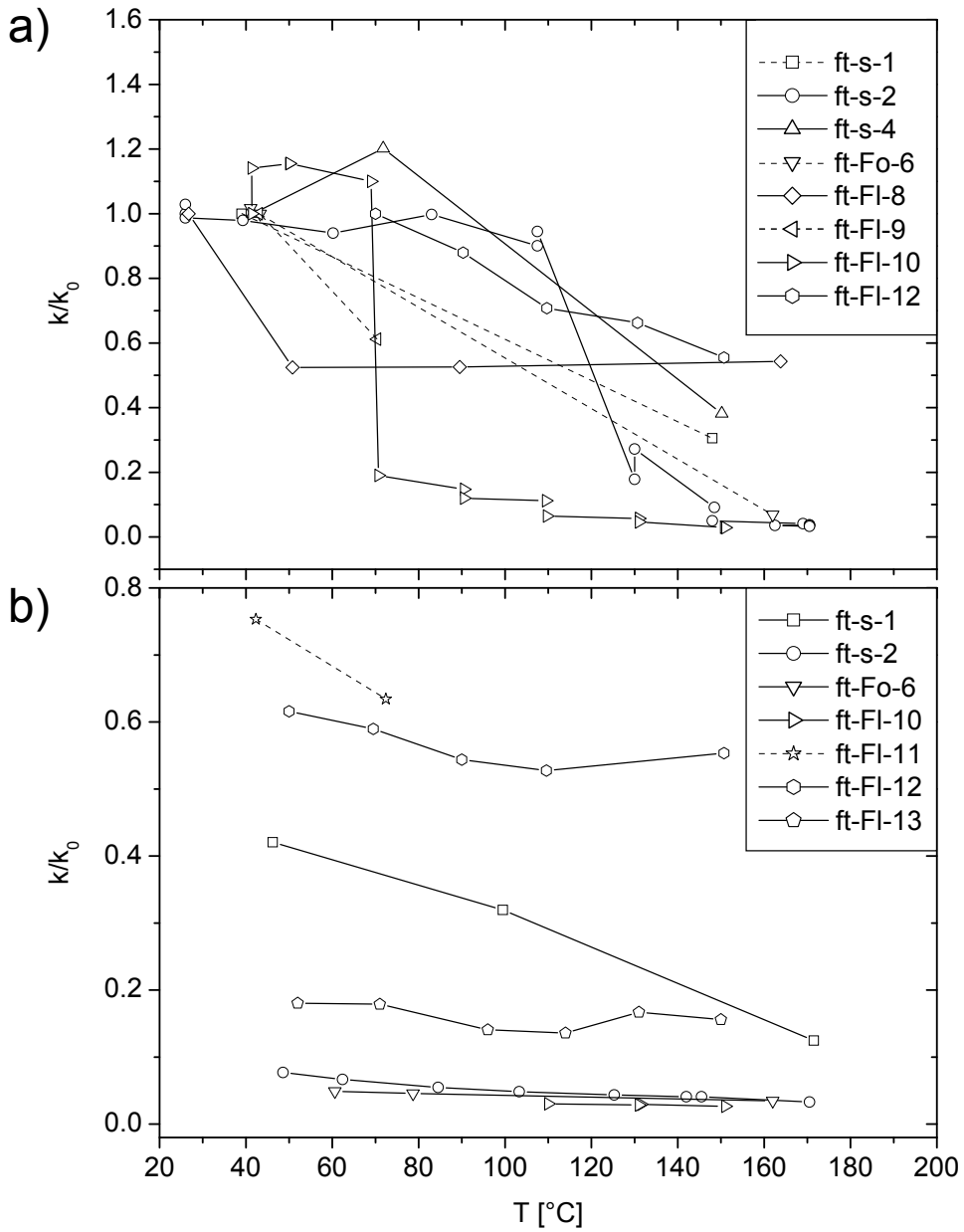

Figure 4.10: Normalized permeability k/k_0 as a function of temperature during a) heating and b) cooling of flow-through experiments ft-s-1, ft-s-2, ft-s-4, ft-Fo-6, ft-Fl-8, ft-Fl-9, ft-Fl-10, ft-Fl-11, ft-Fl-12, and ft-Fl-13. Dashed lines are used as interpolations when only two data points are available. ft-s-1, ft-s-2, and ft-s-4 are sandwich samples, ft-Fo-6 is a Fontainebleau sandstone core sample, and ft-Fl-8, ft-Fl-9, ft-Fl-10, and ft-Fl-12 are Flechtinger sandstone core samples. In fluid exchange experiments (ft-Fl-11 and ft-Fl-12) k_0 was determined at the lowest temperatures when H_2O was the pore fluid. One Flechtinger sandstone experiment was performed with 1 mol/L $NaCl_{aq}$ as the pore fluid (ft-Fl-10). The pore fluid in the other experiments was H_2O.

Scientific Technical Report STR 12/07
DOI: 10.2312/GFZ.b103-12079

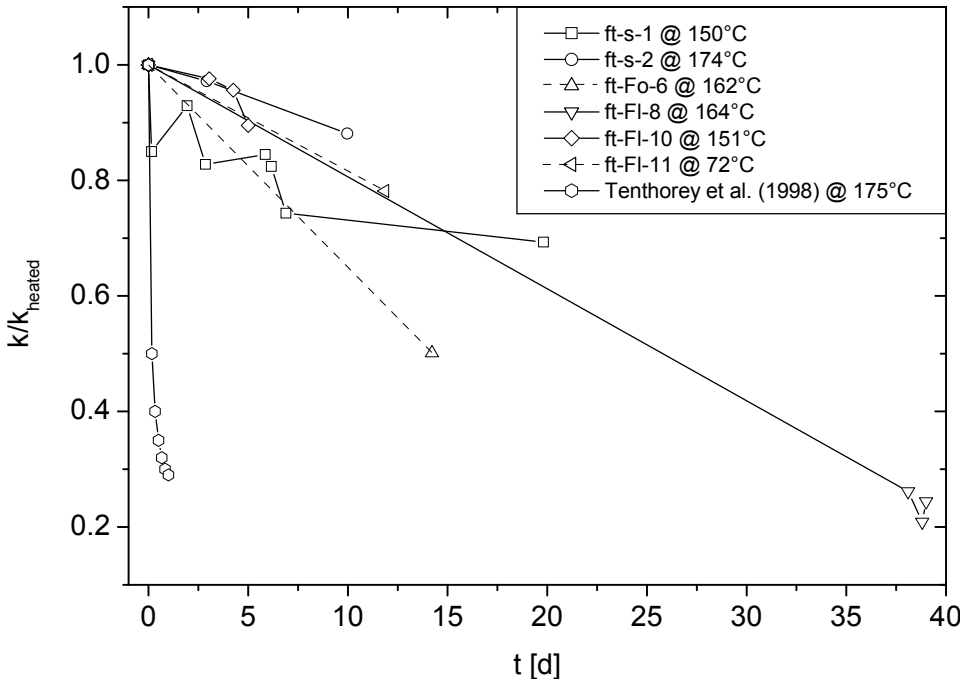

Figure 4.11: Normalized permeability k/k_{heated} as a function of time at constant temperature and confining pressure for flow-through experiments ft-s-1, ft-s-2, ft-Fo-6, ft-Fl-8, ft-Fl-10, and ft-Fl-11. Dashed lines are used as interpolations when only two data points are available. ft-s-1, and ft-s-2 are sandwich samples, ft-Fo-6 is a Fontainebleau sandstone core sample, and ft-Fl-8, ft-Fl-10, and ft-Fl-11 are Flechtinger sandstone core samples. The pore fluid was H_2O, except in ft-Fl-10 (1 mol/L $NaCl_{aq}$). Data from experiments by Tenthorey et al. (1998) are shown for comparison. Their experiment was conducted with labradorite-quartz grain aggregates with a mass ratio of 0.9/0.1 and grain sizes ranging between 210 and 500×10^{-6} m. The starting pore fluid was deionized H_2O. The confining pressure was 100×10^6 Pa, the pore pressure was 50×10^6 Pa, and the experiment was performed under deviatoric stress conditions of 75×10^6 Pa in a triaxial apparatus.

$k_{\text{heated,min}}$ (Table 4.3). Permeability of sandwich samples (ft-s-1 and ft-s-2) exhibited the same decreasing trend with time as the Flechtinger sandstone core samples. However, the data of one sandwich experiment (ft-s-1) is noisy and does not constrain an unambiguous slope. The behavior of a Flechtinger sandstone experiment with 1 mol/L $NaCl_{aq}$ solution as the pore fluid was similar to the experiments performed with H_2O (ft-Fl-10). A Fontainebleau sandstone core sample exhibited a relatively large rate of the k decrease with time at constant temperature (ft-Fo-6). However, only two data points were available for the constant temperature stage of this experiment.

Scientific Technical Report STR 12/07
DOI: 10.2312/GFZ.b103-12079

Table 4.3: Permeability results.

Experiment	k_0 $\times 10^{-15}\,m^2$	k_{min} $\times 10^{-15}\,m^2$	k_{heated} $\times 10^{-15}\,m^2$	$k_{heated,min}$ $\times 10^{-15}\,m^2$	k_{cooled} $\times 10^{-15}\,m^2$
ft-s-1	19	2.01	2.33	2.01	7.99
ft-s-2	38.2	1.26	1.43	1.26	2.94
ft-s-4	0.156	0.006	0.06	0.06	n.a.
ft-s-5	0.001	0.001	0.001	0.001	n.a.
ft-Fo-6	25.1	0.869	1.735	0.869	1.23
ft-P-7	1.337	0.159	n.a.	n.a.	n.a.
ft-Fl-8	0.335	0.005	0.182	0.038	0.005
ft-Fl-9	0.403	0.006	n.a.	n.a.	n.a.
ft-Fl-10*	0.602	0.009	0.018	0.016	0.016
ft-Fl-11**	0.005	0.003	0.004	0.003	0.003
ft-Fl-12**	0.003	0.002	0.002	0.002	0.002
ft-Fl-13	0.274	0.035	0.043	0.043	0.049

* performed with 1 mol/L $NaCl_{aq}$ solution.
** fluid exchange experiments; pretreated with various $NaCl_{aq}$ solutions.

Relative Proportions of Permeability Changes at Different Phases of the Experiments Compared to the Total Permeability Reductions

Permeability reductions due to heating of the samples were generally large, while k changes at constant temperature stages were generally small in comparison (Table 4.4). The absolute values of the observed k changes at the different stages of the experiments, heating, constant temperature, and cooling stage, were compared to the total k reduction of each experiment. The k changes during heating and during the constant temperature stage were generally negative, whereas the k changes during the cooling stage were positive (Figures 4.10 and 4.11). In two Flechtinger sandstone experiments the k decrease during heating was only slightly larger than the k decrease during the constant temperature stage (ft-Fl-8 and ft-Fl-11).

The relative k increases during cooling ranged from approximately 0 to 35 % and showed no regular pattern with respect to duration, sample type, or range of the temperature interval (Table 4.4). For example, two sandwich sample experiments with similar durations of the cooling stage ($\approx$ 2 d) and similar ranges of the temperature interval ($\approx$ 170 to 50 °C) exhibited percentages of the k recovery of 35.2 and 4.5 % relative to the total k reduction (ft-s-1 and ft-s-2).

Evolution of Permeability During Fluid Exchange Experiments

Permeability almost irreversibly decreased during fluid exchange experiments with Flechtinger sandstone samples due to the swelling of clay minerals in the pore space (Figure 4.12). The pore fluids in two Flechtinger sandstone samples were exchanged and permeability was discontinuously measured during this procedure (ft-Fl-11 and ft-Fl-12). $NaCl_{aq}$ solutions with high concentrations were replaced by $NaCl_{aq}$ solutions with lower concentrations and eventually H_2O under isothermal conditions (approximately 42 °C and 70 °C in ft-Fl-11 and ft-Fl-12, respectively).

The data indicate that the k reduction occurred almost instantaneously when the rock was

Scientific Technical Report STR 12/07
DOI: 10.2312/GFZ.b103-12079
Deutsches GeoForschungsZentrum GFZ

Table 4.4: Relative changes of permeability of different stages of the experiments compared to the total permeability decrease. Permeability decreases are displayed as negative numbers.

Experiment	**Heating Stage** %	**Constant Temperature** %	**Cooling Stage** %
ft-s-1	-98.1	-1.9	35.2
ft-s-2	-99.5	-0.5	4.5
ft-Fo-6	-96.4	-3.6	1.5
ft-Fl-8	-46.4	-43.6	n.a.
ft-Fl-10*	-98.6	-0.3	0
ft-Fl-11**	-51.4	-48.6	32.5
ft-Fl-12**	-94.4	0	13.2
ft-Fl-13	-96.8	0	2.8

* performed with 1 mol/L $NaCl_{aq}$ solution.
** fluid exchange experiments; pretreated with various $NaCl_{aq}$ solutions.

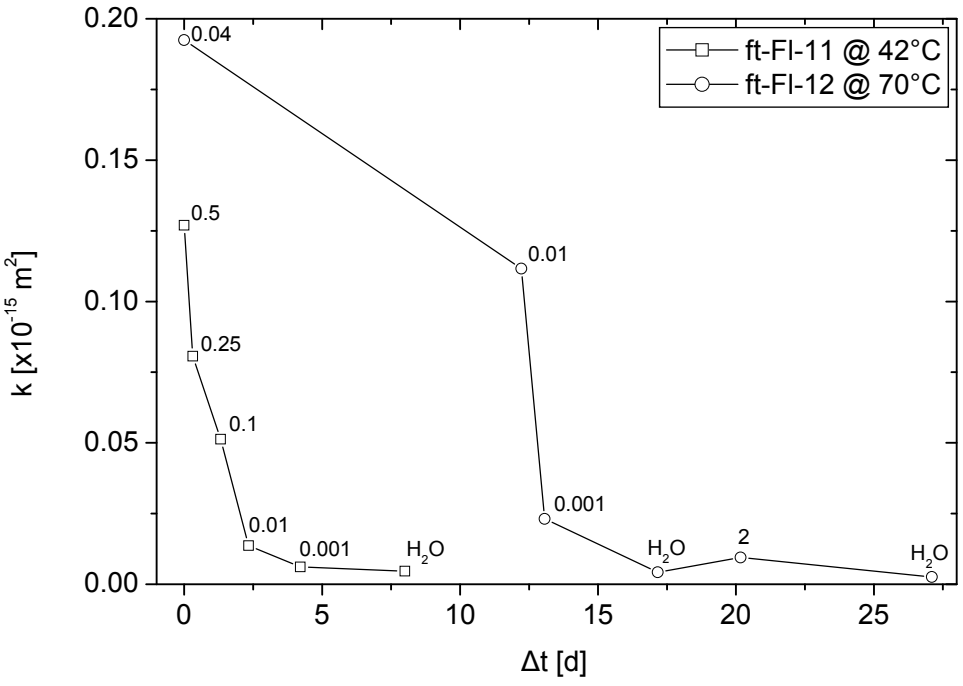

Figure 4.12: Permeability k as a function of elapsed time Δt during fluid exchange procedures of flow-through experiments ft-Fl-11 and ft-Fl-12. The numbers adjacent to the data points indicate the $NaCl_{aq}$ concentration of the respective pore fluid in mol/L.

Scientific Technical Report STR 12/07
DOI: 10.2312/GFZ.b103-12079
Deutsches GeoForschungsZentrum GFZ

in contact with the pore fluid with a lower $NaCl_{aq}$ concentration (ft-Fl-11). This observation was also made in similar experiments conducted with Flechtinger sandstone samples at room temperature (I. Zinz, personal communication). The two Flechtinger sandstone samples showed an apparent time dependence of the k decrease that resulted from very low permeabilities of the samples at low $NaCl_{aq}$ concentrations. With H_2O as the pore fluid, k was in the range of 3 to 5×10^{-18} m^2 and thus two orders of magnitude lower than the k values at the beginning of the fluid exchange procedure. The permeability only partly recovered when the pore fluid H_2O was replaced by 2 mol/L $NaCl_{aq}$ solution (ft-Fl-12). Subsequent flushing with H_2O resulted in a decrease to a similar k value as before k partly recovered. The absolute k values are approximately 4 and 3×10^{-18} m^2 before and after k partly recovered, respectively.

4.1.4 Pore Space Investigations

Mercury Intrusion Porosimetry

The pore space properties, specific surface area, average pore radius, and porosity, generally changed in the course of the flow-through experiments performed with Flechtinger sandstone samples (Table 4.5). The Flechtinger sandstone starting material (5 samples) and the materials resulting from flow-through experiments (6 samples) were analyzed with respect to specific surface area, average pore radius, porosity, bulk density, and apparent density by means of mercury intrusion porosimetry (ft-Fl-9, ft-Fl-10, ft-Fl-11, and ft-Fl-12). The Flechtinger sandstone starting material was rather homogeneous with respect to specific surface area, average pore radius, bulk density, and apparent density (the standard deviations from the mean values were comparatively low). The porosity of the Flechtinger sandstone starting material exhibited a larger variability with $\phi = 9.59 \pm 0.41$ %.

The resulting materials from 4 flow-through experiments with Flechtinger sandstone samples (ft-Fl-9, ft-Fl-10, ft-Fl-11, and ft-Fl-12) plus 2 repeated measurements (ft-Fl-9b and ft-Fl-12b) exhibited significant differences compared to the starting materials and a large variability with respect to specific surface area, average pore radius, and porosity. Bulk and apparent densities showed no significant differences compared to the starting material. The mean value of the specific surface area decreased in comparison to the starting material, whereas the mean value of the average pore radii increased. No clear statement can be made with respect to a porosity alteration of the resulting materials in comparison to the starting materials. The specific surface area and the porosity data resulting from a Flechtinger sandstone flow-through experiment (ft-Fl-9) showed the lowest measured values, while average pore radii values of this sample displayed the highest measured values. This observation was confirmed by a repeated measurement (ft-Fl-9b). The comparison of specific surface areas of repeated measurements (ft-Fl-12a and ft-Fl-12b) yields a relatively high variability suggesting inhomogenities in the sample.

A comparison of the mean values of pore throat radii of the altered material to the mean values of pore throat radii of the starting material generally indicates a decrease of the pore throat classes $< 0.2 \times 10^{-6}$ m and an increase of pore throats with radii between 2 and 8×10^{-6} m in the course of the flow-through experiments (Figure 4.13). Pore throat radii, as calculated with Equation 3.10 for each Hg pressure increment, were reported as a pore throat radius distribution for 16 pore throat radius classes. Relative volumes of intruded Hg pertaining to each pore throat radius class were displayed for the Flechtinger sandstone starting material and altered materials resulting from flow-through experiments (ft-Fl-9, ft-Fl-10, ft-Fl-11, and

Scientific Technical Report STR 12/07
DOI: 10.2312/GFZ.b103-12079

Table 4.5: Mercury porosimetry data of Flechtinger sandstone starting materials and Flechtinger sandstone samples resulting from flow-through experiments.

Sample	**Specific Surface Area** m^2/g	**Average Pore Radius (r50)*** $\times 10^{-6}$ m	**Porosity** %	**Bulk Density** $\times 10^6$ g/m^3	**Apparent Density** $\times 10^6$ g/m^3
Fl-SST-1	1.449	0.53	9.19	n.a.	n.a.
Fl-SST-2	1.597	0.45	9.04	2.36	2.60
Fl-SST-3	1.548	0.60	9.98	2.39	2.65
Fl-SST-4	1.546	0.57	10.01	2.38	2.64
Fl-SST-5	1.497	0.62	9.74	2.40	2.66
mean	1.527 ± 0.05	0.55 ± 0.06	9.59 ± 0.41	2.38 ± 0.01	2.64 ± 0.02
ft-Fl-9a	0.373	1.28	6.98	2.39	2.57
ft-Fl-9b	0.387	1.55	7.61	2.38	2.57
ft-Fl-10	1.451	1.18	8.85	2.35	2.58
ft-Fl-11	1.358	0.67	10.08	2.36	2.62
ft-Fl-12a	1.517	0.44	8.69	2.35	2.57
ft-Fl-12b	1.122	0.75	7.67	2.37	2.57
mean	1.035 ± 0.479	0.98 ± 0.32	8.31 ± 1.06	2.37 ± 0.01	2.58 ± 0.02

* r50 is the pore radius corresponding to the median of cumulative pore volume.
n.a. denotes not analyzed.
Fl-SST denotes Flechtinger sandstone starting material.

ft-Fl-12). No clear statement of changes in the pore throat radius distributions of the starting and altered Flechtinger sandstone material can be made, because of the the large error bars in the pore throat radii region of 1 to 4×10^{-6} m.

BET Gas Adsorption

Specific surface areas (determined by the BET method) of the materials resulting from flow-through experiments with Flechtinger sandstone samples (ft-Fl-9 and ft-Fl-10) distinctly decreased compared to their starting material, whereas the material resulting from a QLM sandwich experiment (ft-s-3) showed a slight increase compared to its staring material (Table 4.6). The specific surface area of Flechtinger sandstone samples resulting from the experiments was lower by up to a factor of approximately 100 compared to the starting material. The specific surface area values of the Flechtinger sandstone starting material were in the same order of magnitude as the respective values obtained from MIP measurements (Table 4.5), whereas the altered samples exhibited lower values by factors of approximately 15 and 35.

Comparability of Mercury Intrusion Porosimetry and BET Gas Adsorption

Several authors compared specific surface areas of various materials obtained by MIP and BET (e.g., Davis, 1984; Milburn and Davis, 1993; Diamond, 2000; Westermarck, 2000; Robens et al., 2002; Fischer and Gaupp, 2004). Experiments with alumina and silica powders yielded that SA_{MIP} is mostly larger than SA_{BET} and that the most uncertain parameters in the calculation of SA_{MIP} are the surface tension of Hg in small pores and the contact angle between Hg and the solid (Davis, 1984). The ratio SA_{MIP}/SA_{BET} can be as high as 14 for limestones with

Scientific Technical Report STR 12/07
DOI: 10.2312/GFZ.b103-12079
Deutsches GeoForschungsZentrum GFZ

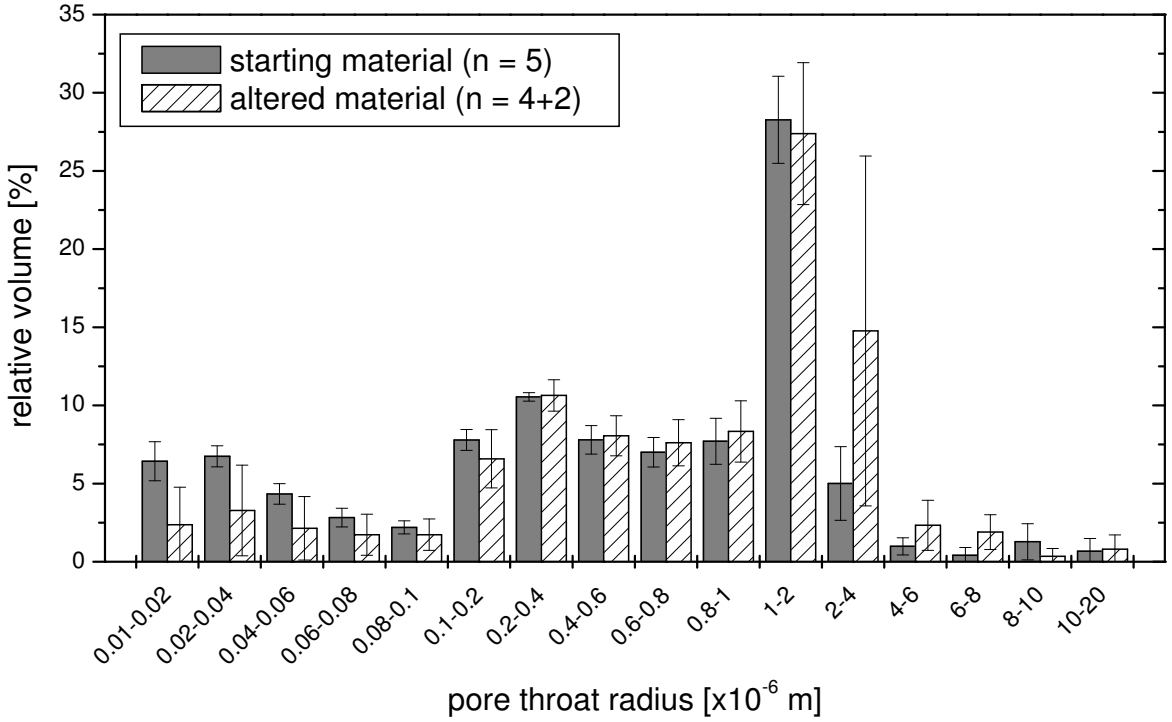

Figure 4.13: Comparison of MIP pore throat radius distributions of the Flechtinger sandstone starting material and altered materials from flow-through experiments ft-Fl-9, ft-Fl-10, ft-Fl-11, and ft-Fl-12. Mean values of 5 measurements of starting material samples and 6 measurements (4 individual samples plus 2 repeated measurements) of altered materials are displayed together with the respective standard deviations from the mean (as error bars).

Table 4.6: BET data of Flechtinger sandstone and QLM starting materials and samples resulting from flow-through experiments ft-s-3, ft-Fl-9, and ft-Fl-10.

Sample	**Specific Surface Area** m^2/g	**Adsorbate**
Flechtinger SST starting material	2.586 ± 0.004	N_2
QLM starting material, 63 to 125 $\times 10^{-6}$ m	0.0431 ± 0.0001	Kr
ft-Fl-9	0.0247 ± 0.0003	Kr
ft-Fl-10	0.0413 ± 0.0001	Kr
ft-s-3	0.0551 ± 0.0001	Kr

Scientific Technical Report STR 12/07
DOI: 10.2312/GFZ.b103-12079

$SA_{BET} < 5\ m^2/g$ (Milburn and Davis, 1993). The geometrical model of a pack of cylindrical capillaries in which all capillaries are entirely and equally connected to the surrounding Hg is an oversimplification of the pore space of cement-based materials. The accessibility of large pores connected to the outer surface of the specimen by smaller pores is restricted, and many pores are connected to the outer surface of the specimen by long percolative chains. Such an arrangement of pores results in an overestimation of specific surface area because large pores that are shielded by smaller pores fill at higher pressures, and so the additional intruded volume of Hg is allocated to smaller pore size classes (Diamond, 2000).

The typical hysteresis in plots of cumulative Hg volume versus pressure indicates that some pores were shielded by smaller ones in the Flechtinger sandstone. To account for this behavior, a conical geometrical model was used for the calculation of SA_{MIP} in the Pascal 140/240/440 software. The geometrical model was not altered throughout the present study, even though changing geometrical properties of the pore space, e.g., in the hydrothermal experiments, may have required a change in the geometrical model. However, an improper geometrical model may have led to erroneous results in the calculated SA_{MIP} values.

Despite of the differences in absolute values of SA_{MIP} and SA_{BET}, both methods are complementary, because they cover different pore sizes (Westermarck, 2000; Fischer and Gaupp, 2004). Investigations of surface area modifications of unweathered and weathered black shale on different pore scales have shown that MIP is valid for the study of macro- and mesopores, i.e., pores with diameters of approximately 0.1^{-3} to 10^{-9} m (Fischer and Gaupp, 2004). The BET method is valid for the investigation of meso- and partly micropores, i.e., pores with diameters of approximately 0.3×10^{-6} m to 0.3×10^{-9} m (Westermarck, 2000).

X-ray Computed Tomography

Scanning of a small Flechtinger sandstone sample using X-ray CT before and after a flow-through experiment (ft-Fl-13) did not show detectable changes in the reconstructed pore space (Figure 4.14). Virtual thin sections were reconstructed from nondestructive X-ray CT perpendicular to the long axis of the sample. By means of a special experimental set-up with a PEEK bushing and stress regulating springs (Figure 3.6), a flow-through experiment was conducted without destroying the small and fragile rock sample. The pore space was reconstructed from the same region of interest of the first and the second scan. The comparison of both reconstructions before and after the experiment showed no changes of the pore space larger than the resolution of the method of approximately 2×10^{-6} m.

4.1.5 Mineralogical Analyses of Solid Samples

X-ray Powder Diffraction

XRD analyses of the Flechtinger sandstone starting material, the Flechtinger sandstone material resulting from a flow-through experiment (ft-Fl-9), the QLM starting material, and the QLM material resulting from a sandwich experiment (ft-s-3) yielded qualitatively similar diffractograms (Figure 4.15). The locations and shapes of peaks in the diffractograms of starting and altered materials are similar. They indicate that mineralogical differences, i.e., differences in crystal lattice parameters, were either below the detection limit of the method (≈ 1 %), or that alteration products were not crystalline. The diffractograms have a different curvature and length along the $^\circ 2\theta$-axis, because two different diffractometers were used. XRD analyses of Flechtinger sandstone samples were performed with a Siemens D5000 diffractometer. The

Scientific Technical Report STR 12/07
DOI: 10.2312/GFZ.b103-12079

Figure 4.14: Virtual thin section of a Flechtinger sandstone obtained from X-ray CT. The voxel size is 2×10^{-6} m. The diameter of the virtual thin section is approximately 2×10^{-3} m, the depth is several micrometers. The reconstructed pore space is presented as solid gray, the mineral grains and the cements comprising the rock sample are presented as hollow space. The reconstruction and visualization was performed with the open source software ParaView (Ahrens et al., 2005) by D. Naumov.

Scientific Technical Report STR 12/07
DOI: 10.2312/GFZ.b103-12079

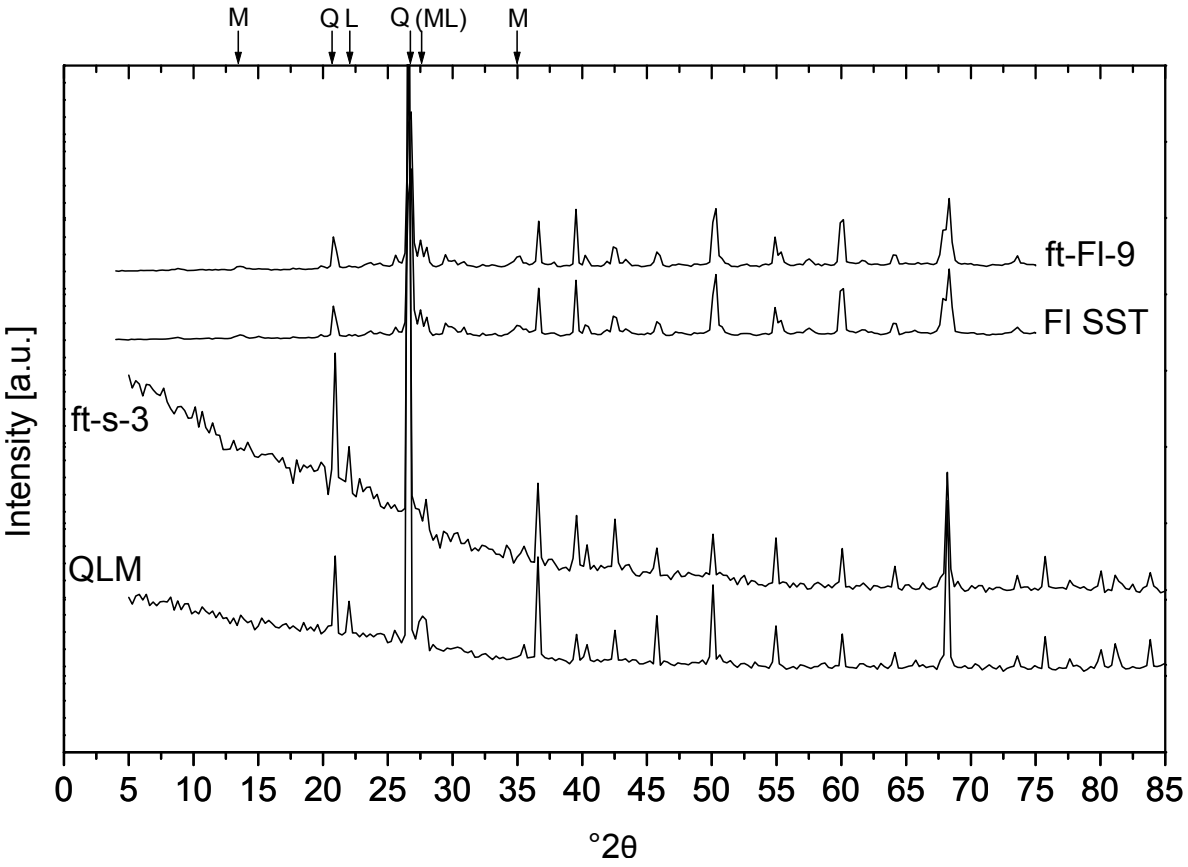

Figure 4.15: XRD patterns of Flechtinger sandstone (Fl SST) and QLM starting materials compared to materials resulting from flow-through experiments ft-Fl-9 and ft-s-3. Intensities are plotted in arbitrary units as a function of $°2\theta$. Characteristic peaks of quartz, labradorite, and microcline, taken from the RRUFF database (Downs, 2006), are indicated by small arrows with Q, L, M notation.

QLM samples were analyzed with a STOE STADIP diffractometer. The comparison of the Flechtinger sandstone materials with the QLM materials shows general consistency among the diffractograms with some slight differences: The QLM materials show a peak at $22.0°2\theta$ which is not present in the Flechtinger sandstone materials.

Rietveld refinements were carried out with the GSAS software package (Section 3.3) resulting in the identification of quartz, labradorite-andesine, and microcline. Reference X-ray powder diffractograms can be found in the free online RRUFF database (Downs, 2006). Characteristic peaks were extracted for quartz (rruff ID R040031), labradorite (rruff ID R060275), and microcline (rruff ID R040154). Characteristic peaks for quartz are at 20.9 and $26.7°2\theta$. All major peaks $> 35°2\theta$ can be attributed to quartz. Characteristic labradorite peaks are at 22, 25.7, and $28°2\theta$. The $22°2\theta$ peak is only present in the QLM materials. The $25.7°2\theta$ peak is covered by the large quartz peak at $26.7°2\theta$. The $28°2\theta$ forms a double peak with microcline (denoted by ML). Small characteristic microcline peaks are located at 13.7, 27.5, and $35°2\theta$. The $13.7°2\theta$ is, especially in the Flechtinger sandstone diffractograms, small and comparatively

Scientific Technical Report STR 12/07
DOI: 10.2312/GFZ.b103-12079
Deutsches GeoForschungsZentrum GFZ

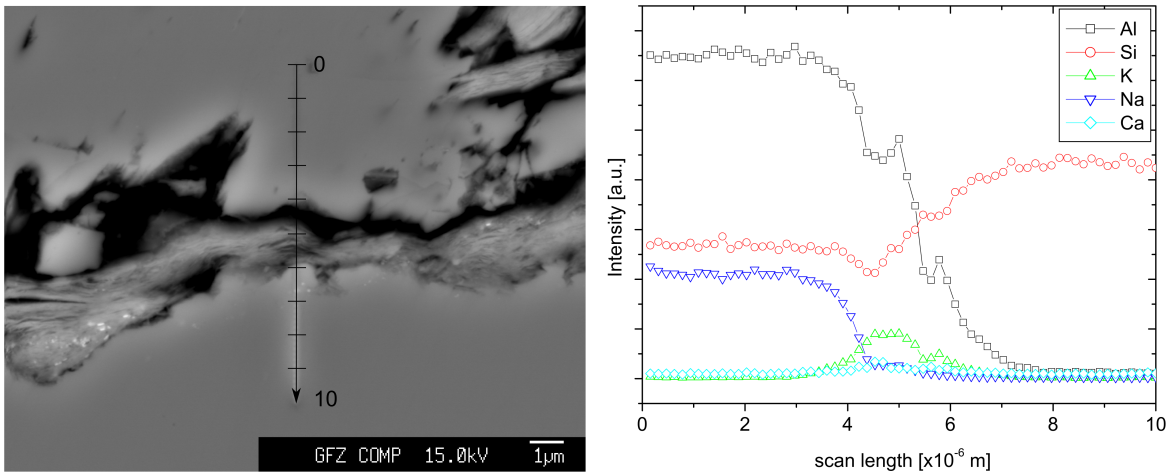

Figure 4.16: EMPA line scan of an altered Flechtinger sandstone sample from experiment ft-Fl-9. The BSE micrograph shows the direction of the line scan starting on a plagioclase (albite) grain, then crossing the pore space, partly filled with fibrous illite that contains minor amounts of fine calcite grains (bright dots), and then ending on a quartz grain. The graph shows relative concentrations of Na, Al, Si, K, and Ca in arbitrary units as a function of the line scan length. The scan was performed with an acceleration voltage of 15×10^3 V and a probe current of 11×10^{-9} A.

broad, and the 27.5°2θ peak is superimposed by a labradorite peak. The 35°2θ peak is clearly detectable in all 4 diffractograms.

Electron Microprobe Analysis

Electron microprobe analysis of a Flechtinger sandstone sample resulting from a flow-through experiment (ft-Fl-9) did not show chemical alterations of the material in comparison to the starting material (Figure 4.16). Line scans were performed over feldspar and quartz grain boundaries including the pore space between them in order to identify reaction rims that may have formed due to the interaction of the pore fluid with the solid phases in the experiment. Polished thin sections of an unaltered Flechtinger sandstone specimen and the altered sample were investigated by EMPA. Point analyses contributed to the identification of individual petrological phases in the materials (Table 3.1 and Figure 4.19).

The spatial resolution of concentration changes was limited by the source region of element characteristic X-rays (approximately 1.8×10^{-6} m). Thus, the apparent decrease of Al and Na concentrations starting at 3×10^{-6} m of the line scan cannot be interpreted as a reaction rim in which Al and Na are depleted compared to the concentrations of the unaltered plagioclase (Figure 4.16). The same limitation holds for the increase of Si concentration in the quartz grain beginning at a scan length of approximately 6×10^{-6} m. The two Al and K peaks at approximately 5 and 6×10^{-6} m are attributed to fibrous illite partly filling the pore.

Scientific Technical Report STR 12/07
DOI: 10.2312/GFZ.b103-12079

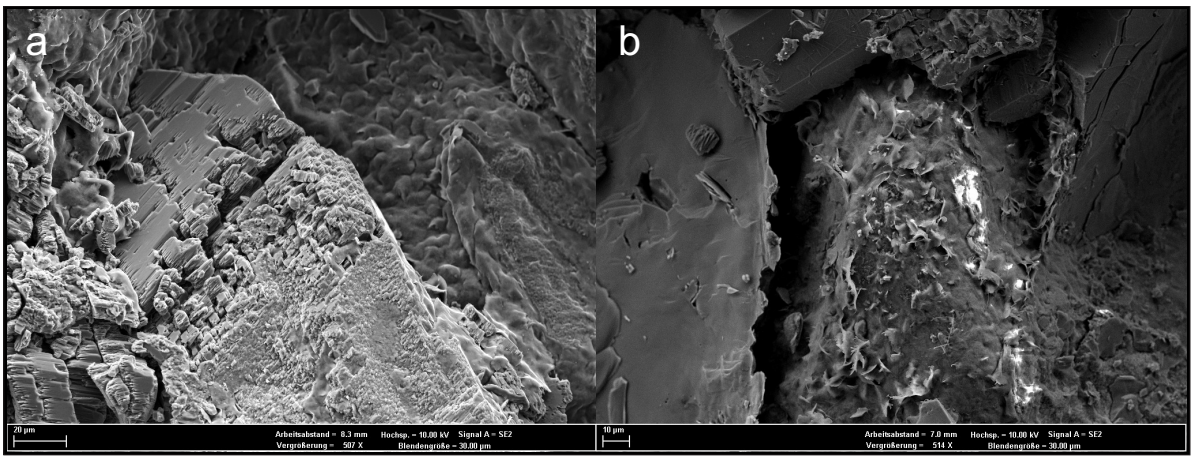

Figure 4.17: SE micrographs of fractured surfaces of a) Flechtinger sandstone starting material and b) the altered material resulting from experiment ft-Fl-8. The scale bar in a) represents 20×10^{-6} m. The scale bar in b) represents 10×10^{-6} m.

4.1.6 Investigations of the Microstructure

Scanning Electron Microscopy of Fractured Rock Mounts

Due to the complexity of the pore space it was not possible to find significant microstructural differences between Flechtinger sandstone starting materials and materials resulting from flow-through experiments using secondary electron, SE, micrographs of fractured rock mounts either at low or high magnifications up to a resolution of approximately 1×10^{-6} m (Figures 4.17 and 4.18). The microscopic features of the pore space of the Flechtinger sandstone starting material and an altered sample from a flow-through experiment (ft-Fl-8) were identical. The SE micrographs were produced with similar acquisition parameters with respect to magnification, working distance, and acceleration voltage. The fractured surface of the Flechtinger sandstone starting material showed a highly corroded plagioclase that was partly covered with a material tentatively identified as fibrous illite (Figure 4.17a). Apart from fibers, the illite formed thin flakes with a diameter of approximately 10×10^{-6} m partly arranged in three dimensional rosettes. Comparison between several fractured rock mounts was ambiguous and led to the result that features like idiomorphic quartz grains coexisting with rounded quartz grains, highly corroded (mainly plagioclase) and intact (mainly K-feldspar) feldspar grains, and fibrous illite covering the grains and growing in the pore space were frequent in the Flechtinger sandstone starting material and the altered material.

Scanning Electron Microscopy of Polished Thin Sections

BSE micrographs of unaltered and altered Flechtinger sandstone material illustrate that the content of minerals, cements, and rock fragments is qualitatively identical in both materials (Figure 4.19). SE and BSE micrographs were taken from polished thin sections of an unaltered Flechtinger sandstone sample and the altered material from a flow-through experiment (ft-Fl-9) to quantify differences in 2D porosity. The thin sections of the starting material and the altered material had an area of 720 and 780×10^{-6} m^2, respectively. A total of 24 and 26 micrographs

Scientific Technical Report STR 12/07
DOI: 10.2312/GFZ.b103-12079

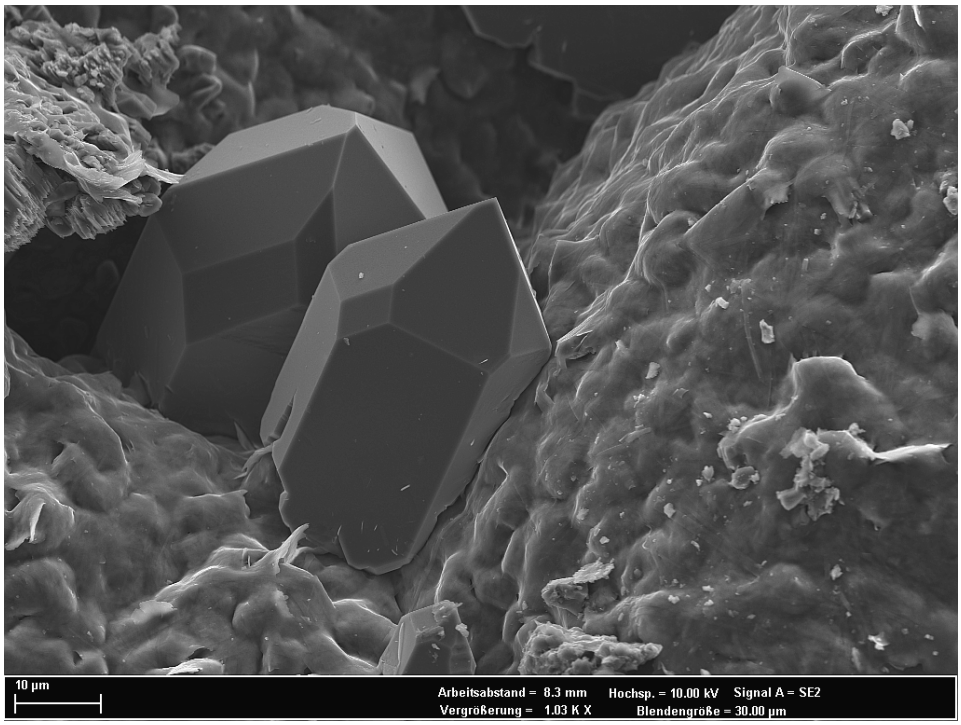

Figure 4.18: SE micrograph of a fractured surface of the altered material resulting from experiment ft-Fl-8. In the center two idiomorphic (authigenic) quartz grains are shown, growing in a complex pore space. A smaller idiomorphic quartz crystal partly overgrown by illite is visible at the bottom of the micrograph. The upper left corner of the image shows a highly corroded plagioclase edge. Most of the materials present are covered by an illite layer that is composed of individual illite fibers. The scale bar represents 10×10^{-6} m.

Scientific Technical Report STR 12/07
DOI: 10.2312/GFZ.b103-12079

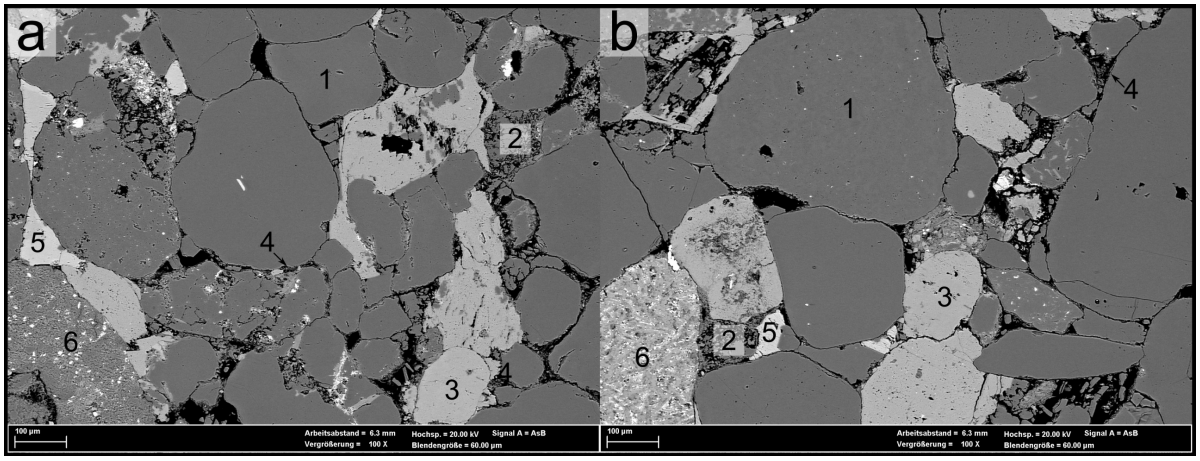

Figure 4.19: BSE micrographs of polished thin sections of Flechtinger sandstone starting material (a) and the altered material resulting from experiment ft-Fl-9 (b). The numbers in each picture indicate petrological phases that both materials have in common: 1) rounded to subangular quartz grains, 2) corroded plagioclase, 3) rounded and partly corroded K-feldspar, 4) pore lining and pore filling illite, commonly intertwined with fine calcite and hematite grains, 5) pore filling calcite cement, and 6) rounded volcanic rock fragments, partly with bright hematite inclusions. Both images were produced with the same acquisition parameters. The scale bars represent 0.1×10^{-3} m.

were produced at different magnifications (30, 50, and 100×) covering approximately 20 % of each thin section area. The acquisition parameters working distance, acceleration voltage, noise reduction, contrast, and brightness were identical in each set of micrographs. With the aid of the software ImageJ, gray-scale value thresholds were set to produce binary images that showed the 2D porosity of each sample (Figure 3.9).

An image analysis of the altered Flechtinger sandstone material resulting from a flow-through experiment yielded a slight increase of 2D porosity compared to the starting material (Table 4.7). The largest area fraction of the thin sections was covered by the SE micrographs at the lowest magnification. In general, it was more difficult to segment these micrographs in comparison to the BSE micrographs due to their lower contrast and resolution, which resulted in a larger estimated error for the segmented 2D porosity. No significant differences in mean 2D porosity could be detected by means of SE micrographs at 30× magnification. Segmentation of the BSE micrographs with higher magnifications and higher contrast was more reliable, yet these micrographs covered only 1.6 and 1.2 % of the thin section area of the Flechtinger sandstone starting material and the material resulting from the experiment, respectively. On the basis of the image analysis of these micrographs, an increase of approximately 2 % mean 2D porosity of the altered material can be deduced compared to the starting material.

Scanning Electron Microscopy of Individual Grain Mounts

Typical SE micrographs which were taken of mounts of granular starting materials and altered materials resulting from a QLM sandwich flow-through experiment (ft-s-4) indicate that the

Scientific Technical Report STR 12/07
DOI: 10.2312/GFZ.b103-12079
Deutsches GeoForschungsZentrum GFZ

Table 4.7: Results of the image analysis with ImageJ.

Thin Section	Magnification	Type	Resolution*	Area Fraction	Mean 2D Porosity	Error**
		BSE / SE	$\times 10^{-6}$ m	%	%	%
Flechtinger SST, starting material	30	SE	14	19.4	6.1	0.8
	100	SE	3	1.6	7.6	0.5
ft-Fl-9	30	SE	14	16.4	6.5	0.8
	50	BSE	6	2.3	9.6	0.6
	100	BSE	3	1.2	9.4	0.5

* defined as the size of the smallest detail clearly visible in the image (Reed, 2005).
** estimated from uncertainty due to threshold setting in the segmentation process.

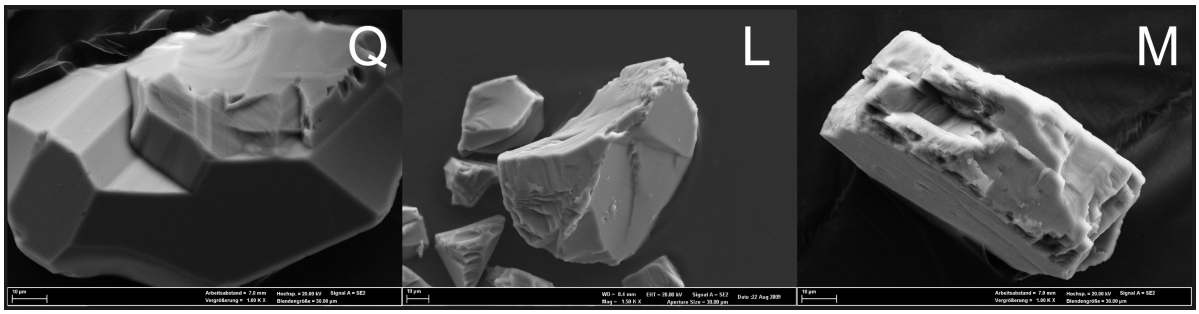

Figure 4.20: SE micrographs of QLM starting materials with a grain size of 63 to 125 $\times 10^{-6}$ m. The scale bar in each micrograph is 10×10^{-6} m.

starting grains had clean surfaces, whereas the resulting QLM materials showed significant surface alterations (Figures 4.20 and 4.21). The quartz grains of the QLM starting material appear free of any fine particles resulting from the preparation process. Labradorite-andesine and microcline grains exhibit rougher surfaces with small particles adhering to them. The surfaces of the altered materials exhibit significant textural alterations, that are most pronounced on labradorite-andesine grains, frequent on microcline grains, and rare on quartz grains. These alteration features were widespread throughout the investigated samples.

EDX spectra of an unaltered and an altered labradorite-andesine surface show that element ratios changed in the course of a QLM sandwich flow-through experiment (Table 4.8). Molar element ratios of Na, Al, Si, K, and Ca were derived from EDX and XRD analyses of unaltered and altered labradorite-andesine materials. Although the source region for element characteristic X-rays (Section 3.3.3) was larger than the small particles (Figure 4.21d), the data display qualitative changes of molar element ratios of Na, Al, Si, K, and Ca between unaltered and altered labradorite-andesine surfaces. The element ratios of the sum of Na, K, and Ca over the sum of Al and Si as well as the ratios K/Si, Ca/Si, K/Al, and Ca/Al show good agreement comparing EDX with XRD data of the labradorite-andesine starting material. The Na/Si and Na/Al ratios show that this specific labradorite-andesine surface analyzed with EDX was a Na-rich part of the grain. Labradorite-andesine is a solid-solution of a Na and a Ca plagioclase

Scientific Technical Report STR 12/07
DOI: 10.2312/GFZ.b103-12079

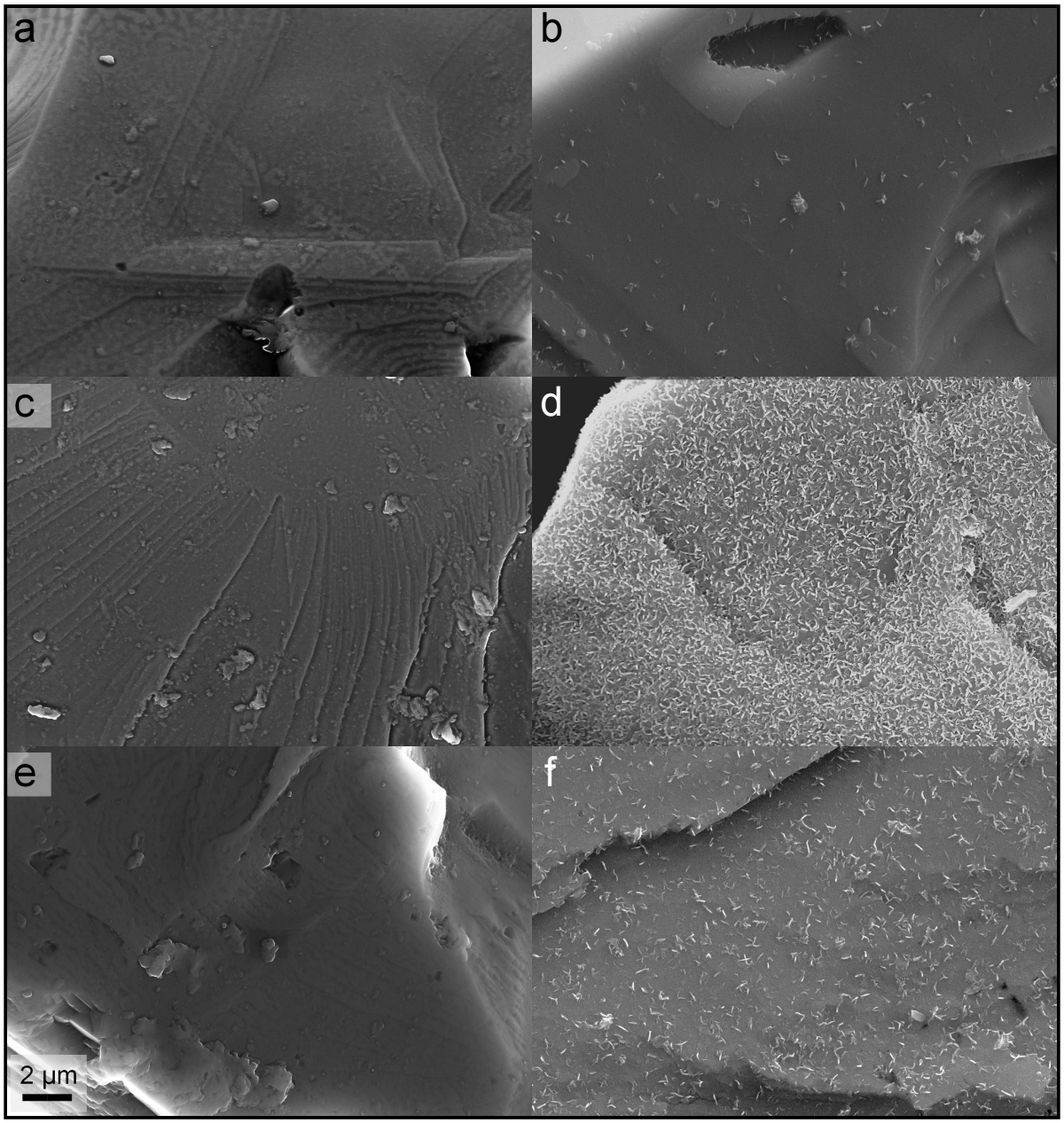

Figure 4.21: Comparison of SE micrographs of QLM starting materials with a grain size of 63 to 125 $\times$ 10^{-6} m (left panel) to materials resulting from experiment ft-s-4 (right panel). a), c), and e) are surfaces of quartz, labradorite-andesine, and microcline, respectively. b), d), and f) are corresponding surfaces of these minerals as resulting from the experiment. Small elongated particles with a length of $< 10^{-6}$ m cover the surfaces of the grains. These alteration features are widespread on the labradorite-andesine grains (d). The scale bar represents 2 $\times$ 10^{-6} m.

Scientific Technical Report STR 12/07
DOI: 10.2312/GFZ.b103-12079

Table 4.8: Element ratios resulting from EDX analyses of unaltered and altered labradorite-andesine surfaces resulting from experiment ft-s-4.

Element Ratio	**Unaltered Surface**	**XRD***	**Altered Surface**
(Na+K+Ca)/(Al+Si)	0.33	0.24	0.36
Na/Si	0.33	0.17	0.04
K/Si	0.01	0.01	0.04
Ca/Si	0.21	0.21	0.44
Na/Al	0.48	0.28	0.1
K/Al	0.02	0.01	0.08
Ca/Al	0.3	0.34	0.97

* from Table 3.1.

Table 4.9: EDX analyses of a small particle on an altered quartz surface resulting from experiment ft-s-4.

EDX Point / Spectrum	**Al** mol %	**Si** mol %	**K** mol %
point 1	0.43	8.89	0.09
point 2	0.4	9.27	
point 3	0.18	10.25	
point 4	0.1	10.09	0.05
spectrum	0.14	9.64	0.08

endmember. Exsolution leads to microscopic twinning of both endmembers. The Na/Si and Na/Al ratios of the altered surface are comparatively low, whereas K and Ca are enriched compared to Si and Al in the altered surface.

Detailed SE micrographs of the altered surfaces of a labradorite-andesine and a quartz grain show the microstructure and yielded details of the chemical composition of the altered surfaces (Figure 4.22a). Results of EDX point analyses and of an EDX spectrum taken from the quartz micrograph (Figure 4.22b) indicate that the particles contain Al and K (Table 4.9). The source region for element characteristic X-rays was larger than the small particle. However, a distinct trend of Al decrease, following the path of the electron beam from point 1 to point 4, can be observed. Si showed lower concentrations compared to the quartz surface when the electron beam was centered on the small particle (points 1 and 2). Points 1 and 4 exhibit small concentrations of K, although in the vicinity of point 4 no material other than quartz is present in the micrograph. Thus, the small K concentration detected in point 4 most probably results from an adjacent K-bearing particle outside of the micrograph. An EDX spectrum was taken from the full area of the micrograph with a long acquisition time of 900 s for a qualitative confirmation of small concentrations of Al and K. The spectrum displayed a pronounced Al peak and a smaller, but still detectable, K peak. The calculated concentrations from the spectrum agree with the EDX point analyses (Table 4.9).

Scientific Technical Report STR 12/07
DOI: 10.2312/GFZ.b103-12079

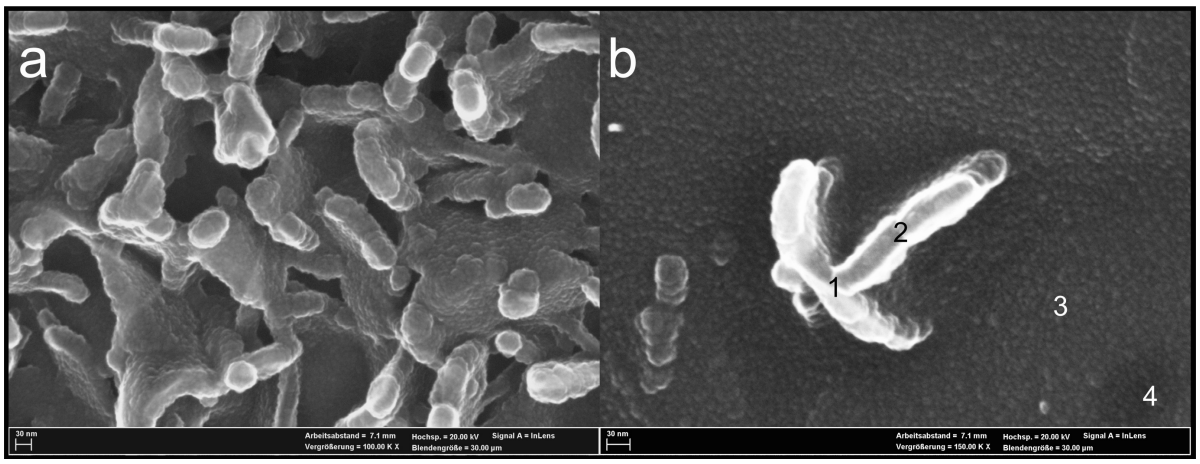

Figure 4.22: Detailed SE micrographs of a) an altered labradorite-andesine surface and b) an altered quartz surface resulting from experiment ft-s-4. The numbers in b) indicate the centers of the spot of the electron beam for EDX point analyses. The scale bars in the micrographs represent 30×10^{-9} m.

Transmission Electron Microscopy

Transmission electron microscopy, TEM, showed that mainly amorphous sub-micrometer sized particles precipitated from the bulk solution on altered surfaces of labradorite-andesine and microcline grains resulting from a QLM sandwich flow-through experiment (Figures 4.23 and Figure 4.24). Two TEM foils were cut by means of the FIB technique (Section 3.3.3). One foil was obtained from a C-coated labradorite-andesine sample, the other foil was obtained from an Au-coated microcline sample. The insert in the bright field image of the foil obtained from the labradorite-andesine sample is a scanning transmission electron microscopy high-angle angular dark field, STEM-HAADF, overview of the foil and illustrates the area from which the bright field image was produced by a small square (Figure 4.23). The white part in the STEM-HAADF image is a Pt strap covering the surface of the labradorite-andesine crystal. Below the Pt strap, the small particles can be seen as irregularly shaped humps in dark gray. The particles are located on top of the light gray colored labradorite-andesine crystal. The bright field image shows that the small particles were inhomogeneously composed of an amorphous matrix which was identified by the lack of diffraction patterns during tilting the sample and/or focusing through the sample. Moreover, the small particles contained darker parts tentatively labeled as fiber stacks (Figure 4.23a). Moreover, STEM-HAADF images of the same area showed a substantial porosity of the small particles. EDX mapping revealed chemical inhomogeneities with respect to Fe and Al clusters. Qualitatively the particles are composed of Mg, Al, Si, Ca, and Fe. The interface between the small particles and the labradorite-andesine crystal is sharp on the nanometer scale.

A montage of two TEM bright field images produced from the foil that was obtained from the Au-coated microcline sample shows that the small particles are composed of a mixture of an amorphous phase and a crystalline phase (Figure 4.24). An EDX area analysis of the crystalline phase yielded a composition of 21.1 % Al, 64.2 % Si, and 14.7 % K (numbers are atomic percent values). The same analyis of the microcline crystal yielded atomic percent values of 3.7 % Na,

Scientific Technical Report STR 12/07
DOI: 10.2312/GFZ.b103-12079

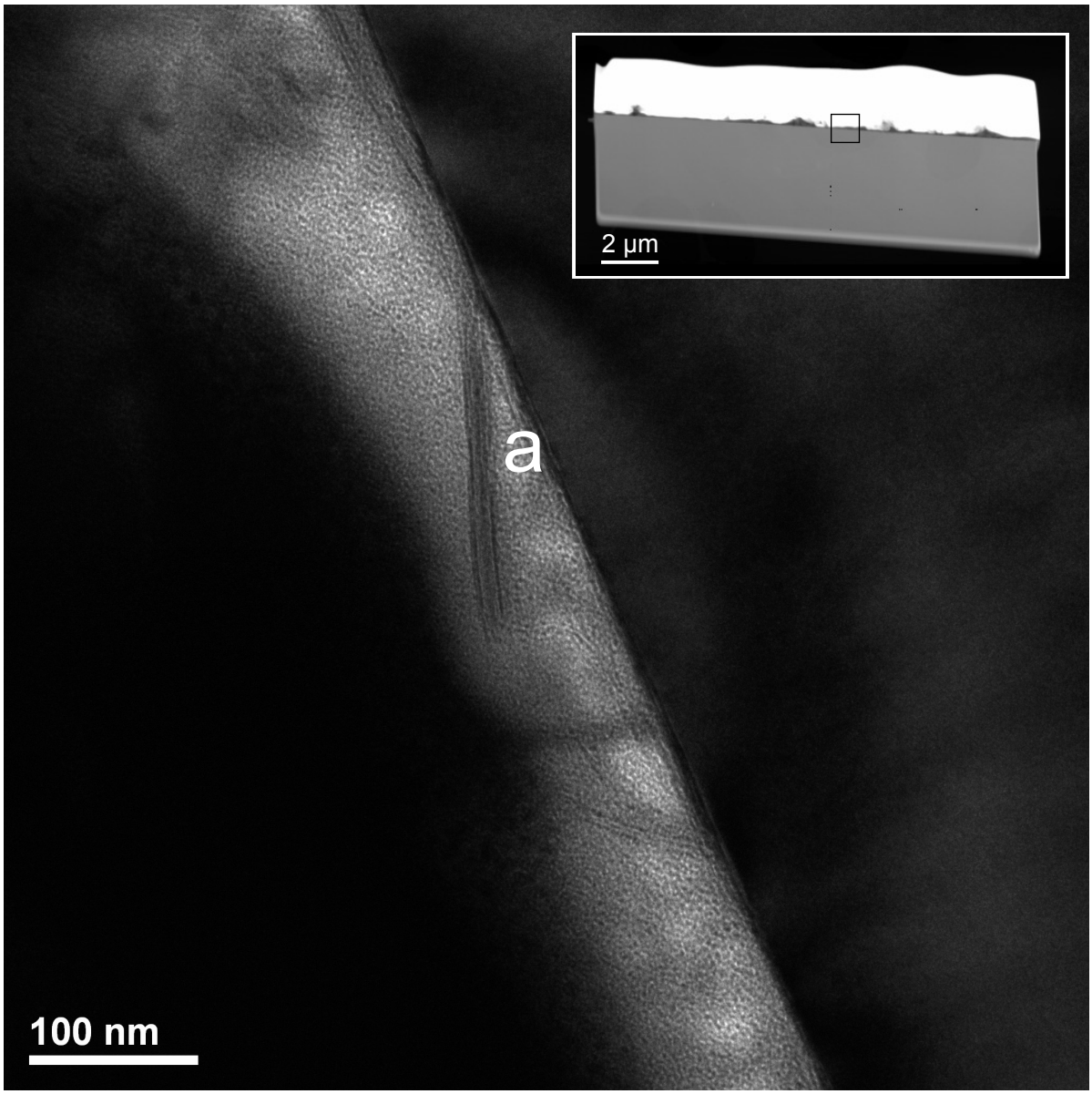

Figure 4.23: TEM bright field image of a cross section through an altered labradorite-andesine surface resulting from flow-through experiment ft-s-4. The insert is a STEM-HAADF overview of the TEM foil. The small square indicates the area shown in the larger image. The dark gray material on the right is the original labradorite-andesine crystal. The bright gray material in the middle is a small particle on the altered surface. a) indicates layered structures that are tentatively labeled as fiber stacks in an otherwise bright gray amorphous matrix. Tilting of the image is due to magnification in the TEM.

Scientific Technical Report STR 12/07
DOI: 10.2312/GFZ.b103-12079

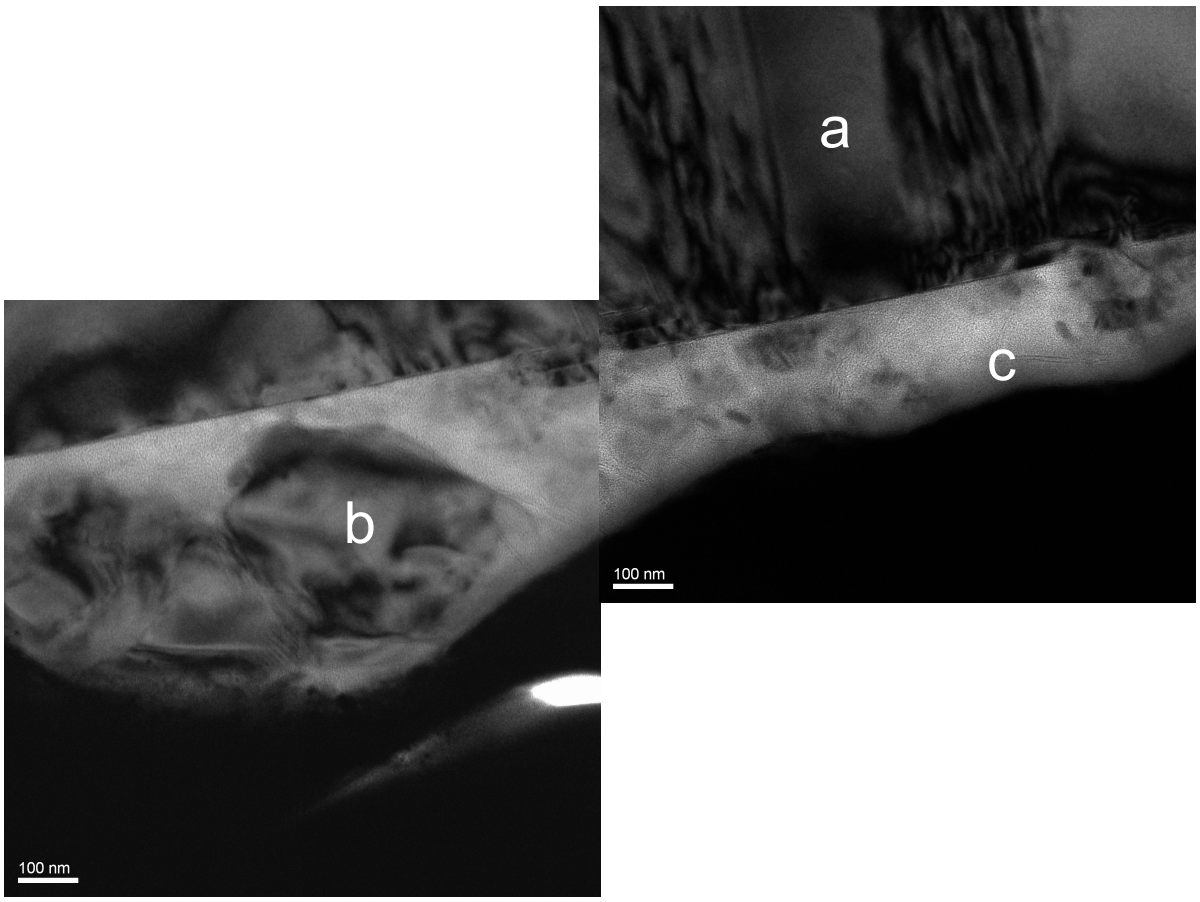

Figure 4.24: Montage of TEM bright field images of a cross section through an altered microcline surface resulting from flow-through experiment ft-s-4. a) denotes the microcline crystal in which diffraction patterns are visible. Perthitic exsolution lamellae, oriented perpendicular to the crystal surface, are discriminable by gray-scale value contrasts. b) denotes crystalline particles with diffraction patterns. These particles are surrounded by a bright gray amorphous matrix (c).

20.1 % Al, 60.1 % Si, and 16.1 % K. Thus, the crystalline phase is stoichiometrically almost identical to the microcline crystal, except that Na is not present in the material. Taking the semiquantitative nature of EDX analyses into account, the crystalline phase could either be a residuum from the preparation of the starting material or a newly formed crystalline phase with a similar composition as the microcline crystal, except that Na is not incorporated in the material. The amorphous phase is composed of slightly more Si and slightly less Al and K than the crystalline phase. The amorphous phase is divided from the microcline crystal by a sharp interface on the nanometer scale.

Scientific Technical Report STR 12/07
DOI: 10.2312/GFZ.b103-12079

4.2 Batch Experiments

Batch experiments were performed to investigate the effects of fluid-mineral reactions on porous samples, granular aggregates, and fluids in contact with the solid materials under controlled p-T and chemical conditions. The results of the batch experiments are subdivided into the electrical conductivity of a Flechtinger sandstone sample, electrical conductivity of fluid samples, chemical analyses and hydrogeochemical modeling of a Flechtinger sandstone pore fluid and bulk fluids that were in contact with Flechtinger sandstone and QLM samples, investigations of the porosity and specific surface area of rock and granular samples, and investigations of mineralogical and microstructural changes.

In total, 17 batch experiments were performed (Table 3.3). Experiments with granular aggregates of quartz, feldspars, illite, and calcite were conducted to investigate effects of variable compositions, grain size fractions, fluid/solid mass ratios, preparation methods, temperature, and total duration of the experiments (b-QL-1 to b-QLMIC-14). Experiments with Flechtinger sandstone samples were carried out to examine effects of variable fluid/solid mass ratios, temperature, and total duration (b-Fl-15 to b-Fl-17).

4.2.1 Electrical Conductivity of a Flechtinger Sandstone Sample

The evolution of the electrical conductivity of an initially H_2O saturated Flechtinger sandstone sample is qualitatively similar in a batch experiment at constant temperature (b-Fl-17, Figure 4.25) compared to the transient σ_r increase observed in a flow-through experiment (ft-Fl-9, Figure 4.1). After an initial σ_r increase from approximately 9 to approximately 22×10^{-3} S/m in the first 3 d of the experiment, σ_r slowly increased to approximately 25×10^{-3} S/m in the remainder of the experiment.

Interface phenomena like polarization, capacitance, and inductance had negligible effects on the σ_r measurements, as indicated by a ratio of ohmic resistance over complex impedance, R/Z, close to unity (Figure 3.8). This observation implies that σ_r was dominated by σ_f in the Flechtinger sandstone batch experiment (e.g., Schön, 1996). There was neither a temperature nor a time dependence in R/Z. At the starting conditions with H_2O as the initial pore fluid and 20 °C, R/Z behaved similar as at a run duration of 3 d at 70 °C. The change of R/Z with AC frequency was not affected by the run duration at a constant temperature of 70 °C.

4.2.2 Electrical Conductivity of Fluids Resulting From Batch Experiments

Electrical Conductivity of Fluids Resulting From Batch Experiments With Granular Aggregates

The electrical conductivity at standard temperature, $\sigma_f(T_0)$, of fluids in contact with granular aggregates of quartz, labradorite-andesine, microcline, and partly illite increased with time at a constant temperature of 150 °C (Figure 4.26). The evolution of $\sigma_f(T_0)$ follows three different trends depending on the grain sizes of the granular aggregates and on the fluid/solid mass ratios: (i) Highest $\sigma_f(T_0)$ values were attained in experiments with very small grains ($<< 63 \times 10^{-6}$ m) and fluid/solid mass ratios equal to 5 (b-QLM-7 and b-QLMI-11). (ii) Lowest $\sigma_f(T_0)$ values were obtained in experiments with larger grains ($< 63 \times 10^{-6}$ m) and larger fluid/solid mass ratios equal to 15 (b-QLM-8 and b-QLMI-12). (iii) Experiments with grain size fractions $< 63 \times 10^{-6}$ m and 63 to 125×10^{-6} m as well as fluid/solid mass ratios equal to 5 yielded intermediate $\sigma_f(T_0)$ values (b-QLM-3 (H_2O), b-QLM-5, b-QLM-9, b-QLM-10, and b-QLMI-13).

Scientific Technical Report STR 12/07
DOI: 10.2312/GFZ.b103-12079

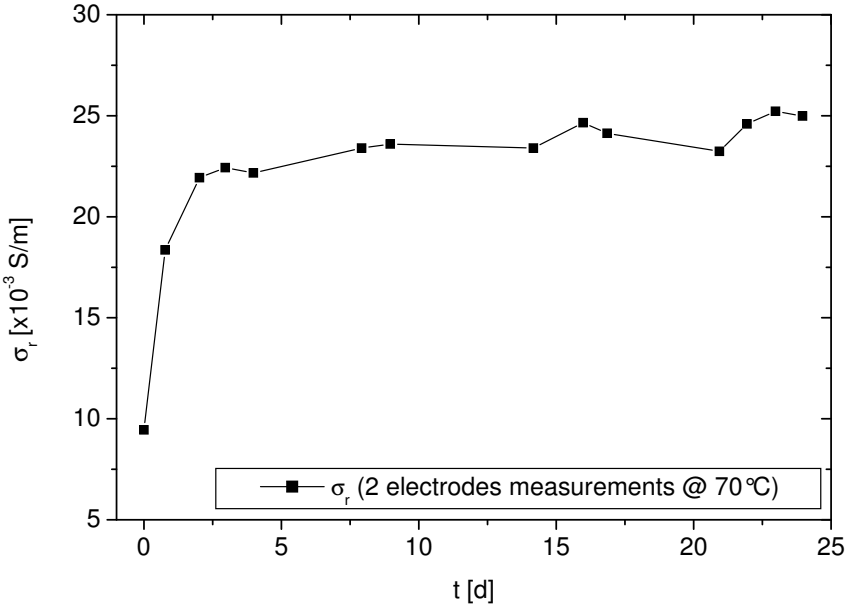

Figure 4.25: Electrical conductivity, σ_r, of a Flechtinger sandstone sample as a function of time in experiment b-Fl-17 at a constant temperature of 70 ± 2 °C. The data result from impedance spectroscopic measurements performed in a two-electrodes arrangement at 12 Hz AC frequency.

Scientific Technical Report STR 12/07
DOI: 10.2312/GFZ.b103-12079

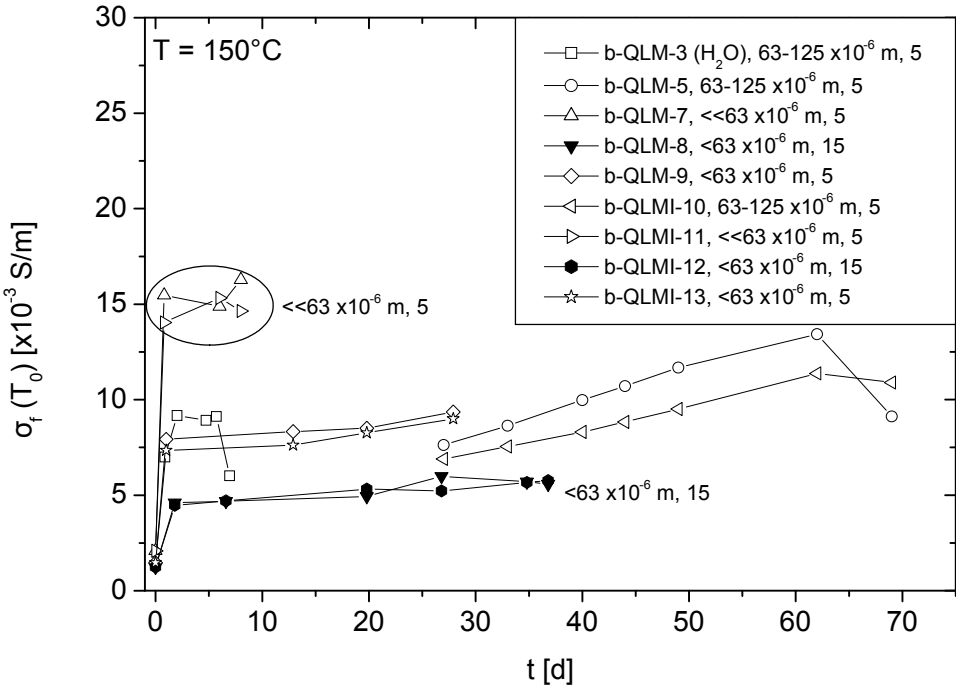

Figure 4.26: Electrical conductivity of fluids, $\sigma_f(T_0)$, as a function of time for batch experiments b-QLM-3 (H_2O), b-QLM-5, b-QLM-7, b-QLM-8, b-QLM-9, b-QLM-10, b-QLMI-11, b-QLMI-12, and b-QLMI-13 at 150 °C constant temperature. Grain sizes and fluid/solid mass ratios are reported in the legend. An ellipse indicates the highest $\sigma_f(T_0)$ values obtained in the experiments (b-QLM-7 and b-QLMI-11). Solid symbols refer to the lowest $\sigma_f(T_0)$ values (b-QLM-8 and b-QLM-12). The other experiments yielded intermediate $\sigma_f(T_0)$ values.

Scientific Technical Report STR 12/07
DOI: 10.2312/GFZ.b103-12079

The addition of approximately 8 % illite did not influence the evolution of $\sigma_f(T_0)$ compared to similar experiments without illite (e.g., b-QLM-7 versus b-QLMI-11). Experiments conducted with identical fluid/solid ratios equal to 5 but with different grain sizes of 63 to 125×10^{-6} m and $< 63 \times 10^{-6}$ m yielded similar $\sigma_f(T_0)$ values (b-QLM-5/b-QLMI-10 versus b-QLM-9/b-QLMI-13). Experiments conducted with the same material and the same fluid/solid ratio but with very small grains ($<< 63 \times 10^{-6}$ m) produced significantly higher $\sigma_f(T_0)$ values (b-QLM-7/b-QLMI-11). As a consequence, the interface between fluid and solid phases is an important factor for the $\sigma_f(T_0)$ evolution.

Electrical Conductivity of Fluids Resulting From Batch Experiments With Flechtinger Sandstone Samples

The electrical conductivity of bulk fluids in contact with Flechtinger sandstone samples increased with time at 70 and 150 °C constant temperature in batch experiments (Figure 4.27). In the first ≈ 20 d at 70 °C, $\sigma_f(T_0)$ increased with time with decreasing rates (b-Fl-15 and b-Fl-16). Further heating to 150 °C led to a further increase of $\sigma_f(T_0)$. From a runtime of ≈ 35 d to the end of the experiments, $\sigma_f(T_0)$ was independent on temperature changes (e.g., $\sigma_f(T_0)$ increased during the third 70 °C stage and decreased during the third 150 °C stage of experiment b-Fl-15). Different pressures ($p_{\max} \approx 0.45 \times 10^6$ Pa and $p = 5 \times 10^6$ Pa) and different fluid/solid mass ratios (5.4 and 3.6) did not significantly influence the evolution and the temperature dependence of $\sigma_f(T_0)$.

The electrical conductivity of a pore fluid sample resulting from a Flechtinger sandstone batch experiment was high ($\sigma_f(T_0) = 0.477$ S/m) compared to electrical conductivities of bulk fluids in contact with the rock material (b-Fl-17, Table 5.5 versus ft-Fl-15 and ft-Fl-16, Figure 4.27). The bulk fluids resulted from experiments with Flechtinger sandstone samples performed in batch reactors at higher temperatures (up to 150 °C) and for longer durations (≈ 90 d) than the experiment yielding the pore fluid sample. The fluid/solid mass ratio of the Flechtinger sandstone experiment that yielded the pore fluid sample was 19.57 g/468.94 g ≈ 0.04 and was thus the lowest of the conducted batch experiments (fluid/solid mass ratios were 5.4 and 3.6 in ft-Fl-15 and ft-Fl-16, respectively). Comparison of the fluid/solid mass ratios highlights the importance of the fluid-solid interface and the fluid/solid mass ratio for the evolution of σ_f in the experiments.

4.2.3 Fluid Chemistry

Evolution of Apparent Normalized Element Losses

Apparent normalized element losses, nl_i (with i = Na, Al, Si, K, Ca), were used to compare batch experiments conducted with different grain sizes, solid materials, fluid/solid mass ratios, and fluid compositions. A comparison of the experiment series with different grain size fractions of quartz and labradorite-andesine revealed that nl_i values of Na, Si, K, and Ca agreed well, but Al values were approximately 10 times higher in the experiment with the larger grain size fraction (b-QL-1 and b-QL-2, Figure 4.28).

Batch experiment series with granular aggregates of quartz and feldspars at 150 °C constant temperature yielded trends of nl_i that suggested the dissolution of ions from the solid material until a quasi steady state was reached and the subsequent removal of ions from the solutions. The apparent normalized Al loss generally decreased with time in the experiments irrespective of the different experimental conditions. There was a decreasing trend of apparent normalized Ca

Scientific Technical Report STR 12/07
DOI: 10.2312/GFZ.b103-12079
Deutsches GeoForschungsZentrum GFZ

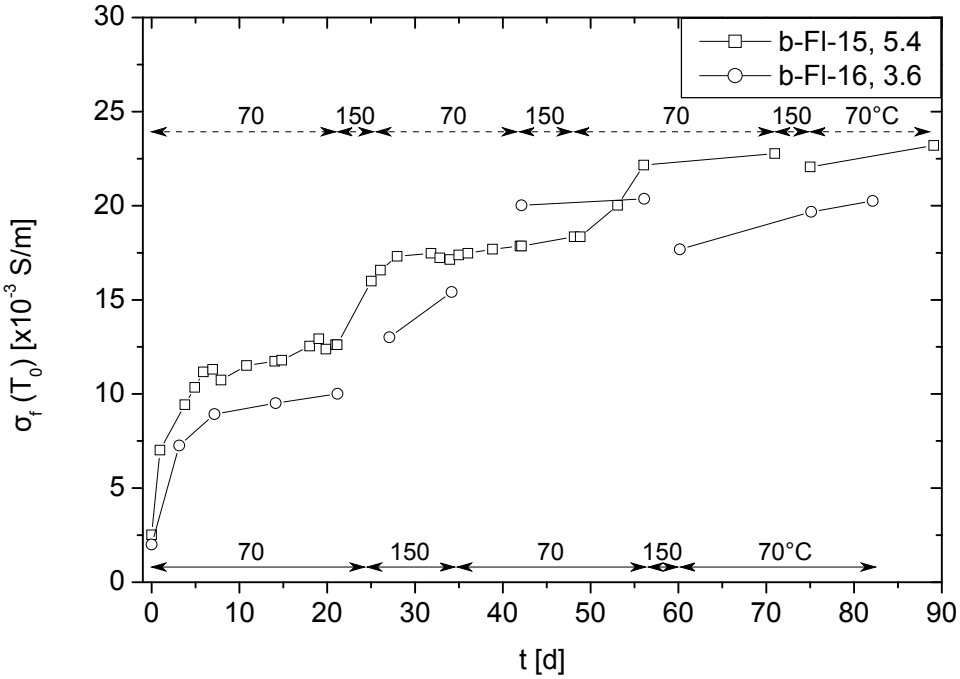

Figure 4.27: Electrical conductivity of fluids, $\sigma_f(T_0)$, as a function of time for Flechtinger sandstone batch experiments b-Fl-15 and b-Fl-16 at 70 and 150 °C. Fluid/solid mass ratios are shown in the legend. The temperature histories of experiments b-Fl-15 and b-Fl-16 are illustrated as dashed and solid arrows, respectively. Experiment b-Fl-15 was performed in a 10×10^{-3} L PTFE batch reactor at a maximum pressure of $\approx 0.45 \times 10^6$ Pa. Experiment b-Fl-16 was conducted in a 300×10^{-3} L BR-300 pressurized batch reactor at a constant pressure of 5×10^6 Pa.

Scientific Technical Report STR 12/07
DOI: 10.2312/GFZ.b103-12079

loss with time, whereas nl_{Na}, nl_{Si}, and nl_K either slightly increased or remained stable (b-QL-1 and b-QL-2). The average pH-value was 9.5 and was stable throughout one experiment series (b-QL-2). Si, K, and Ca initially increased with time in experiments with quartz, labradorite-andesine, and microcline and H_2O and 0.1 mol/L $NaCl_{aq}$ as the starting fluids (b-QLM-3). After approximately 2 d Si and Ca reached constant values and K slightly decreased in the sub series performed with H_2O. In the sub series performed with 0.1 mol/L $NaCl_{aq}$ Si, K, and Ca tend to decrease after approximately 6 d.

Batch experiment series with H_2O and 0.1 mol/L $NaCl_{aq}$ as the starting fluids indicated that concentrations of Si, K, and Ca were independent on salinity, while Al was depleted in the saline solution (b-QLM-3, Figure 4.28). The solid starting materials (ultrasonically cleaned and wet sieved granular QLM aggregates of the grain size fraction 63 to 125 $\times 10^{-6}$ m) yielded $SA_{BET} = 0.0431 \pm 0.0001$ m^2/g. Si values were almost identical in both experiments, K and Ca had slightly higher values in the experiment conducted with the saline solution, whereas nl_{Al} was significantly lower in the saline solution.

The evolution of nl_i (with i = Na, Al, Si, K, Ca) showed a complicated relationship to temperature in a batch experiment with a Flechtinger sandstone sample (b-Fl-16, Figure 4.29). Upon heating from 70 to 150 °C at approximately 24 d run duration, Na, Al, Si, and K values increased, whereas Ca values decreased. A similar behavior, yet less pronounced, can be observed during the second heating from 70 to 150 °C at approximately 56 d. After the first increase of nl_{Al} due to heating, a decreasing trend can be observed from a run duration of approximately 27 d to the end of the experiment.

Apparent normalized element losses were independent on different p-T-histories and fluid/solid mass ratios in batch experiments with Flechtinger sandstone samples (b-Fl-15 versus b-Fl-16, Figure 4.29). Apart from different experimental conditions (pressures were ≈ 0.45 and 5×10^6 Pa, the durations of constant temperature phases were different, and the fluid/solid mass ratios were 5.4 and 3.6, Figure 4.27) the data resulting from the experiment at low pressure (b-Fl-15) confirmed the data resulting from the experiment at higher pressure (b-Fl-16).

The Pore Fluid of a Flechtinger Sandstone Sample

A Flechtinger sandstone pore fluid sample yielded high concentrations of K, Ca, and Cl^- (b-Fl-17, Table 5.5). The composition of the pore fluid sample was analyzed with respect to Na, Mg, Al, Si, K, Ca, F^-, Cl^-, SO_4^{2-}, pH, and $\sigma_f(T_0)$. It was possible to analyze concentrations of dissolved cations and anions as well as pH and $\sigma_f(T_0)$ on aliquot samples, because the cumulative volume of the pore fluid sample was comparatively large (6.5×10^{-3} L). Since a noble gas, Ar, was used for sampling, no contamination of the pore fluid with other fluids occurred. The measured cation and anion concentrations thus reflect the actual pore fluid composition of the Flechtinger sandstone sample held at a constant temperature of 70 °C for 38 d.

Hydrogeochemical Modeling

Several low temperature hydrothermal mineral phases were supersaturated in the fluids resulting from batch experiments at 70 °C according to hydrogeochemical modeling with PHREEQC (Figure 4.30). The concentrations of cations in solution were used as input parameters for the simulations (Table 5.5). The simulations with PHREEQC using the LLNL.dat database yielded many stable mineral phases with saturation indices as high as approximately 350 (e.g.,

Scientific Technical Report STR 12/07
DOI: 10.2312/GFZ.b103-12079

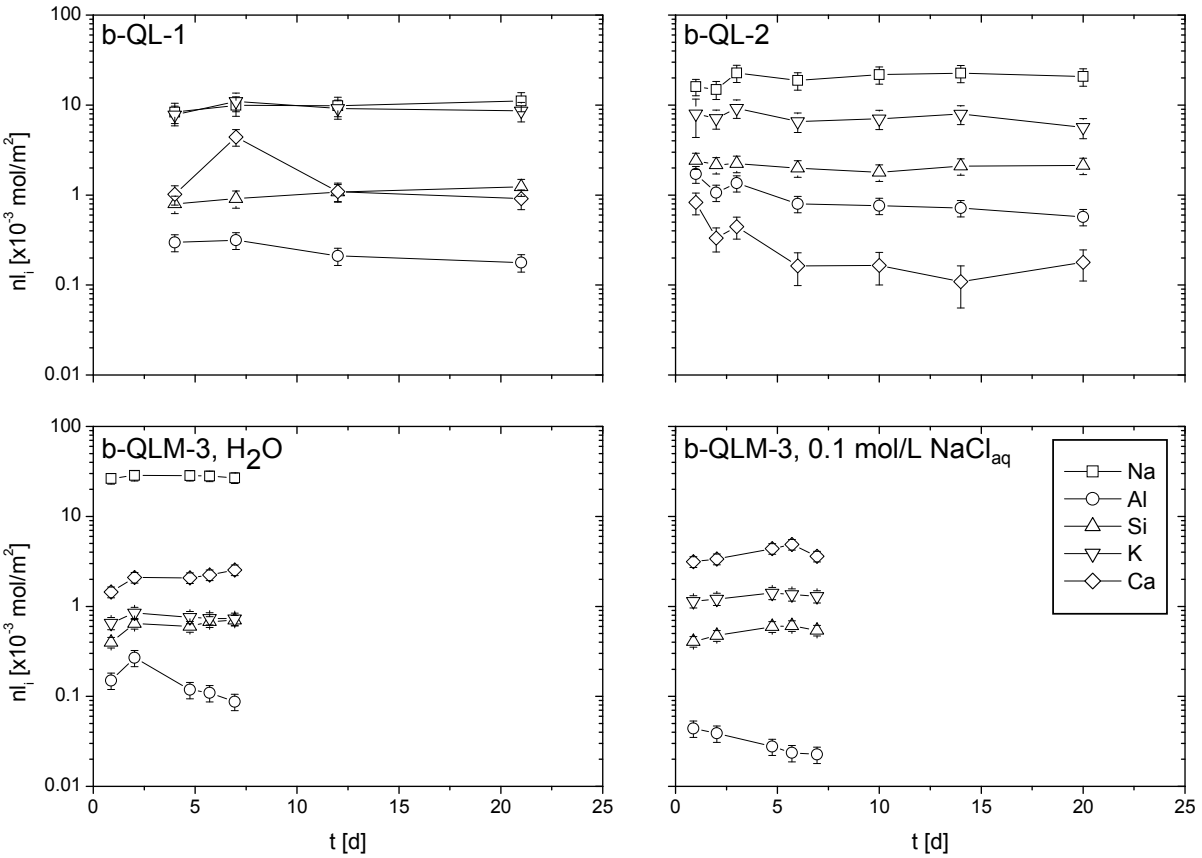

Figure 4.28: Apparent normalized element losses, nl_i, as a function of time in batch experiments b-QL-1, b-QL-2, and b-QLM-3. All experiments were performed at 150 °C. Surface areas were determined using geometric specific surface areas, SA_{geo}, and BET derived specific surface areas, SA_{BET}. SA_{geo} of experiments b-QL-1 and b-QL-2 were 0.01 and 0.025 m^2/g, respectively, SA_{BET} of experiment b-QLM-3 was 0.0431 m^2/g. The average pH-value was 9.5 in experiment series b-QL-2. Fluid/solid mass ratios were 2.5, 5, and 5 in b-QL-1, b-QL-2, and b-QLM-3, respectively.

Scientific Technical Report STR 12/07
DOI: 10.2312/GFZ.b103-12079

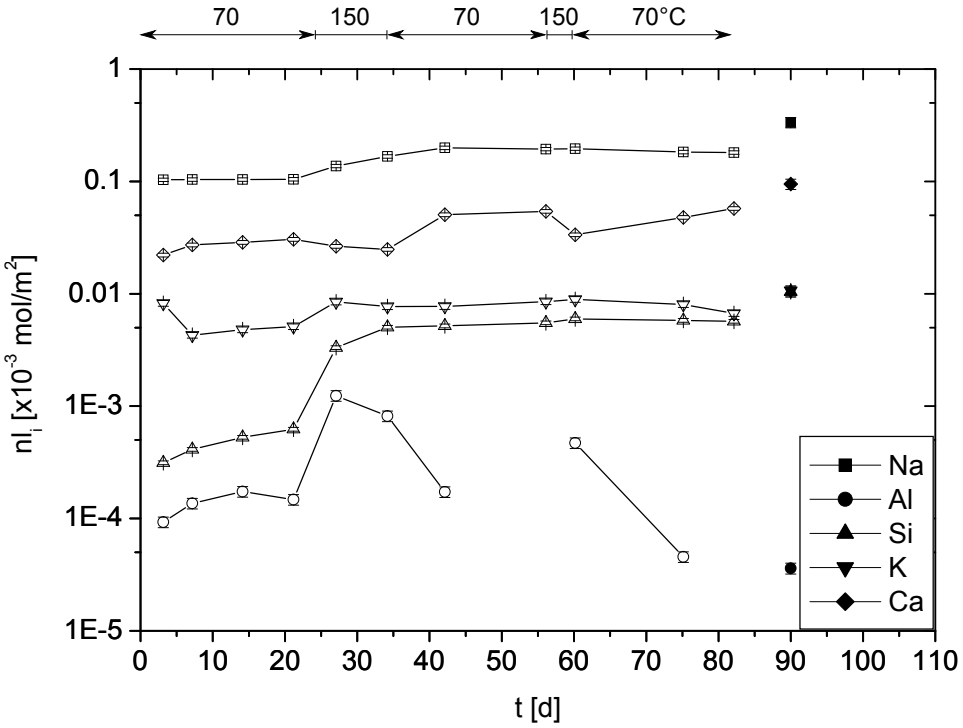

Figure 4.29: Apparent normalized element losses, nl_i, as a function of time in batch experiments b-Fl-15 and b-Fl-16. Solid symbols refer to experiment b-Fl-15, open symbols refer to experiment b-Fl-16. Durations of constant temperature stages in experiment b-Fl-16 are indicated by arrows.

Scientific Technical Report STR 12/07
DOI: 10.2312/GFZ.b103-12079

Table 4.10: MIP results of a Flechtinger sandstone sample resulting from batch experiment b-Fl-16 compared to the starting material.

Sample	**Specific Surface Area** m^2/g	**Average Pore Radius (r50)*** $\times 10^{-6}$ m	**Porosity** %	**Bulk Density** $\times 10^6$ g/m^3	**Apparent Density** $\times 10^6$ g/m^3
mean Fl-SST**	1.527 ± 0.05	0.55 ± 0.06	9.59 ± 0.41	2.38 ± 0.01	2.64 ± 0.02
b-Fl-16	1.492	0.62	10.29	2.37	2.64

* r50 is the pore radius corresponding to the median of cumulative pore volume.
** Table 4.5.
Fl-SST denotes Flechtinger sandstone starting material.

antigorite). Most of these phases are high temperature and high pressure phases indicative of metamorphic conditions. Mineral phases pertaining to low temperature hydrothermal and sedimentary conditions were stable in the fluids: (i) Analcime, laumontite, Mesolite, mordenite, natrolite, scolecite, stilbite, and wairakite, belong to the zeolite group of aluminosilicates. (ii) Beidellite, clinochlore, kaolinite, saponite, and sepiolite are clay minerals. (iii) Celadonite, margarite, muscovite, pyrophyllite, and tobermorite are phyllosilicates partly belonging to the mica group. (iv) Gibbsite and portlandite are hydroxides.

Modeled pH-values were significantly higher than measured pH-values of a Flechtinger sandstone pore fluid sample, which indicates that the simulations did not reflect all reactions in the fluid. Charge balance was achieved by adjusting the pH-value of each solution yielding modeled pH-values in the range of 9.4 to 11.3. The average pH-value of a batch experiment series with quartz and labradorite-andesine granular aggregates (b-QL-2) was 9.5 and is thus within the limits of the modeled pH-values. The measured pH-value of a Flechtinger sandstone pore fluid was 7.47 and is thus in contradiction to the modeled values. This contradiction suggests that OH^- consuming reactions occurred in the pore fluid lowering the pH-value of the solution. The simulations did not account for these OH^- consuming reactions.

4.2.4 Porosity and Specific Surface Area

Mercury Intrusion Porosimetry

Mercury intrusion porosimetry, MIP, of a Flechtinger sandstone sample resulting from a batch experiment (b-Fl-16) showed insignificant differences compared to the starting material except that the porosity was slightly higher in the altered sample (Table 4.10). A small ϕ increase of ≈ 0.3 % was measured compared to the starting material. Complementary porosity measurements by H_2O saturation using Archimedes' Principle (Ulusay and Hudson, 2007) yielded an initial porosity of 9.97 % for the starting material and $\phi = 11.04$ % for the altered material resulting from a batch experiment (b-Fl-16), indicating a ϕ increase of ≈ 1 %. The comparison of the MIP results to the H_2O saturation results suggests but does not clearly proove a small increase in porosity during the batch experiment.

BET Gas Adsorption

The specific surface area determined by BET, SA_{BET}, of a Flechtinger sandstone sample did not change significantly in a batch experiment (b-Fl-16), whereas SA_{BET} of QLM materials

Scientific Technical Report STR 12/07
DOI: 10.2312/GFZ.b103-12079

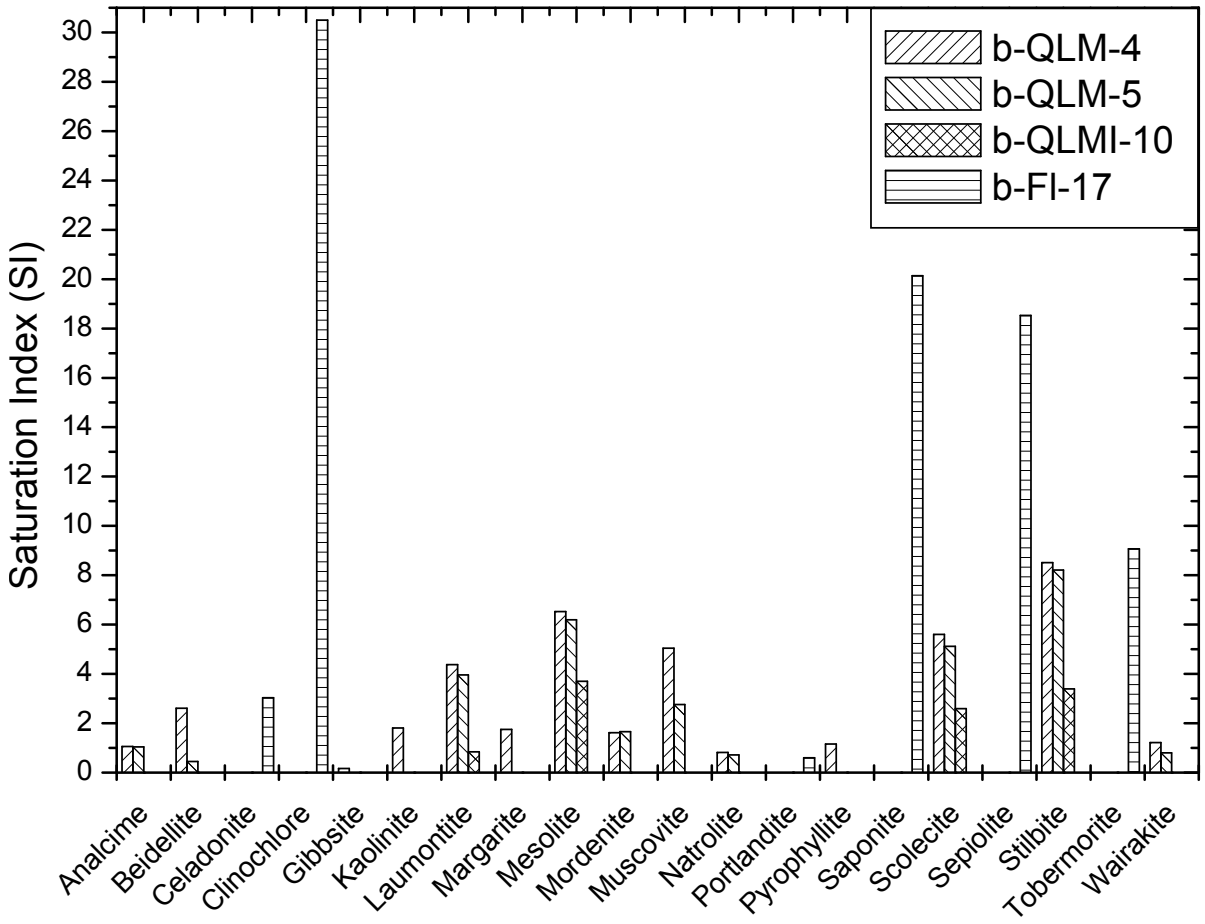

Figure 4.30: Saturation indices calculated with PHREEQC for the fluids resulting from batch experiments b-QLM-4, b-QLM-5, b-QLMI-10, and b-Fl-17. The temperature of the fluid is 70 °C. The PHREEQC built-in LLNL.dat database was used for the simulation. Modeled pH-values were 9.4, 9.4, 10.1, and 11.3 for b-QLM-4, b-QLM-5, b-QLMI-10, and b-Fl-17, respectively.

Scientific Technical Report STR 12/07
DOI: 10.2312/GFZ.b103-12079

Table 4.11: BET results of samples resulting from batch experiments b-Fl-16, b-QLM-4, b-QLM-5, and b-QLM-8 compared to the starting materials.

Sample	**Grain Size** $\times 10^{-6}$ m	**Specific Surface Area** m^2/g	**Adsorbate**
Flechtinger SST starting material	n.a.	2.586 ± 0.004	N_2
QLM starting material	63 to 125	0.0431 ± 0.0001	Kr
QLM starting material	< 63	0.317 ± 0.003	Kr
b-Fl-16	n.a.	2.647 ± 0.003	N_2
b-QLM-4	63 to 125	0.0493 ± 0.0003	Kr
b-QLM-5	63 to 125	0.0379 ± 0.0001	Kr
b-QLM-8	< 63	0.488 ± 0.0003	Kr

n.a. denotes not applicable.

both increased (b-QLM-4 and b-QLM-8) and decreased (b-QLM-5) compared to the starting materials (Table 4.11). The increase of SA_{BET} of the Flechtinger sandstone sample was ≈ 2.4 % relative to the starting material. QLM samples yielded SA_{BET} increases of ≈ 14.4 % (b-QLM-4) and ≈ 53.9 % (b-QLM-8) but also a SA_{BET} decrease of ≈ 12 % (b-QLM-5) relative to the starting material.

4.2.5 Mineralogical Analyses of Solid Samples

X-ray Powder Diffraction

XRD analyses of the QLM starting material and the materials resulting from batch experiments yielded qualitatively similar diffractograms, suggesting that mineralogical differences between the samples were either below the detection limit of the method or not crystalline (Figure 4.31). Two different diffractometers were used for the analyses resulting in diffractograms with a different shape and length along the $°2\theta$-axis. Diffractograms of samples from experiments with different run durations are similar. The diffractograms of the starting material compared to the altered materials are identical with respect to the location of the peaks, which shows that the crystal lattice parameters of the mineral grains did not change significantly in the course of the batch experiments.

Electron Microprobe Analysis

EMPA line scans over small elongated particles on labradorite-andesine grains resulting from a QLM batch experiment did not explicitly show the composition of the alteration features (Figure 4.32). Ca, Si, and Al were slightly depleted in the particles crossed by the line scan (especially at $\approx 3 \times 10^{-6}$ m scan length), while C and S were slightly enriched compared to the background (the original labradorite-andesine surface). Due to the size of the source region for element characteristic X-rays of $\approx 0.35 \times 10^{-6}$ m (Subsection 3.3.3), the displayed relative concentrations of Ca, C, S, Si, and Al resulted from the small particles and the underlying original labradorite-andesine surface.

Scientific Technical Report STR 12/07
DOI: 10.2312/GFZ.b103-12079

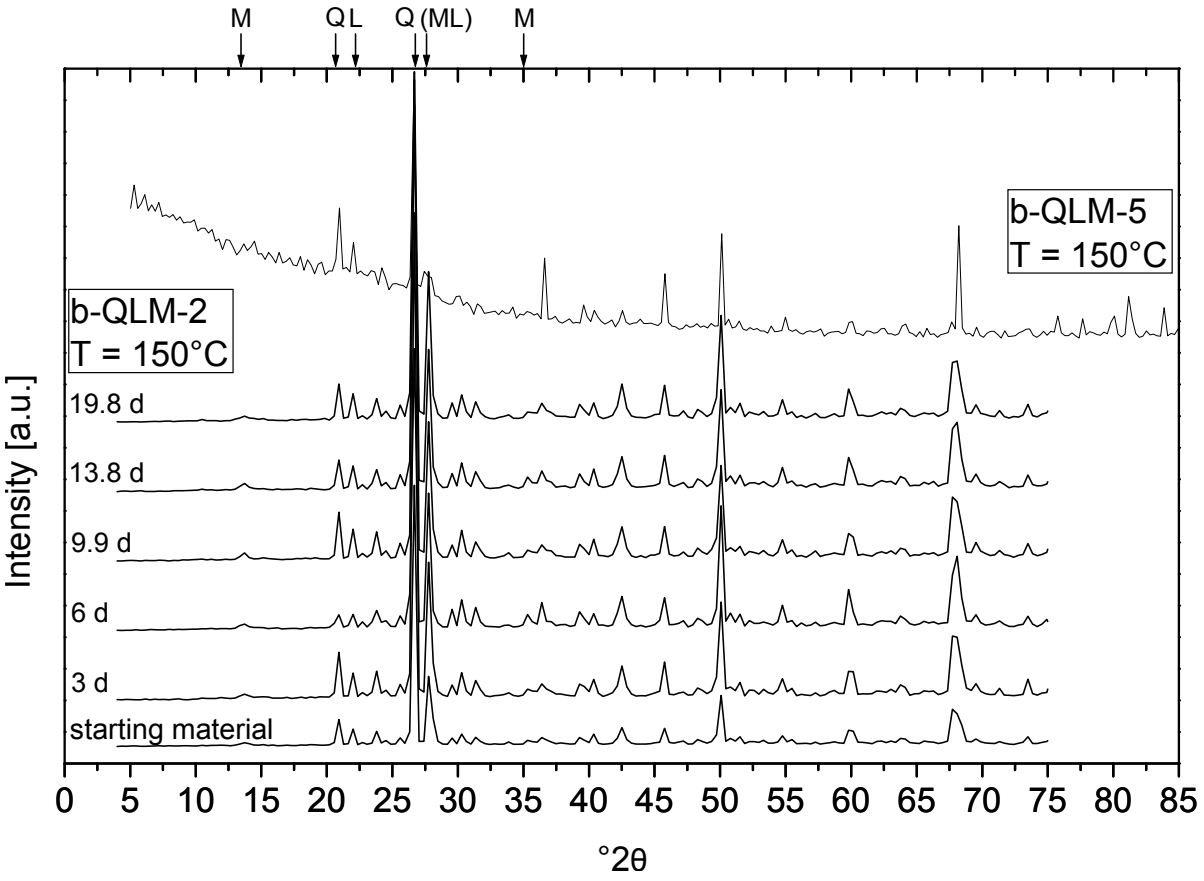

Figure 4.31: Comparison of XRD patterns of the QLM starting material to samples resulting from b-QLM-2 at different run durations as well as to a sample resulting from experiment b-QLM-5 (run duration ≈ 70 d). Intensities in arbitrary units are displayed as a function of $°2\theta$. Characteristic peaks of quartz, labradorite, and microcline, taken from the RRUFF database (Downs, 2006), are indicated by small arrows with Q, L, M notation. The b-QLM-2 samples were analyzed with a Siemens D5000 diffractometer. The b-QLM-5 sample was analyzed with a STOE STADIP diffractometer. The detection limit of the method for individual mineral phases is ≈ 1 %.

Scientific Technical Report STR 12/07
DOI: 10.2312/GFZ.b103-12079

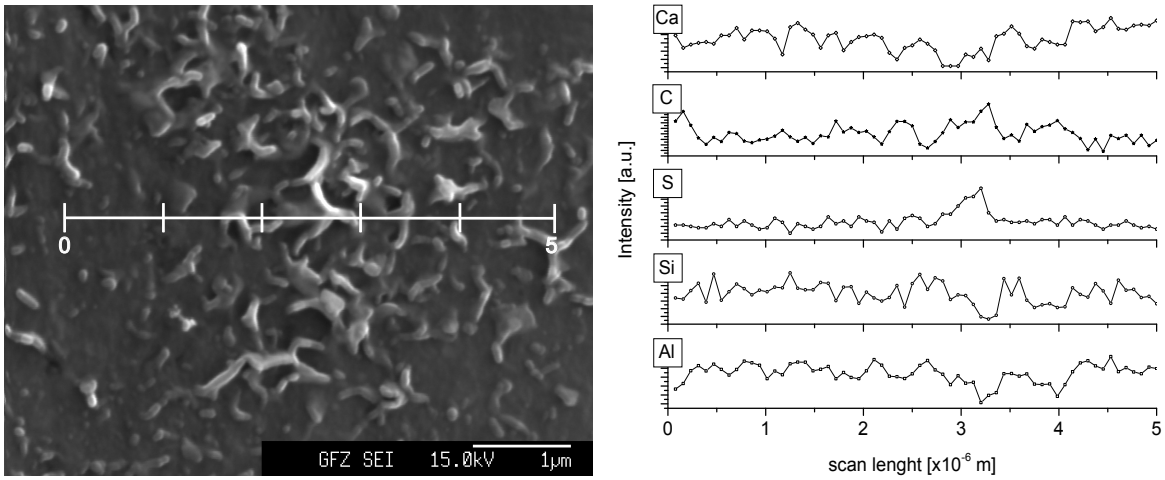

Figure 4.32: EMPA line scan on an altered sample from experiment b-QLM-5. The SE micrograph shows the direction of the line scan starting on the original labradorite-andesine surface and then crossing small elongated structures. The graph displays relative concentrations of Ca, C, S, Si, and Al in arbitrary units as a function of line scan length. The scan was performed with an acceleration voltage of 5×10^3 V and a probe current of 13.5×10^{-9} A.

4.2.6 Microstructural Investigations of Alteration Products by Scanning Electron Microscopy

Alteration features were present on labradorite-andesine and microcline grain surfaces resulting from a batch experiment with granular QLM aggregates (Figure 4.33). Small elongated particles ($< 10^{-6}$ m) precipitated on altered labradorite-andesine surfaces. Altered surfaces of microcline grains show platy aggregates that were absent on the starting material. The small elongated particles were widespread on labradorite-andesine grains, whereas the platy aggregates were rare on altered microcline surfaces. Thus, the small elongated particles on labradorite-andesine surfaces were probably products resulting from the interaction between the minerals and the aqueous solution, but the platy aggregates cannot be clearly labeled as reaction products. The small elongated particles on labradorite-andesine surfaces are similar to those present on altered grain surfaces of the material resulting from flow-through experiments with sandwiched granular QLM aggregates (Figure 4.21).

Scientific Technical Report STR 12/07
DOI: 10.2312/GFZ.b103-12079

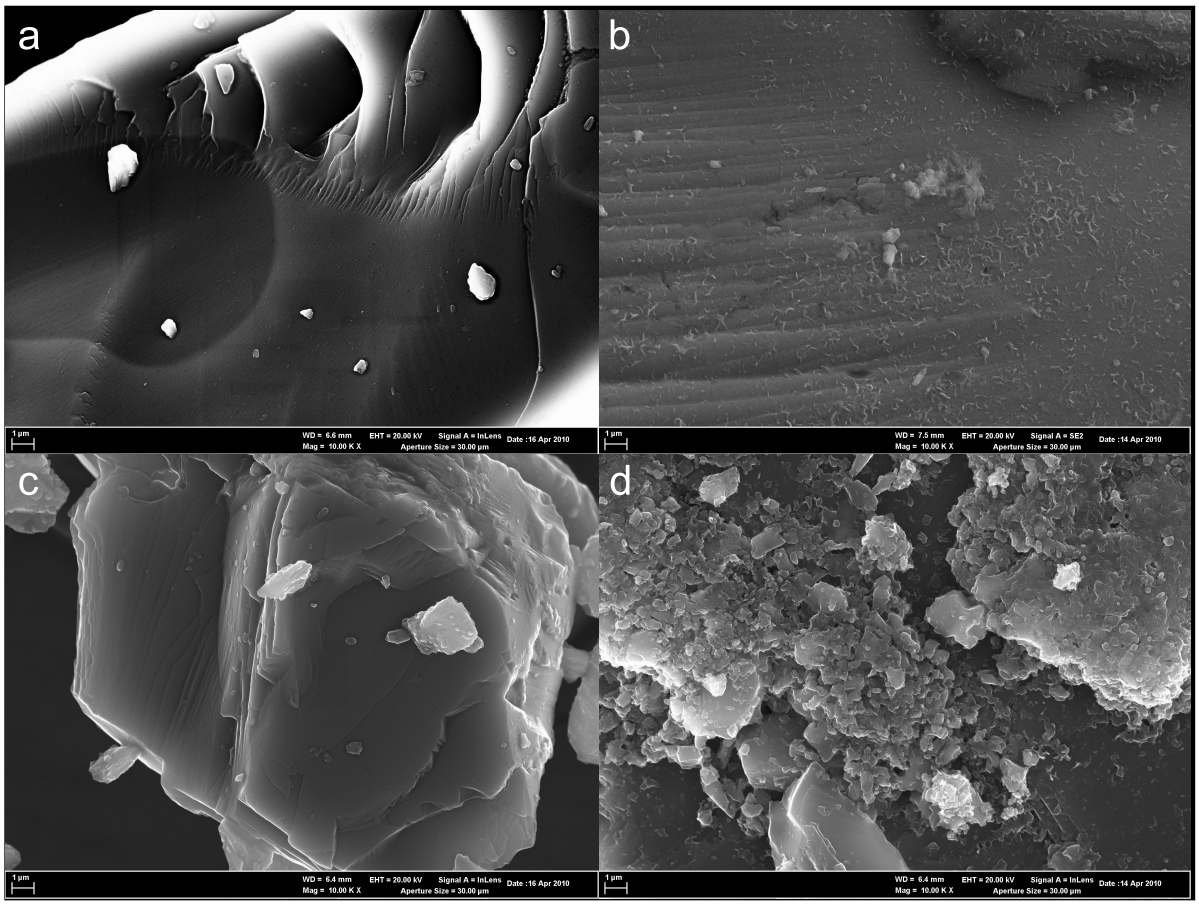

Figure 4.33: SE micrographs of labradorite-andesine (a) and microcline (c) starting materials compared to materials resulting from experiment b-QLM-5 (run duration ≈ 70 d). Altered surfaces of labradorite-andesine (b) and microcline (d) are covered with sub micrometer to micrometer sized elongated and platy aggregates, respectively. The scale bar in the micrographs represent 10^{-6} m.

Scientific Technical Report STR 12/07
DOI: 10.2312/GFZ.b103-12079

Scientific Technical Report STR 12/07
DOI: 10.2312/GFZ.b103-12079

5 Discussion

The electrical conductivity, σ_r, and permeability k evolution of porous samples were used to monitor the evolution of fluid-solid interactions in the flow-through experiments. The electrical conductivity of fluid samples, σ_f, and σ_r were employed as a proxy for time-dependent changes of the chemical state of the fluid-solid systems. Investigation of the permeability evolution at constant temperature and pressure conditions gave insight into the effect of dissolution-precipitation reactions on the hydraulic transport properties of the porous samples.

The questions addressed in the course of the discussion are: (i) Which mineral phases participated in the dissolution-precipitation reactions? (ii) What are the timescales of the reactions in the present fluid-solid system? (iii) Where in the pore space did the reactions take place? (iv) What were the effects of dissolution-precipitation reactions on the permeability of the porous samples? (v) What are the implications of dissolution-precipitation reactions for a real fluid-rock system?

Results of chemical analyses of fluid samples and of investigations of the microstructure of the solid samples are discussed in order to answer the first question. The second question is addressed by the discussion of time-dependent changes of σ_r of Flechtinger sandstone samples at constant temperature and pressure conditions. The results of SEM, MIP, and BET investigations, as well as porosity measurements, and investigations on the formation resistivity factor are discussed in the context of the third question. The fourth question is related to Permeability-porosity relationships and the role of the structure of the pore space for permeability. Finally, the fifth question is discussed with respect to formation damage due to fluid-rock interactions in geotechnical applications.

5.1 Electrical Conductivity as an Indicator for Dissolution-Precipitation Reactions

The use of the electrical conductivity of porous materials as a monitoring tool for dissolution-precipitation reactions in the pore space is based on two hypotheses: (i) The time-dependent changes of σ_r during stagnant phases of the flow-through experiments reflected time-dependent changes of the electrical conductivity of the pore fluids, σ_f. (ii) Dissolution-precipitation reactions changed the concentration of dissolved ionic species, c_i, and thus σ_f.

The first hypothesis has been supported by flow-through experiments with Flechtinger sandstone samples and QLM sandwich samples (Figure 4.1). The electrical conductivity of the porous samples at stagnant conditions of the pore fluid and at constant temperature and pressure showed increases with time with decreasing rates. Flushing the porous samples with H_2O for permeability measurements and/or fluid sampling led to a reset of σ_r to temperature dependent base levels indicating that changes in σ_f were related to changes in σ_r.

Scientific Technical Report STR 12/07
DOI: 10.2312/GFZ.b103-12079
Deutsches GeoForschungsZentrum GFZ

5.1.1 The Electrical Conductivity of Rock Samples in Relation to Electrical Conductivity Models

Moreover, the first hypotheses has been supported by investigations of the response of σ_r to temperature changes. The rationale of these investigations is the following: In two hypothetical cases of porous media with $\sigma_s = 0$ and $\sigma_f = 0$, the simple model for the electrical conductivity of sedimentary rocks (Equation 2.6) becomes $\sigma_r = \phi^m \sigma_f$, and $\sigma_r = \sigma_s$, respectively. In these two extreme cases, the response of σ_r to temperature should be dependent on the response of either σ_f or σ_s to temperature. Thus, the temperature correction coefficient for the electrical conductivity of bulk samples, α_r, should be indicative for the dominant electrical conduction mechanism. In a rock sample, α_r should be dependent on a combination of the responses of σ_f and σ_s to temperature changes. The simple model for the electrical conductivity of sedimentary rocks (Equation 2.6) then yields (Kristinsdóttir et al., 2010):

$$\alpha_r = \frac{\alpha_s \, \sigma_s(T_0) + \alpha_f \, \sigma_f(T_0) \, \phi^m}{\sigma_r(T_0)}. \tag{5.1}$$

The comparison of the relationship between the normalized electrical conductivity and temperature of Flechtinger sandstone samples saturated with water and a saline solution supports this rationale (Figure 5.1). One Flechtinger sandstone sample was initially saturated with H_2O (ft-Fl-12), while the other sample was initially saturated with a 1 mol/L $NaCl_{aq}$ solution (ft-Fl-10). The slopes, i.e., α_r, of linear regressions in the $\sigma_r(T)/\sigma_r(T_0)$ versus T plot were different for both samples ($\alpha_r \approx 0.03\ °C^{-1}$ for ft-Fl-12 and $\alpha_r \approx 0.01\ °C^{-1}$ for ft-Fl-10). The different responses of σ_r of the two samples to heating are indicative for different electrical conduction mechanisms. Electrical conduction through the pore space should have been the dominant conduction mechanism in the sample saturated with the saline solution (ft-Fl-10), whereas a combination of electrical conduction through the pore space and at the fluid-mineral interfaces should have contributed to σ_r in the sample saturated with H_2O (ft-Fl-12).

Furthermore, published data of experiments with sandstones as well as volcanic rocks supports the rationale that the temperature dependence of σ_r should be indicative for the dominant electrical conduction mechanism. Investigations of shaly sandstones saturated with 0.09 to 5.76 mol/L $NaCl_{aq}$ solutions at temperatures ranging from 22 to 200 °C yielded linear temperature correction coefficients that approached $0.033\ °C^{-1}$ for low salinities and $0.024\ °C^{-1}$ for high salinities. At high salinities σ_r was dominated by electrical conduction through the pore space, but at low salinities electrical conduction at the solid-fluid interface mainly contributed to σ_r (Waxman and Thomas, 1974). Experiments with clay-free sandstone samples (Kimachi sandstone) saturated with a 0.001 mol/L KCl_{aq} solution at temperatures ranging from 60 to 180 °C yielded $\alpha_r \approx 0.02\ °C^{-1}$ (Llera et al., 1990). This observation suggests that even when the salinity of the saturating fluid was relatively low, the electrical conduction pathways were concentrated in the pore fluid and not at the solid-fluid interface. Experiments with Fontainebleau sandstone and altered volcanic rocks in the temperature range of 25 to 250 °C yielded $\alpha_r \approx 0.018\ °C^{-1}$ and $\alpha_r \leq 0.035\ °C^{-1}$, respectively. The volcanic rocks included various clay minerals as alteration products. The pore fluids of the experiments were synthetic formation fluids with a low salinity and low electrical conductivity ($\sigma_f \approx 97 \times 10^{-3}$ S/m). The experiments were conducted at confining pressures up to 28×10^6 Pa and pore pressures up to 10×10^6 Pa. It has been concluded that $\alpha_r \approx 0.018\ °C^{-1}$ is an indicator for electrical conduction through the pore space of the Fontainebleau sandstone sample (almost pure SiO_2), and that $0.02 < \alpha_r \leq 0.035\ °C^{-1}$ is an indicator for electrical conduction at the clay mineral-

Scientific Technical Report STR 12/07
DOI: 10.2312/GFZ.b103-12079

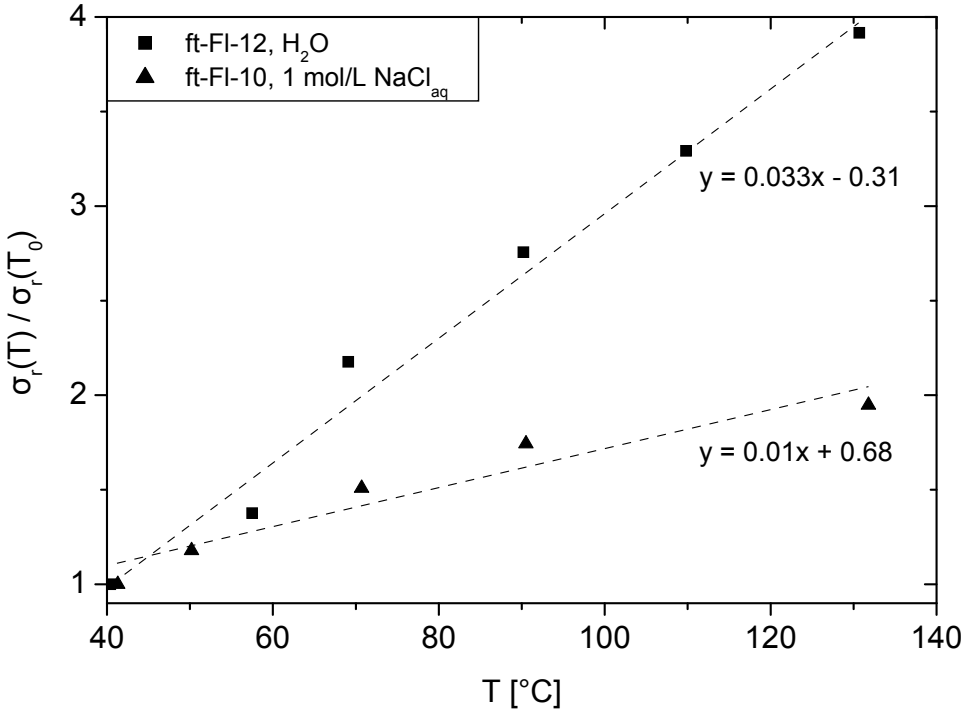

Figure 5.1: Normalized electrical conductivity, $\sigma_r(T)/\sigma_r(T_0)$, of Flechtinger sandstone samples as a function of temperature for flow-through experiments ft-Fl-10 and ft-Fl-12. Experiment ft-Fl-10 was conducted with 1 mol/L $NaCl_{aq}$ solution as the initial pore fluid. ft-Fl-12 was initially saturated with H_2O. Linear regressions are displayed as dashed lines.

Scientific Technical Report STR 12/07
DOI: 10.2312/GFZ.b103-12079

fluid interfaces of the altered volcanic rock samples (Kristinsdóttir et al., 2010). The comparison of these studies suggests that the dominant electrical conduction mechanism is reflected by α_r approaching values of $\alpha_f \approx 0.023\ °C^{-1}$ for electrical conduction through the pore fluid and $\alpha_s \approx 0.040 \pm 0.002\ °C^{-1}$ for electrical conduction at the solid-fluid interface (Sen and Goode, 1992; Revil and Glover, 1998).

In the present study, the mean temperature correction coefficients of rock samples, a porous PTFE sample, and a QLM sandwich sample were in the range of 0.012 ± 0.008 to $0.06 \pm 0.02\ °C^{-1}$ (Table 4.1) and thus covered typical values of α_f and α_s. The mean α_r values of Flechtinger sandstone flow-through experiments with H_2O and 1 mol/L $NaCl_{aq}$ as the starting fluids were in the area of 0.016 and $\approx 0.013\ °C^{-1}$, respectively. The mean α_r values of experiments with Fontainebleau sandstone and porous PTFE samples ($\alpha_r \approx 0.013\ °C^{-1}$) were similar to the Flechtinger sandstone with 1 mol/L $NaCl_{aq}$ as the starting fluid. Following the rationale described above, these α_r values indicate that electrical conduction occurred mainly by electrolytic conduction through the pore space. A QLM sandwich experiment (ft-s-3) yielded $\alpha_r \approx 0.06 \pm 0.02\ °C^{-1}$ in the temperature interval 70 to 150 °C (Table 4.1). One Flechtinger sandstone experiment (ft-Fl-8a) had $\alpha_r \approx 0.038 \pm 0.006\ °C^{-1}$ in the temperature interval 27 to 50 °C, and one Fontainebleau sandstone experiment (ft-Fo-6) yielded $\alpha_r \approx 0.032 \pm 0.005\ °C^{-1}$ in the temperature interval 141 to 164 °C(Figure 4.3). The α_r values suggest that electrical conduction at the fluid-solid interface was the dominant conduction mechanism in these three samples.

Trends of α_r with temperature were opposite for clay-bearing Flechtinger sandstone samples and clay-free Fontainebleau sandstone and PTFE samples (Figure 4.3). Calculated values of α_r (Equation 4.1) decreased with temperature in the experiments with Flechtinger sandstone samples irrespective of the initial pore fluid (H_2O in ft-Fl-8, ft-Fl-9, and ft-Fl-12 or 1 mol/L $NaCl_{aq}$ in ft-Fl-10). The clay-free Fontainebleau sandstone and PTFE samples (ft-Fo-6, ft-Fo-7, and ft-P-7) showed an increasing trend of α_r with temperature. It is so far not known whether these opposite trends of α_r with temperature result from sample-dependent electrical conduction mechanisms or from experimental artifacts. The finding that α_r decreases with temperature in the Flechtinger sandstone experiments with H_2O as the initial pore fluid is controversial, because the effect of σ_s on σ_r should increase with temperature in a clay-bearing material as the Flechtinger sandstone saturated with a fluid with low σ_f (Revil et al., 1998). With H_2O as the pore fluid, α_r should be in the range of α_s, because interface-effects between clay minerals and pore fluid have a significant contribution to σ_r in the low σ_f region (e.g., Waxman and Smits, 1968; Rink and Schopper, 1976; Sen et al., 1988; Glover et al., 1994; Revil et al., 1998; Glover et al., 2000; Leroy and Revil, 2004; Roberts and Wildenschild, 2004; Taylor and Barker, 2006; Leroy and Revil, 2009). A possible explanation for this behavior is that highly soluble minerals dissolved quickly during the heating of the Flechtinger sandstone samples leading to a larger contribution of σ_f to σ_r.

However, models for the electrical conductivity of clay-bearing sandstones indicated that σ_r of Flechtinger sandstone samples was not only dependent on σ_f, but also on the electrical conduction at fluid-mineral interfaces. The tested models agreed generally well with the experimental data obtained from fluid exchange experiments (Figure 5.2). In a plot of σ_r as a function of σ_f, a fit to the data yielded the formation resistivity factor for shaly sandstones, F^* (Table 5.2), and geometrical parameters of the pore space as the cementation exponent m, which is related to the electrical tortuosity τ_e of the pore space (Equation 2.5). The parameters for the models were mostly obtained from the literature (Table 5.1).

Scientific Technical Report STR 12/07
DOI: 10.2312/GFZ.b103-12079
Deutsches GeoForschungsZentrum GFZ

Table 5.1: Parameters of models for the electrical conductivity of Flechtinger sandstone samples resulting from fluid exchange experiments ft-Fl-11 and ft-Fl-12.

Parameter	**Model 1**	**Model 2**	**Model 3**	**Model 4**	**Source**
ϕ	0.1	0.1	0.1	0.1	measured*
m	1.9	1.9	1.9	1.9	linear regression**
μ_{dl} [$\times 10^{-3}$ Sm^2/eq]		1.93	1.93	1.93	Sen et al. (1988)
Q_v [eq/m^3]	510	510	510	510	Waxman and Smits (1968), Sen et al. (1988)
B [$\times 10^{-3}$ Sm^2/eq]	1.85				Equation 2.8
C [$\times 10^{-3}$ Sm^2/eq]		1.37			Sen et al. (1988)
E [$\times 10^{-5}$ Sm^2/eq]		3.92			Sen et al. (1988)
σ_s [S/m]			$\approx$0.02		y-axis intercept at $\sigma_f = 0$***
σ_s [S/m]				$\approx$0.07	Equation 2.14

Model 1: Waxman and Smits (1968), Equations 2.7 and 2.8.
Model 2: Sen et al. (1988), Equation 2.9.
Model 3: Glover et al. (2000)a, Equations 2.12 and 2.13.
Model 4: Glover et al. (2000)b, Equations 2.12, 2.13, and 2.14.
* by H_2O saturation using Archimedes' Principle after Ulusay and Hudson (2007).
** $\phi^m = \sigma_r/(\sigma_f + \sigma_s)$, Equation 2.6.
*** Equation 2.6.

A Comparison of the model results (Table 5.2) to the results of Flechtinger sandstone flow-through experiments (Table 4.2) shows that the compared models approximate the measured $\sigma_r(T)$ values well, although the physical principles of the models are quite different (Section 2.1.1). The relative differences between the modeled values and the measured values are larger at low σ_f values (up to $\approx$110 %) than at high σ_f values (up to $\approx$6 %).

Clay-bearing sandstones and other systems with surface charges like ion exchange resins, suspensions of charged polystyrene balls, and clay suspensions generally exhibit a pronounced curvature convex upwards in a plot of σ_r as a function of σ_f (e.g. Waxman and Smits, 1968; Sen et al., 1988; Glover et al., 2000; Taylor and Barker, 2006). A simple model adds a constant surface conductivity term, σ_s, to Archie's law (Equation 2.6) and thus yields a straight line with slope $1/F$ or ϕ^m and a y-axis intercept equal to σ_s at zero fluid conductivity. Thus, this model is only applicable when $\sigma_f >> \sigma_s$ (as Archie's law).

Archie's law has been extended by the product of the mobility of ions in the double layer ($B = \mu_{\mathrm{dl}}$) and the volume density of charges Q_v (Model 1, Equation 2.7). This product equals the electrical conductivity of the clay minerals. Q_v is constant, and B is a function of σ_f (Equation 2.8). Implications of this model are that the electrical conduction through the pore space follows the same tortuous pathways as the electrical conduction at the clay mineral-fluid interface and that B (or equivalently μ_{dl}) increases with σ_f (Waxman and Smits, 1968). The latter has been regarded as contradictory because the double layer thickness decreases with increasing σ_f (Revil et al., 1998) leading to a closer packing of charge carriers near the mineral surface and thus to a decreasing mobility of ions in the double layer (Johnson and Sen, 1988; Sen et al., 1988; Ruffet et al., 1995).

Empirically derived geometrical fitting parameters have been introduced for electrical conduction through the pore space and at the mineral-fluid interface (Model 2, Equation 2.9). The

Scientific Technical Report STR 12/07
DOI: 10.2312/GFZ.b103-12079
Deutsches GeoForschungsZentrum GFZ

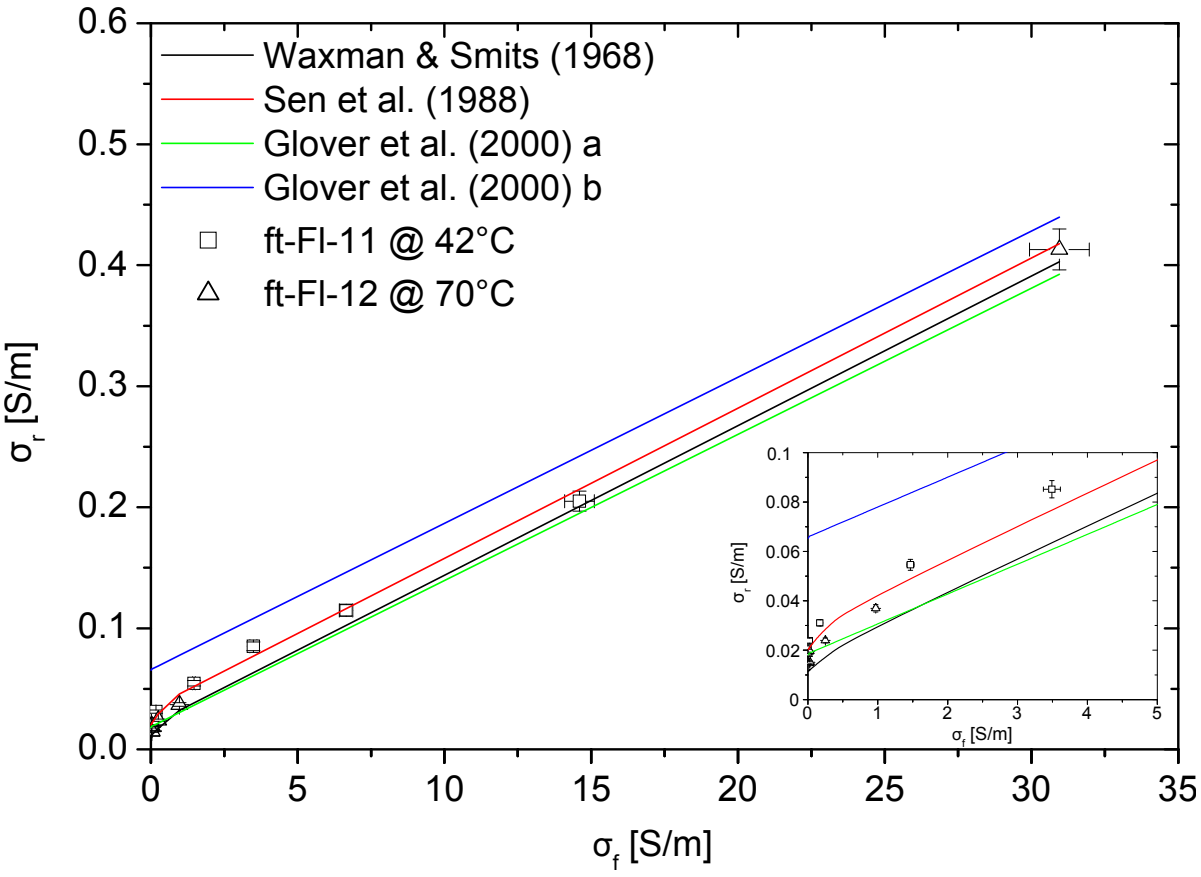

Figure 5.2: Electrical conductivity of Flechtinger sandstone samples, σ_r, as a function of the electrical conductivity of pore fluids, σ_f, for fluid exchange experiments ft-Fl-11 and ft-Fl-12. Experiment ft-Fl-11 was conducted at approximately 42 °C but experiments ft-Fl-12 was carried out at approximately 70 °C. Results of models for the electrical conductivity of sedimentary rocks are displayed as solid lines. Suffixes a and b denote the model by Glover et al. (2000) with a graphically estimated σ_s term at $\sigma_f = 0$ S/m and with $\sigma_s = \phi^m\, m\, \mu_{\mathrm{dl}}\, Q_v$ (Equation 2.14), respectively. The parameters for the models were derived from a linear regression of the σ_r versus σ_f data (Equation 2.6) or from the literature (Table 5.1). The inset shows the low σ_f region with $\sigma_f \leq 5$ S/m.

Scientific Technical Report STR 12/07
DOI: 10.2312/GFZ.b103-12079

Table 5.2: Results of models for the electrical conductivity of Flechtinger sandstone samples in fluid exchange experiments ft-Fl-11 and ft-Fl-12.

$\sigma_f(T)$	**Model 1**		**Model 2**		**Model 3**	**Model 4**
	$\sigma_{\mathrm{r,calc}}$	F^*	$\sigma_{\mathrm{r,calc}}$	F^*	$\sigma_{\mathrm{r,calc}}$	$\sigma_{\mathrm{r,calc}}$
S/m	S/m		S/m		S/m	S/m
0.0035 ± 0.0001	0.011		0.02		0.02	0.04
0.0219 ± 0.0008	0.012	40	0.021	22	0.02	0.04
0.171 ± 0.006	0.016	41	0.027	26	0.022	0.042
0.97 ± 0.03	0.032	48	0.046	42	0.051	0.078
1.47 ± 0.05	0.041	58	0.054	60	0.038	0.057
3.5 ± 0.1	0.069	70	0.082	72	0.062	0.082
6.6 ± 0.2	0.109	80	0.122	79	0.101	0.12
14.6 ± 0.5	0.205	83	0.219	82	0.197	0.217
31 ± 1	0.403	83	0.418	82	0.413	0.44

model keeps the volume density of charges Q_v constant and it accounts for different tortuosities of σ_f and σ_s (Sen et al., 1988). The model states that the pronounced convex upwards curvature in the low σ_f region of a σ_r versus σ_f plot (Figure 5.2) arises from changes of dominant electrical current pathways with increasing σ_f that shift from the mineral-fluid interface to the pore space and therefore are subjected to different tortuosities (Sen and Goode, 1992).

An effective medium model with variable exponents (m and p) accounts for different tortuosities pertaining to σ_f and σ_s (Glover et al., 2000). The model has been validated against experimental data resulting from fluid exchange experiments conducted with several porous media consisting of semiconductor Cu_2O particles saturated with $NaCl_{aq}$ solutions ranging in salinity from 0 to 2 mol/L. Furthermore, the applicability of the model to clay-bearing sandstones has been shown. The Models 3 and 4 yield a very small convex upwards curvature in the σ_r versus σ_f plot as well as lower and upper bounds for the measured data when a graphically estimated σ_s term was used (as in Equation 2.6) or when σ_s was calculated by Equation 2.14 (Figure 5.2).

The tested models yielded similar values of F^* (the inverse of the slope in a σ_r versus σ_f plot) of approximately 83 at high σ_f values equal to the Archie's law formation resistivity factor, $F = a\phi^{-m}$, with $a = 1$. Model 1 and Model 2 yielded small F^* values at low σ_f values and a constant value of ≈ 83 at $\sigma_f > 14.6$ S/m. Models 3 and 4 yielded a constant F^* of ≈ 83.

To summarize, all tested models agree with the experimental data (Figure 5.2). Uncertainties were not known of the model parameters that were derived from a linear regression of the σ_r versus σ_f data and from the literature. Yet, the best fit to the data was achieved by Model 2 (Sen et al., 1988) that represents the convex upwards curvature of the low σ_f region, the non-zero y-axis intercept, and the slope of the high σ_f region (Figure 5.2). However, the empirical Model 1 (Waxman and Smits, 1968) and the effective medium Model 3 (Glover et al., 2000) with a graphically estimated σ_s term yield good fits as well. It has been shown that Model 1 involves physical inconsistencies. The common feature of Model 2 and Model 3 is that electrical conduction through the pore space and electrical conduction at the mineral-fluid interface follows different pathways. This implies that different tortuosities pertaining to σ_f and σ_s must be taken into account when the low σ_f region in a σ_r versus σ_f plot is investigated. The Flechtinger sandstone pore fluid with $\sigma_f(T) = 0.97$ S/m (b-Fl-17, Table 5.5) plots in the

Scientific Technical Report STR 12/07
DOI: 10.2312/GFZ.b103-12079
Deutsches GeoForschungsZentrum GFZ

low σ_f region as indicated by the convex upwards curvature of the σ_r versus σ_f plot (Figure 5.2). Thus, electrical conduction at the mineral-fluid interfaces contributed significantly to σ_r in the experiments with Flechtinger sandstone samples.

5.1.2 Consistency Between the Electrical Conductivity and the Chemical Composition of Fluid Samples

The second hypothesis (dissolution-precipitation reactions changed the concentration of dissolved ionic species, c_i, and thus σ_f) is supported by the time-dependent evolution of bulk fluids in batch experiments. The electrical conductivity of bulk fluids increased in the beginning of the batch experiments indicating time-dependent dissolution of mineral phases. Some batch experiments with granular QLM(I) aggregates yielded decreasing trends of $\sigma_f(T_0)$ with time pointing to the removal of ions from the solutions due to precipitation of solid phases (Figure 4.26). EMPA and SEM investigations showed secondary solid phases on grains resulting from one batch experiment (b-QLM-5, Figures 4.32 and 4.33).

Time-dependent changes of σ_r of Flechtinger sandstone samples were consistent with the following scenario for the evolution of the fluid-rock system: Approach of a quasi-equilibrium at the first 70 °C stage, supersaturation due to heating to 150 °C, and approach of the 70 °C quasi-equilibrium from supersaturated conditions during the second 70 °C stage (Figure 4.1b). Stepwise heating and cooling was also performed in batch experiments (b-Fl-15 and b-Fl-16) in analogy to the stepwise heating and cooling procedure performed in flow-through experiments. The discontinuously measured time-dependent evolution of $\sigma_f(T_0)$ at the first 70 and 150 °C constant temperature stages showed a qualitatively similar behavior as σ_r in the flow-through experiment.

Moreover, the time-dependent evolution of $\sigma_f(T_0)$ exhibited features indicative for the progress of overall dissolution-precipitation reactions in Flechtinger sandstone batch experiments (Figure 4.27). The electrical conductivity of the bulk fluids exhibited no decreasing trend during the second 70 °C stage but increased steadily in subsequent heating and cooling cycles indicating that no simple kinetic dissolution reaction, which should obey an Arrhenius relationship, occurred in the Flechtinger sandstone batch experiments but that a complex interaction of dissolution and precipitation took place that changed with time. Examples of the evolution of rock-water systems with respect to concentration of different dissolved ionic species and stable mineral phases show that intermediate species occur during overall reactions in rock-water systems when the evolutions of the systems are kinetically controlled (Mueller and Saxena, 1977; Busenberg, 1978; Lin and Clemency, 1980; Lasaga, 1983). The $\sigma_f(T_0)$ evolution reflected the overall concentration of dissolved ions in solution. Individual reactions leading to intermediate species cannot be followed by σ_f monitoring. A scenario can be proposed that in the first two constant temperature stages of the batch experiments $\sigma_f(T_0)$ reflected the approach of a quasi steady-state with respect to the dissolution of initially accessible minerals. Cooling to 70 °C did not lead to decreasing trends of $\sigma_f(T_0)$, as in the flow-through experiment (ft-Fl-9), but to a further increase requiring the dissolution of more minerals than were initially available. Such a scenario is consistent with the development of micro cracks due to cooling which yields more minerals exposed to the solvent than in the initial state. The further time-dependent evolution of $\sigma_f(T_0)$ is then controlled by competing effects of dissolution and precipitation (e.g., Lasaga, 1983).

Chemical analyses of the fluids resulting from Flechtinger sandstone batch experiments indicated that the evolution of $\sigma_f(T_0)$ of the Flechtinger sandstone pore fluid and the batch

Scientific Technical Report STR 12/07
DOI: 10.2312/GFZ.b103-12079

reactor fluids was dependent on the dissolution and precipitation of sparingly soluble mineral phases, like quartz and feldspars, as well as on the dissolution of highly soluble phases, like chlorides and sulfates. The chemical analysis of the Flechtinger sandstone pore fluid (b-Fl-17) showed that the dissolution of phases other than the main mineral phases of the rock led to high values of $\sigma_f(T_0) = 0.477$ S/m (Table 5.5). Compared to that, experiments performed with the main mineral phases (i.e., quartz, feldspars, and illite) yielded significantly lower values of $\sigma_f(T_0) \approx 15 \times 10^{-3}$ S/m in the batch reactor fluid (Figure 4.26). The Flechtinger sandstone pore fluid sample showed significantly higher K and Ca concentrations ($c_{\mathrm{K}} \approx 19 \times 10^{-3}$ mol/L and $c_{\mathrm{Ca}} \approx 8 \times 10^{-3}$ mol/L) compared to fluids resulting from the QLM(I) experiments ($c_{\mathrm{K}} \approx 0.1 \times 10^{-3}$ mol/L and $c_{\mathrm{Ca}} \approx 0.2 \times 10^{-3}$ mol/L). Moreover, relatively high concentrations of Cl^- ($c_{\mathrm{Cl}} \approx 81 \times 10^{-3}$ mol/L) were observed in the pore fluid sample.

A combined interpretation of a Flechtinger sandstone batch experiment (b-Fl-17) and flow-through experiments (ft-Fl-9 and ft-Fl-12) yielded constraints for the steady state σ_f value of a Flechtinger sandstone pore fluid that was approached at 70 °C in a flow-through experiment. A pore fluid sample from a Flechtinger sandstone batch experiment underwent a transient increase of σ_r at 70 °C (Figure 4.25). The electrical conductivity of the rock sample, measured by impedance spectroscopy in a two-electrodes arrangement, had a maximum value of approximately 25×10^{-3} S/m at ≈ 70 °C. The electrical conductivity of the pore fluid was $\sigma_f(T_0) = 0.477$ S/m corresponding to $\sigma_f(T) = 0.97$ S/m at $T = 70$ °C (Equation 2.2). An aqueous solution of 0.0432 mol/L NaCl with the same electrical conductivity as the Flechtinger sandstone pore fluid sample was flushed into a Flechtinger sandstone core at 70 °C in a flow-through experiment (ft-Fl-12) resulting in a measured $\sigma_r \approx 37 \times 10^{-3}$ S/m (Table 4.2). The constant value, that σ_r approached at a constant temperature of 70 °C in another flow-through experiment (ft-Fl-9), was 37.2×10^{-3} S/m (Figure 4.1b) and was thus almost identical to the value obtained in the fluid exchange experiment. The conclusion from the analogy of the evolution of the electrical conductivity of Flechtinger sandstone samples at 70 °C in the batch and flow-through experiments is that the evolution of the pore fluids in both experiment types was similar regardless of different pressure conditions (pore and confining pressure were approximately 0.1×10^6 Pa in the batch experiment, whereas the pore pressure was 5×10^6 Pa and the confining pressure was 10×10^6 Pa in the flow-through experiment). The difference in σ_r at 70 °C in the batch and the flow-through experiment (25×10^{-3} S/m in b-Fl-17 versus 37.2×10^{-3} S/m in ft-Fl-9) arose from additional contact resistances in the two-electrodes arrangement of the batch experiment compared to the four-electrodes arrangement of the flow-through experiment.

Comparison to the literature suggests that the transient behavior of σ_r was independent of the evolution of the electrical conductivity of mineral-fluid interfaces, σ_s. Investigations of shaly sandstones filled with a NaCl-bearing pore fluid have shown that σ_s is constant if the concentration of dissolved ionic species, $c_i > 10^{-3}$ mol/L (Revil et al., 1998). The sum of c_i, with i = Na, Al, Si, K, Ca, was higher than 10^{-3} mol/L in the fluid samples from a Flechtinger sandstone and a QLM sandwich flow-through experiment ($c_i \approx 25.9 \times 10^{-3}$ mol/L in ft-Fl-9 and 4.4×10^{-3} mol/L in ft-s-3).

The decreasing rate of the σ_r increase with time was indicative for a decreasing driving force (i.e., decreasing chemical potential) for dissolution as the fluids approached a chemical equilibrium with respect to dissolved ionic species (e.g., Figures 4.1 and 4.27). Published results of batch experiments with Soxhlet extracted and as received clay- and carbonate-bearing Pictured Cliffs sandstone samples at approximately 25 °C with tap water as the starting fluid support this interpretation. The rate of increase of σ_r with time was larger in the as

Scientific Technical Report STR 12/07
DOI: 10.2312/GFZ.b103-12079
Deutsches GeoForschungsZentrum GFZ

received material compared to the Soxhlet extracted material from which relatively easily soluble minerals were removed before the experiment. Steady state conditions of σ_r and σ_f were reached after approximately 187 d. A three step process was suggested for the observed fluid-rock interactions: inward diffusion of tap water through the pore structure of the rock, dissolution and outward diffusion of water-soluble material lining the pores of the rock, and clay-water exchange. Clay-water exchange was concluded to have been the dominant factor for the increase of σ_f after approximately 1 d run duration of the experiments (Piwinskii and Weed, 1976).

Minerals with different solubilities affected σ_f and thus σ_r in different phases of the experiments. A comparison of the σ_r evolution at 70 °C before and after fluid sampling in a Flechtinger sandstone flow-through experiment shows two phases (ft-Fl-9a and ft-Fl-9b in Figure 4.2). The rate of increase of σ_r with time was smaller after the fluid sampling (ft-Fl-9b) than before the fluid sampling (ft-Fl-9a) although the starting conditions were identical (H_2O as the pore fluid, 70 °C). The analysis of anions in the pore fluid sample resulting from a Flechtinger sandstone batch experiment yielded high Cl^- concentrations of $\approx 81 \times 10^{-3}$ mol/L (Table 5.5). However, chlorides were not found in the Flechtinger sandstone starting material by XRD, XRF and SEM investigations (Table 3.1 and Figure 4.19). As a consequence, there probably were small amounts of chlorides in the Flechtinger sandstone starting material, not detectable by the former methods, that dissolved time-dependently and thus contributed to the transient increase of σ_f and σ_r. Relatively easy soluble minerals may have been removed by flushing out the pore fluid during fluid sampling leaving behind the sparingly soluble silicates of the bulk rock which led to a smaller rate of increase of σ_r with time.

Pure dissolution of quartz and feldspars in QLM sandwich flow-through experiments yielded comparatively low values of σ_r compared to σ_r of the clay-bearing Flechtinger sandstone samples. The QLM sandwich experiment (ft-s-3) in which the minerals were present in the relative mass proportions of the Flechtinger sandstone (Figures 4.1c and 4.2) showed a maximum σ_r value at 70 °C of 0.27×10^{-3} S/m. This value is approximately 140 times lower than the maximum σ_r value at 70 °C obtained in a Flechtinger sandstone flow-through experiment (ft-Fl-9). The electrical conductivity of a fluid sample, $\sigma_f(T_0)$, resulting from another QLM sandwich flow-through experiment (ft-s-4) was only lower by a factor of approximately 10 compared to a Flechtinger sandstone pore fluid sample (b-Fl-17) highlighting the significance of σ_s in the clay-bearing Flechtinger sandstone compared to the clay-free QLM material (Tables 5.4 and 5.5).

However, the applicability of $\sigma_f(T_0)$ as a proxy for dissolution-precipitation reactions was limited because the evolution of $\sigma_f(T_0)$ was dependent on the specific conditions of the experiments as the grain sizes of the starting material, the specific surface areas of the starting materials, fluid/solid mass ratios, the presence of minor amounts of highly soluble mineral phases in Flechtinger sandstone samples, and different crystallization thresholds in pores compared to bulk fluids. These limitations were illustrated by the following observations:

(i) Electrical conductivities of fluids resulting from batch experiments with Flechtinger sandstone samples were not directly comparable to σ_f of fluids resulting from experiments with granular QLM aggregates because the specific surface area of the rock samples were higher (Table 4.11). The maximum electrical conductivity of fluids resulting from batch experiments with Flechtinger sandstone samples (b-Fl-15 and b-Fl-16) was $\sigma_f(T_0) \approx 22 \times 10^{-3}$ S/m and was thus slightly higher than the maximum $\sigma_f(T_0) \approx 15 \times 10^{-3}$ S/m obtained in experiments conducted with quartz, labradorite-andesine, microcline, and/or illite grains (b-QLM-7 and b-QLM-11). The granular aggregates experiments were performed at a constant temperature of

Scientific Technical Report STR 12/07
DOI: 10.2312/GFZ.b103-12079

150 °C whereas the Flechtinger sandstone experiments were performed at 70 °C most of the time (Figures 4.26 and 4.27). It is likely that the higher $\sigma_f(T_0)$ of Flechtinger sandstone batch experiments (b-Fl-15 and b-Fl-16) resulted from the higher specific surface area of the Flechtinger sandstone starting material compared to the QLM starting material. A Flechtinger sandstone pore fluid sample was obtained from an experiment with the lowest fluid/solid mass ratio. The pore fluid sample showed the highest $\sigma_f(T_0)$ value of all conducted experiments (0.477 S/m). This $\sigma_f(T_0)$ value is approximately 21 times higher than the maximum $\sigma_f(T_0)$ values obtained in Flechtinger sandstone batch experiments (b-Fl-15 and b-Fl-16) and approximately 32 times higher than the maximum $\sigma_f(T_0)$ values obtained in QLM(I) batch experiments (b-QLM-7 and b-QLMI-11). The fluid/solid mass ratio of the Flechtinger sandstone experiment that yielded the pore fluid was approximately 0.04 whereas the fluid/solid mass ratios of the other experiments were much higher (approximately 5.4, 3.6, and 5 for b-Fl-15, b-Fl-16, and b-QLM-7/b-QLMI-11, respectively). These observations suggest a correlation between low fluid/solid mass ratios and high σ_f values.

(ii) Chemical fluid analyses have shown that chlorides and sulfates were present in the Flechtinger sandstone pore fluid, but not in fluids resulting from QLM(I) batch experiments. Chlorides and sulfates have a significantly higher solubility than the main mineral phases (quartz, feldspar, and illite) of the Flechtinger sandstone. The QLM(I) material was composed of these main mineral phases. Thus, the dissolution of highly soluble mineral phases in Flechtinger sandstone samples has led to different $\sigma_f(T_0)$ values compared to fluids resulting from QLM(I) batch experiments.

(iii) Electrical conductivity measurements on fluids resulting from different Flechtinger sandstone experiments performed at similar p-T conditions showed that comparable dynamic chemical equilibria were not achieved. One experiment was performed at 70 ± 2 °C (b-Fl-17), the other experiment was performed at mainly 70 °C with relatively short excursions to 150 °C (b-Fl-15). Different $\sigma_f(T_0)$ values at the end of the experiments indicate that either the pore fluid sample (b-Fl-17) was highly supersaturated or that the fluids from the batch reactors (b-Fl-15) were undersaturated with respect to dissolved ionic species. Fluids in small pores can maintain a higher supersaturation with respect to crystallization than fluids in large pores or bulk fluids due to a complex contribution of an interfacial energy term to the crystallization threshold (Putnis and Mauthe, 2001). So, either the fluid in the batch reactor was simply farther from equilibrium than the pore fluid or the pore fluid approached a state of higher supersaturation than the bulk fluid when both fluids approached a quasi-equilibrium state dependent on the environment (pore or batch reactor).

A further limitation of the applicability of $\sigma_f(T_0)$ as a proxy for dissolution-precipitation reactions results from the observation that a simple correlation between the measured concentrations of ions in solution and the measured $\sigma_f(T_0)$ did not exist. In general, $\sigma_f(T_0)$ is proportional to the sum of the products of the degree of dissociation, α_i, the concentrations of ions in solution, c_i, the valence z_i, and the mobility of ions in solution, μ_i (Equation 2.1). It is assumed that α_i is unity, c_i was measured (Table 5.3), and valences of Na, Al, Si, K, and Ca were taken as 1, 3, 4, 1, and 2, respectively. The mobilities of ions in solution are: $\mu_{\mathrm{Na}} = 5.19$, $\mu_{\mathrm{K}} = 7.61$, and $\mu_{\mathrm{Ca}} = 6.16$ with units of $10^{-8}\,\mathrm{m^2 s^{-1} V^{-1}}$ (Revil et al., 1998). The mobilities of Al^{3+} and Si^{4+} were roughly estimated to be ≈ 4 and $\approx 3 \times 10^{-8}\ \mathrm{m^2 s^{-1} V^{-1}}$ from their position in the periodic table of the elements. Calculated sums of products of α_i, c_i, z_i, and μ_i have thus the unit $10^{-8}\,\mathrm{mol\,m^{-1} s^{-1} V^{-1}}$. Their relationship to $\sigma_f(T_0)$ (Figure 5.3) illustrates that proportionality prevails for the data points from a Flechtinger sandstone batch experiment (b-Fl-16) but not for the full data set.

Scientific Technical Report STR 12/07
DOI: 10.2312/GFZ.b103-12079
Deutsches GeoForschungsZentrum GFZ

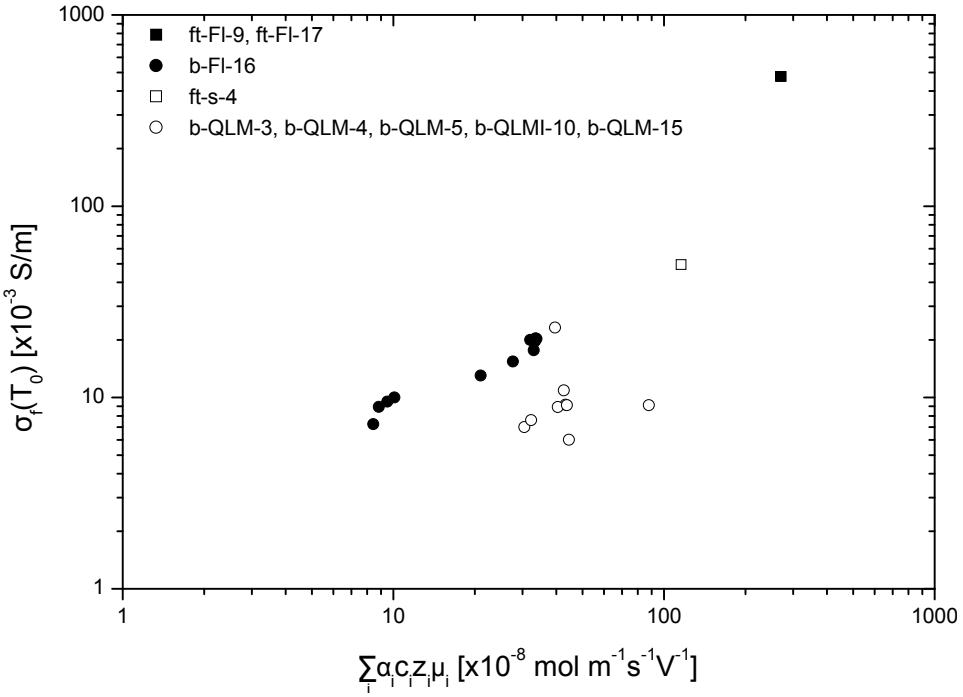

Figure 5.3: Electrical conductivity of fluids, $\sigma_f(T_0)$, as a function of the sum of the products of the degree of dissociation, α_i, the concentrations of ions in solution, c_i, the valence z_i, and the mobility of ions in solution, μ_i, for fluid samples from experiments ft-Fl-9, ft-s-4, b-QLM-3-, b-QLM-4, b-QLM-5, b-QLMI-10, b-QLM-16, and b-Fl-17.

Scientific Technical Report STR 12/07
DOI: 10.2312/GFZ.b103-12079

Table 5.3: Comparison of concentrations of ions in solution, measured electrical conductivity of fluids, $\sigma_f(T_0)$, and calculated $\sigma_f(T_0)$ resulting from multiple linear regression (Equation 5.3).

Experiment	Na $\times 10^{-3}$	Al $\times 10^{-3}$	Si $\times 10^{-3}$	K $\times 10^{-3}$	Ca $\times 10^{-3}$ mol/L	$\sigma_f(T_0)$ $\times 10^{-3}$ S/m	calculated $\sigma_f(T_0)$ $\times 10^{-3}$ S/m
ft-Fl-9	6.12	0.003	4.95	0.52	14.3	477	477
b-Fl-17	3.57	0.001	0.412	18.9	8.28	477	477
b-Fl-16	0.679	0.0025	0.092	0.156	0.21	7.26	6.4
b-Fl-16	0.682	0.0036	0.121	0.0811	0.2584	8.93	8.7
b-Fl-16	0.682	0.0046	0.155	0.0908	0.2722	9.51	7.5
b-Fl-16	0.686	0.0039	0.182	0.0967	0.2897	10.01	7.7
b-Fl-16	0.899	0.033	0.971	0.1605	0.2511	13.02	8.3
b-Fl-16	1.095	0.0217	1.476	0.1458	0.2358	15.42	8.4
b-Fl-16	1.306	0.0046	1.514	0.1463	0.4798	20.02	14.4
b-Fl-16	1.272	0	1.614	0.1612	0.5145	20.37	7.1
b-Fl-16	1.285	0.0125	1.75	0.169	0.3185	17.68	21.9
b-Fl-16	1.199	0.0012	1.698	0.1523	0.4541	19.67	10.9
b-Fl-16	1.186	0	1.665	0.1268	0.5456	20.25	11.7
ft-s-4	2.2	0.0054	7.07	0.099	1.511	49.5	49.8
b-QLM-3	2.078	0.0436	1.435	0.0826	0.1085	7	12.2
b-QLM-3	2.247	0.0780	2.325	0.1073	0.1578	9.17	12.9
b-QLM-3	2.242	0.0343	2.153	0.0961	0.1562	8.92	12.5
b-QLM-3	2.208	0.0317	2.429	0.0933	0.168	9.12	11.3
b-QLM-3	2.11	0.0253	2.521	0.0924	0.1911	6.02	18.8
b-QLM-4	1.262	0.1424	1.859	0.0917	0.0819	7.61	20
b-QLM-5	4.238	0.0352	4.912	0.255	0.38	9.12	13.8
b-QLMI-10	3.31	0.0201	1.879	0.0608	0.1802	10.9	17.9
b-QLM-15	1.434	0.0006	1.99	0.1319	0.587	23.2	20.7

However, a multiple linear regression, yielded a linear relationship between c_i and $\sigma_f(T_0)$ for the full data set (Table 5.3) including data from different experiment types (batch and flow-through experiments) as well as data from experiments conducted with different sample types (Flechtinger sandstone core samples, and granular aggregates of quartz, labradorite-andesine, microcline, and/or illite).

The general model for the multiple linear regression is:

$$y = m_1 x_1 + m_2 x_2 + ... + m_n x_n + b, \tag{5.2}$$

where y is the dependent variable, x_n are n independent variables, m_n are the coefficients of each independent variable, and b is a constant. Applied to the concentrations of ions in solution as the independent variables and $\sigma_f(T_0)$ as the dependent variable, we obtain:

$$\sigma_f(T_0) = \sum_i m_i c_i + b, \tag{5.3}$$

where i denotes Na, Al, Si, K, and Ca. The data used for the regression analysis and the calculated $\sigma_f(T_0)$ values are given in Table 5.3.

Multiple linear regression using the LINEST function of Microsoft Excel resulted in the

Scientific Technical Report STR 12/07
DOI: 10.2312/GFZ.b103-12079
Deutsches GeoForschungsZentrum GFZ

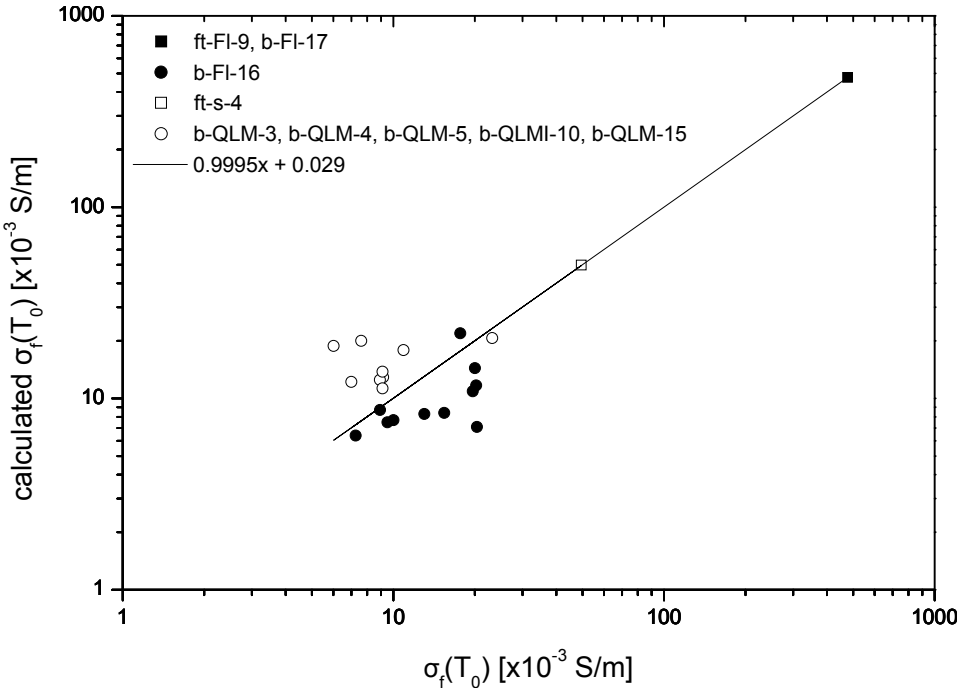

Figure 5.4: Calculated electrical conductivity of fluids, $\sigma_f(T_0)$ (Equation 5.3), as a function of measured $\sigma_f(T_0)$ for fluid samples from experiments ft-Fl-9, ft-s-4, b-QLM-3-, b-QLM-4, b-QLM-5, b-QLMI-10, b-QLM-16, and b-Fl-17.

following m_i values in Equation 5.3: $m_{\mathrm{Na}} = -0.55$, $m_{\mathrm{Al}} = 25.03$, $m_{\mathrm{Si}} = -0.41$, $m_{\mathrm{K}} = 10.68$, and $m_{\mathrm{Ca}} = 33.16$. The b value was calculated as 2.57. Moreover, the LINEST function returns statistical parameters as the coefficient of determination, R^2, the standard errors of calculated $\sigma_f(T_0)$ values, the observed value of F (a parameter in F-statistics), and the degrees of freedom.

A so-called F-test and a t-test showed that concentrations of K and Ca can be used to predict $\sigma_f(T_0)$. A F-test in which critical values of F are compared to the observed value of F, showed that the observed linear relationship between c_i and $\sigma_f(T_0)$ did not occur by chance. Thus, the regression equation is useful for the prediction of $\sigma_f(T_0)$. A so-called t-test yields the statistical significance of each m_i value in the regression equation. The t-test was conducted by comparing observed values of t, i.e., the ratio of m_i values to their respective standard errors, to critical values of t obtained from tabulated values in statistics databases. The t-test indicated that only the concentrations of K and Ca are statistically significant for the prediction of $\sigma_f(T_0)$ by the multi linear regression (Equation 5.3).

Although only the concentrations of K and Ca are statistically significant for the prediction of $\sigma_f(T_0)$, there is a linear relationship between measured $\sigma_f(T_0)$ values and calculated values using Equation 5.3 with m values for Na, Al, Si, K, and Ca (Figure 5.4). The coefficient of determination of the correlation between measured and calculated $\sigma_f(T_0)$ values over a range of ≈ 7 to $\approx 480 \times 10^{-3}$ S/m is high with $R^2 = 0.9997$.

The interpretation of the above findings is that $\sigma_f(T_0)$ is correlated to the measured concentrations of cations (Na, Al, Si, K, and Ca) and not to the concentrations of anions in solution. Anions in solutions resulting from QLM(I) experiments are OH^- or negatively charged

Scientific Technical Report STR 12/07
DOI: 10.2312/GFZ.b103-12079

species of Al and Si (e.g. AlO_2^- and $HSiO_3^-$ as modeled with PHREEQC). In solutions resulting from experiments with Flechtinger sandstone samples other anions, like F^-, Cl^-, and SO_4^{2-}, were present as can be inferred from the analysis of a Flechtinger sandstone pore fluid sample (b-Fl-17, Table 5.5).

Concentration data resulting from flow-through and batch experiments with Flechtinger sandstone and QLM(I) samples can be linearly correlated to the respective electrical conductivity of the fluid suggesting that $\sigma_f(T_0)$ is quantitatively dependent on the same ions in the different solutions. This implies that the processes leading to changes of σ_f in the different sample materials, i.e., dissolution of ions from the solid material into the fluid and precipitation of solids from the solution, were identical to some extent.

The t-test indicated that only the concentrations of K and Ca are statistically significant for the prediction of $\sigma_f(T_0)$ although Na and Si were present in significant concentrations in most fluid samples (Table 5.5). The mobility of Si^{4+} in solution is expected to be comparatively low ($\mu_{Si} \approx 3 \times 10^{-8}$ $m^2s^{-1}V^{-1}$) due to its relatively large hydrated ionic radius (Volkov et al., 1997; Blume et al., 2010). Thus, its contribution to $\sigma_f(T_0)$ is expected to be comparatively low. However, Na^+ has a medium mobility value of 5.19×10^{-8} $m^2s^{-1}V^{-1}$ compared to relatively high values of K^+ and Ca^{2+} (7.61 and 6.16×10^{-8} $m^2s^{-1}V^{-1}$, respectively). As a consequence, the effect of Na concentrations on $\sigma_f(T_0)$ cannot be fully neglected.

5.2 Permeability as an Indicator for Dissolution-Precipitation Reactions

The investigation of the permeability evolution at constant temperature and pressure gave rise to the hypothesis that dissolution-precipitation reactions in the pore space of the samples led to changes in the structure of the pore space and to permeability reductions. This hypothesis is supported by the following observations:

(i) The rate of the normalized k decreases with time was independent on temperature (Figure 4.11). One Flechtinger sandstone flow-through experiment (ft-Fl-11) was performed at significantly lower temperatures (≈ 72 °C) than the other experiments (150 to 174 °C) but yielded similar rates of the normalized k decrease with time. This observation implies that the k reduction was not a simple function of temperature. Investigations of permeability changes of quartz-labradorite granular aggregates due to dissolution-precipitation reactions have shown that the extent and the rate of permeability reductions were correlated to temperature (Tenthorey et al., 1998). The difference to the observations made in the present study probably results from the different experimental conditions in both studies with respect to p_c, p_p, and deviatoric stress.

(ii) A Flechtinger sandstone flow-through experiment with 1 mol/L $NaCl_{aq}$ solution as the pore fluid (ft-Fl-10) showed a similar behavior as similar experiments performed with H_2O suggesting that clay swelling did not significantly contribute to the normalized k decrease at constant temperature and pressure. In comparison to the experiments conducted with H_2O as the pore fluid, the higher salinity would have prevented the swelling of clays. Moreover, the experiment showed a similar k decrease with time as a clay-free QL sandwich experiment (ft-s-2) during the first 4.25 d indicating that the presence of clay minerals is not a dominant factor controlling the rates of k decreases with time at constant temperature and pressure.

(iii) The frequency of permeability measurements did not influence the rate of the permeability decrease at constant temperature and pressure. Permeability measurements were performed

Scientific Technical Report STR 12/07
DOI: 10.2312/GFZ.b103-12079
Deutsches GeoForschungsZentrum GFZ

from two times (ft-Fl-6) up to eight times (ft-s-1) at constant temperature and pressure. There is no clear relationship between the frequency of the permeability measurements and the rate of the normalized k reduction. This observation implies that there was no filter effect of the porous samples with respect to finely dispersed particles. Thus, fines migration was not the dominant factor in the reduction of permeability at constant temperature and pressure.

(iv) The permeability reductions agreed generally well with published results of experiments that were performed with a granular aggregate of quartz and labradorite (Tenthorey et al., 1998). The chemical inventory of these experiments was similar to the QLM sandwich flow-through experiments performed in the present study (ft-s-1 and ft-s-2, Table 3.2). However, permeability reductions at constant temperature and pressure proceeded relatively slow in the present study. One Flechtinger sandstone flow-through experiment (ft-Fl-8) yielded normalized permeability reductions comparable to the published results but the k reduction rate with time were much lower (Figure 4.11). The experiment by Tenthorey et al. (1998) was conducted with ten times higher pressures (p_c and p_p), under deviatoric stress conditions (75×10^6 Pa), and at slightly higher temperatures of 175 °C. The sample was not subjected to strain and the porosity was largely unaffected at constant temperature and pressure. It has been concluded that the observed k reduction resulted from precipitation of secondary mineral phases, i.e., clay minerals and zeolites, in narrow pores and pore throats (Tenthorey et al., 1998; Tenthorey and Scholz, 2002). Moreover, deviatoric stress conditions affected the dissolution behavior via the production of fine particles due to grain crushing and via pressure solution at highly stressed grain-grain contacts. Enhanced dissolution led to faster precipitation of secondary minerals resulting in enhanced k reduction (Tenthorey et al., 1998).

The permeability-changing processes at constant temperature and pressure, could have been due to dissolution, precipitation, clay swelling, fines liberation and migration, creep compaction, and/or an interaction of these processes. The previous paragraphs have shown that pure dissolution or precipitation, clay swelling, and fines liberation and migration were not the dominant processes leading to permeability reductions of the samples. Pure dissolution or precipitation are typically dependent on temperature, i.e., they show an Arrhenius type behavior, which could not be observed in this study (Figure 4.11). Clay swelling affected k almost instantaneously in fluid exchange experiments (Figure 4.12) and can thus be excluded from being a dominant factor in the time-dependent k changes at constant temperature and pressure. Moreover, experiments performed with H_2O and 1 mol/L $NaCl_{aq}$ solution as well as experiments performed with clay-bearing and clay-free materials showed a similar time-dependent normalized k decrease. The effect of fines liberation and migration on k would have increased with the frequency of the k measurements. The influence of creep compaction on permeability is difficult to ascertain based on the data obtained in the present study, because the volumetric strain of the samples was not measured in the pressure vessel of the HPT-apparatus.

Comparison to literature data indicates that creep compaction was not a significant factor for the observed permeability decreases at constant temperature and pressure. Triaxial creep compaction experiments with granular aggregates of quartz and Si-bearing aqueous solutions as the pore fluids have shown that creep compaction proceeded with decreasing strain rates with time at constant load and reached a maximum volumetric strain of approximately 16 %. Applied temperatures ranged between 150 and 350 °C, maximum confining and pore pressures were 12.5 and 27.5×10^6 Pa, respectively, maximum deviatoric stress was 30.5×10^6 Pa, and the maximum duration of the experiments was 91 d (Schutjens, 1991). The permeability of flown-through sandwich samples with granular aggregates performed in the present study (ft-s-1 and ft-s-2) suggested that the rate of the k reduction was constant with time (Figure 4.11). So,

Scientific Technical Report STR 12/07
DOI: 10.2312/GFZ.b103-12079

the permeability data indicate that strain did not affect the permeability in the present study. Hydrostatic flow-through creep compaction experiments at 150 °C with granular aggregates of quartz and with H_2O as the pore fluid have shown that the degree of undersaturation of the pore fluid with respect to quartz was correlated to the creep compaction rate. Maximum confining and pore pressures were 46.2 and 11.7×10^6 Pa, respectively, and the duration of the experiments was up to 246 d (He et al., 2003, 2007). These findings imply that the frequency of the k measurements, i.e., the frequency of the pore fluid exchange against H_2O, should have had an enhancing effect on the k reduction, if creep compaction occurred in the experiments. The permeability data do not support this conclusion (Figure 4.11). Triaxial deformation experiments with Bentheim, Darley Dale, and Crab Orchard sandstones with H_2O as the initial pore fluid in the temperature range 25 to 75 °C have illustrated that an increase in temperature from 25 to 75 °C at constant load leads to an increase in strain rates by several orders of magnitude. Maximum confining and pore pressures were 50 and 20×10^6 Pa, respectively, and deviatoric stress was as high as 400×10^6 Pa (Heap et al., 2009). Especially the Darley Dale sandstone is comparable to the Flechtinger sandstone with respect to mineralogical composition and porosity. These findings imply that the k reduction in the present study were also temperature-dependent, if deformation was a controlling factor for the k reduction. Such a temperature dependence could not be observed (Figure 4.11).

To summarize, the experiments performed in the present study were conducted at lower pressures than typical creep compaction experiments. Although direct measurements on volumetric strain or porosity changes could not be performed, the permeability data did not show temperature or measurement frequency dependencies indicating that creep compaction was not a significant factor for the observed k decreases. Furthermore, no significant difference between normalized permeabilities of sandwich samples with granular aggregates and already compacted rock samples could be observed.

5.3 Evidence for Dissolution-Precipitation Reactions

5.3.1 Dissolution of Minerals Reflected by Fluid Chemistry

Concentrations of dissolved ions in the fluid samples from flow-through experiments resulted from fluid-rock interactions and not from contaminations due to corrosion of the HPT-apparatus. The low concentrations of Ni in fluid samples from a flow-through experiment with Fontainebleau sandstone (almost pure quartz arenite) constrained the contribution of corrosion of the apparatus to the overall chemical inventory of the fluid (Figure 4.6). The source of Si in the fluid was the rock material. The fluid with the maximum Si concentration was supersaturated with respect to quartz and slightly undersaturated with respect to amorphous silica at 160 °C and saturation vapor pressure (dashed lines in Figure 4.6) as shown by a comparison to data of the solubilities of amorphous silica and quartz in H_2O (Marshall, 1980; Gunnársson and Arnórsson, 2000). Consequently, it is likely that the dissolved Si in the pore fluid resulted mainly from dissolution of amorphous silica cements in the Fontainebleau sandstone sample at 162 °C.

The chemical analyses of Flechtinger sandstone pore fluid samples indicated that the minerals of the rock dissolved in different proportions depending on the experimental conditions. The electrical conductivity of a pore fluid sample from a flow-through and a batch experiment was identical but both samples showed different compositions (ft-Fl-9 versus b-Fl-17, Tables 5.4 and 5.5). The concentrations of Na, Al, and Ca were comparable in both analyses. The concentration of Si was approximately 12 times higher in the fluid sample from the flow-through

Scientific Technical Report STR 12/07
DOI: 10.2312/GFZ.b103-12079
Deutsches GeoForschungsZentrum GFZ

experiment compared to the fluid sample from the batch experiment, whereas the concentration of K was approximately 36 times higher in the fluid sample from the batch experiment than in the fluid sample from the flow-through experiment.

The temperature-dependent retrograde dissolution behavior of calcite was reflected by the evolution of apparent normalized Ca losses, nl_{Ca}, in Flechtinger sandstone batch experiments (Figure 4.29). The evolution of nl_{Ca} showed decreasing trends during heating from 70 to 150 °C (b-Fl-16). Na, Al, Si, and K generally showed increasing trends with temperature. One source of Ca is the $CaCO_3$ cement in the Flechtinger sandstone (Table 3.1). In contrast to the silicates, calcite has a retrograde solubility at the present experimental conditions (e.g., Caciagli and Manning, 2003). Thus, the heating could have led to the precipitation and the cooling could have led to the dissolution of calcite.

The illite content did not influence the evolution of σ_f but the evolution of c_i in batch experiments with granular aggregates of quartz, feldspars, and illite (Figure 4.26 and Table 5.5). A comparison of two batch experiments (b-QLM-5 and b-QLMI-10) performed at identical experimental conditions illustrates the effect of illite on the solution composition. Apparent normalized element losses of Na, Al, and Si were similar in both experiments but nl_{K} was depleted by a factor of ≈ 10 and nl_{Ca} was enriched by a factor of ≈ 9 in the fluid resulting from the illite-containing batch experiment. This observation suggests a cation-exchange of K against Ca in the illite-containing experiments.

Comparisons between nl_i values of fluids resulting from experiments with granular aggregates (ft-s-3 and ft-s-4) and fluids resulting from experiments with a rock sample (ft-Fl-9) were problematic due to the spatial distribution of minerals in the rock. SEM investigations showed that the pores of the Flechtinger sandstone were frequently lined with illite and partly filled with illite and calcite cements (Figures 4.18 and 4.19). Therefore, the fluid-solid interface of illite and calcite was disproportional to the other mineral phases comprising the rock (Table 3.1). The apparent normalized element loss was calculated on the basis of the mass fraction of element i in the mineral phases comprising the whole rock (Equation 3.5). As a consequence, comparisons of nl_i values of pore fluids resulting from experiments with granular aggregates, in which the solid phases are homogeneously distributed, and pore fluids resulting from rock samples with an inhomogeneous distribution of mineral phases are questionable.

Dependence of Fluid Compositions on Residence Times at High Temperatures

The comparison of nl_i values of pore fluid samples from flow-through experiments indicates that high nl_i values, with i = Na, Si, K, Ca, correlated with long residence times of the fluid at 150 °C (Table 5.4). The pore fluid resulting from a QLM sandwich experiment (ft-s-4) not only exhibited the highest nl_i values but also had the longest residence time of the fluid at 150 °C (14 d), the shortest residence time at 71 °C (2 d), and the shortest total residence time (16 d) of the fluid in the porous sample. This correlation indicates that residence times at the high temperature stages of the experiments were more important factors for the concentration of dissolved cations in the pore fluids than total residence times, temperature histories, and pressures.

The values of nl_i varied over several orders of magnitude in the fluid samples from Flechtinger sandstone and QLM sandwich flow-through experiments. Apparent normalized Na, Al, Si, and K losses were lowest in the Flechtinger sandstone experiment whereas Ca showed lowest values in a QLM sandwich experiment (ft-s-3). Apparent normalized Na and Ca losses were high in the range of 0.36 to 2.4×10^{-3} mol/m^2. Values of nl_{Al} were low in the range of

Scientific Technical Report STR 12/07
DOI: 10.2312/GFZ.b103-12079

Table 5.4: Approximate pore fluid compositions with respect to dissolved cationic species, apparent normalized element losses, temperature histories, and effective pressures of flow-through experiments ft-s-3, ft-s-4, ft-Fo-6, and ft-Fl-9.

	ft-s-3	**ft-s-4**	**ft-Fo-6**	**ft-Fl-9**
c_i	$\times 10^{-3}$	$\times 10^{-3}$	$\times 10^{-3}$	$\times 10^{-3}$ mol/L
Na	2.03 ± 0.03	2.20 ± 0.01	1.263 ± 0.009	6.12 ± 0.07
Mg	n.a.	n.a.	0.00467 ± 0.00005	n.a.
Al	0.0252 ± 0.0009	0.0054 ± 0.0001	0.0044 ± 0.0004	0.0030 ± 0.0006
Si	1.93 ± 0.02	7.07 ± 0.06	8.35 ± 0.05	4.95 ± 0.09
K	0.077 ± 0.003	0.099 ± 0.003	0.0186 ± 0.0001	0.52 ± 0.02
Ca	0.307 ± 0.006	1.511 ± 0.007	0.0632 ± 0.0004	14.3 ± 0.3
Mn	n.a.	n.a.	0.0142 ± 0.0001	n.a.
Fe	n.a.	n.a.	0.374 ± 0.002	n.a.
Ni	n.a.	n.a.	0.016 ± 0.003	n.a.
nl_i	$\times 10^{-3}$	$\times 10^{-3}$	n.a.	$\times 10^{-3}$ mol/m^2
Na	2.3 ± 0.3	2.4 ± 0.3	n.a.	0.9 ± 0.1
Al	0.008 ± 0.001	0.016 ± 0.0002	n.a.	0.0001 ± 0.00003
Si	0.047 ± 0.006	0.17 ± 0.02	n.a.	0.016 ± 0.002
K	0.053 ± 0.009	0.07 ± 0.01	n.a.	0.025 ± 0.004
Ca	0.36 ± 0.05	1.7 ± 0.2	n.a.	1.4 ± 0.2
T-stage [°C]	150	150	162	150
r.t. [d]	6	14	4	3
T-stage(s) [°C]	70	71	79	70, 70, 42, 70
r.t. [d]	18	2	3	22, 14, 4, 5
t.r.t [d]	68.5	16	7	48
p_{eff} [10^6 Pa]	5	2.5	5	5
$\sigma_f(T_0)$ [10^{-3} S/m]	n.a.	49.5	n.a.	n.a.

n.a. denotes not applicable or not analyzed.
r.t. denotes residence time.
t.r.t. denotes total residence time.

0.0001 to 0.016×10^{-3} mol/m^2. Si and K showed medium nl_i values ranging from 0.016 to 0.17×10^{-3} mol/m^2.

The composition of bulk fluids in contact with Flechtinger sandstone samples correlated with total residence times of the fluids at 150 °C (Figure 4.29). Apparent normalized element losses resulting from Flechtinger sandstone batch experiments (b-Fl-15 and b-Fl-16) matched well although fluid/solid mass ratios, pressure conditions, and temperature histories were different. Despite the different experimental details of the experiments, nl_i values of Na, Al, Si, K, and Ca of the fluid sample taken at a total run duration of approximately 90 d were in agreement with the sample taken at approximately 82 d. The total duration of the 150 °C stage of the experiments was equal (≈13 d) suggesting that the residence time at 150 °C of the bulk fluid in contact with the solid material was an important factor controlling the concentrations of cations in solution.

However, the comparison of nl_i values obtained from two QLM batch experiments (b-QLM-4 and b-QLM-5) indicates that nl_{Al} was inversely related to the residence time of the bulk fluid

Scientific Technical Report STR 12/07
DOI: 10.2312/GFZ.b103-12079

Table 5.5: Concentrations of ions in solution, apparent normalized element losses, temperature histories, pH, and electrical conductivity of fluids in batch experiments b-QLM-4, b-QLM-5, b-QLMI-10, and b-Fl-17.

	b-QLM-4	**b-QLM-5***	**b-QLMI-10**	**b-Fl-17**
c_i	$\times 10^{-3}$	$\times 10^{-3}$	$\times 10^{-3}$	$\times 10^{-3}$ mol/L
Na	1.262 ± 0.002	4.238 ± 0.007	3.31 ± 0.006	3.57 ± 0.02
Mg	n.a.	n.a.	n.a.	1.24 ± 0.01
Al	$0.1424 \pm 2 \times 10^{-4}$	$0.0352 \pm 6 \times 10^{-5}$	$0.02 \pm 3 \times 10^{-5}$	0.001 ± 0.0001
Si	1.859 ± 0.003	4.912 ± 0.008	1.879 ± 0.003	0.412 ± 0.004
K	0.0917 ± 0.0002	0.255 ± 0.0004	0.0608 ± 0.0001	18.9 ± 0.6
Ca	0.0819 ± 0.0001	0.38 ± 0.0006	0.1802 ± 0.0003	8.28 ± 0.08
F^-	n.a.	n.a.	n.a.	0.016 ± 0.0002
Cl^-	n.a.	n.a.	n.a.	81 ± 0.1
SO_4^{2-}	n.a.	n.a.	n.a.	0.312 ± 0.0008
nl_i	$\times 10^{-3}$	$\times 10^{-3}$	$\times 10^{-3}$	$\times 10^{-3}$ mol/m^2
Na	14 ± 2	15 ± 2	10 ± 1	0.0065 ± 0.0001
Mg	n.a.	n.a.	n.a.	0.0148 ± 0.0003
Al	0.43 ± 0.05	0.033 ± 0.004	0.014 ± 0.002	$4 \times 10^{-7} \pm 4 \times 10^{-8}$
Si	0.45 ± 0.06	0.37 ± 0.05	0.12 ± 0.02	$2 \times 10^{-5} \pm 4 \times 10^{-7}$
K	0.63 ± 0.08	0.5 ± 0.1	0.06 ± 0.01	0.0119 ± 0.0005
Ca	1.0 ± 0.1	1.4 ± 0.2	12 ± 1	0.0104 ± 0.0002
T-stage [°C]	150	150	150	n.a.
r.t. [d]	10	70	70	n.a.
T-stage [°C]	70	n.a.	n.a.	70
r.t. [d]	39	n.a.	n.a.	38
t.d. [d]	52	70	70	38
pH	n.a.	n.a.	n.a.	7.47
$\sigma_f(T_0)$ [S/m]	7.61×10^{-3}	9.12×10^{-3}	10.9×10^{-3}	0.477

* the fluid volume was 1.2×10^{-6} L at the end of the experiment.
n.a. denotes not applicable or not analyzed.
r.t. denotes residence time.
t.d. denotes total duration.

at 150 °C (Table 5.5). The experiments were performed with the same starting materials but with different temperature histories. Apparent normalized Na, Si, K, and Ca losses were almost identical in both experiments but nl_{Al} was lower by approximately one order of magnitude in the experiment with the longer residence time of the bulk fluid at 150 °C (10 d versus 70 d). The apparent normalized Al loss decreased with time at a constant temperature of 150 °C indicating that low nl_{Al} values resulted from time-dependent precipitation of Al-bearing solid phases (Figure 4.28).

Effects of Background Electrolytes on Apparent Dissolution Rates

The comparison of nl_i data of fluids resulting from QLM batch experiments with H_2O and 0.1 mol/L $NaCl_{aq}$ provided insight into the effect of background electrolytes on the nl_i evolution (Figure 4.28). Apparent normalized Na and K losses were slightly enriched, nl_{Si} was approxi-

Scientific Technical Report STR 12/07
DOI: 10.2312/GFZ.b103-12079
Deutsches GeoForschungsZentrum GFZ

mately equal, and nl_{Al} was depleted in the saline solution relative to H_2O. The corresponding Si concentrations in the first samples of batch experiments with H_2O and 0.1 mol/L $NaCl_{aq}$ (approximately 1.4 and 1.5×10^{-3} mol/L) were near to the equilibrium concentration of quartz in H_2O at 150 °C of approximately 2.5×10^{-3} mol/L (Gunnársson and Arnórsson, 2000).

Apparent dissolution rates of Si-bearing solids, $r_{dis,Si}$, indicated a decreasing trend with salinity. Apparent dissolution rates were calculated using Si concentration data, c_{Si}, of the first two samples of QLM batch experiments with H_2O and 0.1 mol/L $NaCl_{aq}$:

$$r_{dis,Si} = \frac{\Delta c_{Si}\, V}{A\, f_{Si}\, \Delta t}, \tag{5.4}$$

where the fluid volume V, the fluid-solid interface area A, and the mass fraction of Si in the solid material, f_{Si}, are constant. The change of c_{Si} with time in this time interval indicated zeroth reaction order and consequently $\log r_{dis,Si} = \log k_{dis,Si}$ (Appelo and Postma, 1999). For the first two samples at $t_1 \approx 0.9$ d and $t_2 \approx 2$ d $\log r_{dis,Si}$ were -8.6 and -9.2 mol m^{-2} s^{-1} in H_2O and 0.1 mol/L $NaCl_{aq}$, respectively. Published values of $\log r_{dis,Si}$ are -8.27 mol m^{-2} s^{-1} for experiments conducted with quartz and 0.05 mol/L $NaCl_{aq}$ solutions at 100 °C (Dove and Crerar, 1990). Published values of $\log r_{dis,Si}$ are -9.39 mol m^{-2} s^{-1} for a short (4 h) experiment conducted at 150 °C with andesine and H_2O at near-neutral pH (Hellmann, 1994). Thus, the apparent dissolution rates of the solids in the batch experiment with 0.1 mol/L $NaCl_{aq}$ were lower than published dissolution rates of quartz in fluids with lower temperatures and lower salinities. Furthermore, the apparent dissolution rates in the batch experiment with H_2O were higher than published dissolution rates of andesine at similar temperature and pH conditions.

The decreasing trend of $r_{dis,Si}$ suggest that the dissolution of feldspars was reduced by the presence of Na^+ in the background electrolyte, as a comparison to literature data indicates. Experiments in a hydrothermal mixed flow reactor with near-neutral pH solutions of NaCl, KCl, LiCl, and $MgCl_2$ with concentrations of up to approximately 0.15 mol/L have shown that the dissolution rate of quartz was enhanced by up to 1.5 orders of magnitude relative to experiments conducted with H_2O (Dove and Crerar, 1990). Moreover, the experiments have shown that the dissolution rates of silicates other than quartz were not affect by the presence of small concentrations of background electrolytes. In contrast, batch reactor experiments with quartz and feldspar grains and solutions containing organic acids and up to 2.2 mol/L $NaCl_{aq}$ have illustrated that the presence of Na^+ decreased feldspar dissolution rates by competing with H^+ for reactive sites on the feldspar surface (Blake and Walter, 1999). Thus, the decreasing trend of $r_{dis,Si}$ can be explained by decreasing feldspar dissolution rates in the experiments with the 0.1 mol/L $NaCl_{aq}$ solution.

5.3.2 Evolution of Fluid Chemistry as an Indicator for the Precipitation of Secondary Phases

Secondary phases were identified by SEM, EDX, and TEM on QLM samples resulting from a batch (b-QLM-5) and a flow-through sandwich experiment (ft-s-4) (Figures 4.21, 4.22 and 4.33). SEM investigations of Flechtinger sandstone samples resulting from batch and flow-through experiments yielded no information on mineralogical changes (Figures 4.17 to 4.19). The alteration features on the altered QLM materials were typically sub-micrometer sized elongated particles covering mostly the labradorite-andesine grains, to a lesser extent the microcline grains, and barely could be found on quartz. A Flechtinger sandstone and a QLM sandwich flow-through experiment (ft-Fl-9 and ft-s-4) were similar with respect to content of main mineral

Scientific Technical Report STR 12/07
DOI: 10.2312/GFZ.b103-12079
Deutsches GeoForschungsZentrum GFZ

phases, fluid/solid mass ratio, residence time of the fluid at high temperature, and temperature history. This analogy suggests that processes occurring in the QLM sandwich experiments should also have occurred in the rock sample. It can be assumed that the sub-micrometer sized elongated particles were also present in the Flechtinger sandstone flow-through experiment but that they could not be detected due to the complexity of the rock microstructure.

EDX analyses of unaltered and altered labradorite-andesine grains resulting from a QLM flow-through experiment suggested that K and Ca were enriched whereas Na was depleted relative to Al and Si in the altered surfaces of the grains (ft-s-4, Table 4.8). Despite the semi-quantitative nature of the EDX analyses, they agreed to the XRD data of the labradorite-andesine starting material. EDX analyses of a quartz surface resulting from the experiment showed that sub-micrometer sized particles not only occurred on labradorite-andesine surfaces but also on quartz (Figure 4.22b). The small particle on the quartz grain surface contained K and Al which obviously could not be obtained from the original quartz (Table 4.9). The small particle covered the quartz surface and attenuated the original Si X-ray signal of quartz. The chemical data of the fluid has shown that K and Al were depleted in the fluid sample relative to the solid material (Tables 5.4 and 5.6). This observation is consistent with the precipitation of K- and Al-bearing solid phases from the fluid and agrees with the EDX analyses of the sub-micrometer sized particles present on the quartz grains.

TEM investigations of two feldspar samples resulting from a QLM flow-through experiment (ft-s-4) gave insight into dissolution-precipitation processes occurring on the sub-micrometer scale (Figures 4.23 and 4.24). The lack of C in the small particles on the altered microcline surface strongly suggests that the particles were not of organic origin. The amorphous phases on the labradorite-andesine and the microcline surfaces were not present on the starting materials and were thus secondary formations. STEM-HAADF images showed that the amorphous phases were porous. Layered structures were present within the amorphous phase on the altered labradorite-andesine surface (fiber stacks) but it could not be confirmed that these structures were crystalline. The crystalline phase surrounded by an amorphous phase on the altered microcline surface was either a fragment of the microcline starting material or a newly formed phase with a similar stoichiometry as the original microcline. The lack of Na in the crystalline phase (Figure 4.24b) suggests the latter. Although there was a substantial amount of Na in both feldspars (Table 3.1), no Na was detected in the precipitates. The observation that the amorphous precipitates contain Al, Si, and K is consistent with the analysis of a fluid sample from the experiment indicating that the proportions of these elements relative to Ca were lower in the fluid compared to the solid starting material (Table 5.6). The interfaces between the secondary formations and the original feldspar surfaces were sharp on the nanometer scale and a reaction rim could not be observed.

The alteration features on feldspars resulting from the QLM sandwich experiment are comparable to alteration features on feldspar surfaces resulting from early weathering stages of rocks as reported in the literature. TEM investigations of altered plagioclase sampled from an alteration halo of a sulfide-bearing vein yielded a sequence of smectite, intermediate phyllosilicate phases, and sericite (Page and Wenk, 1979). A granitic rock exposed to the atmosphere showed metastable amorphous aluminum hydroxide phases on weathered K-feldspars (Kawano and Tomita, 1996). Amorphous layers that were depleted in Al and enriched in Si relative to the original feldspar material developed on bytownite in volcanic ash exposed to weathering (Kawano and Tomita, 2001). Naturally weathered K-feldspar surfaces recovered from a sandstone aquifer saturated with slightly alkaline groundwater revealed that the K-feldspar surfaces were coated with an approximately 10×10^{-9} m thick amorphous layer enriched in Si and depleted in K

Scientific Technical Report STR 12/07
DOI: 10.2312/GFZ.b103-12079
Deutsches GeoForschungsZentrum GFZ

relative to the original feldspar material. Moreover, the K-feldspar grains were partially coated with tightly adhered kaolinite platelets and authigenic smectite covered large areas of the fluid-rock interface (Zhu et al., 2006). Sub-micrometer sized Fe-K aluminosilicates, probably smectite, have been detected in an amorphous matrix on weathered K-feldspar grains recovered from a granite (Lee et al., 2008). These Fe-K aluminosilicates resemble the fiber stacks in the precipitates on an labradorite-andesine grain resulting from the QLM sandwich experiment (Figure 4.23a).

However, the identity and chemical composition of the secondary phases could not be determined by XRD and EMPA investigations. XRD investigations of quartz-feldspar aggregates and Flechtinger sandstone samples showed no changes in mineralogical compositions of the altered materials in comparison to the starting materials (Figures 4.15 and 4.31). This observation either indicates that potentially occurring changes in the mineralogical compositions were below the detection limit of the method (≈ 1 %) or that secondary phases were not crystalline.

Electron microprobe analyses did not yield information about chemical alterations of the solid materials relative to the starting materials because of the small size of the alteration products. EMPA analyses were performed on polished thin sections of the Flechtinger sandstone sample resulting from a flow-through experiment and on small elongated particles occurring on labradorite-andesine grains resulting from a QLM batch experiment (Figures 4.16 and 4.32). Dissolution or precipitation features were not detectable in the rock sample. Small sub-micrometer sized elongated particles were detectable on the surfaces of labradorite-andesine grains. Because the size of the source region for element characteristic X-rays was $\approx 0.35 \times 10^{-6}$ m in the present case, the electron microprobe analysis of the small particles on the labradorite-andesine grains comprised contributions from the particles themselves and from the underlying feldspar crystal.

Apparent normalized element losses reflected the removal of ions from bulk solutions with time, and thus the time-dependent adsorption of ions onto solids or the precipitation of secondary solid phases. Apparent normalized element losses of batch experiments with granular aggregates of quartz and feldspar (b-QL-1, b-QL-2, and b-QLM-3) showed that nl_i values initially increased rapidly, then increased slowly, and/or even decrease with time in the remainder of the experiments (Figure 4.28). The initial increase and later decrease of nl_i is consistent with dissolution of ions from the solid material into solution until a quasi steady state was reached and subsequent removal of ions from the solution in the remainder of the experiments. This behavior is most pronounced for Al but can also be observed for Si, K, and Ca.

Modeling the saturation indices, SI, of different minerals with PHREEQC based on chemical fluid analyses revealed that several mineral phases were supersaturated in the fluids at 70 °C. Minerals with a positive SI tend to precipitate when the fluid-rock system approaches thermodynamic equilibrium (Appelo and Postma, 1999). Hydrogeochemical modeling provides information on the relative stabilities of different mineral phases in fluid-rock systems. Thus, qualitative predictions on the dissolution-precipitation behavior of the quartz-feldspar-water system can be made.

The modeling of fluid compositions resulting from fluid-mineral interactions (Figures 4.8 and 4.30) indicates that mainly low temperature phyllosilicates (clay minerals) and tectosilicates (zeolites) are stable in the fluids at 70 °C. The modeling results are confirmed by experiments reported in the literature. Hydrothermal experiments with plagioclase-quartz granular aggregates as the solid starting materials under deviatoric stress conditions, that favored enhanced dissolution due to grain crushing and pressure solution, yielded smectite, smectite-illite phases,

Scientific Technical Report STR 12/07
DOI: 10.2312/GFZ.b103-12079

Table 5.6: Comparison of element ratios in the QLM starting material, n_i/n_{Ca}, and the pore fluid resulting from experiment ft-s-4 relative to Ca, c_i/c_{Ca}.

	Na	**Al**	**Si**	**K**	**Ca**
n_i in QLM starting material [10^{-3} mol]	0.8	2.5	29.8	0.8	0.4
c_i in fluid [10^{-3} mol/L]	2.2	0.0054	7.07	0.099	1.511
n_i/n_{Ca}	1.8	5.7	67.4	1.7	1
c_i/c_{Ca}	1.5	0.004	4.7	0.07	1

and zeolites (Tenthorey et al., 1998; Tenthorey and Scholz, 2002). Batch experiments with $KAlSi_3O_8$ and KCl-bearing aqueous solutions at 200 °C and 30×10^6 Pa resulted in metastable mineral assemblages of boehmite and kaolinite (Fu et al., 2009). Furthermore, literature data indicate that the fluid composition of batch experiments in the quartz-feldspar-water system is controlled by a coupled dissolution-precipitation process. It has been concluded that feldspar dissolution is coupled to clay-mineral precipitation and that the clay-mineral precipitation is the slow, i.e., rate-controlling, step in the overall reaction (Fu et al., 2009; Zhu and Lu, 2009).

However, the time-dependent changes of $\sigma_f(T_0)$ and c_i in flow-through and batch experiments suggests that disequilibrium prevailed between solid and fluid phases during the longest phases of most experiments. As a consequence, modeling saturation indices (Equation 2.45) indicates trends in which direction the mineral assemblages may evolve but cannot represent actual mineralogical changes in the experiments. In case of the sluggish reaction kinetics of silicates, thermodynamic equilibrium may be reached in geological time scales at the experimental conditions of the present study but not in laboratory time scales.

5.3.3 Relationship between Fluid Chemistry and Kinetically Controlled Dissolution-Precipitation Processes

Proportions of concentrations of dissolved Na, Al, Si, K, and Ca were not in stoichiometric proportions of the solid starting materials of a QLM sandwich flow-through experiment (ft-s-4, Table 5.6) indicating that the pore fluid composition resulted from kinetically controlled dissolution-precipitation processes. The ratios of the amount of substance relative to Ca in the solid starting material, n_i/n_{Ca}, were approximately 1.8, 5.7, 67.4, and 1.7 for Na, Al, Si, and K, respectively. Ca was arbitrarily used as a reference because n_{Ca} was lowest in the solid starting material. The ratios of concentrations of these elements relative to the Ca concentration in the pore fluid, c_i/c_{Ca}, resulting from the experiment were approximately 1.5, 0.004, 4.7, and 0.07. The data suggests that the minerals did not dissolve in proportion to their stoichiometry, i.e. the dissolution was incongruent (Lasaga, 1983). The proportion of Na relative to Ca in the fluid was similar to the stoichiometric proportions in the solid starting material but c_i/c_{Ca}, with i = Al, Si, K, were highly depleted compared to the solid material.

The overall reaction of, e.g., K-feldspar with water incorporates not only the dissolution of feldspar but also the precipitation of gibbsite (Lasaga, 1983):

$$KAlSi_3O_8 + 4H^+ + 4H_2O \rightleftharpoons Al^{3+} + 3H_4SiO_4 + K^+, \tag{5.5}$$

$$Al^{3+} + 3OH^- \rightleftharpoons Al(OH)_3, \tag{5.6}$$

Scientific Technical Report STR 12/07
DOI: 10.2312/GFZ.b103-12079
Deutsches GeoForschungsZentrum GFZ

where H^+ and OH^- result from the dissociation reaction of water. Equations 5.5 and 5.6 are written as equilibrium reactions for which the law of mass action can be used to calculate the equilibrium constants K_s. Precipitation of $Al(OH)_3$ occurs when Al^{3+} and OH^- are supersaturated with respect to gibbsite. According to the PHREEQC LLNL-database the logarithm of the equilibrium constant is $\log K_s = 7.74$ for Equation 5.6 indicating that $Al(OH)_3$ is supersaturated at very small activities of Al^{3+} and OH^- in the fluid. In the present case a mixture of quartz, plagioclase (labradorite-andesine), and K-feldspar (microcline) was used as the solid starting material leading to several potential reactions, like Equations 5.5 and 5.6, comprising the overall fluid-solid reaction. Moreover, each individual reaction proceeds with its individual reaction rate according to kinetic theory yielding a complex evolution of the fluid chemistry with time.

Na was released in quasi-stoichiometric proportions into the fluid indicating that the Na-bearing minerals, labradorite-andesine and microcline, were at quasi-equilibrium with the fluid (Table 5.6). The depletion of Si in the pore fluid relative to the solid material may have resulted from the low solubility of quartz under the present conditions. The depletion of Al and K in the fluid indicates that removal of these species from the solution (adsorption and/or precipitation) of Al- and K-bearing solid phases must have occurred.

5.3.4 Identification of the Reaction Mechanism

Reaction Mechanism in Quartz-Feldspar Granular Aggregates

Fluid chemical and microstructural investigations point to a reaction mechanism of dissolution of ions from the crystals into the pore fluid and precipitation of mainly amorphous materials from the solution in the experiments with quartz-feldspar (and partly illite) granular aggregates. The decreasing trends with time of σ_f in QLM batch experiments indicate that ions were time-dependently removed from the bulk solutions in contact with quartz-feldspar-(illite) granular aggregates at a constant temperature of 150 °C (Figure 4.26). Chemical fluid analyses support this interpretation and showed that especially Al but also K and Ca species were time-dependently removed from the bulk solutions (Figure 4.28). Moreover, chemical fluid analyses of samples recovered from QLM(I) flow-through and batch experiments showed that the solids did not dissolve in stoichiometric proportions (Tables 5.4, 5.5 and Figure 4.28) indicating incongruent dissolution or precipitation (e.g., Lasaga, 1983).

Microstructural changes, resulting from incongruent dissolution and/or precipitation, were observed on solids resulting from two QLM experiments (b-QLM-5 and ft-s-4). These experiments featured long residence times of the fluids at approximately 150 °C (approximately 70 and 29 d) and low fluid/solid mass ratios (approximately 0.24 and 0.5 in b-QLM-5 and ft-s-4, respectively). SEM and TEM investigations of solids recovered from the experiments illustrated that alteration products occurred on grain surfaces, especially on labradorite-andesine grain surfaces, as sub-micrometer sized particles (Figures 4.22, 4.21, 4.23, 4.24, 4.33, and 4.32). TEM investigation of a labradorite-andesine and a microcline grain, recovered from a QLM sandwich flow-through experiment, showed that the alteration products were porous, mainly amorphous, and that the interfaces between the secondary formations and the original feldspar surfaces were sharp on the nanometer scale. A spatial coupling exists between the precipitates and the original feldspar material, i.e., a K-bearing phase precipitated on the microcline grains and a Ca-bearing phases precipitated on the labradorite-andesine grains.

The underlying processes of the formation of altered layers on feldspar surfaces are a subject

Scientific Technical Report STR 12/07
DOI: 10.2312/GFZ.b103-12079
Deutsches GeoForschungsZentrum GFZ

of debate. The altered layers on weathered feldspars are commonly referred to as leached layers and have a composition different from both the bulk mineral and the fluid (Chardon et al., 2006). The contrasting models for the formation of altered layers on feldspar surfaces are: (i) Preferential leaching of alkali metal ions including volume diffusion of these ions and H^+ through the leached layer (e.g., Chou and Wollast, 1985; Hellmann et al., 1990; Walther, 1996; Nesbitt and Skinner, 2001), versus (ii) a surface reaction model including stoichiometric dissolution coupled to precipitation of a secondary phase and release of ions into solution (e.g., Putnis, 2002; Hellmann et al., 2003; Zhu et al., 2006). A review on the reactions of feldspar surfaces with aqueous solutions has shown that a model of stoichiometric dissolution of feldspar coupled to the precipitation of secondary phases depleted in alkali metal ions can be used to describe many features like non-stoichiometric molar proportions of ions in solution and depletion of the leached layer with respect to alkali metal ions. Furthermore, the model is valid over the full range of pH (Chardon et al., 2006).

Flow-through experiments with albite and labradorite granular aggregates at variable pH-values, temperatures up to 300 °C, and pressures up to 17×10^6 Pa have shown that interfacial dissolution-reprecipitation was the underlying process leading to altered layers on feldspar surfaces (Hellmann et al., 1990, 1997, 2003). Na-, Al-, and O-depleted zones on albite surfaces were approximately 90×10^{-9} m thick. The depth of the depleted layer was pH-dependent, i.e., it was deeper at basic and acid pH than at neutral pH. Furthermore, more equivalents of H^+ were consumed than equivalents of Na^+ and Al^{3+} were released into solution. Ions of the background electrolytes (Cl^- and Ba^{2+}) were incorporated into the depleted layer. Al concentrations in the effluent fluid showed an initial increase and later decrease with time (Hellmann et al., 1990). Leached layers formed on albite due to H^+-Na^+ ion exchange reactions in experiments at 300 °C under acidic conditions (Hellmann et al., 1997). However, the interface between Na-, Al-, K-, and Ca-depleted layers and original labradorite was sharp on the nanometer scale in experiments with labradorite at acidic conditions and room temperature. The conclusion of this observation was that volume interdiffusion of H^+ and preferential leaching of cations could not account for the observed sharp interface but that interfacial dissolution-reprecipitation was the underlying process leading to the altered layers (Hellmann et al., 2003).

The microstructural features observed in the present study support the surface reaction model. The initial increase and later decrease of c_{Al} with time (Hellmann et al., 1990) is consistent with the observations made in the present study (e.g., Figure 4.28). The microstructural features are indicative for an interface coupled dissolution-precipitation process that has been observed in many mineral replacement reactions involving a fluid phase (Putnis, 2002). However, the interface between the amorphous precipitate and the original microcline was not affected by the lamellar microstructure of the microcline (Figure 4.24). Investigations of the dissolution of a perthitic alkali feldspar in natural weathering environment and in HF-etching experiments have shown that the dissolution is concentrated at core dislocations associated to perthitic (albite) exsolution lamellae (Lee and Parsons, 1995). Thus, the interface pertaining to an interface coupled dissolution-precipitation process should have been affected by the microstructure. As a consequence, the amorphous phases on the feldspar grains precipitated from the bulk solution but were nevertheless spatially coupled to the original feldspar material.

Hypothesis for the Reaction Mechanism in Rock Samples

Although there is no direct observation of alteration features in the Flechtinger sandstone samples, the dissolution-precipitation reactions observed in the QLM model systems point to

Scientific Technical Report STR 12/07
DOI: 10.2312/GFZ.b103-12079

similar reactions in the rock. Alteration features, resulting from fluid-mineral interactions of water with quartz-feldspar granular aggregates, were observable on samples resulting from flow-through and batch experiments (ft-s-4 and b-QLM-5). A combined interpretation of microstructural features and the evolution of σ_f and c_i in QLM(I) batch experiment supports a reaction mechanism of kinetically controlled dissolution of solid phases and precipitation of small, mainly amorphous, particles from the bulk solution. This reaction mechanism would lead to small changes in porosity of the rock samples and to a redistribution of mass from larger pores to smaller pores during flow. The small size, the amorphous nature, and the low mass of the proposed precipitates may have prevented their identification by SEM and XRD in the rock samples.

The permeability reductions at constant temperature and pressure, the σ_r evolution, as well as the chemical analyses in combination with hydrogeochemical modeling support a dissolution-precipitation mechanism in the Flechtinger sandstone experiments. The permeability evolution at constant temperature and pressure showed that permeability reductions were independent on measurement frequency indicating that the permeability reduction was only partly due to hydrodynamic mobilization of fine particles (Figure 4.11). The σ_r evolution of a Flechtinger sandstone flow-through experiment (ft-Fl-9) yielded a slight decrease of σ_r with time after cooling from approximately 150 to 70 °C (Figure 4.1b). This observation is consistent with the time-dependent precipitation of solids from the pore fluid. The chemical analyses of the fluids resulting from experiments with Flechtinger sandstone material in combination with hydrogeochemical modeling showed that the fluids resulting from flow-through and batch experiments were generally supersaturated with respect to various minerals (Figures 4.8 and 4.30).

5.4 Kinetics of the Dissolution-Precipitation Reactions

The evolution of the normalized electrical conductivity, $\sigma_r(t)/\sigma_r(0)$, of Flechtinger sandstone samples was used as a proxy for the kinetics of dissolution-precipitation processes. The initial rates of the $\sigma_r(t)/\sigma_r(0)$ increases with time were dependent on temperature (Figures 5.5 and 5.7). Two different phases of the σ_r evolution of the experiments were investigated: *phase a* denotes the experimental stage prior to heating to maximum temperatures and *phase b* stands for the experimental stage after the samples were heated to maximum temperatures. The rock samples were initially flushed with H_2O at $\Delta t = 0$ of each constant temperature stage.

Empirical rate laws were derived for the evolution of $\sigma_r(t)/\sigma_r(0)$ of the rock samples (Figure 5.5) in analogy to the differential method for the determination of the activation energy, E_a, of a chemical reaction (Appelo and Postma, 1999). For processes, in which competing and/or simultaneously operating mechanisms with different individual activation energies are involved, the term apparent activation energy, E_a^*, has been introduced (Nicholas, 1959). Since there are at least two mechanisms governing the electrical conductivity of rocks, i.e., electrical conduction at the mineral-fluid interfaces and electrolytic conduction through the pore fluid, it is appropriate to use the term apparent activation energy in the context of the present study. Plots of $\ln[\mathrm{d}(\sigma_r(t)/\sigma_r(0))/\mathrm{d}t]$ versus $\ln(\sigma_r(t)/\sigma_r(0))$ yielded the natural logarithm of the rate constant, $\ln k^*$, according to:

$$\ln \frac{\mathrm{d}(\sigma_r(t)/\sigma_r(0))}{\mathrm{d}t} = \ln k^* + n \ln(\sigma_r(t)/\sigma_r(0)), \tag{5.7}$$

Scientific Technical Report STR 12/07
DOI: 10.2312/GFZ.b103-12079

Table 5.7: Apparent activation energies calculated from experiments ft-Fl-8 and ft-Fl-9.

Compared Data	**Compared Temperatures** (T_1/T_2) °C	**Period** (Δt) d	E_a^* $\times 10^3$J/mol
ft-Fl-8a/ft-Fl-9a	51/70	1	49
ft-Fl-8a/ft-Fl-9a	51/70	2	41
ft-Fl-8b/ft-Fl-9b	55/70	1	49
ft-Fl-8b/ft-Fl-9b	55/70	2	31
ft-Fl-8b/ft-Fl-8b	55/90	1	42
ft-Fl-8b/ft-Fl-8b	55/90	2	29
ft-Fl-9b/ft-Fl-8b	70/90	1	37
ft-Fl-9b/ft-Fl-8b	70/90	2	27

where n is the reaction order. Equation 5.7 is analogous to the general rate equation of a hypothetical reaction A $\rightarrow$ B (Equation 2.49). The apparent activation energy can be calculated from the slopes of linear regressions in a plot $\ln k^*$ versus $1/T$ (Figure 5.6) by means of the Arrhenius equation (Equation 2.53). The resulting E_a^* were approximately 66×10^3 J/mol for *phase a* (Figure 5.5a) and approximately 87×10^3 J/mol for *phase b* of the experiments (Figure 5.5b).

The method of fitting empirical rate equations for the determination of E_a^* has the disadvantages that the value of k^* depends on the empirical selection of the rate equation and that it is not possible to ascertain whether E_a^* changes during the course of an isothermal process (Putnis, 1992). An alternative approach to the determination of E_a^* is (Kada-Benameur et al., 2000):

$$E_a^* = R^* \left(\frac{T_{\mathrm{abs},1}\, T_{\mathrm{abs},2}}{T_{\mathrm{abs},1} - T_{\mathrm{abs},2}} \right) \left(\ln \frac{\Delta(\sigma_r(t)/\sigma_r(0))_1}{\Delta t_1} - \ln \frac{\Delta(\sigma_r(t)/\sigma_r(0))_2}{\Delta t_2} \right), \qquad (5.8)$$

where R^* is the gas constant, $T_{\mathrm{abs},1,2}$ are the thermodynamic temperatures of T stages 1 and 2, and $\Delta(\sigma_r(t)/\sigma_r(0)_1)/\Delta t_1$ and $\Delta(\sigma_r(t)/\sigma_r(0)_2)/\Delta t_2$ are the slopes of the normalized σ_r per time at $T_{\mathrm{abs},1}$ and $T_{\mathrm{abs},2}$, respectively. These slopes are analogous to k^* in the Arrhenius equation. Following this approach, E_a^* can be presented as a continuous function of time (Figure 5.7).

The apparent activation energy shows a decreasing trend in *phase a* of the experiments (Figure 5.7a) and it exhibits substantial noise in *phase b* of the experiments (Figure 5.7b). Simple moving averages, SMA, with a period of 1 d were used to smooth the curves. The slopes of the individual $\sigma_r(t)/\sigma_r(0)$ curves for the different temperatures are significantly different in the beginning (< 3 d) and are approximately equal in the remainder of the experiments. Thus, $\Delta(\sigma_r(t)/\sigma_r(0))/\Delta t$ is clearly temperature-dependent in the initial stage of the experiments but appears to be not so in the later stage of the experiments.

In *phase a* of the experiments, E_a^* (as determined by Equation 5.8) is approximately 49 and 41×10^3 J/mol for $\Delta t = 1$ d and $\Delta t = 2$ d, respectively (Table 5.7). The slopes of the SMA of the 51 and the 70 °C data are almost identical at $\Delta t > 3$ d leading to noisy E_a^* with values in the range of 0 to 25×10^3 J/mol (Figure 5.7a). In *phase b* of the experiments, mean E_a^* are 43 ± 5 and $29 \pm 2 \times 10^3$ J/mol for $\Delta t = 1$ d and $\Delta t = 2$ d, respectively. The slopes of the SMA of the 70 and 90 °C data are almost identical at $\Delta t > 2$ d and are partly negative due to temperature fluctuations (Figure 5.7b). Equal or negative slopes of SMA yielded $E_a^* = 0$ and

Scientific Technical Report STR 12/07
DOI: 10.2312/GFZ.b103-12079
Deutsches GeoForschungsZentrum GFZ

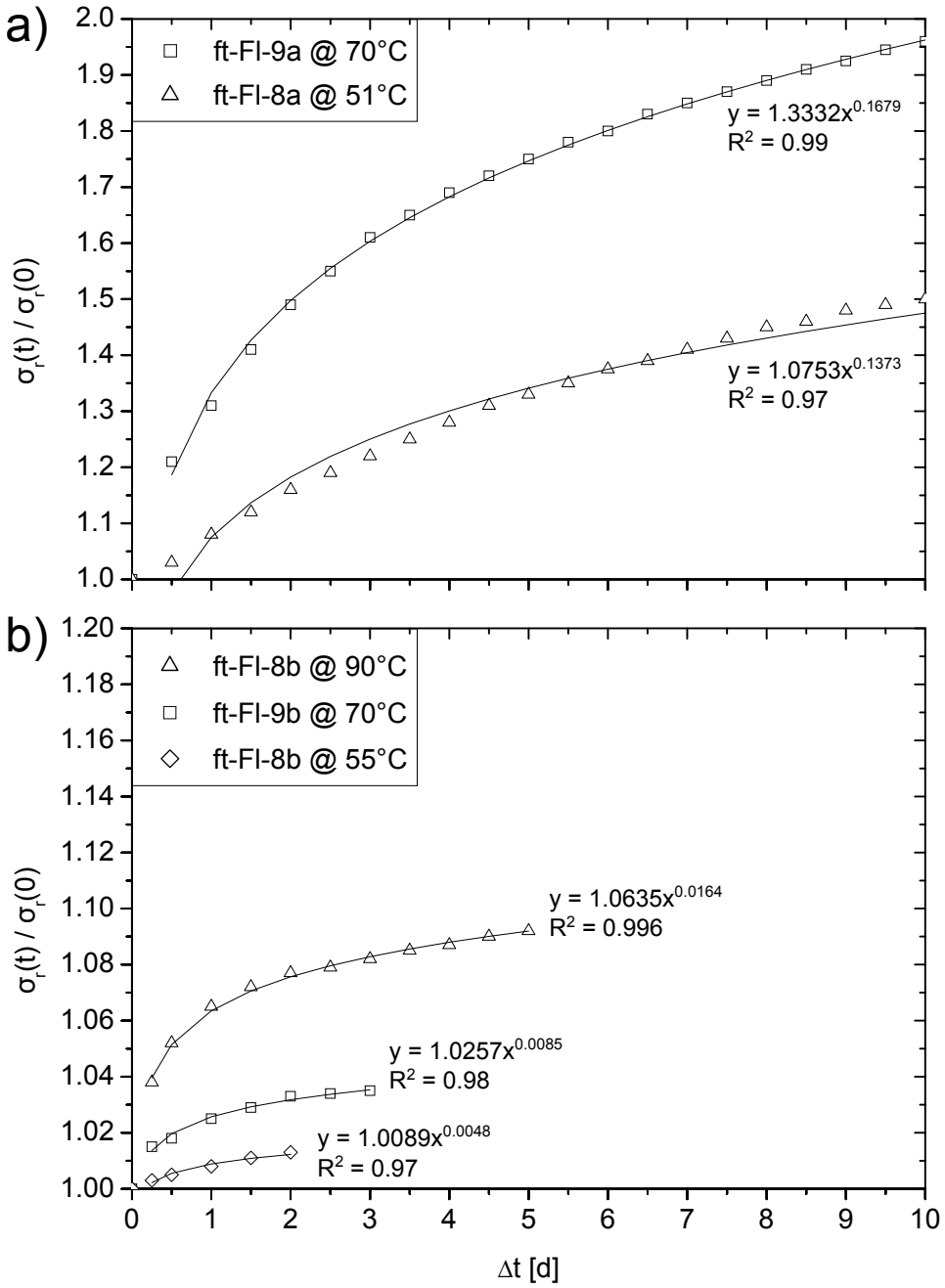

Figure 5.5: Power-laws for the normalized electrical conductivity, $\sigma_r(t)/\sigma_r(0)$, of Flechtinger sandstone samples as a function of elapsed time, Δt, for different temperatures in experiments ft-Fl-8 and ft-Fl-9. (a) The curves ft-Fl-8a at 51 °C and ft-Fl-9a at 70 °C resulted from the experimental stage prior to heating to maximum temperatures (*phase a*). (b) The data resulted from experimental stages after the samples were heated to maximum temperatures (*phase b*). The fitted power-laws are drawn as solid lines for each graph.

Scientific Technical Report STR 12/07
DOI: 10.2312/GFZ.b103-12079

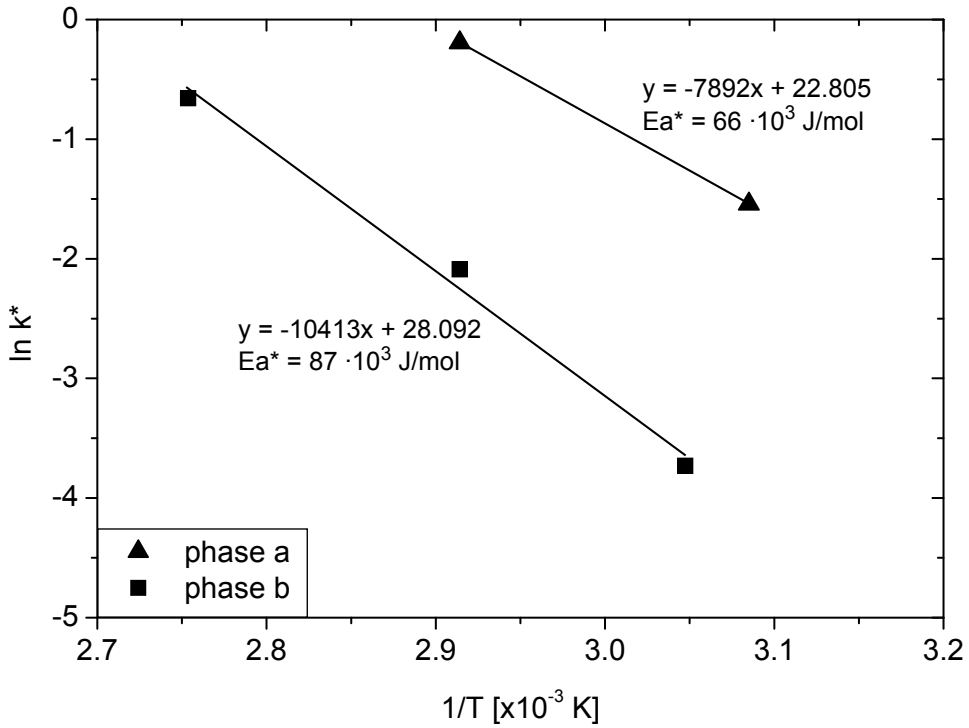

Figure 5.6: Arrhenius plots for the electrical conductivity evolution of Flechtinger sandstone samples at different temperatures. The logarithm of the rate constant, $\ln k^*$, was derived from Equation 5.7. The apparent activation energies, E_a^*, for *phase a* and *phase b* of the electrical conductivity evolution of Flechtinger sandstone samples are approximately 66 and 87×10^3 J/mol, respectively (Equation 2.53).

Scientific Technical Report STR 12/07
DOI: 10.2312/GFZ.b103-12079

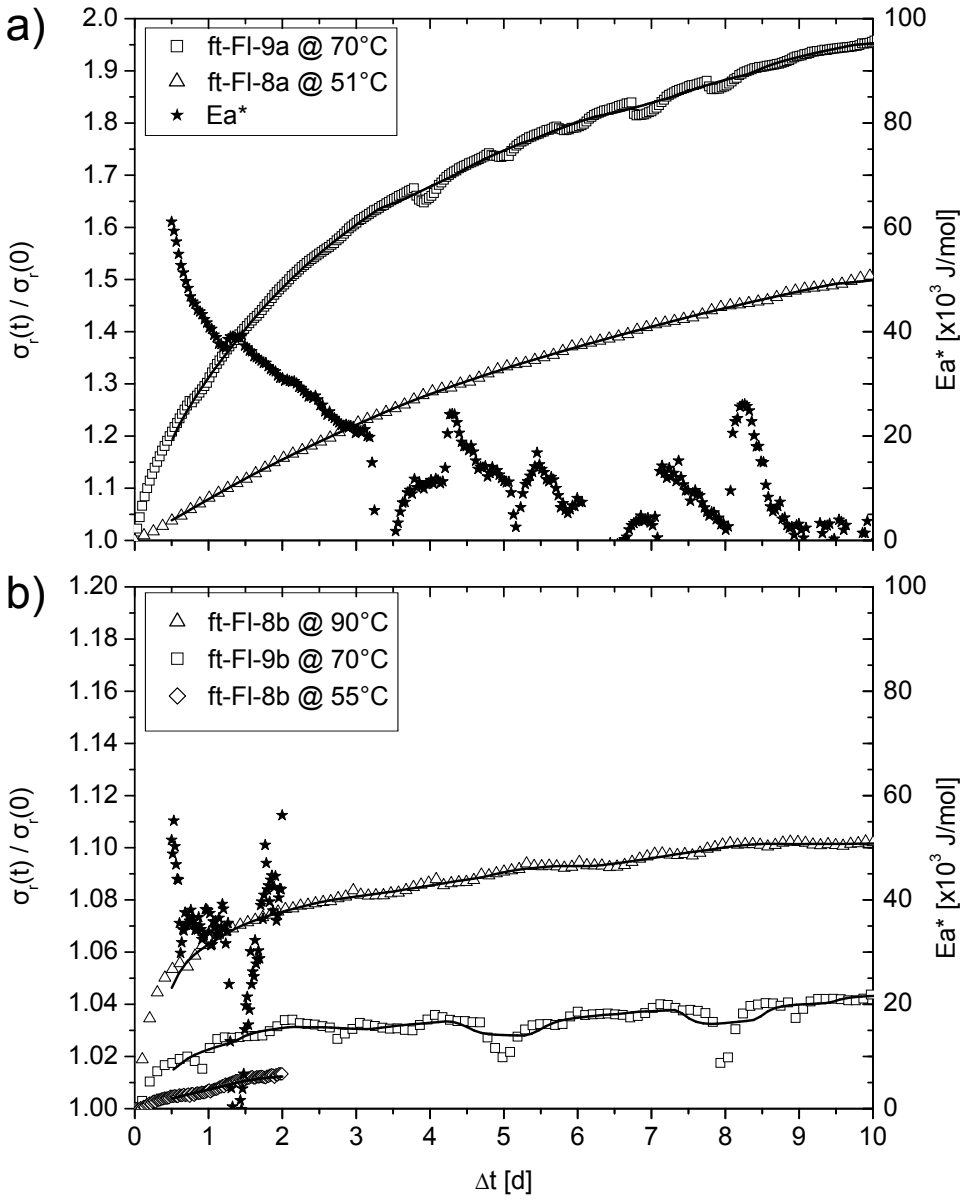

Figure 5.7: Normalized electrical conductivity, $\sigma_r(t)/\sigma_r(0)$, of Flechtinger sandstone samples as a function of elapsed time, Δt, for different temperatures in Flechtinger sandstone experiments ft-Fl-8 and ft-Fl-9. (a) The curves ft-Fl-8a at 51 °C and ft-Fl-9a at 70 °C result from the experimental stage prior to heating to maximum temperatures (*phase a*). (b) The data result from experimental stages after the samples were heated to maximum temperatures (*phase b*). Simple moving averages, SMA, with a period of 1 d are drawn as solid lines for each graph. Calculated apparent activation energies, E_a^* (Equation 5.8), are plotted for $\Delta t = 10$ d (a) and for $\Delta t = 2$ d (b), $T_{\mathrm{abs},1} = 328.15$ K, and $T_{\mathrm{abs},2} = 363.15$ K.

Scientific Technical Report STR 12/07
DOI: 10.2312/GFZ.b103-12079

Table 5.8: Activation energies of dissolution in aqueous solutions from selected references.

Dissolving Material	**Fluid**	T**-Range** °C	E_a $\times 10^3$J/mol	**Reference**
Fused quartz (amorphous)	H_2O	25–250	74.5 ± 1.4	Icenhower and Dove (2000)
Fused quartz (amorphous)	0.05 mol/L $NaCl_{aq}$	80–200	83.4 ± 3.3	Icenhower and Dove (2000)
Fused quartz (amorphous)	H_2O	25–300	60.9–64.9	Rimstidt and Barnes (1980)
Quartz	H_2O	25–300	67.4–76.6	Rimstidt and Barnes (1980)
Quartz	H_2O	25–625	89 ± 5	Tester et al. (1994)
Illite	pH 7.7 buffer solution	4.5–50	14	Köhler et al. (2003)
Kaolinite	pH 3 0.001 mol/L $HClO_4$	25–80	29.3 ± 4.6	Ganor et al. (1995)
K-feldspar (adularia)	H_2O	25–650	≈ 38	Helgeson et al. (1984)
Plagioclase	soil pore fluid	6–19	75 ± 14	Williams et al. (2010)
Plagioclase (anorthite)	H_2O	25–70	35	Lasaga (1984)

$E_a^* < 0$. Thus, only data obtained for $\Delta t \leq 2$ d were used for the calculation of E_a^*.

Apparent activation energies of the $\sigma_r(t)/\sigma_r(0)$ evolution of Flechtinger sandstone flow-through experiments (Figures 5.6 and 5.7) are comparable to activation energies of dissolution of the main mineral phases of the rock (Table 5.8). The mean and the standard deviation from the mean of all reported E_a values are $59 \pm 23 \times 10^3$ J/mol. A compilation of E_a values of different common minerals has shown that the mean of E_a of dissolution of minerals is mostly in the range of 60×10^3 J/mol (Lasaga, 1984). Apparent activation energies calculated for the thermally activated increase of $\sigma_r(t)/\sigma_r(0)$ as a function of time is in the range of 29 to 87×10^3 J/mol. Thus, E_a values of the dissolution of the main phases of the Flechtinger sandstone and E_a^* values for the initial phase of the $\sigma_r(t)/\sigma_r(0)$ evolution are in the same range. This observation may indicate that the $\sigma_r(t)/\sigma_r(0)$ evolution was dominated by the dissolution of minerals in the initial phases of each constant temperature stage of the experiments, when H_2O was the initial pore fluid.

The decrease of E_a^* with time could be attributed to a change in the dominant mechanisms governing the $\sigma_r(t)/\sigma_r(0)$ evolution. The Arrhenius equation shows that the temperature dependence of the reaction rate constant vanishes as E_a^* approaches zero (Equation 2.53). It can be assumed that the linear trends of each $\sigma_r(t)/\sigma_r(0)$ curve after approximately 3 to 4 d reflected phases in which σ_r-increasing and σ_r-decreasing processes were at equilibrium. After a suitably long time (> 30 d at 70 °C), σ_r values approached horizontal lines in Flechtinger sandstone flow-through experiments (Figures 4.1b and c). This behavior is consistent with dynamic equilibria of dissolution of the main mineral phases of the solid material and precipitation of secondary phases from the pore fluid eventually leading to steady-state conditions.

5.5 Consequences of Pore-Scale Dissolution-Precipitation Reactions for Permeability

5.5.1 Comparison of Different Permeability-Changing Processes

In the course of the flow-through experiments, different permeability-changing processes took place: clay swelling due to initial saturation with H_2O of most Flechtinger sandstone samples, thermo-mechanically induced changes of the pore space during heating, and dissolution-precipitation reactions. Clay swelling and thermo-mechanically induced permeability changes can be interpreted as experimental artifacts:

Scientific Technical Report STR 12/07
DOI: 10.2312/GFZ.b103-12079
Deutsches GeoForschungsZentrum GFZ

(i) Permeability decreased almost instantaneously and almost irreversibly due to clay swelling in the course of fluid exchange procedures in Flechtinger sandstone flow-through experiments (ft-Fl-11 and ft-Fl-12, Figure 4.12). In the pore fluid exchange procedures, $NaCl_{aq}$ solutions were replaced by fluids with lower salinities (down to H_2O) at constant temperatures and pressures. The experiments showed that clay swelling affected k as soon as the pore fluid was completely replaced by a fluid with a lower salinity. Replacement of H_2O by a 2 mol/L $NaCl_{aq}$ solution as the pore fluid led to a minor k increase, indicating that the k reduction due to clay swelling was only partly reversible.

The significance of the formation damage prior to the experiments can be deduced from a comparison of the initial permeabilities of rock samples in fluid exchange experiments (ft-Fl-11 and ft-Fl-12) to a Flechtinger sandstone sample that was initially saturated with a 1 mol/L $NaCl_{aq}$ solution (ft-Fl-10). The samples in the fluid exchange experiment were initially saturated with H_2O. The initial k decrease before the experiments amounts to a factor of approximately 2 to 3 due to clay swelling induced by saturation with H_2O at room temperature (k_0 values were 0.602, 0.16, and 0.284×10^{-15} m^2 in ft-Fl-10, ft-Fl-11, and ft-Fl-12, respectively).

Although the clay swelling had a significant impact on the permeability of clay-bearing Flechtinger sandstone samples, the process was completed in the initial phase of the experiments. Thus, in the constant temperature and constant pressure stages of the experiments, which were investigated with respect to the effect of dissolution-precipitation reactions on permeability, clay swelling did not occur. Clay swelling is therefore an experimental artifact with respect to the investigation of the effect of dissolution-precipitation reactions on permeability.

(ii) Permeability decreased significantly with temperature during the heating stages of flow-through experiments to values ranging between approximately 1 and 54 % of initial permeability (Figure 4.10a and Table 4.4). The normalized permeability k/k_0 decreased with temperature in relatively short periods of time (< 3 d in most experiments) compared to the total durations of the experiments (up to 139 d). Thus, the decrease of permeability as a function of temperature was not kinetically controlled but was due to thermo-mechanical effects that changed the pore space structure of the samples.

Permeability reductions with temperature have also been observed in experiments with Berea, Boise, Bandera, and Gosford sandstones (Somerton et al., 1981; Fischer and Paterson, 1992; Somerton, 1992). Experiments with Berea, Boise, and Bandera sandstones at variable hydrostatic confining pressures $p_c < 27.6 \times 10^6$ Pa, pore pressures $6.9 < p_p < 20.7 \times 10^6$ Pa, and temperatures $30 < T < 175$ °C have shown that k decreased with temperature. It has been concluded that the k decrease with temperature resulted from an anisotropic thermal expansion of mineral grains, especially quartz, in the confined rocks. Moreover, it has been observed that the k decrease was permanent due to a permanent deformation of the rock samples (Somerton et al., 1981; Somerton, 1992). Permeability measurements on deforming Gosford sandstone with a strain of up to 20 % have shown that porosity decreased by a factor of approximately 2 due to heating at constant effective pressure. Furthermore, porosity increased with decreasing effective pressure. The permeability behaved in a similar way as the porosity. The Gosford sandstone samples had an initial porosity of approximately 15 %, p_c was constant at 300×10^6 Pa, p_p was varied in the range of 20 to 270×10^6 Pa, and the temperature was varied in the range of 25 to 600 °C. Permeability measurements were performed on undeformed and deformed specimens using a p_p-oscillation method with Ar as the confining pressure medium and the pore fluid. Deformed samples were measured at strain intervals of 10 %. During permeability measurements of deformed samples, deformation was continued at a strain rate that gave rise to zero dilatancy. The general effect of an increase in temperature was a k decrease accompanied

Scientific Technical Report STR 12/07
DOI: 10.2312/GFZ.b103-12079
Deutsches GeoForschungsZentrum GFZ

by a decrease in porosity due to increased thermal relaxation effects and a reduction of dilatancy during deformation. Furthermore, k changed irreversibly during a heating and cooling cycle due to non-elastic changes in the pore structure (Fischer and Paterson, 1992).

However, the response of permeability to heating seems to be dependent on the sample material. A long-term flow-through experiment with a Lower Permian (Rotliegend) sandstone sample cored from a prospective oil and gas well in Eberswalde, Germany, did not show permeability changes within the temperature interval of 30 to 150 °C. The initial porosity and permeability of the sample were 11.1 % and $\approx 5 \times 10^{-15}$ m^2, respectively. The pore fluid was a synthetic formation fluid (Ca-Na-Cl type) with a high salinity (≈ 255 g/L). The experiment was conducted at 50×10^6 Pa confining pressure, 5×10^6 Pa pore pressure, and at a maximum temperature of 150 °C (Milsch et al., 2009). It can be assumed that the differences in the response of permeability to temperature changes were related to the origin of the tested rock samples. The Flechtinger, Berea, Boise, Bandera, and Gosford sandstone samples originated from outcrops, whereas the Rotliegend (Eberswalde) sample originated from a borehole. This interpretation suggests that the response of permeability to temperature changes was related to the microstructure of the samples (i.e., the grain-grain contacts may have been firmer in the core sample from a borehole than in the outcrop samples that underwent mechanical stress relaxation during uplift).

The permeability of different sample types generally increased with decreasing temperature in the experiments performed in the present study (Figure 4.10b and Table 4.4). This observation was made on experiments with cooling stages with durations < 3 d (ft-s-1, ft-s-2, ft-Fl-10, and ft-Fl-11). Thus, it can be deduced that the observed k increases with decreasing temperature were not due to kinetically controlled processes but were of thermo-mechanical origin (as the k decrease due to heating). Changes in k were in the range of almost zero to approximately 35 % relative to the total k changes and showed no regular pattern with respect to duration of the experiment, sample type, or range of the temperature interval from high to low temperatures. A Flechtinger sandstone sample with 1 mol/L $NaCl_{aq}$ as the pore fluid (ft-Fl-10), for example, showed a negligible k increase with decreasing temperature, suggesting that not only the thermal expansion of the quartz and feldspar grains affected the permeability of the sample but also the swelling behavior of the clay minerals in the rock. In contrast to this, a Flechtinger sandstone experiment (ft-Fl-11) and a labradorite-andesine sandwich experiment (ft-s-1) yielded a permeability recovery of > 30 % of the total permeability change (Table 4.3).

To summarize, the k changes with temperature due to thermo-mechanical effects were mainly irreversible and had only a small elastic component. Experimental strategies that aim at investigating k changes of porous media due to chemical interactions between the solids and the pore fluids should therefore be performed with samples preheated to maximum temperatures at constant confining pressures in order to avoid artifacts resulting from the irreversible component of thermo-mechanical effects.

Although permeability changes with temperature were generally large, these processes were completed when the maximum temperature of the flow-through experiments was reached. Thus, the thermo-mechanically induced permeability changes did not affect the permeability in the constant temperature and constant pressure stages of the experiments. Permeability changes due to heating can therefore be regarded as an experimental artifact with respect to the investigation of the effect of dissolution-precipitation reactions on permeability at constant temperature and pressure conditions.

(iii) Permeability reductions at constant temperature and pressure were generally small compared to the k changes due to heating (Table 4.4). However, two Flechtinger sandstone

Scientific Technical Report STR 12/07
DOI: 10.2312/GFZ.b103-12079
Deutsches GeoForschungsZentrum GFZ

flow-through experiments (ft-Fl-8 and ft-Fl-11) showed comparable k reductions in the heating stage and at constant temperatures. One sample (ft-Fl-8) had a relatively large permeability reduction with temperature during heating from 30 to 51 °C followed by an insignificant permeability change during further heating to 164 °C (Figure 4.10). The permeability of the sample exhibited a comparatively large reduction during the constant temperature and constant pressure stage (Figure 4.11). The durations of the 51 and 164 °C constant temperature and pressure stages of the experiment were long (39 d, Figure 4.1a). The long durations of the 51 and 164 °C constant temperature and pressure stages are in accordance with two interpretations: (a) thermo-mechanically induced permeability changes may have been completed during the lower temperature stage. Thus, further heating did not influence the permeability. This interpretation would be in line with the observation that the response of permeability to heating was sample dependent. It can be assumed that the long residence time of the sample at 51 °C and 5×10^6 Pa effective pressure led to firmer grain-grain contacts giving rise to a similar behavior as the (Eberswalde) sandstone core from a borehole (Milsch et al., 2009). (b) The long residence time of the sample at 164 °C is probably related to kinetically controlled permeability-changing processes (dissolution-precipitation reactions). Both permeability-changing processes have similarly contributed to the overall permeability reduction (Table 4.4).

Another Flechtinger sandstone sample (ft-Fl-11) showed a comparatively large permeability reduction during a relatively low constant temperature stage ($\approx$ 72 °C, 12 d). The permeability in the beginning of the constant temperature stage was low ($k_{\text{heated}} = 3.8 \times 10^{-18}$ m^2) due to the replacement of $NaCl_{aq}$ solutions by H_2O before the heating of the sample (Figure 4.12). The effect of small changes in the pore space on the already low permeability of the sample can be estimated under the assumption that the porosity can be approximated by a pack of cylindrical pipes with a constant radius. Evaluation of the Kozeny-Carman equation (e.g., Equations 2.21, 2.22, and 2.24) states that k is proportional to the square of the radius of a cylindrical pipe provided that the flow is laminar, and that the flow rate, the geometry of the sample, and the dynamic viscosity of the fluid are constant. Equation 2.24 yields a capillary radius $r \approx 0.11 \times 10^{-6}$ m, when the porosity and the electrical tortuosity are assumed to be $\phi = 11.5$ % and $\tau_e = 6.6$, respectively (Table 4.2). The measured permeability at the end of the constant temperature stage of the experiment was $k_{\text{heated,min}} = 2.9 \times 10^{-18}$ m^2. Accordingly, the capillary radius is $r \approx 0.1 \times 10^{-6}$ m, when ϕ and τ_e are assumed to be constant. Thus, a small change in the capillary radius of $\approx 0.01 \times 10^{-6}$ m could have accounted for the observed permeability decrease.

5.5.2 Changes in the Volume and the Structure of the Pore Space

There is no clear trend of specific surface area changes in the flow-through and batch experiments with quartz-feldspar granular aggregates (Table 5.9). For the experiments with granular aggregates only BET surface areas were available. A sample from a QLM sandwich flow-through experiment (ft-s-3) showed a slight increase of SA_{BET} compared to the QLM starting material of the grain size fraction 63 to 125×10^{-6} m. Samples from the QLM batch experiments (b-QLM-4 and b-QLM-5) showed a slight increase and a slight decrease of SA_{BET} compared to the QLM starting material. A sample from a batch experiment with the grain size fraction $< 63 \times 10^{-6}$ m (b-QLM-8) showed an increase of SA_{BET} compared to the QLM starting material. SEM investigations have shown that surfaces of grains resulting from a QLM batch experiment (b-QLM-5) were covered with alteration products and appeared to be rough compared to the starting material (Figures 4.33 and 4.32). Additional roughness would be expected to increase

Scientific Technical Report STR 12/07
DOI: 10.2312/GFZ.b103-12079
Deutsches GeoForschungsZentrum GFZ

Table 5.9: Comparison of specific surface areas and porosities obtained by different methods for Flechtinger sandstone and QLM starting materials and altered samples.

Sample	SA_{BET} m^2/g	SA_{MIP} m^2/g	ϕ_{MIP} %	ϕ_{2D} %	$\phi_{Archimedes}$ %
Fl-SST	2.586 ± 0.004	1.527 ± 0.05	9.59 ± 0.41	7.6 ± 0.5	10.4 ± 0.8
QLM (63-125)	0.0431 ± 0.0001	n.a.	n.a.	n.a.	n.a.
QLM (<63)	0.317 ± 0.003	n.a.	n.a.	n.a.	n.a.
ft-Fl-9	0.0247 ± 0.0003	0.38	7.3	9.4 ± 0.5	7.5
ft-Fl-10	0.0413 ± 0.0001	1.451	8.85	n.a.	n.a.
ft-Fl-11	n.a.	1.358	10.08	n.a.	n.a.
ft-Fl-12	n.a.	1.32	8.18	n.a.	n.a.
ft-s-3 (63-125)	0.0551 ± 0.0001	n.a.	n.a.	n.a.	n.a.
b-Fl-16	2.647 ± 0.003	1.492	10.29	n.a.	11.04
b-QLM-4 (63-125)	0.0493 ± 0.0003	n.a.	n.a.	n.a.	n.a.
b-QLM-5 (63-125)	0.0379 ± 0.0001	n.a.	n.a.	n.a.	n.a.
b-QLM-8 (<63)	0.488 ± 0.0003	n.a.	n.a.	n.a.	n.a.

n.a. denotes not applicable.
Fl-SST denotes Flechtinger sandstone starting material.
QLM (63-125) denotes the QLM starting material of the grain size fraction 63 to 125×10^{-6} m.
QLM (<63) denotes the QLM starting material of grain size fraction $< 63 \times 10^{-6}$ m.

the specific surface area. This increase was not observed in the BET analysis. A possible explanation for this apparent contradiction is that a decrease of specific surface area due to homogeneous dissolution of the mineral grains super-compensated the increase of specific surface area which is due to additional roughness of the altered grain surfaces.

However, MIP and BET measurements on the Flechtinger sandstone material consistently indicate that the specific surface areas decreased in the course of the flow-through experiments but were unchanged in the batch experiment compared to the starting material. However, the absolute values of specific surface areas obtained from MIP and from BET analysis (SA_{MIP} and SA_{BET}) yielded significantly different results for the Flechtinger sandstone samples resulting from flow-through experiments (ft-Fl-9 and ft-Fl-10), whereas the results SA_{MIP} and SA_{BET} for the Flechtinger sandstone starting material were comparable (Table 5.9). A Comparison of specific surface areas of the Flechtinger sandstone starting material and the sample resulting from a Flechtinger sandstone batch experiment (b-Fl-16) showed that SA_{BET} was larger than SA_{MIP}. In contrast, SA_{BET} was much smaller than SA_{MIP} in case of the materials resulting from the flow-through experiments.

The inconsistency between SA_{MIP} and SA_{BET} of the Flechtinger sandstone samples from flow-through experiments (ft-Fl-9 and ft-Fl-10) probably resulted from the fundamental differences in the calculation of specific surface areas in MIP and BET. The calculation of SA_{MIP} is based on the assumption that the pore space of a porous medium can be approximated by a pack of cylindrical capillaries and that the radius of each capillary-class is inversely proportional to the pressure necessary to force a non-wetting fluid, Hg, into the porous medium (Equation 3.10). The calculation of SA_{BET} is based on a gas adsorption model that assumes the adsorption and desorption of a monolayer of inert gas molecules at low temperature isotherms.

To summarize, the MIP and BET investigations of the Flechtinger sandstone samples resulting from flow-through and batch experiments showed that the pore space geometry changed in

Scientific Technical Report STR 12/07
DOI: 10.2312/GFZ.b103-12079
Deutsches GeoForschungsZentrum GFZ

the course of the flow-through experiments, however, it was not affected in the course of the batch experiment. The batch experiment was performed at a hydrostatic pressure of 5×10^6 Pa, whereas the flow-through experiments were performed at an effective pressure of 5×10^6 Pa. Further differences between the two experiment types were the fluid/solid mass ratio and the flow conditions. The discrepancy between SA_{MIP} and SA_{BET} of the Flechtinger sandstone samples resulting from the flow-through experiment can be explained by the different models underlying the calculation of specific surface areas in both methods. The comparatively large SA_{MIP} values possibly are indicative for an increased shielding of larger pores by smaller ones in the course of the flow-through experiments. An increased shielding of larger pores suggests a decreased accessibility or connectivity of the pore space (Diamond, 2000). A decrease in the connectivity of the pore space would agree with the observed permeability reductions in the flow-through experiments (e.g., Figure 4.11).

A comparison of porosity measurements by MIP, image analysis, and a water saturation method of Flechtinger sandstone samples resulting from experiments with different p-T conditions suggests that: (i) ϕ changes were related to confining pressure and high temperatures, and (ii) large pores expanded while small pores closed in the flow-through experiments (Table 5.9). Porosity was measured by MIP (ϕ_{MIP}), partly by image analysis (ϕ_{2D}), and partly by a water saturation method ($\phi_{Archimedes}$). Three samples (ft-Fl-9, ft-Fl-10, and ft-Fl-12) showed decreasing ϕ_{MIP} trends, whereas two samples (ft-Fl-11 and b-Fl-16) showed no significant ϕ_{MIP} changes compared to the starting material. The flow-through experiment that yielded the sample without a significant ϕ_{MIP} change (ft-Fl-11) was performed at a maximum temperature of 74 °C, whereas the other flow-through experiments were performed at a maximum temperature of ≈ 150 °C. The batch experiment that yielded a sample without a significant ϕ_{MIP} change (b-Fl-16) was conducted at a hydrostatic pressure of 5×10^6 Pa, whereas the flow-through experiments were performed at effective pressures of 5×10^6 Pa. Thus, the comparison of ϕ_{MIP} values of samples from flow-through and batch experiments suggests that confining pressure together with high temperatures accounted for the ϕ decreases. The porosity determined by water saturation, $\phi_{Archimedes}$, of the Flechtinger sandstone starting material and a sample resulting from a batch experiment was in agreement with ϕ_{MIP}. However, a comparison of ϕ_{2D} to ϕ_{MIP} yielded contrasting ϕ values (i.e., $\phi_{2D} < \phi_{MIP}$ for the Flechtinger sandstone starting material and $\phi_{2D} > \phi_{MIP}$ for sample ft-Fl-9). The increase of ϕ_{2D} of the sample relative to the starting material possibly resulted from the limited resolution of the SEM micrographs ($\approx 3 \times 10^{-6}$ m) that were used for the image analysis (Table 4.7). The interpretation of the MIP investigation in combination with the image analysis is that pores $> 3 \times 10^{-6}$ m expanded while pores $< 3 \times 10^{-6}$ m closed in the Flechtinger sandstone flow-through experiment. Such a behavior would be consistent with the observed permeability reduction and with a process of dissolution of pore filling cements and redistribution of mass to small pores. Yet, the comparison of porosity measurements of starting and altered materials reflects pore space-changing processes that occurred during the total duration of the experiments including clay swelling and thermo-mechanically induced changes of the pore space.

The investigation of the pore space of Flechtinger sandstone starting and altered materials by means of X-ray CT yielded no information on pore space changes in a Flechtinger sandstone flow-through experiment (ft-Fl-13, Figure 4.14). SEM and TEM investigations have shown that mineralogical changes and mass redistributions in the porous samples were very small, i.e., on the sub-micrometer scale. MIP pore throat radius distributions indicate that decreases in pore throat radii were mainly restricted to pore throats $< 0.2 \times 10^{-6}$ m. The resolution of the X-ray CT was approximately 2×10^{-6} m in the present study. Thus, decreases in pore (throat)

Scientific Technical Report STR 12/07
DOI: 10.2312/GFZ.b103-12079
Deutsches GeoForschungsZentrum GFZ

Table 5.10: Comparison of F, m, and τ_e before and after k reduction of Flechtinger sandstone samples ft-Fl-11 and ft-Fl-12.

Sample	k $\times 10^{-15}$ m^2	T °C	c $NaCl_{aq}$ mol/L	$\sigma_f(T_0)$ S/m	$\sigma_f(T)$ S/m	$\sigma_r(T)$ S/m	ϕ_0 %	F	m	τ_e
ft-Fl-11	0.127	42	0.5	4.78	6.65	0.115	11.5	58	1.9	6.6
ft-Fl-12	0.009	70	2	15.33	31.2	0.41	11.5	76	2	8.8

k denotes permeability.
ϕ_0 denotes initial porosity determined by saturation with 1 mol/L $NaCl_{aq}$.
F denotes formation resistivity factor (Equation 2.3).
m denotes cementation exponent (Equation 2.3).
τ_e denotes electrical tortuosity (Equation 2.5).

radii due to precipitation could not be measured using X-ray CT.

Investigations of the formation resistivity factor, F (Equation 2.3), before and after hydrothermally induced changes of permeability are a way to get insights into concurrent changes in microstructural properties of a porous material. In general, microstructural parameters of the rock, like ϕ and the cementation exponent m change in a complex way when the permeability changes. Since m is related to the electrical tortuosity τ_e of the material (Equation 2.5), changes in F would indicate changes in τ_e. An investigation of F before and after hydrothermally induced changes of the permeability of a porous material would require performing fluid exchange experiments with fluids with a large range of σ_f. Ideally, such fluid exchange experiments should be performed before and after pore space alterations have occurred. In the case of the illite-bearing Flechtinger sandstone samples, this strategy was precluded, because the fluid exchange procedure itself caused swelling of the illite in the pore space, leading to an alteration of the microstructural properties of the rock samples (Figure 4.12).

Yet, a comparison of F, m, and τ_e of an unaltered Flechtinger sandstone sample (ft-Fl-11) and a sample that had shown significant permeability reduction (ft-Fl-12) yielded changes in the microstructural parameters (Table 5.10). The data of the unaltered sample resulted from a flow-through experiment conducted with a 0.5 mol/L $NaCl_{aq}$ solution at 42 °C before a significant permeability reduction had occurred. The data of the altered sample resulted from a similar experiment, but after a significant permeability decrease had occurred. The porosity of the samples at the time of the measurements was not known. So, the initial porosity was assumed for both samples ($\phi \approx 11.5$ %). The altered sample with the lower permeability (ft-Fl-12) showed a higher value of F (Equation 2.3) and a higher value of τ_e (Equation 2.5). The higher value of τ_e is consistent with a lower permeability and an unchanged porosity compared to the unaltered sample (ft-Fl-11).

5.5.3 Relationships Between Permeability and the Structure of the Pore Space

Investigations of different types of porous materials have shown that the relationship between permeability and porosity (i.e., the volume of the pore space) can generally be described by power-laws (Bourbie and Zinszner, 1985; Mavko and Nur, 1997; Mok et al., 2002; Bernabé et al., 2003). Experimental values obtained for the porosity and permeability of Fontainebleau sandstone samples and sandwich samples with Fontainebleau sandstone as the confining porous discs (Figure 5.8) agree qualitatively with published data. Two distinct power-law k-ϕ

Scientific Technical Report STR 12/07
DOI: 10.2312/GFZ.b103-12079
Deutsches GeoForschungsZentrum GFZ

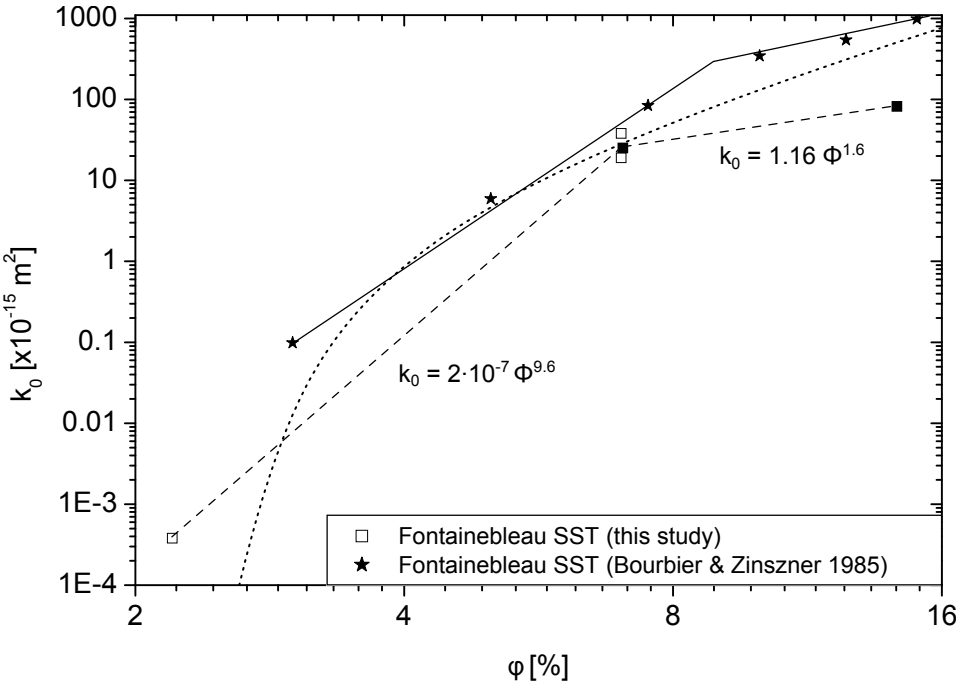

Figure 5.8: Logarithmic plot of the permeability-porosity relationship for Fontainebleau sandstone samples in comparison to published data (Bourbie and Zinszner, 1985). The solid lines indicate power-law k-ϕ correlations for the porosity ranges 3 to 9 % and 9 to 28 % for a large data set of Fontainebleau sandstone (Equations 2.30 and 2.31). The dashed lines represent similar power-law k-ϕ relationships found for Fontainebleau sandstone samples and sandwich samples of the present study. The dotted line represents the continous model by Mavko and Nur (1997) incorporating a percolation threshold of $\phi_c = 0.025$ (Equation 2.32). Core samples are displayed as filled symbols and sandwich samples are shown as open symbols.

correlations have been proposed for Fontainebleau sandstone in a porosity range of 3 to 28 %. For low porosities of 3 to 9 % and for high porosities of 9 to 28 %, exponents of ≈ 7.3 and ≈ 3, respectively, have been determined (Bourbie and Zinszner, 1985). In analogy to this approach, two power-law k-ϕ correlations with exponents of ≈ 9.6 and ≈ 1.6 for low porosities of 2.2 to 7 % and for higher porosities of 7 to 14.3 %, respectively, were determined in the present study.

The k-ϕ relationship of Fontainebleau sandstone has also been interpreted in terms of percolation theory (Mavko and Nur, 1997). The notion of a percolation threshold in percolation theory implies a critical value of the porosity effective for hydrodynamic flow. Thus, k is not only related to the volume but also to the structure of the pore space. The k-ϕ data obtained for Fontainebleau sandstone samples in the present study also agrees with a continuous k-ϕ relationship (Equation 2.32). The qualitative agreement of the present data with this model suggests that the investigated Fontainebleau sandstone samples approached the percolation threshold as porosity decreased. The k-ϕ data and Equation 2.32 show that the percolation threshold of the Fontainebleau sandstone samples is at approximately 2 to 3 % (Figure 5.8).

An interpretation of k-ϕ data of Flechtinger sandstone samples in the light of a fractal pore

Scientific Technical Report STR 12/07
DOI: 10.2312/GFZ.b103-12079
Deutsches GeoForschungsZentrum GFZ

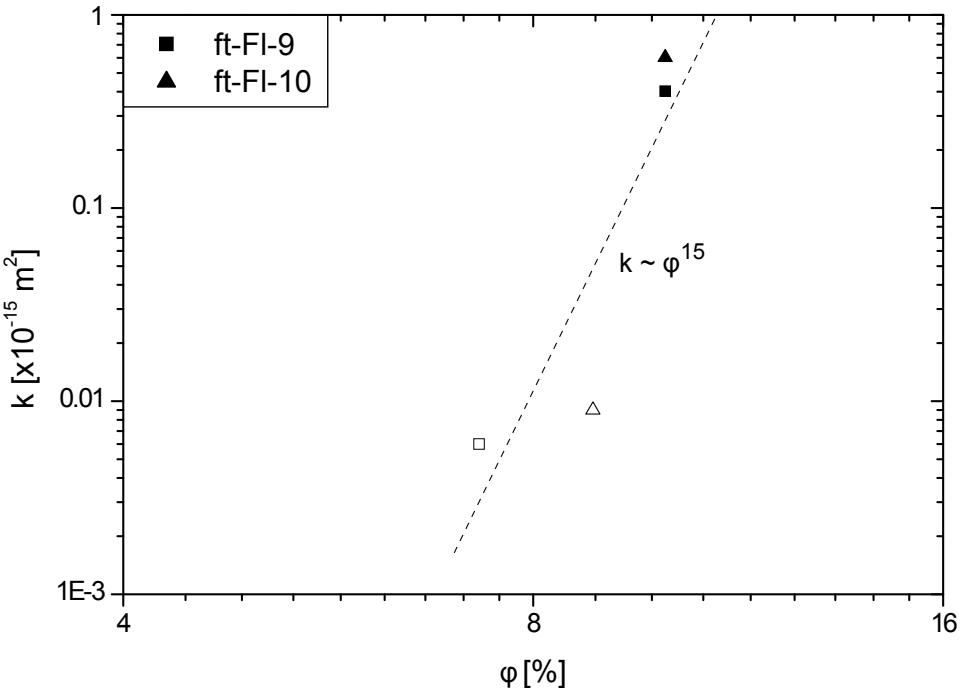

Figure 5.9: Logarithmic plot of the permeability-porosity relationship for Flechtinger sandstone starting material (solid symbols) and altered samples from flow-through experiments ft-Fl-9 and ft-Fl-10 (open symbols). The dashed line represents a linear regression through the data ($k \approx 10^{-15}\,\phi^{15}$, with $R^2 = 0.78$).

space model suggests that the permeability of this material is dependent on the self-similar and rough pore structure (Pape et al., 1999). For the Flechtinger sandstone samples, no k-ϕ relationship could be found, because k-ϕ data were only available for a limited porosity range (Figure 4.9). However, the fractal pore space model for Lower Permian Rotliegend sandstones from northeast Germany (Equation 2.27) yields $k \approx 10^{-15}$ m^2 for $\phi = 10$ %. These values agree with the experimentally determined permeability $k \approx 0.4 \times 10^{-15}$ m^2 (Figure 4.9) and the porosity $\phi \approx 10$ % (Table 5.9) of the Flechtinger sandstone starting material.

Moreover, investigations of k-ϕ relationships of various porous materials have shown that the exponent in the power-law relationship is dependent on the permeability-changing process and covers a large range of ≈ 1 to ≈ 25. Large values of the exponent (> 10) can be generated by brittle compaction or chemical alteration of sedimentary rocks (Bernabé et al., 2003). A permeability-porosity relationship for the Flechtinger sandstone starting material in comparison to altered samples from flow-through experiments (ft-Fl-9 and ft-Fl-10) yielded an exponent of ≈ 15 (Figure 5.9). Since brittle compaction was not observed in the flow-through experiments, the large exponent probably results from a chemical alteration of the samples.

A study on porous silica glass subjected to chemical alteration has found that large exponents in the power-law k-ϕ relationship are related to the roughening of the pores and to the heterogeneity of the pore space (Mok et al., 2002). The heterogeneity of the pore space can be described as the ratio of the pore space that is noneffective to the pore space that is effective for hydrodynamic flow. Moreover, flow-through experiments with granular quartz-feldspar

Scientific Technical Report STR 12/07
DOI: 10.2312/GFZ.b103-12079
Deutsches GeoForschungsZentrum GFZ

aggregates under chemical disequilibrium conditions have shown that permeability decreased, while porosity decreases were negligible (Tenthorey et al., 1998). It has been concluded that secondary minerals precipitating in narrow pores or pore throats led to the permeability decreases of the altered samples (Tenthorey and Scholz, 2002). Thus, increased roughening and heterogeneity of the pore space resulting from dissolution-precipitation processes and redistribution of mass can be an explanation for comparatively large permeability changes in the flow-through experiments, although the porosity changed only slightly (Figure 5.9, Table 5.9).

5.6 Geotechnical Implications

Laboratory studies on model fluid-rock systems can give insight into processes acting on the pore scale and can thus provide information on the long-term behavior of natural or engineered systems. In the present study, experiments were performed with analogue materials and fluids of simple compositions in order to imitate the real and more complex fluid-rock system of a deep sedimentary geothermal reservoir in the North German Basin. However, the findings obtained in the present study cannot be directly transferred to the real fluid-rock system, because of differences between the experiments and the real system with respect to chemical complexity, pressure, scale, and pore space geometry, i.e., the reservoir rocks have a dual-porosity nature (the void space is represented by pores and fractures). The last point is especially important, because enhanced geothermal systems are typically fractured systems in which the fluid flow is focused in fractures. Despite these limitations, investigations of the effects of fluid-rock interactions on the permeability of reservoir rocks require analyses of the pore space which are only feasible in laboratory experiments under controlled conditions.

Changes in the structure of the pore space of a reservoir rock are related to changes of the permeability. It has been shown that dissolution-precipitation reactions were an important factor for the observed permeability impairment of quartz-feldspar granular aggregates. Experiments conducted with quartz-feldspar granular aggregates and Flechtinger sandstone samples exhibited similar normalized permeability decreases at constant temperature and pressure. The analogy between both model materials suggests that dissolution-precipitation reactions were important factors for permeability reductions at constant temperature and pressure in the Flechtinger sandstone samples and the sandwich samples with quartz-feldspar granular aggregates. Porosity-permeability relationships of Rotliegend reservoir sandstones have shown that the permeability of the rocks is dependent on the structure of the pore space. Thus, alterations of the roughness and/or the heterogeneity of the pore space can lead to permeability changes even though the volume of the pore space can be largely unchanged.

The geothermal fluids of the North German Basin are assumed to be initially at equilibrium with the reservoir rock at 150 °C. In the geothermal loop (e.g., the Groß Schönebeck geothermal doublet system), the fluid is produced at ≈ 150 °C, heat is extracted in the aboveground installations, and the fluid is re-injected into the reservoir at ≈ 70 °C. Thus, the cooled fluid is supersaturated with respect to various mineral phases in the technical installations, in the injection borehole, and in the reservoir in the vicinity of the injection borehole. The present study has shown that dissolution-precipitation reactions occurred in the model materials, when the fluids were initially undersaturated with respect to the minerals of the porous samples. The combined interpretation of hydrogeochemical simulations and chemical analyses of fluids resulting from the experiments suggested that the fluids became supersaturated in the course

Scientific Technical Report STR 12/07
DOI: 10.2312/GFZ.b103-12079

of the experiments. The findings of the present study suggest that it is likely that, e.g., Al- and Si-containing amorphous phases, $Al(OH)_3$, phyllosilicates, and/or zeolites will precipitate from the cooled geothermal fluid after the extraction of heat. Studies on the long-term performance of geothermal systems during production of geothermal heat and injection of the cooled fluid into the reservoir have shown that cooling induced mineral precipitation in the technical equipment (e.g., pipes and heat exchangers) and the pore space of the reservoir rocks affects especially the injectivity of geothermal boreholes (e.g., Vuataz et al., 1989; Vuataz and Giroud, 2011).

A rough estimate of the formation damage of Rotliegend sandstone reservoir rocks due to dissolution-precipitation reactions can be made on the basis of the permeability reductions observed in the flow-through experiments with Flechtinger sandstone samples at constant temperature and pressure (Figure 5.10). The underlying assumptions for this rough estimate are that the reservoir rocks have an initial porosity of ≈ 10 %, that the fluid flow is concentrated in the pore space, and that the response of the permeability to chemical reactions is comparable to the effects of dissolution-precipitation reactions on permeability observed in the flow-through experiments. Linear extrapolation of the permeability evolution of two Flechtinger sandstone samples (ft-Fl-8 and ft-Fl-10) at constant temperature and pressure conditions suggests that a typical permeability of a "tight" sandstone, $k = 10^{-20}$ m^2 (Zisser and Nover, 2009), will be reached after approximately 50 to 70 d.

However, the chemical conditions of the flow-through experiments represent a worst case scenario for a geothermal doublet system. The experiments were performed with fluids with simple compositions (H_2O in ft-Fl-8 and a 1 mol/L $NaCl_{aq}$ solution in ft-Fl-10). The investigated fluid-rock system was initially far from equilibrium. In a geothermal doublet system, the deviations from equilibrium due to the cooling of the fluid will be comparatively low. A long-term flow-through experiment with a Rotliegend (Eberswalde) sandstone sample and a synthetic formation fluid has shown that permeability reductions at constant temperature and pressure were significantly lower than in the present study. The permeability of the sample decreased in approximately 50 d from 2.2 ± 0.8 to $0.9 \pm 0.1 \times 10^{-15}$ m^2 at 150 °C and an effective pressure of 45×10^6 Pa. In the remainder of the experiment (up to ≈ 140 d) the permeability was nearly constant (Milsch et al., 2009).

The present study investigated the role of pore space alterations for permeability changes, whereas the flow of fluids is assumed to be concentrated in the fractures of a dual-porosity geothermal reservoir. Thus, the implications of this study for the permeability evolution of a fractured reservoir are limited to the porous part of the reservoir. Yet, investigations on a fractured novaculite sample under net dissolution have shown that the permeability decreased due to dissolution of propping asperities in the fracture (e.g., Yasuhara et al., 2006). Moreover, it can be assumed that the efficiency of the production of the geothermal fluids will decrease, when the matrix permeability decreases.

Furthermore, the experiments suggest that on short timescales the permeability of the reservoir near the injection borehole may increase due to thermo-mechanical contraction of the solids during a cooling of the initial reservoir temperature from approximately 150 to 70 °C. This statement is based on the observation that the permeability of most samples increased with decreasing temperature in the flow-through experiments.

The present study indicates that not only supersaturated but also undersaturated fluids have the ability to reduce the permeability of porous feldspar-rich materials. The experiments have shown that porous samples with undersaturated initial pore fluids yielded permeability reductions due to spatially coupled dissolution-precipitation reactions that led to a mass redistribution in the flown-through pore space.

Scientific Technical Report STR 12/07
DOI: 10.2312/GFZ.b103-12079
Deutsches GeoForschungsZentrum GFZ

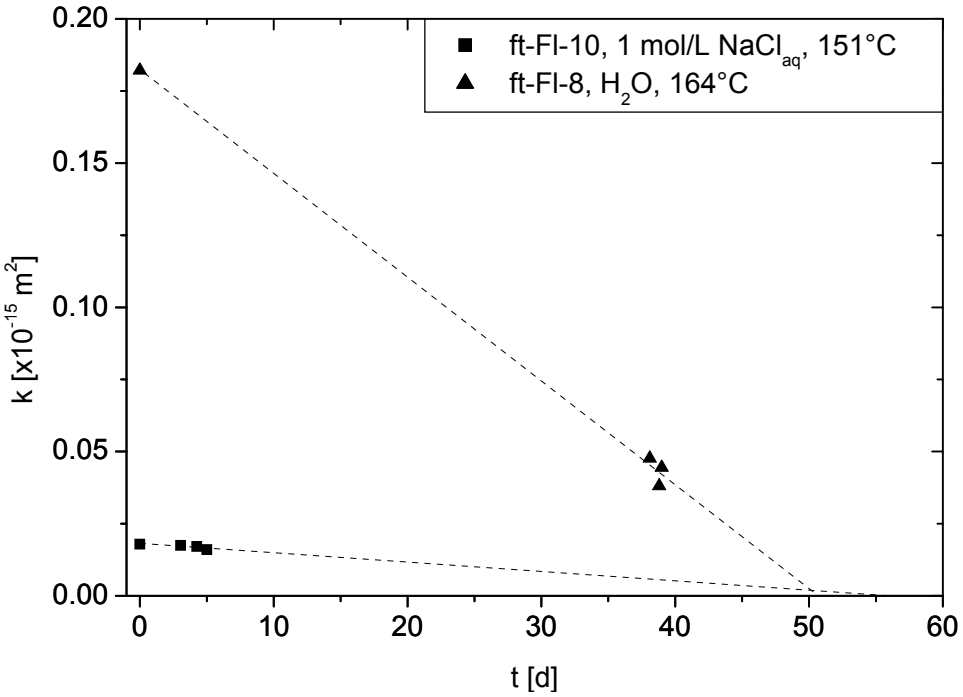

Figure 5.10: Linear extrapolation of the evolution of permeability k of Flechtinger sandstone samples ft-Fl-8 and ft-Fl-10 at constant temperature and pressure conditions to $k = 10^{-20}$ m^2. This value represent low permeabilities of "tight" sandstones (Zisser and Nover, 2009). ft-Fl-8 was performed with H_2O as the initial pore fluid, while the pore fluid in ft-Fl-10 was a 1 mol/L $NaCl_{aq}$ solution. The extrapolations yield that $k = 10^{-20}$ m^2 will be reached after approximately 50 and 70 d in ft-Fl-8 and ft-Fl-10, respectively.

Scientific Technical Report STR 12/07
DOI: 10.2312/GFZ.b103-12079

As a consequence, the main implication for geothermal energy production from deep sedimentary reservoirs is that disequilibrium conditions between the fluid and the solids have the potential of inducing permeability reductions of porous feldspar-rich materials. This implication applies also to other geotechnical applications in which temperature changes may provoke fluid-rock reactions and thus permeability changes (e.g., nuclear waste storage). Generally, dissolution-precipitation reactions can lead to a redistribution of mass in the flown-through pore space and thus to an increase of hydraulic tortuosity. The precipitation of small particles from the flowing pore fluids can lead to fines migration and eventually to pore throat clogging.

Scientific Technical Report STR 12/07
DOI: 10.2312/GFZ.b103-12079

6 Conclusions

6.1 Summary

The permeability k, as well as the electrical conductivity of the porous samples, σ_r, and the fluids, σ_f, generally showed time-dependent changes at constant temperature and pressure conditions in the flow-through and batch experiments performed with Flechtinger sandstone samples. Experiments performed with granular quartz-feldspar aggregates exhibited qualitatively similar σ_r and σ_f evolutions as the rock samples but the actual values of σ_r and σ_f were much lower. Chemical fluid analyses confirmed that these differences resulted from the presence of minor amounts of highly soluble mineral phases in the pore space of the rock samples, i.e., chlorides, sulfates, and carbonates, which were not present in the granular quartz-feldspar aggregates. The observed increase of σ_r and σ_f with time with decreasing rate at constant temperature and pressure resulted from the dissolution of ions from the solid materials into the fluid and from a decreasing driving force for the dissolution reaction, as the fluid-solid systems evolved towards a dynamic dissolution-precipitation equilibrium. In a Flechtinger sandstone experiment (ft-Fl-9), σ_r approached a constant value at 70 °C from initial conditions in which the pore fluid was undersaturated with respect to the minerals of the rock as well as from supersaturated conditions after the fluid-rock system was heated to 150 °C, indicating that precipitation of secondary minerals occurred in the supersaturated phase. Apparent activation energies, E_a^*, of the σ_r evolution at constant temperature and pressure (27 to 87×10^3 J/mol, depending on the method for the determination of E_a^*) are similar to activation energies for silicate dissolution in aqueous solutions ($\approx 60 \times 10^3$ J/mol).

Investigation of the formation resistivity factor for shaly sandstones F^* yielded constant values of ≈ 83 when $\sigma_f(T) > 6.6$ S/m at $T = 42$ °C corresponding to a 0.5 mol/L $NaCl_{aq}$ solution. Below this value, electrical surface conduction contributed significantly to σ_r of the Flechtinger sandstone samples. Formation resistivity factors, obtained before and after a permeability impairment of Flechtinger sandstone samples, indicated that the electrical tortuosity increased with decreasing permeability in the course of the flow-through experiments.

Multiple linear regression analysis of the relationship of σ_f to the concentration of dissolved cations in solution yielded that the concentration of K^+ and Ca^{2+} in the fluid mainly accounted for the evolution of σ_f and thus σ_r in the experiments with Flechtinger sandstone samples and the granular analogue materials. As a consequence, σ_f is a proxy for overall dissolution-precipitation reactions in the rock samples and the analogue materials.

The permeability of all investigated sample types, i.e., Fontainebleau and Flechtinger sandstone samples, and granular analogue materials, decreased with temperature during heating and only partly recovered during the cooling of the samples which indicates a thermo-mechanical k-changing process with a large irreversible and a small thermo-elastic component. At constant temperature and pressure, k decreased time-dependently indicating a kinetically controlled k-changing process which is consistent with a time-dependent dissolution-precipitation process. Creep compaction has been ruled out as the dominant k-changing process at constant temperature and pressure, because pressure conditions were much lower compared to typical creep

compaction experiments, and the k reductions did not show a temperature dependence or a dependence on the k measurement frequency, which would be expected for creep compaction.

Chemical fluid analyses and hydrogeochemical simulations indicated that the fluids resulting from the flow-through and batch experiments were supersaturated with respect to mainly clay minerals and zeolites. However, thermodynamic equilibria between the solid phases and the fluid phase were not reached in the present study. Furthermore, it must be noted that chemical data from batch experiments with granular aggregates cannot be directly compared to chemical data of Flechtinger sandstone pore fluids because of different spatial distributions of minerals in both experiment types, i.e., interfaces between the pore fluid and cement minerals as well as the pore lining illite in the Flechtinger sandstone samples are disproportionate to their mass fractions in experiments with granular aggregates. Apart from these limitations, time-dependent decreases of the concentration of dissolved ions, i.e., mainly Al^{3+} and K^{+}, observed in batch experiments, as well as the apparent incongruent dissolution observed in a fluid sample from a flow-through experiment (ft-s-4) indicated that Al- and K-bearing solid phases precipitated from the fluids.

Mercury intrusion porosimetry, MIP, points to changes in the pore throat radius distribution of altered Flechtinger sandstone samples compared to the starting material. MIP investigations showed a trend of a decrease of small pore throat radius classes, whereas large pore throat radius classes increased in the course of the flow-through experiments. BET analysis revealed large decreases of specific surface areas in flow-through experiments with Flechtinger sandstone samples. A combined interpretation of MIP and BET data suggests that pore space geometrical properties changed in the flow-through experiments with Flechtinger sandstone samples but remained unaltered in batch experiments, pointing to pore space changing effects resulting from flow conditions and/or higher effective pressures in the flow-through experiments.

Microstructural investigations with SEM, EMPA, and TEM showed sub-micrometer sized amorphous particles precipitating mainly on feldspar grains in the course of flow-through and batch experiments with granular quartz-feldspar aggregates. The direct identification of alteration products in the Flechtinger sandstone samples was precluded by the microstructural complexity of the pore space of the rock. Furthermore, the small size and the small amount, as well as the amorphous nature of potentially occurring alteration products precluded their identification in the rock samples. However, the analogy of the main mineral phases and the experimental conditions to the experiments with granular quartz-feldspar aggregates strongly suggests that fluid-rock reactions should be comparable in both materials.

The observations made in this study are consistent with spatially coupled dissolution-precipitation reactions in the quartz-feldspar-water system that led to a redistribution of mass in the pore space and to the clogging of narrow pores and pore throats due to flow. The constriction of flow paths thus led to increasing hydraulic tortuosity and decreasing permeability of the porous materials.

6.2 Outlook

In order to further investigate the effects of dissolution-precipitation on rock physical transport properties of feldspar-rich porous materials, flow-through experiments should be performed with mechanically robust rock analogue samples consisting of sintered quartz and feldspar grains. Synthetic quartz- and feldspar-bearing rocks have been prepared by hot isostatic pressing of anorthite glass powders and crushed quartz single crystals. The porosities of the aggregates

Scientific Technical Report STR 12/07
DOI: 10.2312/GFZ.b103-12079
Deutsches GeoForschungsZentrum GFZ

varied with quartz content and were as high as 12 % (Xiao et al., 2002). In case of a connected porosity, such samples should be permeable and flow-through experiments (as the small sample experiment ft-Fl-13) could be performed with them. The benefit of such experiments would be that the samples were homogeneous, the chemical inventory was known, and the porosity, as well as possibly the permeability could be controlled by the preparation method. Secondary minerals resulting from hydrothermal experiments could be directly identified using microscopic techniques, e.g., EMPA, SEM, and TEM. Direct investigations of changes of the pore space geometry could be performed by X-ray CT.

Furthermore, flow-through experiments performed with clay-free synthetic rock samples would circumvent uncertainties resulting from contributions of σ_s in formation resistivity factor investigations. As the discussion of the formation resistivity factor has shown, experiments conducted without the swelling effect of clay minerals due to different pore fluid salinities could provide a means to investigate changes of the electrical tortuosity by σ_r measurements. Investigations with fluids other than H_2O or $NaCl_{aq}$ solutions, especially highly saline, chloride-bearing, corrosive fluids, should be performed using corrosion resistant machinery in order to approach the chemical inventory of the real fluid-rock system of deep sedimentary geothermal reservoirs in the North German Basin. Flow-through experiments with fractured rock samples would complement the experiments with porous samples to model the dual-porosity nature of enhanced geothermal systems more closely.

Scientific Technical Report STR 12/07
DOI: 10.2312/GFZ.b103-12079

Scientific Technical Report STR 12/07
DOI: 10.2312/GFZ.b103-12079

Bibliography

Aagaard, P., Helgeson, H.C., 1982. Thermodynamic and kinetic constraints on reaction rates among minerals and aqueous solutions. I. Theoretical considerations. American Journal of Science 282, 237–285.

Abramoff, M.D., Magelhaes, P., Ram, S.J., 2004. Image processing with ImageJ. Biophotonics International 11, 36–42.

Adolphs, J., Setzer, M., Heine, P., 2002. Changes in pore structure and mercury contact angle of hardened cement paste depending on relative humidity. Materials and Structures 35, 477–486.

Aharonov, E., Tenthorey, E., Scholz, C.H., 1998. Precipitation sealing and diagenesis - 2. theoretical analysis. Journal of Geophysical Research 103, 23969–23981.

Ahrens, J., Geveci, B., Law, C., 2005. ParaView: An end-user tool for large data visualization. Visualization Handbook, Elsevier.

Anderson, R., Ratcliffe, I., Greenwell, H., Williams, P., Cliffe, S., Coveney, P., 2010. Clay swelling - A challenge in the oilfield. Earth-Science Reviews 98, 201–216.

André, L., Rabemanana, V., Vuataz, F.D., 2006. Influence of water-rock interactions on fracture permeability of the deep reservoir at Soultz-sous-Forêts, France. Geothermics 35, 507–531.

Appelo, C., Postma, D., 1999. Geochemistry, Groundwater and Pollution. Balkema.

Archie, G.E., 1942. The electrical resistivity log as an aid in determining some reservoir characteristics. Transactions of the American Institute of Mining and Metallurgical Engineers 146, 54–62.

Arnórsson, S., Stefánsson, A., 1999. Assessment of feldspar solubility constants in water in the range of 0 to 350 °C at vapor saturation pressures. American Journal of Science 299, 173–209.

Arvidson, R.S., Lüttge, A., 2010. Mineral dissolution kinetics as a function of distance from equilibrium - New experimental results. Chemical Geology 269, 79–88.

Atkins, P., de Paula, J., 2006. Physical Chemistry. Oxford University Press.

Bachu, S., Gunter, W., Perkins, E., 1994. Aquifer disposal of CO_2: Hydrodynamic and mineral trapping. Energy Conversion and Management 35, 269–279.

Bagchi, B., 1998. Microscopic derivation of the Hubbard–Onsager–Zwanzig expression of limiting ionic conductivity. The Journal of Chemical Physics 109, 3989–3993.

Barker, S.L., Cox, S.F., Eggins, S.M., Gagan, M.K., 2006. Microchemical evidence for episodic growth of antitaxial veins during fracture-controlled fluid flow. Earth and Planetary Science Letters 250, 331–344.

Bear, J., 1988. Dynamics of fluids in porous media. Dover Publications, New York.

Bernabé, Y., Mok, U., Evans, B., 2003. Permeability-porosity relationships in rocks subjected to various evolution processes. Pure and Applied Geophysics 160, 937–960.

Blake, R.E., Walter, L.M., 1999. Kinetics of feldspar and quartz dissolution at 70-80 °C and near-neutral pH: Effects of organic acids and NaCl. Geochimica et Cosmochimica Acta 63, 2043–2059.

Blum, A.E., Lasaga, A.C., 1991. The role of surface speciation in the dissolution of albite. Geochimica et Cosmochimica Acta 55, 2193–2201.

Blume, H., Brümmer, G., Horn, R., Kandeler, E., Kögel-Knabner, I., Kretzschmar, R., Stahr, K., Wilke, B., 2010. Scheffer / Schachtschabel: Lehrbuch der Bodenkunde. Spektrum Akademischer Verlag.

Blume, T., Weisbrod, N., Selker, J.S., 2002. Permeability changes in layered sediments: Impact of particle release. Ground Water 40, 466–474.

de Boer, R., Ehlers, W., 1990. The development of the concept of effective stresses. Acta Mechanica 83, 77–92.

Bourbie, T., Zinszner, B., 1985. Hydraulic and acoustic properties as a function of porosity in Fontainebleau sandstone. Journal of Geophysical Research 90, 11524–11532.

Bradbury, M., Baeyens, B., 2009. Sorption modelling on illite part I: Titration measurements and the sorption of Ni, Co, Eu and Sn. Geochimica et Cosmochimica Acta 73, 990–1003.

Brady, P., Walther, J.V., 1990. Kinetics of quartz dissolution at low temperatures. Chemical Geology 82, 253–264.

Brenan, J.M., Watson, E.B., 1988. Fluids in the lithosphere - 2. Experimental constraints on CO_2 transport in dunite and quartzite at elevated p-T conditions with implications for mantle and crustal decarbonation processes. Earth and Planetary Science Letters 91, 141–158.

Bruggeman, D.A.G., 1935. Berechnung verschiedener physikalischer Konstanten von heterogenen Substanzen. I. Dielektrizitätskonstanten und Leitfähigkeiten der Mischkörper aus isotropen Substanzen. Annalen der Physik 416, 636–664.

Brunauer, S., Emmett, P.H., Teller, E., 1938. Adsorption of gases in multimolecular layers. Journal of the American Chemical Society 60, 309–319.

Busenberg, E., 1978. The products of the interaction of feldspars with aqueous solutions at 25 °C. Geochimica et Cosmochimica Acta 42, 1679–1686.

Bussian, A.E., 1983. Electrical conductance in a porous medium. Geophysics 48, 1258–1268.

Caciagli, N., Manning, C., 2003. The solubility of calcite in water at 6–16 kbar and 500–800 °C. Contributions to Mineralogy and Petrology 146, 275–285.

Carter, N.L., Kronenberg, A.K., Ross, J.V., Wiltschko, D.V., 1990. Control of fluids on deformation of rocks. Geological Society, London, Special Publications 54, 1–13.

Chandra, A., Bagchi, B., 1999. Ion conductance in electrolyte solutions. The Journal of Chemical Physics 110, 10024–10034.

Chardon, E.S., Livens, F.R., Vaughan, D.J., 2006. Reactions of feldspar surfaces with aqueous solutions. Earth-Science Reviews 78, 1–26.

Chaudhuri, A., Rajaram, H., Viswanathan, H., Zyvoloski, G., Stauffer, P., 2009. Buoyant convection resulting from dissolution and permeability growth in vertical limestone fractures. Geophysical Research Letters 36, L03401–.

Chen, Y., Brantley, S.L., 1997. Temperature- and pH-dependence of albite dissolution rate at acid pH. Chemical Geology 135, 275–290.

Chou, L., Wollast, R., 1985. Steady-state kinetics and dissolution mechanisms of albite. American Journal of Science 285, 963–993.

Civan, F., 2000. Reservoir formation damage - Fundamentals, modeling, assessment, and mitigation. Gulf Publishing Company, Houston.

Civan, F., 2007. Formation damage mechanisms and their phenomenological modeling - An overview, in: European Formation Damage Conference, 30 May-1 June 2007, Scheveningen, The Netherlands.

Clennell, M.B., 1997. Tortuosity: A guide through the maze. Geological Society, London, Special Publications 122, 299–344.

Colón, C.F.J., Oelkers, E.H., Schott, J., 2004. Experimental investigation of the effect of dissolution on sandstone permeability, porosity, and reactive surface area. Geochimica et Cosmochimica Acta 68, 805–817.

Corti, H.R., Trevanib, L.N., Anderko, A., 2004. Aqueous systems at elevated temperatures and pressures: Physical chemistry in water, steam and hydrothermal solutions. Elsevier. pp. 321–375.

Costa, A., 2006. Permeability-porosity relationship: A reexamination of the Kozeny-Carman equation based on a fractal pore-space geometry assumption. Geophysical Research Letters 33.

von Damm, K.L., Bischoff, J.L., Rosenbauer, R.J., 1991. Quartz solubility in hydrothermal seawater: An experimental study and equation describing quartz solubility for up to 0.5 M NaCl solutions. American Journal of Science 291, 977–1007.

David, C., 1993. Geometry of flow paths for fluid transport in rocks. Journal of Geophysical Research 98, 12267–12278.

David, C., Darot, M., Jeannette, D., 1993. Pore structures and transport properties of sandstone. Transport in Porous Media 11, 161–177.

Davis, B., 1984. A comparison of surface areas derived from mercury penetration and nitrogen adsorption. Applied Catalysis 10, 185–198.

Diamond, S., 2000. Mercury porosimetry: An inappropriate method for the measurement of pore size distributions in cement-based materials. Cement and Concrete Research 30, 1517–1525.

Divis, A.F., McKenzie, J.A., 1975. Experimental authigenesis of phyllosilicates from feldspathic sands. Sedimentology 22, 147–155.

Dove, P.M., 1994. The dissolution kinetics of quartz in sodium chloride solutions at 25 to 300 °C. American Journal of Science 294, 665–712.

Dove, P.M., 1999. The dissolution kinetics of quartz in aqueous mixed cation solutions. Geochimica et Cosmochimica Acta 63, 3715–3727.

Dove, P.M., Crerar, D.A., 1990. Kinetics of quartz dissolution in electrolyte solutions using a hydrothermal mixed flow reactor. Geochimica et Cosmochimica Acta 54, 955–969.

Dove, P.M., Elston, S.F., 1992. Dissolution kinetics of quartz in sodium chloride solutions: Analysis of existing data and a rate model for 25 °C. Geochimica et Cosmochimica Acta 56, 4147–4156.

Dove, P.M., Han, N., Yoreo, J.J.D., 2005. Mechanisms of classical crystal growth theory explain quartz and silicate dissolution behavior. PNAS 102, 15357–15362.

Downs, R.T., 2006. The RRUFF project: An integrated study of the chemistry, crystallography, Raman and infrared spectroscopy of minerals, in: Program and Abstracts of the 19th General Meeting of the International Mineralogical Association in Kobe, Japan, pp. O03–13.

Drouin, D., Couture, A.R., Joly, D., Tastet, X., Aimez, V., Gauvin, R., 2007. CASINO V2.42 - A fast and easy-to-use modeling tool for scanning electron microscopy and microanalysis users. Scanning 29, 92–101.

Duff, M.C., Coughlin, J.U., Hunter, D.B., 2002. Uranium co-precipitation with iron oxide minerals. Geochimica et Cosmochimica Acta 66, 3533–3547.

Dullien, F.A.L., 1992. Porous media: Fluid transport and pore structure. Academic Press, San Diego. 2nd edition.

Durham, W.B., Bourcier, W.L., Burton, E.A., 2001. Direct observation of reactive flow in a single fracture. Water Resources Research 37, 1–12.

Elsworth, D., Yasuhara, H., 2006. Short-timescale chemo-mechanical effects and their influence on the transport properties of fractured rock. Pure and Applied Geophysics 163, 2051–2070.

Etheridge, M.A., Wall, V.J., Cox, S.F., Vernon, R.H., 1984. High fluid pressures during regional metamorphism and deformation: Implications for mass transport and deformation mechanisms. Journal of Geophysical Research 89, 4344–4358.

Etheridge, M.A., Wall, V.J., Vernon, R.H., 1983. The role of the fluid phase during regional metamorphism and deformation. Journal of Metamorphic Geology 1, 205–226.

Evans, K., 2007. Quartz solubility in salt-bearing solutions at pressures to 1 GPa and temperatures to 900 °C. Geofluids 7, 451–467.

Faimon, J., 1996. Oscillatory silicon and aluminum aqueous concentrations during experimental aluminosilicate weathering. Geochimica et Cosmochimica Acta 60, 2901–2907.

Fischer, C., Gaupp, R., 2004. Multi-scale rock surface area quantification - A systematic method to evaluate the reactive surface area of rocks. Chemie der Erde - Geochemistry 64, 241–256.

Fischer, C., Gaupp, R., Dimke, M., Sill, O., 2007. A 3D high resolution model of bounding surfaces in aolian-fluvial deposits: An outcrop analogue study from the Permian Rotliegend, Northern Germany. Journal of Petroleum Geology 30, 257–273.

Fischer, G., Paterson, M., 1992. Fault mechanics and transport properties of rocks. Academic Press. chapter Measurement of permeability and storage capacity in rocks during deformation at high temperature and pressure. pp. 213–252.

Francke, H., Thorade, M., 2010. Density and viscosity of brine: An overview from a process engineers perspective. Chemie der Erde - Geochemistry 70, 23–32.

Fredrich, J., Greaves, K., Martin, J., 1993. Pore geometry and transport properties of Fontainebleau sandstone. International Journal of Rock Mechanics and Mining Sciences & Geomechanics Abstracts 30, 691–697.

Fu, Q., Lu, P., Konishi, H., Dilmore, R., Xu, H., Seyfried Jr, W.E., Zhu, C., 2009. Coupled alkali-feldspar dissolution and secondary mineral precipitation in batch systems: 1. New experiments at 200 °C and 300 bars. Chemical Geology 258, 125–135.

Ganor, J., Huston, T.J., Walter, L.M., 2005. Quartz precipitation kinetics at 180 °C in NaCl solutions - Implications for the usability of the principle of detailed balancing. Geochimica et Cosmochimica Acta 69, 2043–2056.

Ganor, J., Mogollón, J.L., Lasaga, A.C., 1995. The effect of pH on kaolinite dissolution rates and on activation energy. Geochimica et Cosmochimica Acta 59, 1037–1052.

Gaucher, E.C., Blanc, P., 2006. Cement/clay interactions - A review: Experiments, natural analogues, and modeling. Waste Management 26, 776–788.

Gautier, J.M., Oelkers, E.H., Schott, J., 2001. Are quartz dissolution rates proportional to B.E.T. surface areas? Geochimica et Cosmochimica Acta 65, 1059–1070.

Gherardi, F., Xu, T., Pruess, K., 2007. Numerical modeling of self-limiting and self-enhancing caprock alteration induced by CO_2 storage in a depleted gas reservoir. Chemical Geology 244, 103–129.

Giger, S.B., Tenthorey, E., Cox, S.F., Fitz Gerald, J.D., 2007. Permeability evolution in quartz fault gouges under hydrothermal conditions. Journal of Geophysical Research 112, B07202–.

Giggenbach, W.F., 1981. Geothermal mineral equilibria. Geochimica et Cosmochimica Acta 45, 393–410.

Glover, P.W., Hole, M.J., Pous, J., 2000. A modified Archie's law for two conducting phases. Earth and Planetary Science Letters 180, 369–383.

Glover, P.W.J., Meredith, P.G., Sammonds, P.R., Murrell, S.A.F., 1994. Ionic surface electrical conductivity in sandstone. Journal of Geophysical Research 99, 21635–21650.

Guéguen, Y., Palciauskas, V., 1994. Introduction to the physics of rocks. Princeton University Press, Princeton, New Jersey.

Gunnársson, I., Arnórsson, S., 2000. Amorphous silica solubility and the thermodynamic properties of $H_4SiO_4^0$ in the range of 0 °C to 350 °C at P_{sat}. Geochimica et Cosmochimica Acta 64, 2295–2307.

Hajash, A., Bloom, M.A., 1991. Marine diagenesis of feldspathic sand: A flow-through experimental study at 200 °C, 1 kbar. Chemical Geology 89, 359–377.

Hanai, T., 1960. Theory of the dielectric dispersion due to the interfacial polarization and its application to emulsions. Colloid and Polymer Science 171, 23–31.

Hashin, Z., Shtrikman, S., 1963. Conductivity of polycrystals. Physical Review 130, 129–133.

He, W., Hajash, A., Sparks, D., 2003. Creep compaction of quartz aggregates: Effects of pore-fluid flow - A combined experimental and theoretical study. American Journal of Science 303, 73–93.

He, W., Hajash, A., Sparks, D., 2007. Evolution of fluid chemistry in quartz compaction systems: Experimental investigations and numerical modeling. Geochimica et Cosmochimica Acta 71, 4846–4855.

Heap, M.J., Baud, P., Meredith, P.G., 2009. Influence of temperature on brittle creep in sandstones. Geophysical Research Letters 36, L19305–.

Heim, D., 1990. Tone und Tonminerale. Enke, Stuttgart.

Helgeson, H.C., Murphy, W.M., Aagaard, P., 1984. Thermodynamic and kinetic constraints on reaction rates among minerals and aqueous solutions. II. Rate constants, effective surface area, and the hydrolysis of feldspar. Geochimica et Cosmochimica Acta 48, 2405–2432.

Hellmann, R., 1994. The albite-water system: Part I. The kinetics of dissolution as a function of pH at 100, 200 and 300 °C. Geochimica et Cosmochimica Acta 58, 595–611.

Hellmann, R., 1995. The albite-water system: Part II. The time-evolution of the stoichiometry of dissolution as a function of pH at 100, 200, and 300 °C. Geochimica et Cosmochimica Acta 59, 1669–1697.

Hellmann, R., Crerar, D.A., Zhang, R., 1989. Albite feldspar hydrolysis to 300 °C. Solid State Ionics 32-33, 314–329.

Hellmann, R., Dran, J.C., Mea, G.D., 1997. The albite-water system: Part III. Characterization of leached and hydrogen-enriched layers formed at 300 °C using MeV ion beam techniques. Geochimica et Cosmochimica Acta 61, 1575–1594.

Hellmann, R., Eggleston, C.M., Jr, M.F.H., Crerar, D.A., 1990. The formation of leached layers on albite surfaces during dissolution under hydrothermal conditions. Geochimica et Cosmochimica Acta 54, 1267–1281.

Hellmann, R., Penisson, J.M., Hervig, R., Thomassin, J.H., Abrioux, M.F., 2003. An EFTEM/HRTEM high-resolution study of the near surface of labradorite feldspar altered at acid pH: Evidence for interfacial dissolution-reprecipitation. Physics and Chemistry of Minerals 30, 192–197.

Hellmann, R., Tisserand, D., 2006. Dissolution kinetics as a function of the Gibbs free energy of reaction: An experimental study based on albite feldspar. Geochimica et Cosmochimica Acta 70, 364–383.

Hickman, S., Sibson, R., Bruhn, R., 1995. Introduction to special section: Mechanical involvement of fluids in faulting. Journal of Geophysical Research 100, 12831–12840.

Hilgers, C., Tenthorey, E., 2004. Fracture sealing of quartzite under a temperature gradient: Experimental results. Terra Nova 16, 173–178(6).

Holdren, G.R., Berner, R.A., 1979. Mechanism of feldspar weathering - I. Experimental studies. Geochimica et Cosmochimica Acta 43, 1161–1171.

Icenhower, J.P., Dove, P.M., 2000. The dissolution kinetics of amorphous silica into sodium chloride solutions: Effects of temperature and ionic strength. Geochimica et Cosmochimica Acta 64, 4193–4203.

Icenhower, J.P., Strachan, D.M., McGrail, B.P., Scheele, R.D., Rodriguez, E.A., Steele, J.L., Legore, V.L., 2006. Dissolution kinetics of pyrochlore ceramics for the disposition of plutonium. American Mineralogist 91, 39–53.

Jamtveit, B., Austrheim, H., 2010. Metamorphism: The role of fluids. Elements 6, 153–158.

Jamtveit, B., Yardley, B. (Eds.), 1997. Fluid Flow and Transport in Rocks: Mechanisms and effects. Chapman & Hall.

Ji, H., Rouxel, T., Abdelouas, A., Grambow, B., Jollivet, P., 2005. Mechanical behavior of a borosilicate glass under aqueous corrosion. Journal of the American Ceramic Society 88, 3256–3259.

Johnson, D.L., Koplik, J., Schwartz, L.M., 1986. New pore-size parameter characterizing transport in porous media. Physical Review Letters 57, 2564–2567.

Johnson, D.L., Sen, P.N., 1988. Dependence of the conductivity of a porous medium on electrolyte conductivity. Physical Review B 37, 3502–3510.

Kada-Benameur, H., Wirquin, E., Duthoit, B., 2000. Determination of apparent activation energy of concrete by isothermal calorimetry. Cement and Concrete Research 30, 301–305.

Karner, S.L., Schreiber, B.C., 1993. Experimental simulation of plagioclase diagenesis at p-T conditions of 3.5 km burial depth. Pure and Applied Geophysics 141, 221–247.

Kawano, M., Tomita, K., 1996. Amorphous aluminium hydroxide formed at the earliest weathering stages of K-feldspar. Clays and Clay Minerals 44, 672–676.

Kawano, M., Tomita, K., 2001. TEM-EDX study of weathered layers on the surface of volcanic glass, bytownite, and hypersthene in volcanic ash from Sakurajima volcano, Japan. American Mineralogist 86, 284–292.

Keller, G.V., 1989. Practical Handbook of Physical Properties of Rocks and Minerals. CRC Press, Boca Raton. chapter Electrical Properties.

Kestin, J., Khalifa, H.E., Correia, R.J., 1981. Tables of the dynamic and kinematic viscosity of aqueous NaCl solutions in the temperature range 20–150 °C and the pressure range 0.1–35 MPa. Journal of Physical and Chemical Reference Data 10, 71–88.

Kirkpatrick, S., 1973. Percolation and conduction. Reviews of Modern Physics 45, 574–588.

Köhler, S.J., Dufaud, F., Oelkers, E.H., 2003. An experimental study of illite dissolution kinetics as a function of pH from 1.4 to 12.4 and temperature from 5 to 50 °C. Geochimica et Cosmochimica Acta 67, 3583–3594.

Kristinsdóttir, L.H., Flóvenz, O.G., Árnason, K., Bruhn, D., Milsch, H., Spangenberg, E., Kulenkampff, J., 2010. Electrical conductivity and p-wave velocity in rock samples from high-temperature icelandic geothermal fields. Geothermics 39, 94–105. The European I-GET Project: Integrated Geophysical Exploration Technologies for Deep Geothermal Reservoirs.

Kühn, M., Bartels, J., Iffland, J., 2002. Predicting reservoir property trends under heat exploitation: Interaction between flow, heat transfer, transport, and chemical reactions in a deep aquifer at Stralsund, Germany. Geothermics 31, 725–749(25).

Kühn, M., Vernoux, J.F., Kellner, T., Isenbeck-Schroeter, M., Schulz, H.D., 1998. Onsite experimental simulation of brine injection into a clastic reservoir as applied to geothermal exploitation in Germany. Applied Geochemistry 13, 477–490.

La Iglesia, A., Martin-Vivaldi, J.L., Lopez Aguayo, F., 1976. Kaolinite crystallization at room temperature by homogeneous precipitation: III. Hydrolysis of feldspars. Clays and Clay Minerals 24, 36–42.

Larson, A.C., Von Dreele, R.B., 2000. General Structure Analysis System (GSAS), Los Alamos National Laboratory Report LAUR 86-748. Technical Report. Los Alamos National Laboratory.

Lasaga, A.C., 1983. Kinetics of geochemical processes. volume 8 of *Reviews in Mineralogy*. Mineralogical Society of America Geochemical Society.

Lasaga, A.C., 1984. Chemical kinetics of water-rock interactions. Journal of Geophysical Research 89, 4009–4025.

Lasaga, A.C., Lüttge, A., 2003. A model for crystal dissolution. European Journal of Mineralogy 15, 603–615.

Lasaga, A.C., Lüttge, A., 2004. Mineralogical approaches to fundamental crystal dissolution kinetics. American Mineralogist 89, 527–540.

Le Gallo, Y., Bildstein, O., Brosse, E., 1998. Coupled reaction-flow modeling of diagenetic changes in reservoir permeability, porosity and mineral compositions. Journal of Hydrology 209, 366–388.

Ledésert, B., Hebert, R., Genter, A., Bartier, D., Clauer, N., Grall, C., 2010. Fractures, hydrothermal alterations and permeability in the soultz enhanced geothermal system. Comptes Rendus Geoscience 342, 607–615.

Lee, M., 2010. Transmission electron microscopy (TEM) of Earth and planetary materials: A review. Mineralogical Magazine 74, 1–27.

Lee, M.R., Brown, D.J., Hodson, M.E., MacKenzie, M., Smith, C.L., 2008. Weathering microenvironments on feldspar surfaces: Implications for understanding fluid-mineral reactions in soils. Mineralogical Magazine 72, 1319–1328.

Lee, M.R., Parsons, I., 1995. Microtextural controls of weathering of perthitic alkali feldspars. Geochimica et Cosmochimica Acta 59, 4465–4488.

Lefebvre, R., Hockley, D., Smolensky, J., Gelinas, P., 2001. Multiphase transfer processes in waste rock piles producing acid mine drainage: 1. Conceptual model and system characterization. Journal of Contaminant Hydrology 52, 137–164.

Leroy, P., Revil, A., 2004. A triple-layer model of the surface electrochemical properties of clay minerals. Journal of Colloid and Interface Science 270, 371–380.

Leroy, P., Revil, A., 2009. A mechanistic model for the spectral induced polarization of clay materials. Journal of Geophysical Research 114, B10202–.

de Lima, O.A.L., Sharma, M.M., 1990. A grain conductivity approach to shaly sandstones. Geophysics 55, 1347–1356.

Lin, F., Clemency, C., 1980. The kinetics of dissolution of muscovites at 25 °C and 1 atm CO_2 partial pressure. Third International Symposium on Water-Rock Interaction , 44–47.

Liu, J., Sheng, J., Polak, A., Elsworth, D., Yasuhara, H., Grader, A., 2006. A fully-coupled hydrological-mechanical-chemical model for fracture sealing and preferential opening. International Journal of Rock Mechanics and Mining Sciences 43, 23–36.

Llera, F.J., Sato, M., Nakatsuka, K., Yokoyama, H., 1990. Temperature dependence of the electrical resistivity of water-saturated rocks. Geophysics 55, 576–585.

Long, J.C.S., Ewing, R.C., 2004. Yucca Mountain: Earth-science issues at a geologic repository for high-level nuclear waste. Annual Review of Earth and Planetary Sciences 32, 363–401.

Lowell, R.P., Van Cappellen, P., Germanovich, L.N., 1993. Silica precipitation in fractures and the evolution of permeability in hydrothermal upflow zones. Science 260, 192–194.

Lüders, V., Plessen, B., Romer, R.L., Weise, S.M., Banks, D.A., Hoth, P., Dulski, P., Schettler, G., 2010. Chemistry and isotopic composition of Rotliegend and Upper Carboniferous formation waters from the North German Basin. Chemical Geology 276, 198–208.

Mao, S., Duan, Z., 2009. The viscosity of aqueous alkali-chloride solutions up to 623 K, 1000 bar, and high ionic strength. International Journal of Thermophysics 30, 1510–1523.

Marshall, W.L., 1980. Amorphous silica solubilities - I. Behavior in aqueous sodium nitrate solutions; 25–300 °C, 0–6 molal. Geochimica et Cosmochimica Acta 44, 907–913.

Matter, J., Kelemen, P.B., 2009. Permanent storage of carbon dioxide in geological reservoirs by mineral carbonation. Nature Geoscience 2, 837–841.

Mavko, G., Nur, A., 1997. The effect of a percolation threshold in the Kozeny-Carman relation. Geophysics 62, 1480–1482.

Merkel, B.J., Planer-Friedrich, B., 2008. Groundwater Geochemistry: A practical guide to modeling of natural and contaminated aquatic systems. Springer. 2nd edition.

Milburn, D., Davis, B., 1993. Comparison of surface areas calculated from nitrogen adsorption and mercury porosimetry. Ceramic Engineering and Science Proceedings 14, 130–134.

Milsch, H., Seibt, A., Spangenberg, E., 2009. Long-term petrophysical investigations on geothermal reservoir rocks at simulated in situ conditions. Transport in Porous Media 77, 59–78.

Milsch, H., Spangenberg, E., Kulenkampff, J., Meyhöfer, S., 2008. A new apparatus for long-term petrophysical investigations on geothermal reservoir rocks at simulated in-situ conditions. Transport in Porous Media 74, 73–85.

Min, K.B., Rutqvist, J., Elsworth, D., 2009. Chemically and mechanically mediated influences on the transport and mechanical characteristics of rock fractures. International Journal of Rock Mechanics and Mining Sciences 46, 80–89.

Moeck, I., Schandelmeier, H., Holl, H.G., 2009. The stress regime in a Rotliegend reservoir of the Northeast German Basin. International Journal of Earth Sciences 98, 1643–1654.

Mohan, K.K., Fogler, H.S., 1997. Effect of pH and layer charge on formation damage in porous media containing swelling clays. Langmuir 13, 2863–2872.

Mohan, K.K., Reed, M.G., Fogler, H.S., 1999. Formation damage in smectitic sandstones by high ionic strength brines. Colloids and Surfaces A: Physicochemical and Engineering Aspects 154, 249–257.

Mok, U., Bernabé, Y., Evans, B., 2002. Permeability, porosity and pore geometry of chemically altered porous silica glass. Journal of Geophysical Research 107.

Moore, D.E., Morrow, C.A., Byerlee, J.D., 1983. Chemical reactions accompanying fluid flow through granite held in a temperature gradient. Geochimica et Cosmochimica Acta 47, 445–453.

Moore, D.M., Reynolds, R.C., 1989. X-ray diffraction and the identification and analysis of clay minerals. Oxford University Press.

Morrow, C.A., Moore, D.E., Lockner, D.A., 2001. Permeability reduction in granite under hydrothermal conditions. Journal of Geophysical Research 106, 3002–3008.

Mueller, R.F., Saxena, S.K., 1977. Chemical Petrology. Springer, New-York.

Murakami, T., Kogure, T., Kadohara, H., Ohnuki, T., 1998. Formation of secondary minerals and its effect on anorthite dissolution. American Mineralogist 83, 1209–1219.

Nesbitt, H., Skinner, W., 2001. Early development of Al, Ca, and Na compositional gradients in labradorite leached in pH 2 HCl solutions. Geochimica et Cosmochimica Acta 65, 715–727.

Nettelblad, B., Ahlen, B., Niklasson, G.A., Holt, R.M., 1995. Approximate determination of surface conductivity in porous media. Journal of Physics D: Applied Physics 28, 2037–2045.

Nicholas, J.F., 1959. Apparent activation energy and frequency factor for a process involving competing mechanisms. The Journal of Chemical Physics 31, 922–925.

Niedermeier, D., Putnis, A., Geisler, T., Golla-Schindler, U., Putnis, C., 2009. The mechanism of cation and oxygen isotope exchange in alkali feldspars under hydrothermal conditions. Contributions to Mineralogy and Petrology 157, 65–76.

Oelkers, E.H., 2001. General kinetic description of multioxide silicate mineral and glass dissolution. Geochimica et Cosmochimica Acta 65, 3703–3719.

Oelkers, E.H., Schott, J., Devidal, J.L., 1994. The effect of aluminum, pH, and chemical affinity on the rates of aluminosilicate dissolution reactions. Geochimica et Cosmochimica Acta 58, 2011–2024.

Ohm, G., 1826. Bestimmung des Gesetzes, nach welchem Metalle die Contaktelektricität leiten, nebst einem Entwurfe zu einer Theorie des Voltaischen Apparates und des Schweiggerschen Multiplicators, in: Schweigger, J., Schweigger-Seidel, W. (Eds.), Jahrbuch der Chemie und Physik. Verein zur Verbreitung von Naturkenntniss, Halle, pp. 137–166.

Omar, A., 1990. Effect of brine composition and clay content on the permeability damage of sandstone cores. Journal of Petroleum Science and Engineering 4, 245–256.

O'Sullivan, M.J., Pruess, K., Lippmann, M.J., 2001. State of the art of geothermal reservoir simulation. Geothermics 30, 395–429.

Page, R., Wenk, H.R., 1979. Phyllosilicate alteration of plagioclase studied by transmission electron microscopy. Geology 7, 393–397.

Pape, H., Clauser, C., Iffland, J., 1999. Permeability prediction based on fractal pore-space geometry. Geophysics 64, 1447–1460.

Parkhurst, D., Appelo, C., 1999. User's guide to PHREEQC (Version 2) - A computer program for speciation, batch-reaction, one-dimensional transport, and inverse geochemical calculations. U.S. Geological Survey Water-Resources Investigations Report 99-4259, 312 p.

Pettijohn, F., Potter, P., Siever, R., 1987. Sand and sandstone. Springer.

Piwinskii, A.J., Weed, H.C., 1976. Study of rock-solution interaction and its effect on Archie's Law. IEEE Transactions on Geoscience Electronics 14, 221–223.

Polak, A., Elsworth, D., Yasuhara, H., Grader, A., Halleck, P., 2003. Permeability reduction of a natural fracture under net dissolution by hydrothermal fluids. Geophysical Research Letters 30.

Putnis, A., 1992. Introduction to mineral sciences. Cambridge University Press.

Putnis, A., 2002. Mineral replacement reactions: From macroscopic observations to microscopic mechanisms. Mineralogical Magazine 66, 689–708.

Putnis, A., 2009. Mineral replacement reactions. Reviews in Mineralogy and Geochemistry 70, 87–124.

Putnis, A., Austrheim, H., 2010. Fluid-induced processes: Metasomatism and metamorphism. Geofluids 10, 254–269.

Putnis, A., John, T., 2010. Replacement processes in the earth's crust. Elements 6, 159–164.

Putnis, A., Mauthe, G., 2001. The effect of pore size on cementation in porous rocks. Geofluids 1, 37–41.

Reed, S.J.B., 2005. Electron microprobe analysis and scanning electron microscopy in geology. Cambridge University Press, Cambridge, New York, Melbourne. 2 edition.

Regenspurg, S., Wiersberg, T., Brandt, W., Huenges, E., Saadat, A., Schmidt, K., Zimmermann, G., 2010. Geochemical properties of saline geothermal fluids from the in-situ geothermal laboratory Groß Schönebeck (Germany). Chemie der Erde - Geochemistry 70, Supplement 3, 3–12.

Revil, A., Cathles, L. M., I., Losh, S., Nunn, J.A., 1998. Electrical conductivity in shaly sands with geophysical applications. Journal of Geophysical Research 103, 23925–23936.

Revil, A., Glover, P.W.J., 1997. Theory of ionic-surface electrical conduction in porous media. Physical Review B 55, 1757–1773.

Revil, A., Glover, P.W.J., 1998. Nature of surface electrical conductivity in natural sands, sandstones, and clays. Geophysical Research Letters 25, 691–694.

Rimstidt, J.D., Barnes, H.L., 1980. The kinetics of silica-water reactions. Geochimica et Cosmochimica Acta 44, 1683–1699.

Rink, M., Schopper, J.R., 1976. Pore structure and physical properties of porous sedimentary rocks. Pure and Applied Geophysics 114, 273–284.

Robens, E., Benzler, B., Büchel, G., Reichert, H., Schumacher, K., 2002. Investigation of characterizing methods for the microstructure of cement. Cement and Concrete Research 32, 87–90.

Roberts, J.J., Bonner, B.P., Kasameyer, P.W., 2001. Electrical resistivity measurements of intact and fractured geothermal reservoir rocks, in: Proceedings Twenty-Sixth Workshop on Geothermal Reservoir Engineering, Stanford University, Stanford, California.

Roberts, J.J., Wildenschild, D., 2004. Electrical properties of sand-clay mixtures containing trichloroethylene and ethanol. Journal of Environmental and Engineering Geophysics 9, 1–10.

Roberts, J.N., Schwartz, L.M., 1985. Grain consolidation and electrical conductivity in porous media. Physical Review B 31, 5990–5997.

Rowe, A.M., Chou, J.C.S., 1970. Pressure-volume-temperature-concentration relation of aqueous sodium chloride solutions. Journal of Chemical & Engineering Data 15, 61–66.

Ruffet, C., Darot, M., Guéguen, Y., 1995. Surface conductivity in rocks: A review. Surveys in Geophysics 16, 83–105.

Rutqvist, J., Tsang, C.F., 2003. Analysis of thermal-hydrologic-mechanical behavior near an emplacement drift at Yucca Mountain. Journal of Contaminant Hydrology 62-63, 637–652.

Sahimi, M., 1994. Applications of percolation theory. Taylor & Francis.

Scholz, C.H., Léger, A., Karner, S.L., 1995. Experimental diagenesis: Exploratory results. Geophysical Research Letters 22, 719–722.

Schön, J., 1996. Physical Properties of Rocks - Fundamentals and Principles of Petrophysics. volume 18 of *Handbook of geophysical exploration - seismic exploration*. Pergamon.

Schott, J., Pokrovsky, O.S., Oelkers, E.H., 2009. The link between mineral dissolution/precipitation kinetics and solution chemistry. Reviews in Mineralogy and Geochemistry 70, 207–258.

Schutjens, P., 1991. Experimental compaction of quartz sand at low effective stress and temperature conditions. Journal of the Geological Society 148, 527–539.

Sen, P.N., Goode, P.A., 1992. Influence of temperature on electrical conductivity on shaly sands. Geophysics 57, 89–96.

Sen, P.N., Goode, P.A., Sibbit, A., 1988. Electrical conduction in clay bearing sandstones at low and high salinities. Journal of Applied Physics 63, 4832–4840.

Shao, H., Dmytrieva, S.V., Kolditz, O., Kulik, D.A., Pfingsten, W., Kosakowski, G., 2009. Modeling reactive transport in non-ideal aqueous - solid solution system. Applied Geochemistry 24, 1287–1300.

Somerton, W., 1992. Effects of temperature on rock properties, in: Somerton, W. (Ed.), Thermal properties and temperature-related behavior of rock/fluid systems. Elsevier. volume 37 of *Developments in Petroleum Science*, pp. 181–198.

Somerton, W., Janah, A., Ashquar, P., 1981. Thermal expansion of fluid-saturated rocks under stress. SPWLA 22nd Annual Logging Symposium, Mexico City, June 1981 , 1–8.

Song, I., Renner, J., 2008. Hydromechanical properties of Fontainebleau sandstone: Experimental determination and micromechanical modeling. Journal of Geophysical Research 113, B09211–.

Stillings, L., Brantley, S.L., 1995. Feldspar dissolution at 25 °C and pH 3: Reaction stoichiometry and the effect of cations. Geochimica et Cosmochimica Acta 59, 1483–1496.

Stober, I., Bucher, K., 2002. Water-rock interaction. Kluwer Academic Publishers.

Taron, J., Elsworth, D., 2009. Thermal-hydrologic-mechanical-chemical processes in the evolution of engineered geothermal reservoirs. International Journal of Rock Mechanics and Mining Sciences 46, 855–864.

Taron, J., Elsworth, D., 2010. Coupled mechanical and chemical processes in engineered geothermal reservoirs with dynamic permeability. International Journal of Rock Mechanics and Mining Sciences 47, 1339–1348.

Taylor, S., Barker, R., 2006. DC electrical properties of Permo-Triassic sandstone. Geological Society, London, Special Publications 263, 199–217.

Tenthorey, E., Cox, S.F., Todd, H.F., 2003. Evolution of strength recovery and permeability during fluid-rock reaction in experimental fault zones. Earth and Planetary Science Letters 206, 161–172.

Tenthorey, E., Fitz Gerald, J.D., 2006. Feedbacks between deformation, hydrothermal reaction and permeability evolution in the crust: Experimental insights. Earth and Planetary Science Letters 247, 117–129.

Tenthorey, E., Scholz, C.H., 2002. Mapping secondary mineral formation in porous media using heavy metal tracers. Journal of Geophysical Research 107.

Tenthorey, E., Scholz, C.H., Aharonov, E., Léger, A., 1998. Precipitation sealing and diagenesis - 1. Experimental results. Journal of Geophysical Research 103, 23951–23967.

Terzaghi, K., 1923. Die Berechnung der Durchlässigkeitsziffer des Tones aus dem Verlauf der hydrodynamischen Spannungserscheinungen. Sitzungsber. Akad. Wiss. Wien, Math. Naturwiss. Kl., Abt. 2A 132, 105–124.

Tester, J.W., Worley, W., Robinson, B.A., Grigsby, C.O., Feerer, J.L., 1994. Correlating quartz dissolution kinetics in pure water from 25 to 625°C. Geochimica et Cosmochimica Acta 58, 2407–2420.

Toby, B., 2001. EXPGUI, a graphical user interface for GSAS. Journal of Applied Crystallography 34, 210–213.

Trautwein, U., Huenges, E., 2005. Poroelastic behaviour of physical properties in Rotliegend sandstones under uniaxial strain. International Journal of Rock Mechanics and Mining Sciences 42, 924–932.

Tsuzuki, Y., Suzuki, K., 1980. Experimental study of the alteration process of labradorite in acid hydrothermal solutions. Geochimica et Cosmochimica Acta 44, 673–683.

Ulusay, R., Hudson, J., 2007. The complete ISRM suggested methods for rock characteriszation, testing and monitoring: 1974-2006. International Society for Rock Mechanics (ISRM). chapter Suggested Methods for Determining Water Content, Porosity, Density, Absorption and Related Properties and Swelling and Slake-Durability Index Properties. pp. 85–98.

Volkov, A.G., Paula, S., Deamer, D.W., 1997. Two mechanisms of permeation of small neutral molecules and hydrated ions across phospholipid bilayers. Bioelectrochemistry and Bioenergetics 42, 153–160. 13th International Symposium on Bioelectrochemistry and Bioenergetics.

Vuataz, F.D., Czernichowski-Lauriol, I., Fouillac, C., Detoc, S., 1989. Chemical study of a low temperature geothermal fluid in a Triassic sandstone aquifer: Scaling potential and fluid treatment (Melleray, France). Geothermics 18, 313–320.

Vuataz, F.D., Giroud, N., 2011. Keynote: Review of geochemical problems and mitigation during the production of geothermal reservoirs. Mineralogical Magazine 75, 2104. Goldschmidt conference 2011 abstract.

Wagner, K.W., 1914. Erklärung der dielektrischen Nachwirkungsvorgänge auf Grund Maxwellscher Vorstellungen. Electrical Engineering (Archiv für Elektrotechnik) 2, 371–387.

Walther, J.V., 1996. Relation between rates of aluminosilicate mineral dissolution, pH, temperature, and surface charge. American Journal of Science 296, 693–728.

Watson, E.B., Brenan, J.M., 1987. Fluids in the lithosphere - 1. Experimentally-determined wetting characteristics of CO_2–H_2O fluids and their implications for fluid transport, host-rock physical properties, and fluid inclusion formation. Earth and Planetary Science Letters 85, 497–515.

Waxman, M.H., Smits, L.J.M., 1968. Electrical conductivities in oil-bearing shaly sands. Transactions of the American Institute of Mining, Metallurgical, and Petroleum Engineers 243, 107–122.

Waxman, M.H., Thomas, E.C., 1974. Electrical conductivities in shaly sands - I. The relation between hydrocarbon saturation and resistivity index; II. The temperature coefficient of electrical conductivity. Transactions of the American Institute of Mining, Metallurgical, and Petroleum Engineers 257, 213–225.

Weed, H.C., Piwinskii, A.J., Keller, P.R., 1977. Time dependent electrical properties of rock-solution systems. SPE International Oilfield and Geothermal Chemistry Symposium, 27-28 June 1977, San Diego, California , 213–220.

Westermarck, S., 2000. Use of mercury porosimetry and nitrogen adsorption in characterisation of the pore structure of mannitol and microcrystalline cellulose powders, granules and tablets. Ph.D. thesis. University of Helsinki.

White, S.P., Mroczek, E.K., 1998. Permeability changes during the evolution of a geothermal field due to the dissolution and precipitation of quartz. Transport in Porous Media 33, 81–101.

Wildenschild, D., Roberts, J.J., Carlberg, E.D., 2000. On the relationship between microstructure and electrical and hydraulic properties of sand-clay mixtures. Geophysical Research Letters 27, 3085–3088.

Williams, J., Bandstra, J., Pollard, D., Brantley, S., 2010. The temperature dependence of feldspar dissolution determined using a coupled weathering-climate model for Holocene-aged loess soils. Geoderma 156, 11–19.

Wirth, R., 2004. Focused ion beam (FIB): A novel technology for advanced application of micro- and nanoanalysis in geosciences and applied mineralogy. European Journal of Mineralogy 16, 863–876.

Wirth, R., 2009. Focused ion beam (FIB) combined with SEM and TEM: Advanced analytical tools for studies of chemical composition, microstructure and crystal structure in geomaterials on a nanometre scale. Chemical Geology 261, 217–229.

Xiao, X., Wirth, R., Dresen, G., 2002. Diffusion creep of anorthite-quartz aggregates. Journal of Geophysical Research 107, 2279–.

Xu, T., Sonnenthal, E., Spycher, N., Pruess, K., 2006. TOUGHREACT - A simulation program for non-isothermal multiphase reactive geochemical transport in variably saturated geologic media: Applications to geothermal injectivity and CO_2 geological sequestration. Computers and Geosciences 32, 145–165.

Yardley, B.W., 2009. The role of water in the evolution of the continental crust. Journal of the Geological Society 166, 585–600.

Yasuhara, H., Elsworth, D., 2006. A numerical model simulating reactive transport and evolution of fracture permeability. International Journal for Numerical and Analytical Methods in Geomechanics 30, 1039–1062.

Yasuhara, H., Elsworth, D., Polak, A., 2004. Evolution of permeability in a natural fracture: Significant role of pressure solution. Journal of Geophysical Research 109, –.

Yasuhara, H., Kinoshita, N., Ohfuji, H., Lee, D.S., Nakashima, S., Kishida, K., 2011. Temporal alteration of fracture permeability in granite under hydrothermal conditions and its interpretation by coupled chemo-mechanical model. Applied Geochemistry , –.

Yasuhara, H., Polak, A., Mitani, Y., Grader, A.S., Halleck, P.M., Elsworth, D., 2006. Evolution of fracture permeability through fluid-rock reaction under hydrothermal conditions. Earth and Planetary Science Letters 244, 186–200.

Zhang, L., Lüttge, A., 2007. Al,Si order in albite and its effect on albite dissolution processes: A Monte Carlo study. American Mineralogist 92, 1316–1324.

Zhang, L., Lüttge, A., 2009a. Morphological evolution of dissolving feldspar particles with anisotropic surface kinetics and implications for dissolution rate normalization and grain size dependence: A kinetic modeling study. Geochimica et Cosmochimica Acta 73, 6757–6770.

Zhang, L., Lüttge, A., 2009b. Theoretical approach to evaluating plagioclase dissolution mechanisms. Geochimica et Cosmochimica Acta 73, 2832–2849.

Zhu, C., Lu, P., 2009. Alkali feldspar dissolution and secondary mineral precipitation in batch systems: 3. Saturation states of product minerals and reaction paths. Geochimica et Cosmochimica Acta 73, 3171–3200.

Zhu, C., Veblen, D.R., Blum, A.E., Chipera, S.J., 2006. Naturally weathered feldspar surfaces in the Navajo Sandstone aquifer, Black Mesa, Arizona: Electron microscopic characterization. Geochimica et Cosmochimica Acta 70, 4600–4616.

Zisser, N., Nover, G., 2009. Anisotropy of permeability and complex resistivity of tight sandstones subjected to hydrostatic pressure. Journal of Applied Geophysics 68, 356–370.

Zuddas, P., Michard, G., 1993. Experimental mineral-fluid interaction in the Na-Ca-(Sr)-Al-Si system. European Journal of Mineralogy 5, 807–818.

List of Figures

Scientific Technical Report STR 12/07
DOI: 10.2312/GFZ.b103-12079

Scientific Technical Report STR 12/07
DOI: 10.2312/GFZ.b103-12079

Scientific Technical Report STR 12/07
DOI: 10.2312/GFZ.b103-12079

List of Tables

Scientific Technical Report STR 12/07
DOI: 10.2312/GFZ.b103-12079

Scientific Technical Report STR 12/07
DOI: 10.2312/GFZ.b103-12079

Experimental Details

Flow-through Experiments

- Experiment **ft-s-1**: Stepwise heating and cooling of a L-sandwich was performed. The confined grain pack consisted of 2 g labradorite-andesine grains. The quartz-feldspar mass ratio in this experiment is not comparable to the Flechtinger sandstone. T-steps were performed with constant T-stages of 40, 150, 172, 100, and 46 °C with a duration of approximately 1, 36, 4, 1, and 1 d, respectively. At each T-stage k was measured at least once.

- Experiment **ft-s-2**: Stepwise heating and cooling of a QL-sandwich was performed. 7.215 g quartz and 2.016 g labradorite-andesine were used for the confined grain pack. T-steps were performed with constant T-stages of 43, 115, 153, 174, 146, and 88 °C with a duration of approximately 1, 1, 5, 14, 1 and 1 d, respectively. k was measured at irregular intervals during the experiment and at least once per T-stage.

- Experiment **ft-s-3**: Stepwise heating and cooling of a QLM-sandwich was performed. The confined grain pack was composed of 1.447 g quartz, 0.229 g labradorite-andesine, and 0.33 g microcline grains. T-steps were performed with constant T-stages of 60, 70, 150, and 70 °C with a duration of approximately 2, 46, 6, and 18 d, respectively. Due to the very low permeability of the specific Fontainebleau sandstone, which was used as the confining porous discs ($k \approx 3.8 \times 10^{-19}$ m^2), only two k measurements were performed. σ_r was continuously monitored. At the end of the experiment a fluid sample was taken on the downstream side of the sample through a pressure relief valve PRV.

- Experiment **ft-s-4**: Stepwise heating and cooling of a QLM-sandwich was performed. The confined grain pack consisted of 1.446 g quartz, 0.233 g labradorite-andesine, and 0.328 g microcline grains. T-steps were performed with constant T-stages of 40, 71, 150, 71, 150, and 70 °C with a duration of approximately 8, 5, 15, 18, 14, and 5 d, respectively. k measurements were performed once per T-stage. At approximately 30 d run duration of the experiment a fluid sample was taken on the downstream side of the sample through a PRV. To prevent the porous PTFE discs from collapsing p_c and p_p were set to lower values than in the previous experiments ($p_c = 5 \times 10^6$ Pa and $p_p = 2.5 \times 10^6$ Pa).

- Experiment **ft-s-5**: Stepwise heating and cooling of a QLMI-sandwich was performed. 1.328 g quartz, 0.211 g labradorite-andesine, 0.302 g microcline, and 0.164 g illite were used for the granular aggregate. T-steps were performed with constant T-stages of 40, 71, 150, 71, 150, and 70 °C with a duration of approximately 8, 5, 15, 18, 14, and 5 d, respectively. Due to the very low permeability of this specific sandwich ($k \approx 7.6 \times 10^{-19}$ m^2) only three measurements were performed. To prevent the porous PTFE discs from collapsing p_c was set to 5×10^6 Pa and p_p was set to 2.5×10^6 Pa.

Scientific Technical Report STR 12/07
DOI: 10.2312/GFZ.b103-12079

- Experiment **ft-Fo-6**: Stepwise heating and cooling of a Fontainebleau SST sample was performed. T-steps were made with constant T-stages of 40, 70, 100, 140, 162, 98, 79 and 40 °C with a duration of approximately 1, 1, 6, 2, 22, 1, 1, and 1 d, respectively. k measurements were carried out at least once per T-stage. σ_r was continuously monitored. At the end of the experiment a fluid sample was taken on the downstream side of the sample.

- Experiment **ft-Fo-P-7**: Fluid exchange experiments (H_2O against 0.1 mol/L $NaCl_{aq}$) were performed with a porous PTFE core ($\phi = 20$ %) and a Fontainebleau sandstone core ($\phi = 14.25$ %) at 60 °C. k of the PTFE core was measured prior and after the experiment. k of the Fontainebleau sandstone core was measurered only once. σ_r measurements were performed continuously during the Fontainebleau sandstone experiment. In the PTFE experiment σ_r measurements showed significant noise and failed after approximately 20 d. Stepwise heating from 60 to 150 °C was performed with H_2O and 0.1 mol/L $NaCl_{aq}$ as the pore fluids in the Fontainebleau sandstone and PTFE experiments, respectively, following the fluid exchange procedure.

- Experiment **ft-Fl-8**: Stepwise heating and cooling of a Flechtinger sandstone core was performed. k measurements were performed at the end of each T-stage. Apart from that stagnant flow conditions prevailed during each T-stage. σ_r was continuously monitored. T-steps were performed with constant T-stages of 30, 51, 90, 164, 90, 51, and 90 °C with a duration of approximately 1, 39, 14, 39, 8, 11, and 16 d, respectively.

- Experiment **ft-Fl-9**: Stepwise heating and cooling of a Flechtinger sandstone sample was performed at stagnant conditions. σ_r was continuously monitored. T-steps were performed with constant T-stages of 70, 150, 70, 42, 70, 150, and 70 °C with a duration of approximately 24, 3, 14, 4, 17, 7, and 16 d, respectively. A k measurement and a fluid sampling were performed during the third 70 °C-stage. A further k measurement was performed at the end of the experiment. σ_r was continuously monitored.

- Experiment **ft-Fl-10**: Stepwise heating and cooling of a Flechtinger sandstone was performed at stagnant conditions with 1 mol/L $NaCl_{aq}$ as the pore fluid. k measurements were performed at least at the beginning and the end of each T-stage. σ_r was continuously monitored. T-steps were performed with an up-ramp of 41, 50, 70, 90, 110, 131, and 151 °C, and a down-ramp with the same T-steps. The duration of each T-stage was approximately $1 - 2$ d except the 151 °C-stage and the second 70 °C-stage which lasted approximately 5 d and 22 d, respectively.

- Experiment **ft-Fl-11**: A fluid exchange experiment was performed with a Flechtinger sandstone sample in which H_2O was exchanged against NaCl-solutions up to a concentration of 0.5 mol/L at 42 °C. Two of these fluid exchange cycles were performed. Between the cycles T was increased to 74 °C with H_2O as the initial pore fluid. During the experiment k was measured 12 times at irregular intervals. The duration of the first 42 °C-stage was approximately 22 d. The second 42 °C-stage and the 74 °C-stage lasted approximately 13 d each. σ_r was continuously monitored.

- Experiment **ft-Fl-12**: Fluids of various composition were injected under isothermal conditions from a BR-300 autoclave into a Flechtinger sandstone sample at 70 °C. Fluid

Scientific Technical Report STR 12/07
DOI: 10.2312/GFZ.b103-12079
Deutsches GeoForschungsZentrum GFZ

compositions ranged from H_2O, over solutions in contact with quartz–labradorite-andesine–microcline grains and quartz–labradorite-andesine–microcline–illite–calcite grains, to $NaCl_{aq}$ solutions with a concentration of up to 2 mol/L. During the first 40 d of the experiment H_2O was the pore fluid. The following fluid exchange sequence started with the solution resulting from the QLM batch experiment with $\sigma_f = 15.97 \times 10^{-3}$ S/m. At 61 d a fluid with $\sigma_f = 10.33 \times 10^{-3}$ S/m resulting from the QLMIC batch experiment was injected into the HPT-permeameter. This was followed by the injection of 0.04 mol/L $NaCl_{aq}$ with $\sigma_f = 477 \times 10^{-3}$ S/m at 72 d. Subsequently this fluid was replaced with 0.01 and 0.001 mol/L $NaCl_{aq}$ with $\sigma_f = 122.7$ and 14.7×10^{-3} S/m at 84 and 85 d, respectively. After this procedure the sample was flushed with H_2O. T-steps were performed with constant T-stages of 40, 70, and 150 °C with a duration of approximately 19, 106, and 8 d, respectively. k was measured several times at irregular intervals during the experiment. σ_r was continuously monitored.

- Experiment **ft-Fl-13**: A small Flechtinger sandstone sample ($L = 20 \times 10^{-3}$ m, $r = 3 \times 10^{-3}$ m) was heated and cooled stepwise. The performed T-steps were 43, 53, 71, 89, 108, 150, 131, 114, 96, 71, and 53 °C. The first two T-stages at 43 °C and 53 °C lasted 8 and 7 d, respectively. The other T-stages lasted approximately 1 d each. k measurements were performed at least once per T-stage. σ_r was continuously monitored using a two electrode arrangement.

Batch Experiments

- Experiment **b-QL-1**: A series of experiments with quartz and labradorite-andesine grains or a mixture of both mineral phases was conducted. Either 2 ± 0.016 g of the pure mineral phases or 1 ± 0.012 g of each mineral phase in the mixture were used as starting materials in each PTFE autoclave. This mass ratio does not reflect the mass ratio of quartz and feldspar determined for the Flechtinger sandstone. 5×10^{-3} L H_2O were used as the starting fluid. 4 experiments were conducted with each starting material which were stopped after approximately 5, 8, 13, and 22 d, respectively. A blank experiment with a duration of 21 d was conducted to identify the input of dissolved ionic species from the autoclaves. At the end of each experiment the fluid was sampled according to the technique described in Section 3.3.1 and the solids were recovered for SEM and XRD investigations.

- Experiment **b-QL-2**: A series of experiments was conducted in the same way as described above. Either 1 ± 0.004 g of the pure mineral phases or 0.5 ± 0.007 g of each mineral phase in the mixture were used as the starting material in each PTFE autoclave. 5×10^{-3} L H_2O were used as the starting fluid. 7 experiments were conducted with each starting material which were stopped after approximately 1, 2, 3, 6, 10, 14, and 20 d, respectively. At the end of each experiment a fluid aliquot was sampled according to the technique described in Section 3.3.1. First σ_f and then the pH value were measured in the rest of the fluid in the autoclave. This sequence was important because the used pH-probe releases K^+ ions into the solution and thus changes σ_f. The solids were recovered for SEM and XRD investigations.

- Experiment **b-QLM-3**: A series of experiments with quartz, labradorite-andesine, and microcline grains was performed. 0.724 ± 0.004 g quartz, 0.115 ± 0.003 g labradorite-

andesine, and 0.164 ± 0.004 g microcline were used as the starting materials in each PTFE autoclave. 5 experiments were performed with 5×10^{-3} L H_2O and 5 experiments were performed with 5×10^{-3} L 0.1 mol/L $NaCl_{aq}$ as the starting fluids. With each starting fluid a blank experiment lasting approximately 7 d was conducted. The experiments were stopped after approximately 1, 2, 5, 6, and 7 d. At the end of each experiment a fluid aliquot was sampled according to the technique described in Section 3.3.1. σ_f of the rest of the fluid was measured in the autoclave. The solids were recovered for SEM and XRD investigations. The solids resulting from the experiments with 0.1 mol/L $NaCl_{aq}$ were rinsed with H_2O prior to drying and preparation for SEM and XRD investigations.

- Experiment **b-QLM-4**: A single experiment was carried out with quartz, labradorite-andesine, and microcline grains in a PTFE autoclave. 0.724 g quartz, 0.115 g labradorite-andesine, and 0.164 g microcline were used as the starting materials. σ_f was measured at irregular intervals 20 times during the experiment. T-steps were performed with constant T-stages of 70, 150, 70, and again 150 °C with a duration of approximately 17, 7, 22, and 3 d, respectively. At the end of each experiment a fluid aliquot was sampled according to the technique described in Section 3.3.1. σ_f of the rest of the fluid was measured in the autoclave and the solids were recovered for SEM investigation.

- Experiment **b-QLM-5**: A single experiment was conducted with quartz, labradorite-andesine, and microcline grains in a PTFE autoclave at a constant temperature of 150 °C. 0.724 g quartz, 0.118 g labradorite-andesine, and 0.164 g microcline were used as the starting materials. Due to vapor diffusion mainly through the lid of the autoclave the fluid volume decreased from initially 5×10^{-3} L to 1.2×10^{-3} L at the end of the experiment, thus decreasing the fluid-solid ratio in the autoclave significantly. σ_f was measured at irregular intervals 8 times during the experiment. At the end of the experiment a fluid aliquot was sampled according to the technique described in Section 3.3.1 and the solids were recovered for EMPA, SEM and XRD investigation.

- Experiment **b-QLM-6**: A single experiment was conducted with quartz, labradorite-andesine, and microcline grains in a BR-100 autoclave. 1.447 g quartz, 0.23 g labradorite-andesine, and 0.33 g microcline were used as the starting materials. T-steps were performed with constant T-stages of 150, 70, and 25 °C with a duration of approximately 10, 73, and 58 d, respectively. A magnetic stirrer was used rotating with 1400 rounds per minute during the first 10 d of the experiment. After this period the fluid was sampled through the dip tube of the autoclave with an attached 0.2×10^{-6} m syringe filter. The fluid sample was centrifuged afterwards with 3500 rounds per minute for 600 s. An aliquot of this sample was taken according to the technique described below in Section 3.3.1. The rest of the fluid was inserted into a PTFE autoclave for the remainder of the experiment. The solids were sampled for SEM investigation. After 66 d total duration 0.01 ± 0.004 g of quartz, labradorite-andesine, and microcline were inserted into the PTFE autoclave as potential crystallization sites. σ_f was measured at irregular intervals 23 times during the experiment.

- Experiment **b-QLM-7**: A single experiment was carried out with quartz, labradorite-andesine, and microcline grains in a PTFE autoclave with a 150 to 70 °C T-step. 0.725 g quartz, 0.117 g labradorite-andesine, and 0.164 g microcline were used as the starting materials. The 150 °C-stage lasted the first 8 d, the subsequent 70 °C-stage lasted the

Scientific Technical Report STR 12/07
DOI: 10.2312/GFZ.b103-12079

remaining 33 d of the experiment. σ_f was measured at irregular intervals 9 times during the experiment. The solids were recovered and prepared for SEM investigation at the end of the experiment.

- Experiment **b-QLM-8**: A single experiment was performed with quartz, labradorite-andesine, and microcline grains in a PTFE autoclave with a 150 to 70 °C T-step. 0.723 g quartz, 0.117 g labradorite-andesine, and 0.165 g microcline were used as the starting materials. The 150 °C-stage lasted the first 37 d of the experiment, the subsequent 70 °C-stage lasted the remaining 33 d of the experiment. σ_f was measured at irregular intervals 12 times during the experiment. The solids were recovered and prepared for SEM investigation at the end of the experiment.

- Experiment **b-QLM-9**: A single experiment was carried out with quartz, labradorite-andesine, and microcline grains in a PTFE autoclave with a 150 to 70 °C T-step. 0.726 g quartz, 0.116 g labradorite-andesine, and 0.165 g microcline were used as the starting materials. The 150 °C-stage lasted the first 28 d of the experiment, the subsequent 70 °C-stage lasted the remaining 35 d of the experiment. σ_f was measured at irregular intervals 10 times during the experiment. The solids were recovered and prepared for SEM investigation at the end of the experiment.

- Experiment **b-QLMI-10**: A single experiment was carried out with quartz, labradorite-andesine, microcline, and illite grains in a PTFE autoclave at a constant temperature of 150 °C. 0.665 g quartz, 0.103 g labradorite-andesine, 0.152 g microcline, and 0.081 g illite were used as the starting materials. All other experimental parameters are the same as in experiment b-QLM-5.

- Experiment **b-QLMI-11**: A single experiment was conducted with quartz, labradorite-andesine, microcline, and illite grains in a PTFE autoclave with a 150 to 70 °C T-step. This experiment was performed with the same experimental parameters as experiment b-QLM-7 except that 0.663 g quartz, 0.107 g labradorite-andesine, 0.149 g microcline, and 0.083 g illite were used as the starting materials.

- Experiment **b-QLMI-12**: A single experiment was carried out with quartz, labradorite-andesine, and microcline grains in a PTFE autoclave with a 150 to 70 °C T-step. 0.665 g quartz, 0.107 g labradorite-andesine, 0.151 g microcline, and 0.082 g illite were used as the starting materials. All other experimental parameters were the same as in experiment b-QLM-8.

- Experiment **b-QLMI-13**: A single experiment was performed with quartz, labradorite-andesine, and microcline grains in a PTFE autoclave with a 150 to 70 °C T-step. 0.665 g quartz, 0.105 g labradorite-andesine, 0.151 g microcline, and 0.082 g illite were used as the starting materials. All other experimental parameters were the same as in experiment b-QLM-9.

- Experiment **b-QLMIC-14**: A single experiment was conducted with quartz, labradorite-andesine, microcline, illite, and calcite grains in a PTFE autoclave at 70 °C. 6.431 g quartz, 1.025 g labradorite-andesine, 1.449 g microcline, 0.784 g illite, and 0.312 g calcite were used as the starting materials. σ_f was measured 4 times at irregular intervals during the experiment. At the end of the experiment pH was measured on an aliquot fluid sample.

- Experiment **b-Fl-15**: A single experiment was performed with a 0.931 g fragment of Flechtinger sandstone in a PTFE autoclave. T-steps were conducted with constant T-stages of 70, 150, 70, 150, 70, 150, and 70 °C with a duration of approximately 21, 4, 16, 6, 22, 3, and 15 d, respectively. σ_f was measured 33 times at irregular intervals throughout the experiment. At the end of the experiment a fluid sample was taken according to the procedure described in Section 3.3.1 and the solid material was recovered and prepared for SEM investigation.

- Experiment **b-Fl-16**: A single experiment was carried out with a 66.85 g Flechtinger sandstone core in a BR-300 Ar-pressurized batch reactor (p.b.r.) at 5×10^6 Pa. T-steps were performed with constant T-stages of 70, 150, 70, 150 and 70 °C with a duration of approximately 24, 10, 22, 3, and 22 d, respectively. Throughout the experiment 11 fluid samples with an approximate volume of 4×10^{-3} L each were taken through a dip tube while the BR-300 autoclave was kept at constant temperature and pressure. After σ_f measurements the samples were prepared for further analysis according to the technique described in Section 3.3.1. At the end of the experiment pH was measured on an aliquot sample and the solid material was recovered and prepared for SEM and MIP investigation.

- Experiment **b-Fl-17**: A single experiment was conducted with a jacketed Flechtinger sandstone core with a length of 0.1 m, a radius of 0.025 m, and a mass of 468.94 g at 70 ± 2 °C constant temperature. The set-up and the procedure of the experiment are described in Section 3.2.2. At the end of the experiment the bores in the steel plugs and the Swagelok fittings were dried and cleaned. Subsequently, the pore fluid was sampled with the aid of an Ar gas flow at a constant upstream pressure of 0.1×10^6 Pa. Sample tubes on the downstream side of the assembly were sealed against the atmosphere with Parafilm® to prevent fluid loss by vaporization. Using this method three pore fluid samples were recovered with a cumulative volume of 6.5×10^{-3} L. The second sample was assumed to best approximate the actual pore fluid composition because here the fewest mixing with fluids potentially remaining in the upstream or downstream steel plug occurred. Aliquots were sampled and prepared for cation and anion analyses according to the technique described in Section 3.3.1. σ_f and pH were measured on the original and an aliquot sample, respectively.

Scientific Technical Report STR 12/07
DOI: 10.2312/GFZ.b103-12079
Deutsches GeoForschungsZentrum GFZ

Acknowledgements

I would like to thank Harald Milsch, my advisor at the Helmholtz Centre Potsdam - German Research Centre for Geosciences GFZ, for his support during my time at the GFZ and his constructive suggestions, which helped to improve my work. I would also like to thank my advisor Jörg Renner, professor of experimental geophysics at the Ruhr Universität Bochum, for very fruitful discussions and several eye-openers on geophysics. Furthermore, I would like to express my gratitude to Thomas Müller, assistant professor at the Institute for Mineralogy-Petrology, and Michael Alber, professor of engineering geology and rock engineering at the Ruhr Universität Bochum, for evaluating my work.

This study was performed while I was employed in the Reservoir Technologies Section at the GFZ. Therefore, I would like to thank Ernst Huenges, head of the section, for giving me the opportunity to pursue my PhD project during my time at the GFZ. I am also grateful for the help by the members of the Reservoir Technologies Section, especially Tanja Ballerstedt, Ronny Giese, Andreas Kratz, Siegfried Raab, and Erik Spangenberg, who were always willing to solve technical problems regarding the experimental equipment and made valuable suggestions for carrying out and interpreting the experiments. The GFZ machine shop staff and Andreas Kratz gave technical support for the flow-through apparatuses.

The GFZ provided a wide variety of analytical techniques which were employed in this study. I wish to thank Rudolf Naumann and Hans-Peter Nabein for performing the XRD measurements. Tobias Meier helped me with the MIP and Dieter Rhede performed the electron microprobe analyses and discussed the results and the limitations of the method with me. Richard Wirth operated the TEM, and his profound knowledge of microscopic structures on mineral surfaces and the capabilities of TEM helped to constrain the reaction mechanism of the observed reactions. I want to thank Anja Schreiber for the preparation of the TEM foils with the FIB. Erik Rybacki, Tobias Meier and Dmitri Naumov supported me in performing and interpreting the X-ray CT scans. Monika Koch-Müller and Fiorenza Deon helped me with analytical problems, especially with spectroscopic and XRD problems. Sabine Tonn and Andrea Gottsche skillfully performed ICP-OES and IC measurements, respectively. I would also like to thank Stefan Gehrmann, Hartmut Liep, and Marina Ospald for the preparation of solid starting materials and thin sections. Sandra Kons did an internship at the GFZ under my supervision, and helped me with preparing solid starting materials and performing batch experiments.

I want to thank my colleagues Jonathan Banks, Henning Francke, Dmitri Naumov, Thomas Reinsch, and Matthis Thorade, who also were/are PhD students at the GFZ, for fruitful discussions on various aspects of my work and PhD projects in general. Furthermore, I would like to express my gratitude to Eva Zumhasch for proof-reading the manuscript. This work was possible thanks to financial support by the Federal Ministry for the Environment, Nature Conservation and Nuclear Safety under grants BMU 0327682 and BMU 0325069A as well as by the Federal Ministry of Education and Research under grant BMBF 03G0671A.

ISSN 1610-0956